

# Radiation Shielding during Deep-Space Missions: Dose Measurements, Monte Carlo Simulations, and Nuclear Cross-Sections

**Strahlungsabschirmung bei Weltraummissionen: Dosismessungen, Monte-Carlo-Simulationen und nukleare Wirkungsquerschnitte**

Zur Erlangung des Grades eines Doktors der Naturwissenschaften (Dr. rer. nat.)

Genehmigte Dissertation von Francesca Luoni aus Busto Arsizio

Tag der Einreichung: 11. Mai 2022, Tag der Prüfung: 18. Juli 2022

1. Gutachten: Prof. Dr. Marco Durante

2. Gutachten: Prof. Dr. Markus Roth

Darmstadt



TECHNISCHE  
UNIVERSITÄT  
DARMSTADT

Festkörperphysik

GSI Helmholtzzentrum für  
Schwerionenforschung

Biophysics

Radiation Shielding during Deep-Space Missions: Dose Measurements, Monte Carlo Simulations, and Nuclear Cross-Sections

Strahlungsabschirmung bei Weltraummissionen: Dosismessungen, Monte-Carlo-Simulationen und nukleare Wirkungsquerschnitte

Accepted doctoral thesis by Francesca Luoni

Date of submission: 11th May 2022

Date of thesis defense: 18th July 2022

Darmstadt

Bitte zitieren Sie dieses Dokument als:

URN: urn:nbn:de:tuda-tuprints-229657

URL: <http://tuprints.ulb.tu-darmstadt.de/22965>

Dieses Dokument wird bereitgestellt von tuprints,

E-Publishing-Service der TU Darmstadt

<http://tuprints.ulb.tu-darmstadt.de>

[tuprints@ulb.tu-darmstadt.de](mailto:tuprints@ulb.tu-darmstadt.de)

Die Veröffentlichung steht unter folgender Creative Commons Lizenz:

Namensnennung – Weitergabe unter gleichen Bedingungen 4.0 International

<https://creativecommons.org/licenses/by-sa/4.0/>

This work is licensed under a Creative Commons License:

Attribution–ShareAlike 4.0 International

<https://creativecommons.org/licenses/by-sa/4.0/>

How well questions of science can be answered to some extent depends on the techniques available at the time.

Nikjoo et al., *Int. J. Radiat. Biol.* (1998)



---

# Abstract

---

Deep-space radiation is among the biggest hindrances to human space exploration. Therefore, radiation protection in space is a very active field of research. Passive shielding is currently the most promising radiation protection strategy and it consists of adding shielding material to the walls of the spacecraft and the planetary bases. This thesis work presents results obtained in accelerator-based experimental campaigns with some of the most relevant ion beams for radiation protection in space and several structural, *in situ*, standard, and innovative shielding materials. Lithium-based hydrides stabilised with paraffin were proved to combine the promising dose attenuation properties of the pure hydrides and the mechanical and chemical stability of the paraffin, resulting in good candidate shielding materials for space missions. The experimental data were compared with the simulation results of the most commonly used Monte Carlo codes in this field of research, namely FLUKA, PHITS, and Geant4. The simulations showed significant and systematic differences among the codes mainly due to the different implemented nuclear cross-section models. Therefore, the last part of the work focuses on the presentation of the two nuclear cross-section databases (total reaction cross-sections and fragment production cross-sections) that were generated within this thesis work. The collected nuclear reaction cross-section data were compared to the parametrisations used in the Monte Carlo codes to understand which of them are more reliable. It was concluded that no parametrisation can well reproduce all the experimental data for every system and energy region. Therefore, an optimisation of the Tripathi parametrisation for reaction cross-sections was proposed. Additionally, an important gap in the experimental data was pointed out for high energies. The databases were uploaded online and made open access to provide the research communities interested in such data, with the possibility to access them and plot them alongside the parametrisations.



---

# Zusammenfassung

---

Die Strahlung im tiefen Weltraum ist eines der größten Hindernisse für die bemannte Raumfahrt. Daher ist der Weltraumstrahlenschutz ein sehr aktives Forschungsgebiet. Trotz einiger Einschränkungen ist die passive Abschirmung derzeit die vielversprechendste Abschirmungsstrategie. Bei dieser Methode werden Abschirmmaterialien an den Wänden des Raumfahrzeugs und der planetaren Basis angebracht. In dieser Arbeit werden Ergebnisse vorgestellt, welche in beschleunigerbasierten experimentellen Kampagnen mit für den Strahlenschutz im Weltraum relevanten Ionenstrahlen und verschiedenen strukturellen, *in situ*, Standard- und innovativen Abschirmmaterialien gewonnen wurden. Dabei hat sich gezeigt, dass mit Paraffin stabilisierte Hydride auf Lithiumbasis die vielversprechenden Dosisabschwächungseigenschaften der reinen Hydride mit der mechanischen und chemischen Stabilität von Paraffin kombinieren. Dies macht sie als zu guten Kandidaten für Abschirmmaterialien in Weltraummissionen. Die experimentellen Daten wurden mit den Simulationsergebnissen der in diesem Forschungsbereich am häufigsten verwendeten Monte-Carlo-Codes, FLUKA, PHITS und Geant4, verglichen. Die Simulationen zeigten signifikante systematische Unterschiede, welche hauptsächlich auf die unterschiedlichen in den Codes implementierten Kernreaktionsmodelle zurückzuführen sind. Daher konzentriert sich der letzte Teil der Arbeit auf die Präsentation von zwei Datenbanken mit Kernreaktions- und Produktionsquerschnitten, welche im Rahmen dieser Arbeit erstellt wurden. Die gesammelten Daten zu totalen nuklearen Reaktionsquerschnitten wurden mit den in den Monte-Carlo-Codes verwendeten Parametrisierungen verglichen, um zu verstehen welche von ihnen zuverlässiger sind. Es wurde festgestellt, dass keine Parametrisierung alle experimentellen Daten für jedes System und jeden Energiebereich gut reproduzieren kann. Daher wurde eine Optimierung der Tripathi-Parametrisierung für totaler Reaktionsquerschnitte vorgeschlagen. Außerdem wurde auf eine wichtige Lücke in den experimentellen Daten für hohe Energien hingewiesen. Die Datenbanken wurden online hochgeladen und frei zugänglich gemacht, um den an solchen Daten interessierten Forschungsgruppen die Möglichkeit zu geben, sie einzusehen, herunterzuladen und sie zusammen mit den Parametrisierungen darzustellen.





---

# Contents

---

<b>1</b>	<b>Introduction</b>	<b>1</b>
<b>2</b>	<b>Theoretical Background</b>	<b>3</b>
2.1	Radiation Protection . . . . .	4
2.1.1	Dose, Dose Equivalent, and Effective Dose . . . . .	4
2.1.2	Radiation Damage to Living Tissue . . . . .	5
2.1.3	Deterministic and Stochastic Effects of Radiation Exposure . . . . .	6
2.1.4	The ALARA Principle . . . . .	8
2.2	Space Exploration . . . . .	8
2.3	Space Radiation Environment . . . . .	9
2.3.1	Solar Particle Events . . . . .	10
2.3.2	Galactic Cosmic Rays . . . . .	10
2.4	Radiation Exposure Scenarios . . . . .	12
2.5	Interaction of Heavy Charged Particles with Matter . . . . .	13
2.5.1	Electronic Interactions . . . . .	14
2.5.2	Nuclear Interactions . . . . .	16
2.5.3	Bragg Curves . . . . .	19
2.5.4	Dose Build-up . . . . .	21
2.6	Radiation Protection in Space . . . . .	22
2.6.1	A More Suitable Dose Equivalent Definition . . . . .	22
2.6.2	Radiation-Related Health Risks in Space . . . . .	23
2.6.3	Uncertainties on Space Radiation Risks . . . . .	23
2.6.4	Effective Dose Limits in Space . . . . .	23
2.6.5	The ALARA Principle in Space . . . . .	25
2.7	Shielding in Space . . . . .	25
2.7.1	Active Shielding . . . . .	25
2.7.2	Passive Shielding . . . . .	26
2.7.3	Candidate Materials for Passive Shielding . . . . .	27
2.8	Stochastic and Deterministic Radiation Transport Methods . . . . .	29
2.8.1	Deterministic Methods: Solving Transport Equations . . . . .	30
2.8.2	Monte Carlo Methods: Single Particle Histories . . . . .	30
2.8.3	The Need for Reliable Cross-Section Models . . . . .	31
2.9	Accelerator-Based Experiments . . . . .	32
2.9.1	Facilities . . . . .	33
2.9.2	Ion Beams of Interest for Space . . . . .	33
2.9.3	The ROSSINI3 Project . . . . .	33
2.9.4	The DEIMOS Project . . . . .	34

---

<b>3</b>	<b>Absorbed Dose Measurements</b>	<b>35</b>
3.1	Materials and Methods . . . . .	35
3.1.1	Beams . . . . .	35
3.1.2	Target Materials . . . . .	36
3.1.3	Experimental Setup . . . . .	39
3.1.4	Data Analysis . . . . .	42
3.1.5	Error Bars . . . . .	42
3.2	Results and Discussion . . . . .	44
3.2.1	Iron Ions . . . . .	44
3.2.2	Light Ions . . . . .	47
3.2.3	Lithium Hydride . . . . .	51
3.3	Conclusions of Absorbed Dose Measurements . . . . .	53
<b>4</b>	<b>Monte Carlo Simulations</b>	<b>55</b>
4.1	Materials and Methods . . . . .	55
4.1.1	Simulation Setup and Approximations . . . . .	55
4.1.2	Data Analysis and Error Propagation . . . . .	57
4.2	Results and Discussion . . . . .	57
4.2.1	Iron Ions . . . . .	57
4.2.2	Light Ions . . . . .	62
4.3	Conclusions of the Monte Carlo Simulations . . . . .	64
<b>5</b>	<b>Nuclear Cross-Section Databases</b>	<b>67</b>
5.1	Reaction Cross-Section Database . . . . .	67
5.1.1	The Database . . . . .	67
5.1.2	Parametrisations . . . . .	72
5.1.3	Mass-Changing Cross-Sections as Proxy of Nuclear Reaction Cross-Sections . . . . .	79
5.1.4	Comparison Between Data and Parametrisations . . . . .	80
5.1.5	Discussion . . . . .	87
5.1.6	Proposed Optimisation of the Tripathi Parametrisation . . . . .	89
5.1.7	Recommendations . . . . .	92
5.2	Fragment Production Cross-Section Database . . . . .	97
5.2.1	The Database . . . . .	97
5.2.2	Elemental Cross-Sections . . . . .	99
5.2.3	Isotopic Cross-Sections . . . . .	102
5.2.4	Discussion and Recommendations . . . . .	105
5.3	Web Application . . . . .	112
5.4	Conclusions of the Cross-Section Databases and Future Work . . . . .	114
5.4.1	Reaction Cross-Section Database . . . . .	114
5.4.2	Fragment Production cross-section database . . . . .	114
<b>6</b>	<b>Conclusions and Future Work</b>	<b>117</b>
	<b>Bibliography</b>	<b>119</b>
	<b>List of Figures</b>	<b>145</b>
	<b>List of Tables</b>	<b>153</b>





---

# 1 Introduction

---

Expanding human presence into the Solar System is a common goal of 14 space agencies [1]. Nevertheless, we evolved to survive the dangers encountered on Earth as a species, not what awaits us beyond it. Since our blue planet protects us from deep-space radiation through both its magnetic field and its atmosphere, the radiation levels humans experience in their day-to-day life on Earth are on average significantly lower than in outer space. The Earth's magnetic field deviates the trajectory of charged radiation arriving at the planet's surface. Additionally, when the incoming radiation interacts with the planet's atmosphere, the primary radiation is attenuated and a shower of secondary and less-dangerous particles is generated. Beyond low-Earth orbit (LEO), there are two main sources of cosmic radiation: solar particle events (SPEs) and galactic (and intergalactic) cosmic rays (GCRs). The energy of intergalactic radiation can reach up to the ZeV region ( $10^{21}$  eV) and the particle spectrum contains ions up to Nickel in relevant amounts. Heavier ions are present only in traces [2]. These very-high energies and charges make GCRs among the number one enemies of manned space exploration [3]. SPEs can indeed, be stopped within the few centimetres of matter constituting the structure of the spacecraft. SPEs are, therefore, only harmful if they coincide with an extravehicular activity (EVA), in which our explorers are only protected by the spacesuit they are wearing. What can prevent radiation-related accidents during EVAs is space weather forecast, which can ideally foresee when an SPE will happen. This is indeed a very active field of research.

The principle that guides radiation protection on Earth is called ALARA, which stands for “as low as reasonably achievable”. The three factors one can play with to get ALARA amounts of radiation dose are distance, time, and shielding. When it comes to distance, the idea is to stay as far as possible from the radiation source. For time, it is meant that the exposure time should be minimised. Shielding is any type of material the person can hide behind to stop as much radiation as possible within it. If the ALARA principle is applied to radiation protection in space, distance is not a factor that can be played with because the radiation source is in this case isotropic. Time is only partially. Surely new technologies can allow us to reach our final destination faster. But the intrinsic definition of exploration pushes us towards further and further destinations. Therefore, even if we go faster, it takes more time the further we want to reach. Hence, the only option left is shielding.

Two strategies can be followed to shield from radiation. One is active shielding, the second is passive shielding. Active shielding consists in taking inspiration from the first protection from cosmic radiation our blue planet provides us with and generating a magnetic field around the spacecraft or the *in situ* base of the explorers at their final destination. Because of technological limitations such as the generation of very strong magnetic fields and the state-of-the-art of cryogenic superconducting magnet techniques, this strategy is not pursue-able on time for the mission to Mars [4].

Passive shielding consists in taking inspiration from the second source of protection of our planet and adding material to the spacecraft or the *in situ* base walls. The most challenging aspect is that GCRs are too energetic to be stopped within reasonable amounts of material for the structure of a spacecraft. Surely, after reaching the final-destination planet or satellite, *in situ* resources such as regolith can be naturally exploited to protect our explorers, e.g. by building caves on the hosting planet. And there is no upper limit to the amount of such resources. But what to do during the travel? When cosmic radiation passes through the shielding and structural spacecraft materials, it undergoes nuclear reactions with the nuclei of such

---

materials. As a consequence, a shower of secondary particles is generated, which is normally less harmful to humans than the primary cosmic radiation because of the less complex DNA damage that it causes [4]. One aim is, therefore, to maximise such nuclear reactions. The probability of a nuclear reaction happening is called nuclear reaction cross-section, and it is quantified physically as a geometrical interaction area. Since the costs of a mission scale with the spacecraft mass, the nuclear reaction cross-section of single target nuclei is to be maximised per unit mass of the shielding material. Hence, the best shielding materials in space are low-Z (atomic number) and high hydrogen content materials [5–10], being polyethylene (PE) the gold standard. Recently, even lower-Z materials, such as lithium-based hydrides, have been tested as innovative shields [11, 12]. Their radiation dose attenuation properties are ideal, but their chemical instability makes them too dangerous to be exploited in space.

Full-scale realistic tests of shielding scenarios cannot be done on Earth. It would be impossible to irradiate a full spacecraft, using the exact GCR spectrum and the cosmic radiation intensities. Therefore, we fully rely on calculations, in particular Monte Carlo (MC) simulations. Such stochastic calculations make it possible to predict what the outcome of the interaction between GCR and spacecraft or *in situ* materials will be. Nevertheless, the goodness of the results depends on the goodness of the physics underlying such simulations. Nuclear reaction semi-empirical parametrisations are a key “ingredient” to MC codes. What can be done to test the reliability of MC codes is to compare the outcome of the simulations with the results of simple accelerator-based experiments [12–14]. They can provide us with a lot of information regarding the goodness of the nuclear reaction models that are part of the computational “machinery”.

To tackle these issues, an ESA project named ROSSINI3 [15] was started in 2018, as a follow-up of previous experimental projects ROSSINI [16–18] and ROSSINI2 [11, 12]. This thesis focuses on two of the project endpoints. On the one hand, accelerator-based experimental campaigns were conducted to test different important materials for shielding astronauts in space, and the results were compared with the outcome of MC simulations performed with the most used codes in the framework of space travel. In particular, within this work, the very low-Z lithium-based hydrides have been stabilised in a paraffin matrix and the resulting composite materials have been tested as shields in space. Alongside such innovative shields, also the gold standard PE, potential *in situ* shields such as Moon regolith, and structural materials have been irradiated with relevant beams for space radiation. On the other hand, the state of the art of the experimentally-measured cross-sections was reviewed, a comprehensive open-access database of experimentally-measured total nuclear reaction and fragment production cross-sections was generated, and the data were compared with the semi-empirical cross-section parametrisations that are in the most commonly MC codes used for radiation protection in space purposes.

Chapter 2 provides a theoretical background of radiation shielding in space, starting from the basic concepts of radiation protection on Earth, going through the space radiation environment and the interaction of these radiation fields with matter. After that, the concepts of radiation protection on Earth are applied to the space radiation environment and it is explained why passive shielding is currently the most promising radiation protection strategy. An overview of the importance of MC simulations, nuclear cross-sections, and experiments is then given. Chapter 3 goes into the details of the experiments performed with candidate shielding materials and shows the results obtained. The comparison of these results with MC simulations is presented in Chapter 4. Chapter 5 presents the nuclear cross-section databases generated within this work and the comparison of nuclear reaction cross-section data with the parametrisations implemented in the most commonly used MC codes for radiation protection in space applications. Finally, Chapter 6 presents the conclusions and outlook of the work.

---

## 2 Theoretical Background

---

When hitting a cell of the human body, ionising radiation can cause damage to important chemical structures in macromolecules. In particular, DNA is the most sensitive to damage among them, because it encodes all the information required for the cell's functioning. Based on the type of cellular damage that occurs due to the radiation dose, the effects on the organism can be acute (acute radiation syndromes, e.g. gastrointestinal or neurovascular syndromes) or chronic (late radiation effects, e.g. solid cancer or leukaemia). Radiation protection is a field of research that studies how to effectively protect humans from ionising radiation. When travelling through space, humans are exposed to a radiation field that is different both quantitatively and qualitatively from the radiation to which we are exposed on Earth. Therefore, radiation protection strategies need to be applied to make space exploration as safe as possible.

Within this chapter, the reader will be walked through the physical and mathematical bases of radiation protection in space. Firstly, a general background about the basic radiation protection concepts and quantities is given. After that, the space exploration plans for the next couple of decades are shortly overviewed, and the cosmic radiation environment is presented, followed by the foreseen radiation exposure scenarios. The basic concepts of how radiation interacts with matter are necessary to understand how space radiation interacts with both the space explorers' biological tissue and the materials surrounding them. Therefore, it is then described how heavy charged particles interact with matter. The focus on heavy charged particles is due to their relative importance in the space radiation spectrum.

After that, the reader is made aware of why cosmic radiation is considered one of the main hindrances to space exploration, and why radiation protection is needed for long-term deep-space missions. With "deep space", everything beyond the Earth's atmosphere is included. Because of the differences between the radiation environment on Earth and in space, suitable radiation protection concepts are developed for space travel. Strategies based on emulating how Earth shields space radiation can be exploited. Shielding techniques based on the active generation of electromagnetic fields (active shielding) cannot reach a development advanced enough for the ambitious aim of sending mankind to Mars within the next decade. Therefore, shielding strategies based on the addition of material (passive shielding) need to be exploited. The shielding material choices are based on a deep understanding of radiation interaction with matter. In particular, nuclear reactions that radiation undergoes with the nuclei composing matter are key to understanding the shielding material choices. Since the high energy of GCRs makes it impossible to stop all of them within realistic spacecraft thicknesses, the only option left is to make them less harmful. Generally, when heavier ions hit the DNA structure, the damage caused is more complex and, therefore, more difficult to repair correctly. Hence, the lighter the ion hitting space explorers, the less dangerous it is for them. Therefore, nuclear interactions of space radiation with shielding materials need to be maximised as they cause the breakup of space radiation into smaller ions.

After going through the details of shielding in space strategies, the importance of stochastic and deterministic simulations to prepare for space exploration missions is explained. In particular, they are the means on which it is fully relied to predict how the cosmic radiation field will change when interacting with structural and shielding materials surrounding space explorers. The physics underlying the codes and, in particular, realistic nuclear cross-section parametrisations are key ingredients to obtaining trustable simulation results. Ground-based experiments taking place in particle accelerator facilities are the best way to obtain data

that can be directly compared to simulation results. This comparison leads to a better understanding of the goodness of the physical parameters inside the simulations and allows the improvement of simulation capabilities.

## 2.1 Radiation Protection

Radiation protection is defined by the International Atomic Energy Agency as the protection of individuals from the effects of exposure to ionising radiation [19].

### 2.1.1 Dose, Dose Equivalent, and Effective Dose

Before talking about radiation effects on the organism, a few quantities need to be defined. The absorbed dose  $D$  is defined as [20]:

$$D = \frac{dE}{dm}, \quad (2.1)$$

where  $dE$  is the average energy deposited by ionising radiation into a quantity of matter with mass  $dm$ . The unit of measurement of  $D$  is Gray (Gy=J/kg). It is to be noted that  $D$  does not contain any information regarding the radiation type or energy.

The dose equivalent  $D_{eq}$  to an organ or tissue  $T$  is defined as [21]:

$$D_{eq} = \sum_R w_R D_T, \quad (2.2)$$

where  $R$  are the different radiation types,  $w_R$  is the so-called radiation weighting factor and  $D_T$  is the absorbed dose received by the organ or tissue. The  $w_R$  values reported in ICRP 103 [22] can be found in Table 2.1. The  $w_R$  associated to neutrons is energy dependent. The unit of measurement of  $D_{eq}$  is Sievert (Sv). With the aim of considering also the fact that the irradiation of different organs and tissues

Table 2.1: Radiation weighting factors from ICRP 103 [22].

Radiation type	$w_R$
X and $\gamma$ rays	1
Electrons and muons	1
Protons and charged pions	2
$\alpha$ particles and heavy ions	20
Neutrons	2 to 20

is associated to different risks of stochastic effects, the  $D_{eq}$  values need to be weighted on specific tissue weighting factors  $w_T$ . The quantity that takes this into account is called effective dose  $D_{eff}$  and can be calculated with the following age and gender independent function [22]:

$$D_{eff} = \sum_T w_T \left( \frac{D_{eq}^M + D_{eq}^F}{2} \right), \quad (2.3)$$

where  $T$  are the different tissues and the apices M and F stand for male and female.  $w_T$  factors can be found in Table 2.2.  $D_{eff}$  is also measured in Sievert (Sv). Equation 2.3 is recommended to be used both if the body is exposed uniformly and non uniformly. Since radiation risks strongly depend on age and gender, Equation 2.3 only allows highly inaccurate risk estimations, which derive from the ICRP 103 inherent assumption that the exposure is well below dangerous limits.



Table 2.2: Tissue weighting factors from ICRP 103 [22].

Organ	$w_T$
Breast, bone marrow, lung, colon, stomach	0.12
Gonads	0.08
Bladder, liver, oesophagus, thyroid	0.04
Bone surface, brain, salivary glands, skin	0.01
Other	0.12

### 2.1.2 Radiation Damage to Living Tissue

When radiation interacts with the cells of the human body, it excites and ionises the atoms composing

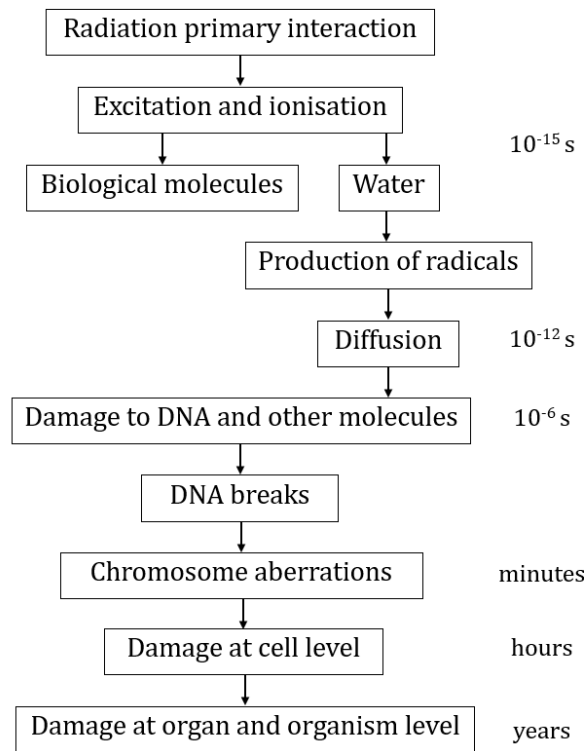


Figure 2.1: Classic paradigm of radiation damage.

the macromolecules and water molecules that the cells are composed of (time scale of  $10 \times 10^{-15}$  s). The macromolecules include DNA, proteins, RNA and lipids, which make up the most important biochemical structures in the cell. In particular, DNA is the most sensitive to damage among them, because it encodes all the primary information required for the cell's functioning. If radiation directly damages the macromolecules, this is called direct damage. Additionally, radiation can break water molecules and generate free radicals that can diffuse within the cell (time scale of  $10 \times 10^{-12}$  s) and damage the DNA. This is called indirect damage. Such damages happen in the time scale of  $10 \times 10^{-6}$  s. Repeated damages, if left unrepaired or if not correctly repaired, can lead to chromosomal aberrations (time scale of minutes), which cause errors in various cellular processes (time scale of hours). In particular, this can the cause production of incorrect amounts of key proteins or of mutant proteins, which enhance or suppress important biochemical

pathways in the cell. As the cell requires a balance between these different biochemical pathways, the unbalancing leads to various types of damage to the cell, which can lead to cell death or promote cancer-type characteristics. This can cause damage to important organs which perform the function of maintaining life support systems in an organism. Such damage can take up to years. This progression is called the classic paradigm of radiation damage and is reported schematically in Figure 2.1.

Focusing on the direct DNA damage, the more complex such damage is, the more difficult it is for the cell repair mechanisms to correct it. For charged particles, the (unrestricted) linear energy transfer (LET) is defined as the energy loss per unit path by a charged radiation particle due to electronic collisions [23]. The higher the LET is, the more excitations and ionisations are caused on the particle path length, which means more localised, and therefore complex, DNA damage (see Figure 2.2).

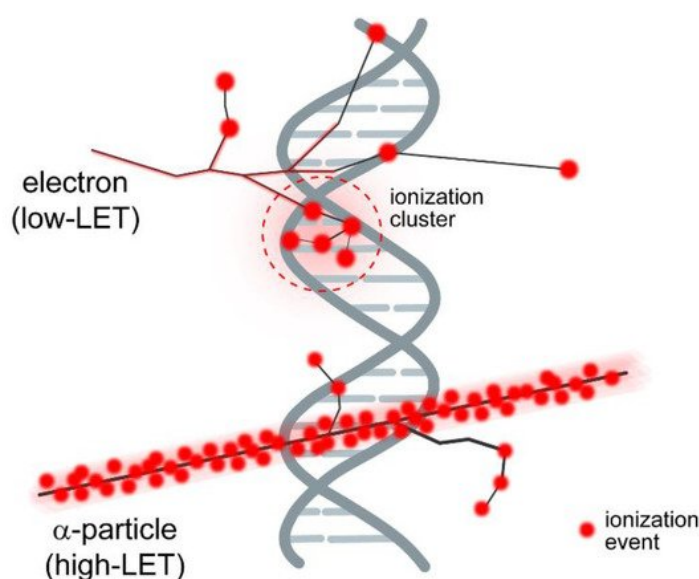


Figure 2.2: Schematic representation of the biological damage caused to the DNA by low and high-LET radiation [24].

Nevertheless, two particles can have the same LET, but different spatial energy deposition patterns. Such distribution is taken into account by the particle track structure. Figure 2.3 reports the example of the track structures of four ions having the same LET. It has been demonstrated [28–32], that the biological effectiveness of radiation not only depends on the LET, but also on the track structure. As a first approximation, a more localised energy release along the particle trajectory corresponds, in fact, to a more localised damage creation, which is more difficult for the cell mechanisms to repair correctly.

### 2.1.3 Deterministic and Stochastic Effects of Radiation Exposure

There are two types of biological effects caused by radiation at an organism level: deterministic and stochastic [33]. The more dose an individual is exposed to, the higher the risk or probability of such effects developing. Nevertheless, the shape of the dose responses of deterministic and stochastic effects are different (see Figure 2.4). On the one hand, deterministic effects (e.g. cataracts or skin erythema) show a threshold in dose below which they do not occur. Right above the threshold, their probability increases rapidly, generating a sigmoid-shaped dose-response curve. On the other hand, stochastic effects are “all-or-nothing” effects (e.g. cancer or leukaemia). Therefore, the severity of the effect does not depend

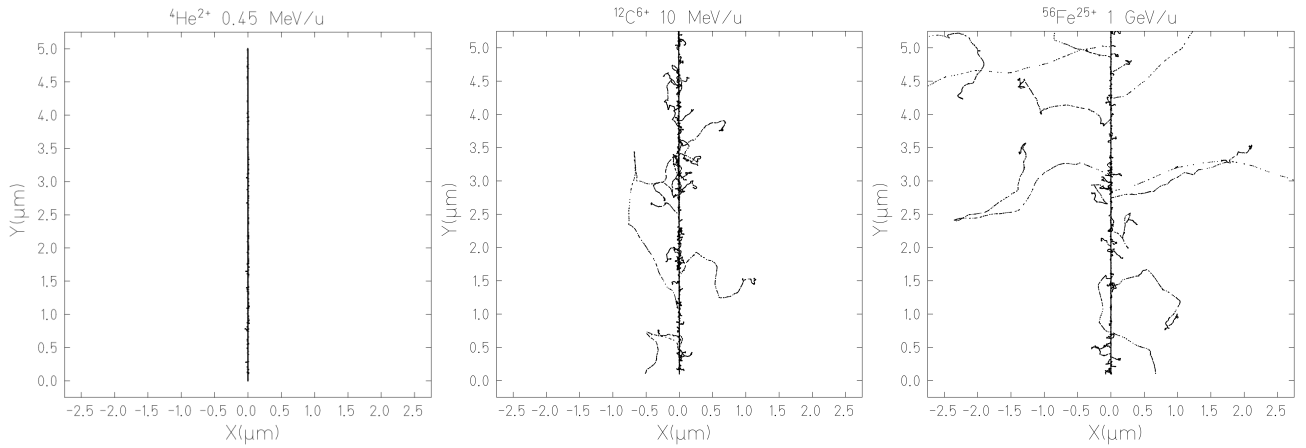


Figure 2.3: Comparison of the tracks of  $0.45 \text{ MeV u}^{-1} {}^4\text{He}$ ,  $10 \text{ MeV u}^{-1} {}^{12}\text{C}$ , and  $1000 \text{ MeV u}^{-1} {}^{56}\text{Fe}$  ions. They all have an LET of  $150 \text{ keV } \mu\text{m}^{-1}$ . The simulations were performed with the TRAX code [25–27] software by Dr. Daria Boscolo.

on the amount of dose received, but the probability of such effects occurring does. There is no dose threshold for such events, and the dose-response curve can be described as linear, or linear with non-linear effects at high doses. The National Council on Radiation Protection and Measurements states that the

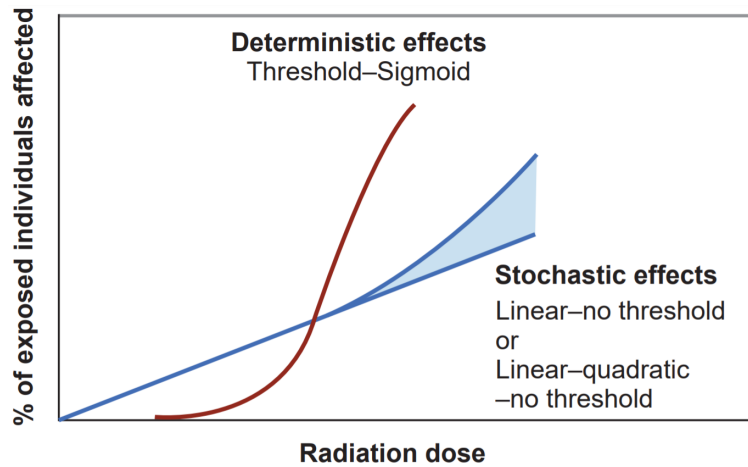


Figure 2.4: Dose response curves of deterministic and stochastic effects [33].

objectives of radiation protection are [33]:

1. preventing clinically significant deterministic radiation-induced effects by reducing exposure to doses below the apparent or practical threshold, and
2. limiting the risk of stochastic effects to a reasonable level.

Therefore, effective dose limits are reported in the ICRP 103 [22]. The effective dose limit for the public is  $1 \text{ mSv year}^{-1}$  and for radiation workers is  $20 \text{ mSv year}^{-1}$  per year, averaged over defined periods of 5 years. These limits do not include natural radiation exposure, which is on average  $2.4 \text{ mSv year}^{-1}$  [34].

### 2.1.4 The ALARA Principle

The second National Council on Radiation Protection and Measurements statement become the ALARA exposure principle, for which the received dose must be reduced to As Low As Reasonably Achievable [35]. There are three ways to do it [4]:

1. Distance: the greater the distance from the radiation source the less radiation is received. In particular, the source intensity scales as  $I \propto r^{-2}$ ,  $r$  being the distance from the source.
2. Time: the shorter the exposure time to the radiation source is, the better.
3. Shielding: adding material between the source and the exposed person reduces the radiation intensity. As a rule of thumb, products of alpha decay can be stopped with a sheet of paper, products of beta decay need a few millimetres of aluminium, and gamma decay several centimetres of lead.

## 2.2 Space Exploration

The third edition of the Global Exploration Roadmap [1] has recently reaffirmed the interest of 14 space agencies including NASA, ESA and the Russian ROSCOSMOS, in expanding the human presence into the Solar System. The mission to Mars is agreed to be a common goal, and going to the Moon again is an important intermediate step. The agreed space exploration roadmap for the next couple of decades [1], is reported in Figure 2.5. In particular, the main aims of space exploration and colonisation are to enable

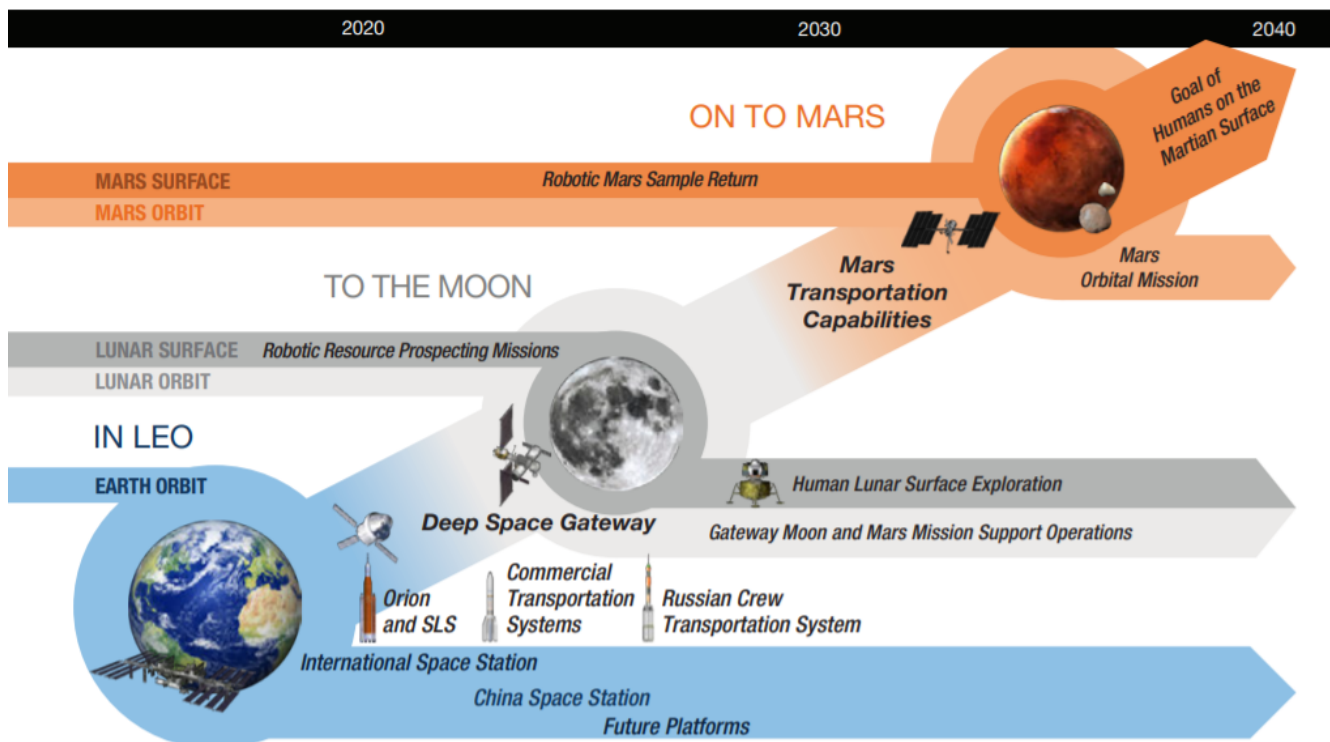


Figure 2.5: The global exploration roadmap [1].

sustainable living and working on the Moon and Mars, to study the origin and evolution of the Earth-Moon

---

system, the Solar system, and the Universe itself, to look for evidence of past or present life outside of our blue planet, and to understand the origin of life on Earth.

Since humans evolved to live on Earth, they are not well suited to be somewhere else. Different air composition, temperature conditions, gravity, and radiation environments can be harmful to us. In the NASA Human Research Roadmap [36], the risks posed to humans by space exploration are grouped into three categories:

1. Physiological and psychological problems caused by microgravity (or reduced gravity). Such problems have been extensively studied, especially in LEO, both on the International Space Station (ISS) and, previously, on the Mir [37]. Some of them are bone loss, skeletal muscle mass reduction, cardiovascular alterations, kidney stone formation, impaired sensory-motor capabilities, and immune system dysfunctions. These risks are well characterised, and several countermeasures are available. The psychological problems related to the absence of gravity are related to the subsequent lack of the spatial coordinate system that gravity naturally generates (what is “up” and what “down”).
2. Psychological and medical problems caused by isolation. On the one hand, psychological problems are mostly induced by isolation, which may lead to serious neurobehavioural problems caused by poor psychosocial adaptation [37], and microgravity, which leads to the disappearance of one of our main reference systems. Isolation-induced psychological problems have been studied through experiments in the Concordia base (Antarctica) and the Mars500 platform (Russia). On the other hand, medical problems due to isolation consist of autonomous medical care (AMC), for which the counter measurements under development (e.g. portable medical equipment and telemedicine) are mostly technological.
3. Acute and late risks caused by exposure to radiation. The radiation doses to which space explorers are exposed in space are much higher than on Earth. Therefore, their biological effects would be severe if the explorers were directly exposed to them. In addition, the Earth’s radiation spectrum is mainly made of gamma, beta and alpha rays, while in space there are mostly protons and heavy ions. As a consequence, terrestrial data cannot be extrapolated to be used in space exposure scenarios, which leads to very high uncertainties in radiation risk estimates, especially for carcinogenesis, central nervous system damages, and late cardiovascular effects [37].

Such risks were rated from 1 to 3 [36], where 1 means that they are so serious that the mission is impossible without their mitigation, and 3 means suspected health consequences with limited impact on the mission design. Among the risks listed above, only AMC and radiation-induced risks are classified as 1. This thesis work solely focuses on how to mitigate the risks induced by exposure to the cosmic radiation environment.

---

## 2.3 Space Radiation Environment

---

The space radiation environment is a complex mixture of particles with solar, galactic or intergalactic origin, and characterised by a broad range of energies [4]. The combined effect of the Earth’s magnetic field and atmosphere ( $1 \text{ kg cm}^{-2}$  of thickness) reduces the space radiation exposure of the planet’s surface to nearly a zero level. Humans evolved to be inhabitants of the surface of Earth. Therefore, we are resistant to the radiation level to which we are exposed on Earth, but unshielded exposure to space radiation poses a life threat to us. Additionally, space radiation also poses a threat to the success of unmanned exploration missions as well, due to the damage it can cause to electronic devices.

The existence of a source of radiation outside the atmosphere was firstly proven by Victor Hess at the beginning of the 20<sup>th</sup> century through seven balloon flights [38]. There are two main sources of space

radiation beyond low-Earth orbit (LEO): solar particle events (SPEs) and galactic cosmic rays (GCRs). In addition to these two, in LEO there is also a third source: trapped radiation belts, also known as Van Allen belts. They consist of charged particles (mainly protons and electrons) trapped and confined in toroidal regions by the Earth's magnetic field. The altitudes of these regions range from about 1000 up to 60 000 km. Since future missions focus on the exploration of other planetary surfaces, only SPEs and GCRs are described in the following.

### 2.3.1 Solar Particle Events

Our Star continuously emits particles alongside electromagnetic radiation. They mainly consist of protons and electrons (the so-called solar wind) that have such low energies (for a proton between 100 eV and 3.5 keV) that they can be stopped within a few hundreds of nanometres of skin. However, sporadic energy releases can accelerate solar energetic particles (SEPs) in the corona and interplanetary medium. Such particles consist mostly of protons and a small fraction of heavier nuclei [39], with energies reaching up to several GeV. They travel in the Solar System spiralling around the interplanetary magnetic field lines. These SPEs have been recorded on Earth since 1942 [40]. Even before this date, very intense SPEs could be witnessed even through visual observations ("Carrington event", 28 August to 2 September 1859 [41]). Typically, major SPEs are observed on Earth once per month, and they last from several hours to days. SPEs show an enormous variability in fluence and energy spectra. The most intense 20<sup>th</sup>-century events are reported in Figure 2.6.

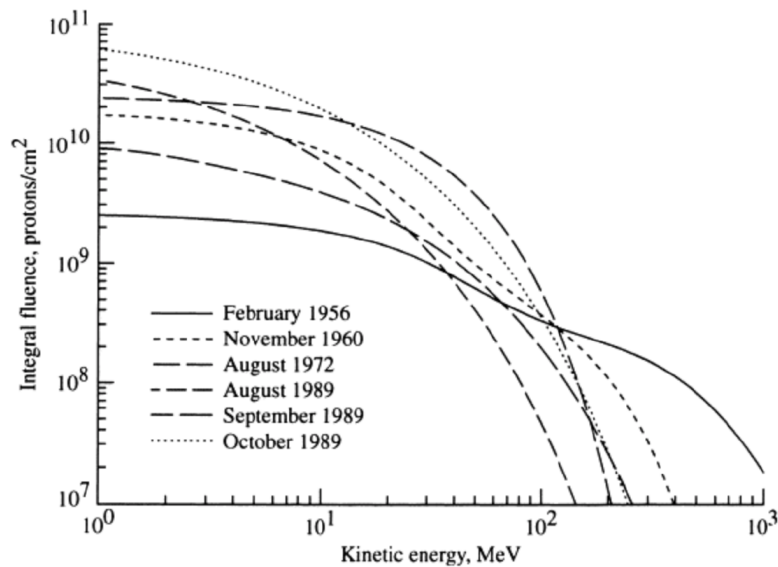


Figure 2.6: Proton fluence spectra of the most intense recorded SPEs [42].

SPEs tend to happen more or less often depending on the solar cycle phase. The solar activity is, modulated with an 11-year-long cycle, and SPEs are more common and stronger during the phase of maximum of such cycle, while they are less common during the solar minimum phase.

### 2.3.2 Galactic Cosmic Rays

According to the current knowledge, GCRs originate from supernovae explosions, merges of neutron stars, pulsars, or other highly energetic astronomical objects and phenomena [43]. Once reached our Solar

System, their trajectory is bent by the solar magnetic field and they impinge isotropically onto planetary surfaces. GCRs consist of 2% electrons and 98% baryons. The baryonic component is made out of 85% protons, 14% helium nuclei, and 1% heavier nuclei. The heavier nuclei component is made of all nuclei of the periodic table until uranium, but everything heavier than nickel is only present in traces. The relative contribution of protons and heavy ions to the GCR spectrum is reported in Figure 2.7. Neutrons are not

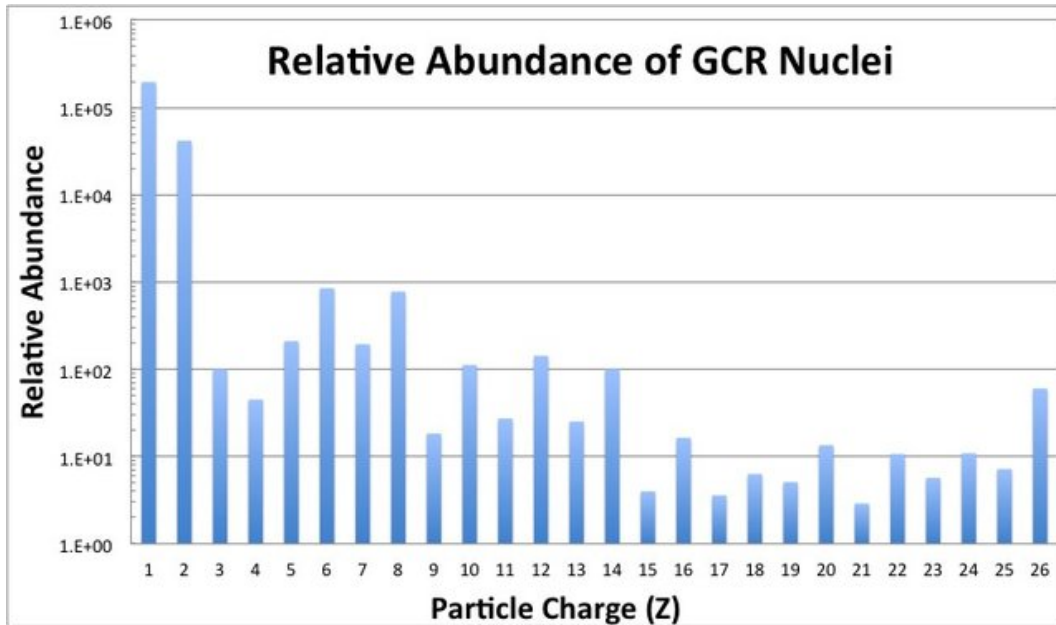


Figure 2.7: Relative contributions of the different elements to the baryonic component of the GCR spectrum [3].

part of the primary GCR spectrum as free neutrons are not stable and have a half life of around 10 minutes.

The 11-year solar cycle modulates the GCR spectrum as well. GCR spectra are anti-correlated with the minima and maxima of the solar cycle: during solar minima, GCR intensities are higher, and vice versa. The GCR energy spectrum is reported in Figure 2.8, where it can be seen that the solar cycle has an effect of a factor that reaches up to 4. GCR energies can reach up to  $10^{11}$  GeV.

It can be seen in Figure 2.8 that the GCR spectrum has a maximum around  $1 \text{ GeV u}^{-1}$  for all ions and for solar maximum modulation, which shifts towards lower energies for solar minimum modulation.



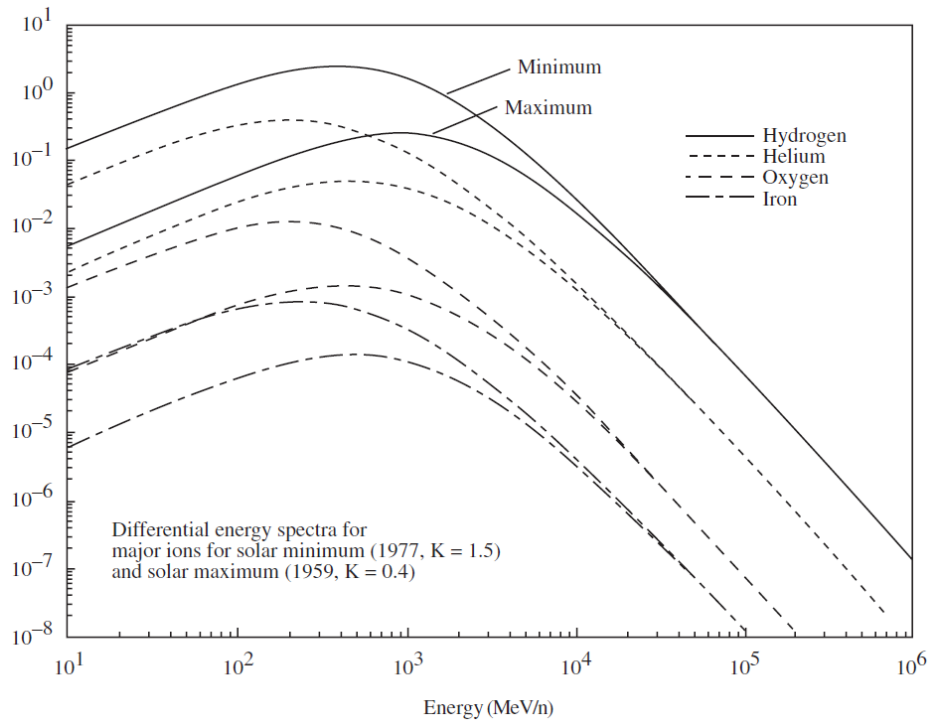


Figure 2.8: Differential energy spectra for hydrogen, helium, oxygen, and iron for the 1977 solar minimum and 1959 solar maximum, which are the two cycles with the strongest modulation of the past 50 years [4].

## 2.4 Radiation Exposure Scenarios

### The Flight

During an interplanetary mission in deep space, SPEs and GCRs will irradiate the spacecraft with fluxes and fluences that depend on the location in the Solar System. On average, every cell nucleus in the body of each crew member will be hit by a proton once every three days, by a helium ion once every few weeks, and by a heavier ion about once every few months [44, 45]. Also, the cell traversals are not statistically independent as the traversal of a cell nucleus corresponds to the simultaneous traversal of around other  $10^9$  cell nuclei. Between 2012 and 2013 (close to a solar minimum), the radiation assessment detector (RAD), which flew on the Curiosity rover, recorded an average dose rate of  $0.46 \text{ mGy day}^{-1}$  and a dose equivalent rate of  $1.84 \text{ mSv day}^{-1}$  [46]. The RAD measurements showed that in this period, 95% of the measured absorbed dose was due to GCRs, and only 5% to SPEs. Depending on the spacecraft and on the SPE, dose rates can fluctuate between 0 and  $100 \text{ mGy hr}^{-1}$  inside a space vehicle throughout a SPE [45]. Flying to the Moon only takes a few days, but the transit to Mars alone takes 6 to 9 months [47] and will already expose the crews to very high doses.

Space explorers have first-hand experienced effects due to the constant flux of GCRs. In particular, most of the explorers that went to the Moon or spent time in LEO, have witnessed the so-called cosmic ray visual phenomena [48, 49]. They consist of “flashes of light” of shapes, depending on the witness, exceptionally colourful (yellowish, pale green, or blue), sometimes moving across the visual field. A temporal correlation



was proven between the observed light flashes and the flux of protons and heavy ions, by experiments performed in LEO with silicon telescopes [50, 51].

---

## On the Moon

---

The Moon has neither a magnetic field nor an atmosphere. Together with the several technical disadvantages that these two planetary characteristics create, a crew on the Moon's surface is exposed to unshielded SPEs and GCRs. The only protection that the Moon offers is geometric because half of the isotropic cosmic radiation flux is naturally shielded by the planetary body itself. Concerning GCRs, the average annual GCR exposure on the Moon's surface is estimated to be 0.38 Sv during solar minima, and 0.11 Sv during solar maxima [52]. Additionally, a worst-case SPE could expose the crew to 1 Sv in a very short time [52].

---

## On Mars

---

The ferromagnetic elements in the core of Mars are solid. Therefore, the planet has no magnetic field. However, differently to the Moon, it has an atmosphere, which is much thinner than Earth's. The RAD recorded an average GCR dose rate of 0.21 mGy day<sup>-1</sup> and a dose equivalent rate of 0.64 mSv day<sup>-1</sup> [53]. The radiation exposure of space explorers on Mars depends on several factors [4, 54]. Firstly, the exposure depends on the atmospheric thickness, which changes with the altitude [55–57]. It ranges from about 2.2 g cm<sup>-2</sup> at an altitude of 25 km, and about 30.5 g cm<sup>-2</sup> in basins [58] located 7 km below the planet surface [59], which is anyway much lower than the ≈ 1000 g cm<sup>-2</sup> at sea level on Earth. Secondly, the exposure also depends on the soil composition as this changes the albedo particle field, which are the particles directed backwards from the planetary surface. The selection of landing sites are based on other requirements than radiation exposure. Nevertheless, the different radiation exposure scenarios need to be taken into account for shielding purposes.

In conclusion, staying on the Moon and Mars means facing both acute and chronic radiation exposure risks.

---

## 2.5 Interaction of Heavy Charged Particles with Matter

---

Before talking about how to protect space explorers from cosmic radiation exposure, it is necessary to go through the physics underlying the interaction of the heavy charged particle composing space radiation with matter, i.e. space explorers' biological tissue, and structural and shielding materials of space habitats.

When charged particles (projectiles) interact with matter (target), they lose energy through different processes. The quantity taking into account this energy loss is the (linear) stopping power  $\frac{dE}{dx}$  of a material, which is defined [23] as the energy lost by a charged particle per unit path. It can be expressed as a sum of individual components:

$$\frac{dE}{dx} = \left(\frac{dE}{dx}\right)_{\text{rad}} + \left(\frac{dE}{dx}\right)_{\text{col}}. \quad (2.4)$$

$\left(\frac{dE}{dx}\right)_{\text{rad}}$  is the radiative stopping power due to emission of bremsstrahlung in the electric fields of atomic nuclei or electrons and the collision stopping power  $\left(\frac{dE}{dx}\right)_{\text{col}}$  is defined as:

$$\left(\frac{dE}{dx}\right)_{\text{col}} = \left(\frac{dE}{dx}\right)_{\text{el}} + \left(\frac{dE}{dx}\right)_{\text{nuc}}, \quad (2.5)$$

where  $\left(\frac{dE}{dx}\right)_{\text{el}}$  is the electronic (or collision) stopping power due to collisions with electrons of the material and  $\left(\frac{dE}{dx}\right)_{\text{nuc}}$  is the nuclear stopping power due to elastic Coulomb collisions in which recoil energy is

imparted to atoms. For protons and heavier ions,  $(\frac{dE}{dx})_{\text{rad}}$  is negligible. For the energies of interest for space radiation, also  $(\frac{dE}{dx})_{\text{nuc}}$  is, as it becomes relevant only at very low energies. Therefore, in the cases of interest for this work:

$$\frac{dE}{dx} \approx (\frac{dE}{dx})_{\text{el}}. \quad (2.6)$$

In addition, the projectile ion can also undergo inelastic interactions with the target material nuclei.

Interactions of radiation with matter are a stochastic process. There is a probability associated with them to happen, which is called cross-section. The cross-section for a certain interaction is [23]:

$$\sigma = \frac{P}{\Phi}, \quad (2.7)$$

where  $P$  is the probability of that interaction for a single target entity when subjected to the particle fluence  $\Phi$ . The cross-section represents the geometrical area that the target entities expose to the projectile for the process of interest to happen. The unit of measurement of cross-sections is the barn ( $1 \text{ b} = 10^{-28} \text{ m}^2$ ).

In the following, the interactions taking place when protons and heavier ions travel through matter are split into two categories: the interactions with the electrons of the material and the interactions with the nuclei.

### 2.5.1 Electronic Interactions

When heavy charged particles travel through matter, they transfer energy to atomic electrons via inelastic Coulomb interactions leading to excitation and ionisation processes. The electrons leaving their atoms are called secondary electrons, and the ones among them that have enough energy to generate another ionisation are called delta rays. A schematic representation of the ionisation processes caused by heavy charged particles traversing a target material is given in Figure 2.9.

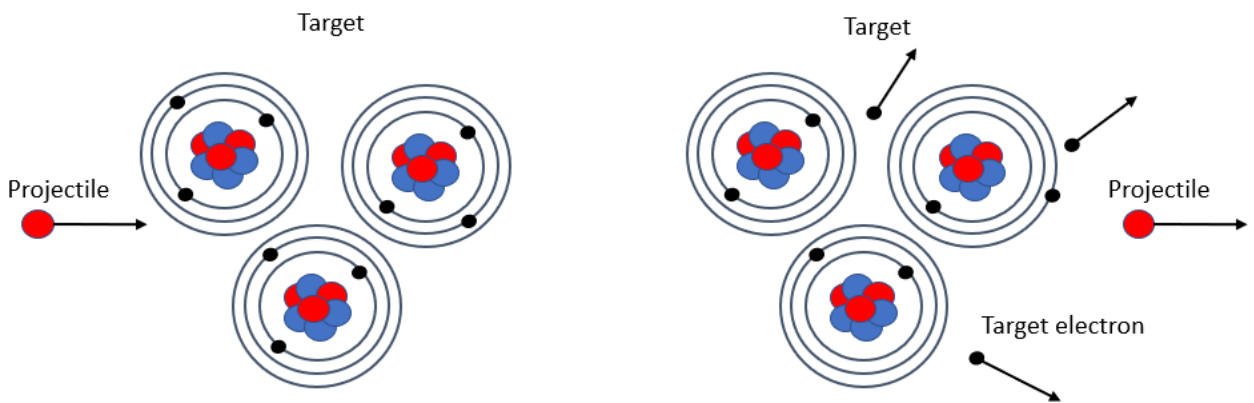


Figure 2.9: Schematic representation of the ionisation processes that occur when heavy charged particles interact with matter ("Projectile" is the incoming particle and "Target" is the material).

---

## The Bethe Formula

---

The mean kinetic energy per unit path length that the ion loses in the excitation and ionisation processes, which is the electronic stopping power  $(\frac{dE}{dx})_{\text{el}}$  can be computed with the Bethe [60] formula as:

$$\langle (\frac{dE}{dx})_{\text{el}} \rangle = 4\pi N_A r_e^2 m_e c^2 \frac{\rho Z_T}{A_T} \frac{Z_p^2}{\beta^2} \left( \frac{1}{2} \ln \left( \frac{2m_e c^2 \beta^2 \gamma^2 E_{\text{max}}}{I^2} \right) - \beta^2 - \frac{\delta(\beta\gamma)}{2} \right), \quad (2.8)$$

where  $N_A$  is the Avogadro constant,  $r_e$  is the classic electron radius,  $m_e$  the electron mass,  $c$  the speed of light,  $\beta = \frac{v}{c}$ , and  $\gamma = \frac{1}{\sqrt{1-\beta^2}}$ . The terms referring to the target material are its density  $\rho$ , its atomic number  $Z_T$ , its mass number  $A_T$ , and its mean ionisation potential  $I$ . The mean ionisation potential of atoms is approximately given by [61]:

$$I = (10 \text{ eV}) Z_T. \quad (2.9)$$

If this approximation is introduced in Equation (2.8), an expression which is often called the Bethe-Bloch formula is obtained. In Equation (2.8), the terms referring to the projectile ion are its atomic number  $Z_p$  and its velocity  $v$ .  $E_{\text{max}}$  is the maximum energy transfer to an electron, and  $\delta(\beta\gamma)$  the relativistic density effect correction that becomes relevant at energies above about  $1 \text{ GeV u}^{-1}$  [62].  $E_{\text{max}}$  can be estimated as:

$$E_{\text{max}} = 4 \frac{m_e}{m_p} E_p \quad (2.10)$$

according to the binary encounter model [63]. In Equation 2.10,  $m_p$  is the projectile mass and  $E_p$  the projectile kinetic energy. The unit generally used in radiobiology for the  $\frac{dE}{dx}$  is  $\text{keV}/\mu\text{m}$ .

It can be seen from Equation 2.8 that the  $\frac{dE}{dx} \propto \frac{Z_p^2}{\beta^2}$ . As the velocity (or kinetic energy  $E_p$ ) of a particle increases,  $\frac{dE}{dx}$  decreases until a minimum, which is reached for a projectile velocity of approximately 90% of the speed of light. At higher energies,  $\frac{dE}{dx}$  increases very slowly due to relativistic effects ( $\delta(\beta\gamma)$ ). As the projectile ion slows down, the  $\frac{dE}{dx}$  increases to a maximum and then very quickly drops to zero [45]. This maximum that occurs very close to the point where the particle loses its remaining energy and stops is called the Bragg peak (see Section 2.5.3).

---

## The Barkas Formula

---

At very low energies the Bethe-Bloch formula ceases to be valid because processes that change the projectile charge state start to occur. In particular, the projectile starts to collect electrons of the surrounding material decreasing its effective charge [64]. The Barkas formula can be used to describe the effective projectile charge  $Z_{\text{eff}}$  (which then substitutes  $Z_p$ ):

$$Z_{\text{eff}} = Z_p (1 - e^{-125\beta Z_p^{-2/3}}). \quad (2.11)$$

This formula does not consider though, the discrete nature of charge states, but only average charge over many projectiles [65, 66].

---

## Stopping Power and LET

---

As defined in Section 2.1.2, the (unrestricted) LET of a material is the energy lost per unit path by a charged particle due to electronic collisions. Therefore [23]:

$$\text{LET} = (\frac{dE}{dx})_{\text{el}}. \quad (2.12)$$

The limitations of quantities such as the stopping power and the LET are, firstly, that different particles can have the same value, as different  $v$  and  $Z_p$  combinations can lead to the same LET or stopping power values. Secondly, they do not take care of the finite dimensions of the target. Finally, they do not consider the stochasticity of the energy loss phenomenon over the particle track. The energy is released in the form of clusters. As a consequence, they are defined as an average over a great number of interactions of the primary ion. Therefore, they cannot be used to define the energy loss in a very small volume, such as the dimensions of a cell or DNA [67].

---

## Particle Ranges

---

Knowing how to compute the stopping power from Equation 2.8, the range  $R$  of the projectile particles can be computed as:

$$R = \int_0^{E_p} \frac{dE}{-dE/dx}. \quad (2.13)$$

To be noted that, if we take two different particles with the same energy per nucleon:

$$\frac{R_2}{R_1} = \frac{Z_{p1}^2 A_{p2}}{Z_{p2}^2 A_{p1}}. \quad (2.14)$$

Therefore, if two particles have the same  $A/Z^2$  ratio they have the same range, e.g. protons and  $^4\text{He}$  ions, while heavier particles have shorter ranges for the same initial energy per nucleon value.

---

## 2.5.2 Nuclear Interactions

---

The second interaction type that ions undergo when travelling through matter is nuclear interactions. They can be either elastic or inelastic processes. When elastic interactions happen, no changes in the composition of the nuclei take place and the total kinetic energy of the system is conserved. On the other hand, there are two outcomes of inelastic interactions. In the first case, projectile and target nuclei remain intact and total kinetic energy is not conserved because of the (nuclear) excitation processes that occur. In the second case, projectile and target react and either or both of them break apart and produce secondary nuclei. This nuclear reaction process is known as fragmentation. The secondary nuclei are called projectile fragments if they originate from the primary ions, or target fragments if from the nuclei composing the target material [68]. Such fragmentation processes occur if the projectile and target nuclei overlap during the collision and the projectile kinetic energy exceeds the Coulomb barrier.

---

## Abrasion-Ablation Model

---

For heavy-ion reactions, these collisions are commonly described through the so-called abrasion-ablation model [4, 69, 70], which can also be called the cascade-evaporation model. In this two-step process, firstly the geometrical overlap between the projectile and target nuclei causes the removal of nucleons from the original nuclei. What remains after it, are parts of them, and a so-called fireball, all of which are normally in an excited state. The remaining parts of the original nuclei can be called spectators. Secondly, during the ablation phase, both the spectators and the fireball de-excite by emitting lighter nuclei, single nucleons, and gamma rays. The process is represented in Figure 2.10. Peripheral collisions lead to small mass removals from the original nuclei, while central collisions can cause their complete disintegration.

---

## Nuclear Cross-Sections

---

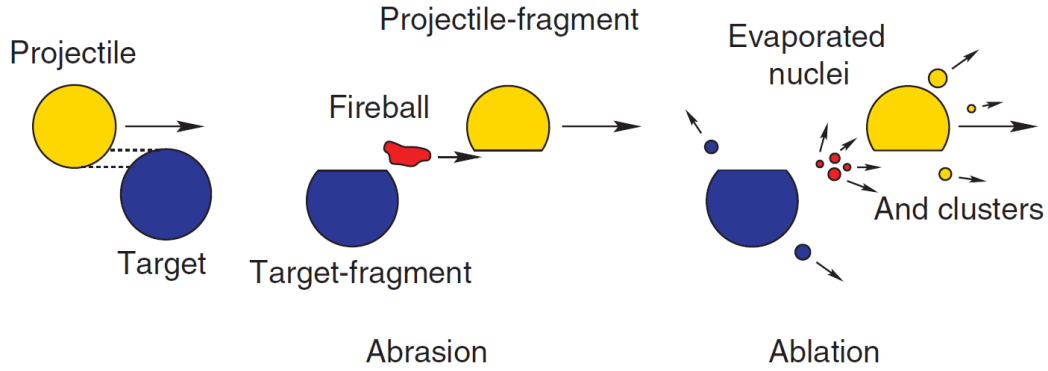


Figure 2.10: Schematic representation of the abrasion-ablation model [4].

---

### Nuclear Reaction Cross-Sections

---

The cross-section (see Equation (2.7)) for an inelastic nuclear process to happen is called the total reaction cross-section ( $\sigma_R$ ). The number  $N$  of ions that reach a thickness  $z$  of a given material with an atomic density  $n$  of atoms per unit volume, can be computed as:

$$N = N_0 e^{-zn\sigma_R}, \quad (2.15)$$

where  $N_0$  is the number of ions entering the material. The atomic density can be computed as:

$$n = \frac{N_A}{M} \rho, \quad (2.16)$$

where  $N_A$  is the Avogadro constant,  $M$  the molar mass, and  $\rho$  the material density. A geometrical approach was used by Bradt and Peters [71] to estimate total reaction cross-sections as:

$$\sigma_R = \pi r_0^2 (A_p^{1/3} + A_T^{1/3} + \delta)^2. \quad (2.17)$$

$A_p$  and  $A_T$  are, respectively, the projectile and target mass numbers,  $r_0$  is the nucleon radius, and  $\delta$  is the overlap transparency parameter. Most of the parametrisations used nowadays to model reaction cross-sections are still based on an energy-dependent Bradt-Peters approach, where the energy dependence is inside the  $\delta$  parameter. Some of these parametrisations will be described in Section 5.1.2.

Reaction cross-sections can be estimated by the measurement of charge and mass-changing cross-sections. On the one hand, charge-changing cross-sections measure the probability of the projectile ion to change its atomic number  $Z_p$  ("charge"), which means to become another element. The case of the projectile only changing its mass number  $A_p$  is not included in the charge-changing cross-section. On the other hand, mass-changing cross-sections measure the probability of the projectile ion to change its mass number  $A_p$ . Mass-changing cross-sections are therefore more inclusive than charge-changing cross-sections.

---

### Nuclear Fragment Production Cross-Sections

---

The cross-section for the production of a specific fragment as a consequence of nuclear fragmentation processes is called the fragment production cross-section [72].

Fragment production cross-sections can be inclusive ( $\sigma_{p,i}$ ) or exclusive ( $\sigma_{p,e}$ ). On the one hand,  $\sigma_{p,i}$  are probabilities of a certain fragment to be produced, no matter the reaction channel taking place.  $\sigma_{p,e}$  on the

other hand, measure the probability of a specific reaction channel to take place. For a reaction:



$P$  is the projectile,  $T$  the target, and  $F$  and  $X$  are the fragments produced.  $\sigma_{p,i}$  does not contain any information about  $X$ , while  $\sigma_{p,e}$  does. Therefore:

$$\sigma_{p,i} = \sum_k \sigma_{p,e\ k}, \quad (2.19)$$

where the sum runs over all the possible exclusive channels  $k$  that generate the fragment of interest of  $\sigma_{p,i}$ .

$\sigma_{p,i}$  can themselves be either elemental or isotopic. If  $\sigma_{p,i}$  expresses the probability of a certain element (no matter its mass number) to be produced, i.e.:



it is called elemental ( $\sigma_{el}$ ). On the other hand, if  $\sigma_{p,i}$  expresses the probability of a specific isotope of that element to be produced, i.e.:



it is called isotopic ( $\sigma_{iso}$ ). In particular:

$$\sigma_{el} = \sum_j \sigma_{iso\ j}, \quad (2.22)$$

where the sum runs over all the isotopes  $j$  of the element of interest.

So far, the focus was put on total cross-sections. A total cross-section for a reaction such as the one of Equation 2.18 describes the probability of the fragment  $F$  to be produced with any energy and direction of motion. Nevertheless, there are also differential cross sections. In particular:

$$\sigma_{p,i} = \int_{\Theta} \int_{\eta} \frac{d^2 \sigma_{p,i}}{dE d\theta}, \quad (2.23)$$

where  $\frac{d^2 \sigma_{p,i}}{dE d\theta}$  is the double differential inclusive production cross-section for a certain fragment to be produced with a certain energy  $E$  and direction of motion  $\theta$ .  $\Theta$  are all the possible directions of motion and  $\eta$  all the possible fragment energies.

The basic equation for calculating the total inclusive production cross-section of a fragment with atomic number  $Z_f$  and mass number  $A_f$  through spallation and fragmentation processes is [73, 74]:

$$\sigma(A_f, Z_f) = Y(A_f)Y(Z_{\text{prob}} - Z_f)|_{A_f}, \quad (2.24)$$

where  $Y(A_f)$  is the sum of all isobaric cross-sections with fragment mass  $A_f$  and  $Y(Z_{\text{prob}} - Z_f)|_{A_f}$  is the distribution of elemental cross-sections (with a given mass  $A_f$ ), whose maximum value is reached at the most probable atomic number  $Z_{\text{prob}}$ .

Nevertheless, the experimental data collected from the 70s onwards allowed improvements in the model. For instance, Equation 2.24 does not take into account the odd-even staggering (OES) [75], which consists in enhanced production of even- $Z$  than odd- $Z$  nuclides because of their higher binding energy per nucleon. Therefore, a more accurate description can be obtained with the following Equation:

$$\sigma(A_f, Z_f) = Y(A_f)Y(Z_{\text{prob}} - Z_f)|_{A_f} \Delta_{\text{OES}}(A_f, Z_f). \quad (2.25)$$

The parametrisations most commonly used in the space radiation field are EPAX3 [76], NUCFRG3 [77], SPACS [78], FRACS [79], and RAADFRG [80]. Older models such as EPAX3 are based on Equation (2.24). More recent models such as FRACS, instead, take also into account the OES (Equation (2.25)) and, therefore, show a better agreement with experimental data.

---

## Measuring Nuclear Cross-Sections

---

When measuring them, mass-changing cross-sections are more difficult to be measured than charge-changing cross-sections, exclusive more than inclusive, isotopic more than elemental, and finally, differential cross-sections more than total. In fact, it is more difficult to identify all of the fragments produced ( $\sigma_{p,e}$ ) than only the ones of interest ( $\sigma_{p,i}$ ), to resolve the mass of an ion ( $\sigma_{iso}$ ) in addition to its atomic number alone ( $\sigma_{iso}$ ), and to resolve the energy and emission angle of a fragment ( $\frac{d\sigma_{p,i}}{dE d\theta}$ ) than its fragment production only (total  $\sigma_{p,i}$ ). Nevertheless, the most meaningful are the most difficult ones, as they allow the benchmark of the theoretical predictions on a more basic level. Once we have reliable exclusive cross-sections, we can sum up all the processes producing the fragment of interest, and obtain the corresponding inclusive cross-section. Following the same reasoning, once having reliable values of all the isotopic cross-sections for all the isotopes of the element of interest, we can obtain the elemental cross-section by summing them up. The same is valid for double-differential cross-sections, which can be integrated once to obtain single-differential cross-sections and twice total cross-sections. In all three cases, the opposite process is not possible.

---

### 2.5.3 Bragg Curves

---

The projectile's electronic and nuclear interactions described in the previous sections dictate the shape of the depth-dose profile for the projectile in the target material. In Panel (a) of Figure 2.11, the simulated depth-dose profiles of protons, helium, carbon and iron ions in polyethylene (PE), are reported. The primary energy of the ions was chosen for them to have the same ranges. The dose values were normalised to the entrance channel (values at  $z = 0$ ). The curves were computed with FLUKA. Such profiles are called Bragg curves and the peaks at the end of them are Bragg peaks. Such peaks are caused by the increase of the  $\frac{dE}{dx}$  of the primary ions right before they are stopped at the end of their range (see Section 2.5.1).

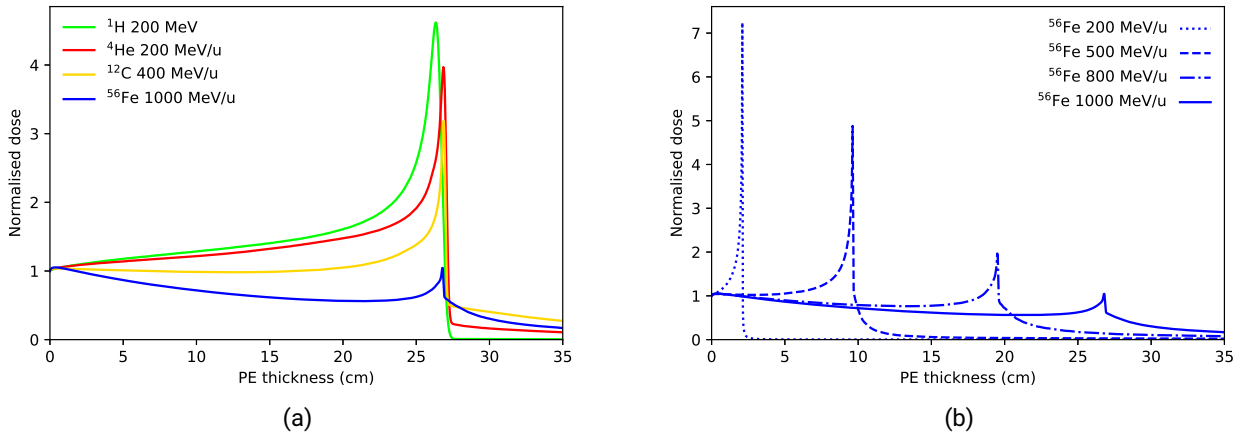


Figure 2.11: Panel (a): simulated Bragg curves of 200 MeV  $^1\text{H}$ , 200 MeV  $\text{u}^{-1}$   $^4\text{He}$ , 400 MeV  $\text{u}^{-1}$   $^{12}\text{C}$ , and 1000 MeV  $\text{u}^{-1}$   $^{56}\text{Fe}$  in polyethylene. The primary energy of the ions have been chosen for them to have the same range, starting from the choice of 1 GeV  $\text{u}^{-1}$  for iron, as it is its peak energy in the GCR spectrum for the case of solar minimum (see Figure 2.8). Panel (b): Bragg curves of 100, 500, 800, and 1000 MeV  $\text{u}^{-1}$   $^{56}\text{Fe}$  ions. This Figure was produced with FLUKA.

The shape of the curves before the Bragg peak is determined by a combination of two main phenomena:



- energy loss due to collisions of the projectile with the electrons of the medium, which makes the dose increase as the penetration depth increases, and
- fragmentation of primary ions through nuclear reactions, which make the dose decrease even if several fragments are produced from one projectile because the projectile fragments have a lower atomic number than the primary ions ( $\frac{dE}{dx} \propto Z_p^2$ ). Since fragments have a lower  $\frac{dE}{dx}$ , they have a longer range and, therefore, contribute to a so-called fragment tail behind the Bragg peak. Examples of the relative contribution to the absorbed dose of primary ions and their fragments in PE are reported in Figure 2.12.

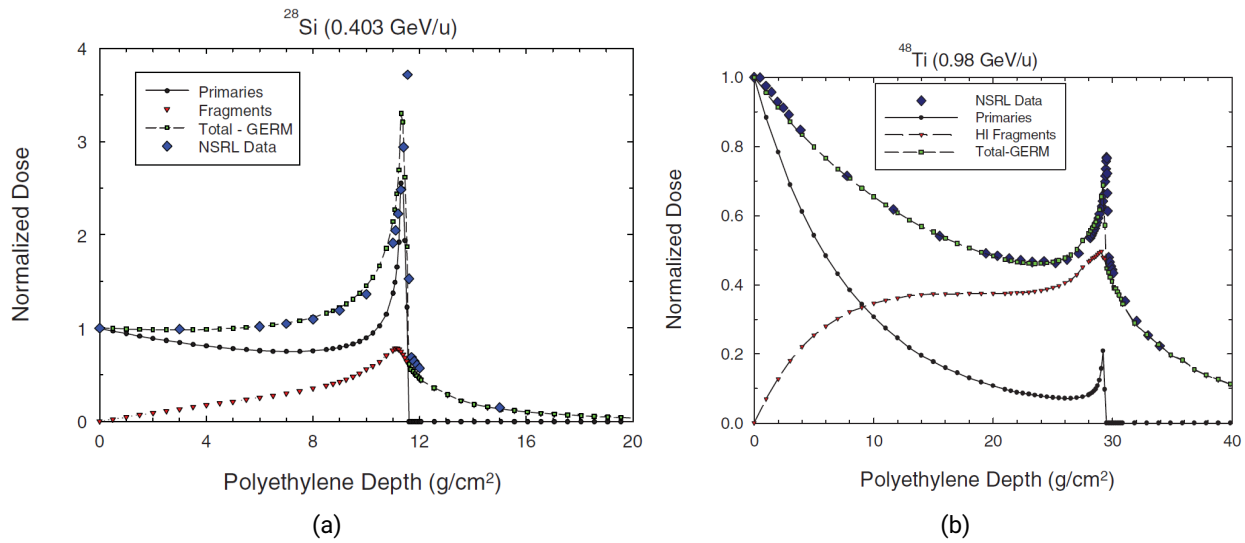


Figure 2.12: Calculated total normalised dose and relative contributions of primary ions and fragments for  $403 \text{ MeV u}^{-1} \text{ } ^{28}\text{Si}$  and  $980 \text{ MeV u}^{-1} \text{ } ^{48}\text{Ti}$  in PE [4, 81]. The total normalised dose is compared with experimental data.

In Panel (a) of Figure 2.11, it can be seen that for the carbon-ion energy considered, such phenomena almost even each other out in the entrance channel. For the energies under study, for hydrogen and helium, the dose increases due to their dominating energy loss, while for iron the dose decreases until the Bragg peak because of the domination of the fragmentation effect. Thus, depending on the ion species and energy one of the two phenomena prevails. In Figure 2.11, it is possible to see that the more fragmentation happens, i.e. steeper the entrance channel of the curve, the bigger the tail behind the Bragg peak is.

In conclusion, the shape of the Bragg peak, the tail behind it and the entrance channel of the curve differ for every ion because of the interactions it undergoes when travelling through matter [82, 83].

In Panel (b) of Figure 2.11, Bragg curves of iron ions having different primary energies are reported. More energetic ions have longer ranges. A larger range corresponds to more fragmentation reactions. This causes:

- a stronger dose attenuation before the Bragg peak,
- a smaller Bragg peak as fewer primary ions contribute to it, and
- a more pronounced tail behind the Bragg peak due to more projectile fragments generated.



Additionally, it can be noticed that the Bragg peak broadens for higher energies. This is due to a phenomenon called energy loss straggling. When the penetration depth in the target increases, the microscopic fluctuations around the mean energy loss sum up into a macroscopic range straggling.

#### 2.5.4 Dose Build-up

Panel (a) of Figure 2.13 shows a zoom-in of the Bragg curves of Panel (a) of Figure 2.11 over the first 0.6 cm of PE for carbon and iron ions. A small dose enhancement can be observed for very small PE thicknesses, i.e. until  $\approx 0.25$  cm for carbon, and  $\approx 0.4$  cm for iron ions. This phenomenon is called dose build-up [84, 85]. It is due to secondary particles (electrons or ions) generated from the target material, which are mainly forward directed. The depth of the dose build-up effect corresponds to the range of such particles in the target material. The effect stops growing when no more secondary particles are added, i.e. the new particles compensate for the loss of those that stop as they have reached the end of their range in the material (see Panel (b) of Figure 2.13). In Figure 2.13, the depth of the dose build-up is larger for iron ions

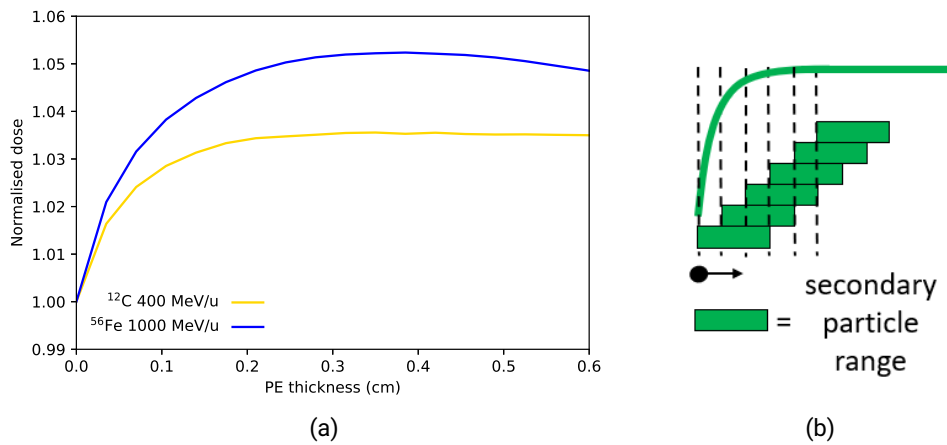


Figure 2.13: Panel (a): zoom-in of Figure 2.11 over the first 0.6 cm of PE for carbon and iron ions. Panel (b): schematic representation of the equilibrium reached in the build up effect. The depth of the effect corresponds to the range of the secondary particles causing it.

than for carbon as the range of the secondary particles is higher for iron because of their higher energy ( $1000 \text{ MeV u}^{-1}$  vs  $400 \text{ MeV u}^{-1}$ ). For the case of iron, the build-up is also more intense. This is actually due to the longer range of the secondary particles as, if the particle range (represented with green rectangles in Panel (b) of Figure 2.13) is longer, the more secondary particles are produced within this range and their contribution builds up to higher doses. After the build-up effect reaches equilibrium at a certain depth, the dose attenuation due to projectile absorption or fragmentation takes over for the projectiles of Figure 2.13, and the dose starts to decrease. The build-up effect is much stronger for lighter ions [11]. For instance, Panel (a) of Figure 2.14 reports the full Bragg curves of  $400 \text{ MeV u}^{-1}$  hydrogen and helium ions in PE. Panel (b) is a zoom-in over the first 30 cm of PE. It is possible to see that, even if helium and hydrogen have lower energies per unit nucleon, the range of their build-up effect is much larger than for the iron and carbon, reaching around 12 cm for helium, and 20 cm for hydrogen.

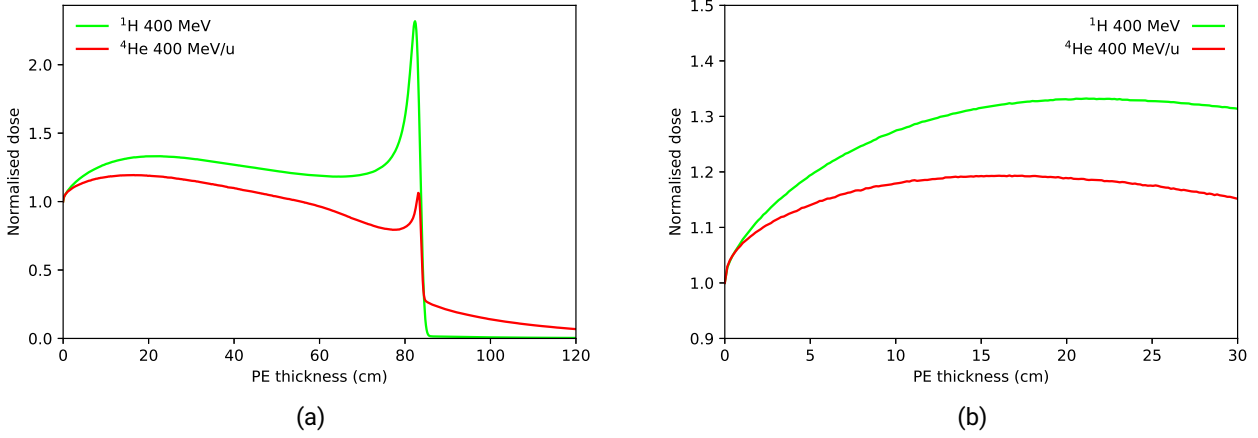


Figure 2.14: Panel (a): simulated Bragg curves of 400 MeV  $u^{-1}$   $^1H$  and  $^4He$  ions in PE. Panel (b): zoom-in over the first 30 cm. This Figure was produced with FLUKA.

## 2.6 Radiation Protection in Space

As discussed in Section 2.4, space explorers are ordinarily exposed to much higher doses than humans on Earth. Table 2.3 compares the dose exposures on Earth, during the flight, on the Moon, and Mars. Due

Table 2.3: Comparison of dose equivalent exposures in different scenarios. The variability on the Moon and Mars is due to the solar cycle and the altitude of the exposure.

Exposure scenario	$D_{eq}$ rate ( $mSv\ year^{-1}$ )	Ref.
Earth	2.4	[86]
Flight	672	[46]
Moon	110-380	[52]
Mars	100-230	[53, 87]

to the different doses and radiation fields characterising space and terrestrial exposures, the radiation protection definitions and measures taken on Earth need to be modified and adapted to space exploration.

### 2.6.1 A More Suitable Dose Equivalent Definition

As already pointed out, the radiation protection definitions reported in Section 2.1 should only be used in the case of dose exposures well below legal limits (see Section 2.1.3), which is not the case for space. When coming to radiation protection in space, radiation quality factors  $w_R$  (see Table 2.1) are not used, nor Equation 2.2 is. If one considers the relative importance of protons and heavy ions, using  $w_R = 20$  for all of them, independently of their energy, is too approximate, and a more realistic approach needs to be used [22]. The National Council for Radiation Protection and Measurements recommends [88] to use the following method [20] to compute the organ  $D_{eq}$  for space applications:

$$D_{eq} = \frac{1}{m} \int_m dm \int Q(LET) F_T(LET) LET dLET, \quad (2.26)$$

where  $m$  is the organ mass,  $F_T$  is the particle fluence through the organ T, and  $Q(LET)$  is a LET-dependent quality factor.  $Q(LET)$  was introduced in ICRP 26 [35], before the introduction of the  $w_R$  factors, and the latest recommendations for it come from ICRP 60 [89]. Equation 2.26 takes into account not the particle type, but its LET. The same particle, in fact, has different LET values depending on its energy. Even if Equation 2.26 is more accurate than Equation 2.2, it is still not optimal because it does not take into account track effects (see Section 2.1.2).

---

## 2.6.2 Radiation-Related Health Risks in Space

---

Space radiation risks of concern to NASA are carcinogenesis, acute and late risks to the central nervous system, degenerative tissue risks such as cardiovascular disease, and acute radiation syndromes [4, 45]. Even if cancer dominates dose risk estimates, non-cancer effects are an increasing source of concern. Cataract is so far the only cosmic radiation-induced effect observed in space explorers [90, 91]. As already pointed out, acute risks (occurring during the mission) are a concern with SPEs, while late risks (occurring after a mission) with both GCRs and SPEs. A large number of risks of concern make it too complicated to try approaches such as genetic selection, as it is very unlikely to find someone resistant to so many diseases. In addition, the chronic radiation exposure and the radiation quality, make the applicability of the radio-protectors developed for terrestrial exposure and usually employed in case of acute exposure to low-LET radiation [4], unfeasible.

---

## 2.6.3 Uncertainties on Space Radiation Risks

---

As mentioned in Section 2.2, the Earth's radiation spectrum is very different to space radiation in energy and composition. In particular, radiation-exposure health data mainly come from epidemiological studies performed on atomic-bomb survivors, who were exposed mainly to gamma, beta and alpha rays. Therefore, very large uncertainties are still associated with space radiation risks because of poor knowledge of (in order of decreasing importance) [4, 45]: relative biological effectiveness factors of heavy ions for late effects (cancer and non-cancer), dose and dose-rate dependencies, transfer of risk across populations, determination of space radiation organ exposures, various errors in human data sources, effects of exposure to a mixed low and high-LET radiation field, the shape of the dose-response curve at low doses for charged particles, and possible synergistic risks from other space environment stressors (in particular microgravity) on radiation risks. Large ground-based experimental radiobiology research programs are ongoing to reduce such uncertainties.

---

## 2.6.4 Effective Dose Limits in Space

---



---

### Risk of Exposure-Induced Death: Model

---

The quantity used to make risk estimates in space is the risk of exposure-induced death (REID). Following the NASA model [92], it can be computed as:

$$REID(a_E, D) = \int_{a_E}^{\infty} dt \lambda_M(a, a_E, D) S_0(t) e^{-\int_{a_E}^t dz \lambda_M(z, a_E, D)}, \quad (2.27)$$

where  $\lambda_M$  is the age and gender-dependent cancer mortality rate,  $a_E$  is the age at exposure,  $a$  is the attained age ( $a - a_E$  is then the time after exposure, or latency), and  $S_0$  the survival fraction of the background population. There are different models recommending different values to be used in the  $\lambda_M$  computation. Therefore, the REID results are model-dependent.

## Age and Gender Dependency

Figure 2.15 reports a comparison of the effective doses that lead to a 3% REID in females and males of different ages, in a 1-year mission, computed with different models, under the assumption of an equal organ dose equivalent for all tissues. The Figure shows that the older a space explorer is, the higher the effective dose value leading to the same REID. Also, the dose values for males are consistently higher than for females.

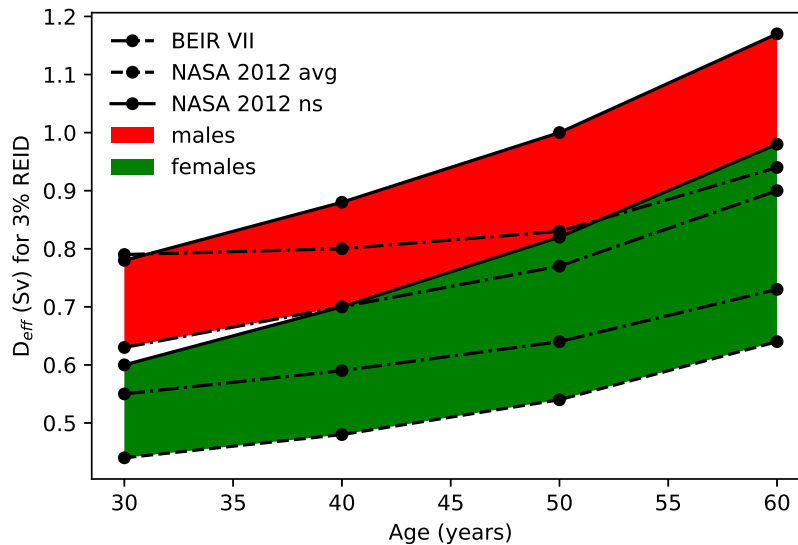


Figure 2.15: Comparison of the effective dose values leading to 3% REID for male and female individuals (data from [92]).

## Dose Limits for Space Explorers

The career effective dose limits (Sv) recommended by different space agencies until 2021 are reported in Table 2.4. It can be noticed that, in the case of NASA and JAXA, they are not only age-dependent, but also gender-dependent. Nevertheless, in 2021, the US National Academy of Science introduced a simplified

Table 2.4: Career effective dose limits (Sv) as recommended by different space agencies before 2021.

Space agency	Gender	Age at first exposure (years)			
		30	35	45	55
NASA (USA)	Female	0.47	0.55	0.75	1.1
	Male	0.62	0.72	0.95	1.5
JAXA (Japan)	Female	0.6	0.8	0.9	1.1
	Male	0.6	0.9	1.0	1.2
ESA (Europe)		1.0	1.0	1.0	1.0
FSA (Russia)		1.0	1.0	1.0	1.0
CSA (Canada)		1.0	1.0	1.0	1.0

---

effective dose limit of 0.6 Sv for all astronauts, independently of their age and gender, with the objective of allowing equivalent flight opportunities to everyone [93, 94]. This number is based on a 3% REID calculation for a 35-year-old female using the operational NASA 2012 [95] model with never smoker parameters. This decision caused a break in the scientific community, as some defined it as a “giant leap backwards” for radiation protection in space [96].

---

### 2.6.5 The ALARA Principle in Space

---

Since the strategies used on Earth to protect humans from radiation are based on the ALARA principle described in Section 2.1, it could be considered to apply it also to radiation protection in space:

1. Distance. In space, it is impossible to increase the distance from the radiation source as GCRs are omnidirectional and as SPE radiation travelling along solar magnetic field lines becomes isotropic within a few hours after the start of an event [97].
2. Time. This point can be addressed in several ways. Manned exploration missions such as the mission to Mars can be limited to a maximum amount of time. But starting a colony on the Moon, Mars, or any other planetary surface beyond them, goes in the very opposite direction, as the aim is for people to live there for long periods. Focusing on travel only, more powerful engines can be employed in space exploration to reach higher velocities and make the travel as short as possible. This is a long-term goal of space programs, but currently has strong limitations [87]. Exploring outer space pushes into the direction of going further and further, and this naturally makes missions longer and longer. On the other hand, the timing, as in when to perform the mission, can play a role. In particular, in Section 2.3, it is explained that SPEs happen with a higher probability during solar maxima, while GCR fluxes are higher during solar maxima. Therefore, the question if it would be better to proceed with the mission to Mars during a solar maximum (less exposition to GCR, but higher SPE risk) or minimum (higher GCR exposition but lower SPE risk) has remained unanswered for a long time. Recently, however, [98] demonstrated through MC calculations that the optimal time to fly to Mars is during a solar minimum, and the mission duration should not exceed 4 years.
3. Shielding. Alongside the choice of an appropriate time of flight, shielding is the only option left to mitigate the risks of crew exposure to space radiation. There are two possible shielding strategies: active and passive shielding.

---

## 2.7 Shielding in Space

---

---

### 2.7.1 Active Shielding

---

Active shielding consists in generating magnetic fields around the space explorers' habitat to deflect the trajectory of cosmic rays [4, 37]. This would be possible since SPEs and GCRs are made of charged particles. The most promising approach is confined magnetic fields. In particular, toroidal fields [99–101] generated around the spacecraft would have the advantage of confining the field outside of the spacecraft's habitable area and consequently, not exposing the space explorers to an intense magnetic field. Nevertheless, there are several technical issues with active shielding. Among them, the cryogenic superconducting magnet technique, which is critical for such applications, is currently not reliable. Also, the active shielding system would need to be redundant as possible failures cannot leave the crew unprotected. For this reason, even if such techniques were already available, they would be combined with passive shielding.

---

## 2.7.2 Passive Shielding

---

Passive shielding consists in adding material to spacecraft and habitat walls to reduce the dose inside the crew's living space [37]. The thickness of the spacecraft wall alone is  $5 \text{ g cm}^{-2}$ , but on the ISS the shielding thickness reaches around  $20 \text{ g cm}^{-2}$  because of the presence of several payloads and racks. Such thickness can stop all protons with energy below 100 to 200 MeV, and therefore efficient against trapped radiation (which is relevant in LEO only) and most SPEs [4]. Because of their different composition and energy spectrum, SPEs and GCRs deserve individual considerations when coming to passive shielding.

---

### Shielding from SPEs

---

Even if most of SPEs are harmless behind thin shields, the most intense can be life-threatening for unshielded space explorers [102]. In particular, there have been about 400 SPEs in the space age, and only 4 of them would have led to blood-forming organ doses behind  $5 \text{ g cm}^{-2}$  aluminium shields, sufficient to possibly cause acute radiation sickness. Furthermore, none of them would have led to acute radiation death [103]. Due to the energy spectra of SPEs, the  $20 \text{ g cm}^{-2}$  shielding thickness foreseen for future long-term exploration missions is sufficient to reduce the doses enough to make the SPEs harmless for space crews. Also, an approach based on having more shielded quarters (e.g. sleeping quarters) can be adopted for keeping the crew protected from SPEs. It is estimated [4] that mass requirements of the order of 1000 kg are needed for such so-called storm shelters for a crew of three using optimal shielding materials and topologies.

Nevertheless, intense SPEs remain a life-threatening risk during extravehicular activities (EVAs), both performed during the travel and *in situ*, i.e. on the explored planetary surfaces. Spacesuit design and the usage of shielding blankets or coats to cover vital organs can be advantageous but are not enough. An adequate forecast system is then necessary as a “warning system” for our space explorers to abandon the ongoing EVA or not start one, and avoid them experiencing acute radiation syndromes or being at risk of death. Unfortunately, the current forecasting abilities are limited. However, [104] showed that the detection of relativistic solar electrons may allow a 1-hour prewarning of SPEs and a prediction of integral proton fluences.

---

### Shielding from GCRs

---

Even if SPEs might be able to cause acute radiation syndrome and in worse case scenarios death, they do not pose as much of a risk as galactic (and intergalactic) cosmic rays (GCR). As explained in the previous section, SPEs can be shielded with spacecraft wall thicknesses already foreseen for long-term deep-space missions. On the other hand, the composition and energy spectra of GCR (see Figures 2.7 and 2.8) reaching up to  $10^{20} \text{ eV}$ , make them impossible to be completely shielded with reasonable amounts of spacecraft material [4]. Average energy GCRs can penetrate tens to hundreds of centimetres of water or aluminium. In addition, the secondary radiation field produced within the interaction of GCRs with the structural or shielding material of the spacecraft is made of lighter particles that can penetrate even further [45].

Even though the fluence of light ions is much higher than that of heavier ions, behind thin shields heavy ions are the main source of dose and dose equivalent. For very thick shieldings, instead, light ions like hydrogen and helium become the most relevant for dose and dose equivalent contributions [105]. In Figure 2.16, the relative contribution of the different ion species to fluence, dose and dose equivalent is shown behind a thin  $5 \text{ g cm}^{-2}$  aluminium shield. For what concerns thicker shields, [106] calculated that, behind a  $20 \text{ g cm}^{-2}$  aluminium shield, 68% of the total effective dose is due to protons, and 10% to helium. These numbers increase behind a  $20 \text{ g cm}^{-2}$  aluminium shield, reaching 70% for protons, and 14% for helium. These results are also supported by Geant4 calculations presented in [105]. The usage of thick

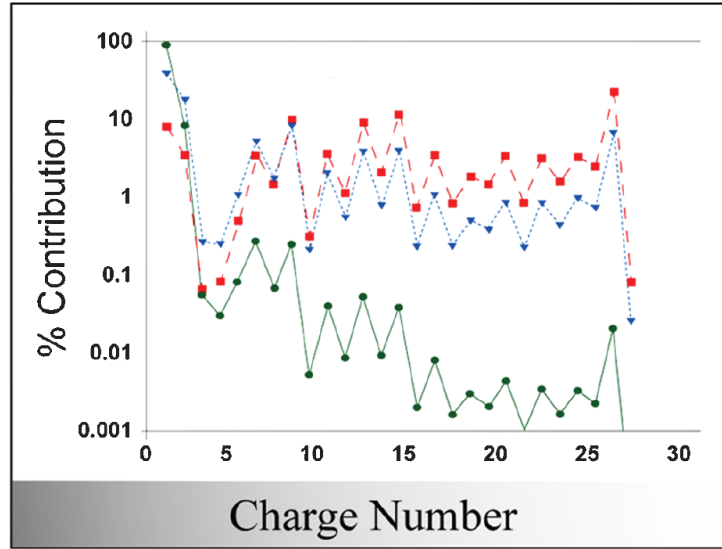


Figure 2.16: Relative contribution in fluence (green circles), dose (blue triangles), and dose equivalent (red squares) of different GCR ion species. The calculation was performed as an average over 1 year of solar minimum (worst case scenario) behind a  $5 \text{ g cm}^{-2}$  aluminium shield [4].

shields also causes an increase in the neutron dose behind them. Because of the high penetration power of neutrons and their high biological effectiveness (see Table 2.1), it is key to focus on their production [14, 107, 108]. The increasing importance of light ions behind thick shields is shown in Figure 2.17.

In conclusion, passive shielding is the winning strategy for near-future space exploration missions [4, 110, 111]. Nevertheless, it also has limitations. The main problem is the travel because of the severe mass (and volume) constraints due to the high cost of the fuel. As the shielding thickness increases, the shielding effectiveness drops due to the secondary radiation field generated through the interaction of cosmic radiation with the shield itself. Because of such mass constraints, engineers have been considering the dual use of necessary resources such as water, fuel, and food storage, as shielding material also. In addition, the so-called *in situ* resources can be exploited on the planetary surfaces, i.e. Lunar or Mars regolith [112, 113]. In fact, it can be moved on top of the crew's habitable structures [4, 114]. Habitable areas can also be obtained by digging caves on the Moon, but the need for light for the psychological well-being of the crew members needs to be taken into account as well. Space explorers cannot spend too much time inside the habitats, depending on the mission aims.

### 2.7.3 Candidate Materials for Passive Shielding

The basic concepts of heavy ion interaction with matter can be used to guide the selection of optimal shielding materials. In space, the aim is to stop low-energy particles and to break up particles whose energy is too high to be completely stopped within the spacecraft shields.

For low-energy particles, the aim is to maximise their slowing down process so that they eventually stop in the shielding. Since  $\frac{dE}{dx} \propto \rho \frac{Z_T}{A_T}$  (see Equation 2.8),

$$\frac{dE/dx}{\rho} \propto \frac{Z_T}{A_T}, \quad (2.28)$$

where  $\frac{dE/dx}{\rho}$  is called mass stopping power and represents the stopping power per unit mass of the material. Quantities per unit mass of the target (in this case shielding) material are interesting because of the severe



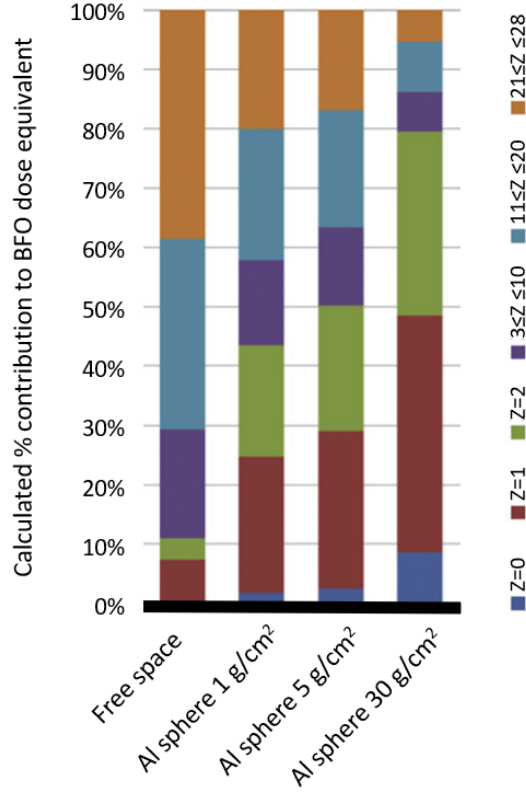


Figure 2.17: Increasing relevance of light ions behind thick shields: calculated contribution (%) of different ions to GCR blood forming organs (BFO) dose equivalent in free space (from the left) and increasing thickness of simple spherical geometries (adapted from [109]).

mass constraints characterising space missions, due to the high cost of the fuel needed to send heavy spacecrafts into space. The materials with higher  $\frac{Z_T}{A_T}$  are low-Z materials, as the greater Z becomes, the higher the number of neutrons per unit proton in the nuclei is ( $\frac{Z}{A} = 1$  for hydrogen, 0.5 for carbon, 0.48 for aluminium, 0.46 for iron, and 0.40 for lead). Low-Z materials have the highest number of electrons per nucleon. Low-Z materials are, therefore, optimal for slowing down and stopping the particles that can be stopped within the viable shielding thicknesses in space.

Additionally to the maximisation of the mass stopping power (i.e. the electronic interactions), a good approach for shielding in space is the maximization of nuclear fragmentation processes as breaking up the primary cosmic rays significantly reduces the dose (see Section 2.5.3). Since the nuclear reaction cross section  $\sigma \propto A_T^{2/3}$  (see Equation 2.17), the nuclear reaction cross-section per unit mass of the shield  $\frac{\sigma}{m_T}$  is:

$$\frac{\sigma}{m_T} \propto \frac{A_T^{2/3}}{A_T} = A_T^{-1/3}. \quad (2.29)$$

Therefore, the nuclear reaction cross-section per unit mass of the shield is also maximised for the case of low-Z materials, as they have small  $A_T$ . This is due to the nuclei of low-Z materials being smaller in size and therefore, more of them can fit into a given mass, so that more nuclear interactions can happen. Low-Z materials are therefore the best option for passive shielding purposes [4–7, 9].

From these considerations, the optimal shielding material from cosmic radiation would be liquid hydrogen. Nevertheless, engineering considerations about the material strength, temperature resistance, UV



degradation and flammability, need to be done. That is why PE (and in particular, high-density polyethylene - HDPE) has been considered the golden standard for radiation protection in space for a few decades [4, 6]. It is chemically stable, cheap, and has a low atomic number. Recent simulation campaigns performed with the full GCR spectrum have confirmed the goodness of PE for dose equivalent reduction also behind thick shields. The production of protons and neutrons in thick targets makes the dose equivalent attenuation of other materials such as aluminium limited. These results are reported in Figure 2.18.

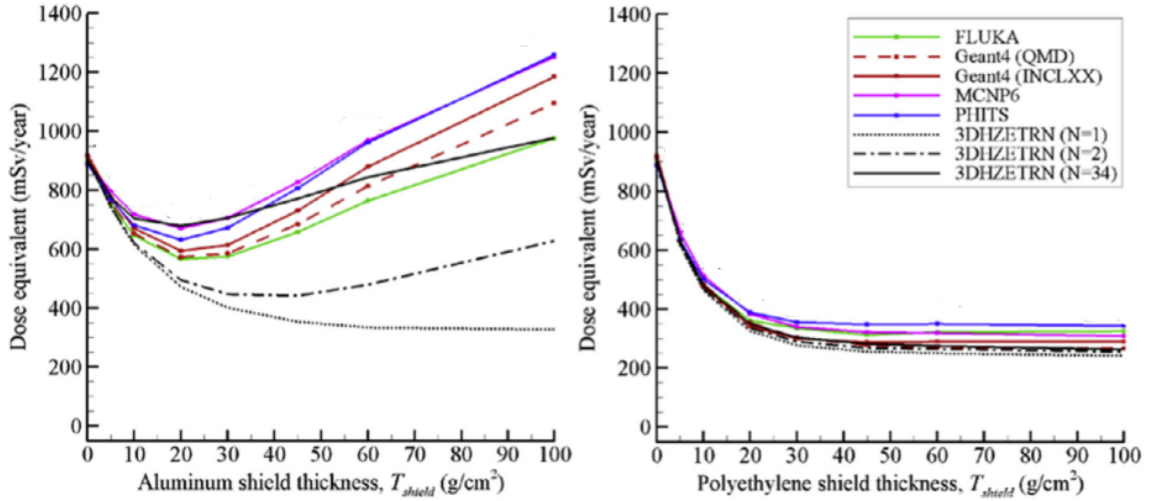


Figure 2.18: Total dose equivalent as a function of aluminium (left) and polyethylene (right) shield thickness for the full GCR spectrum (adapted from [115]).

Experimental [11, 12] and simulation campaigns [116] have recently shown that lithium-based hydrides, which have lower  $Z$  than PE, have promising dose attenuation properties. Therefore, such materials are the focus of the experimental campaigns performed in the scope of this thesis.

## 2.8 Stochastic and Deterministic Radiation Transport Methods

It is unfeasible to irradiate spacecraft and space habitats in ground-based experiments, and it is unfeasible to irradiate them with a homogenous radiation source mimicking the cosmic radiation composition, energy spectra, and rates. Therefore, we have to rely on the results of deterministic and stochastic simulations of how radiation interacts with the materials composing the habitat and the space explorers' bodies. There are two approaches to solving any physical or mathematical problem: stochastic and deterministic.

On the one hand, the deterministic approach consists of directly solving integropartial-differential equations to find the exact solution to the problem. It is usually chosen for simple or one-dimensional problems because when coming to complex or three-dimensional problems, assumptions and simplifications are necessary to make the problem solvable in reasonable amount of time. Therefore, deterministic methods tend to be fast but approximate in the resolution of real-world (complex or three-dimensional) problems.

On the other hand, stochastic methods imply the usage of random numbers, are usually chosen for complex or three-dimensional problems and tend to be very accurate at the cost of highly demanding computational resources. Stochastic methods are also called Monte Carlo (MC) methods [117]. Stochastic methods consist in several ( $N$ ) different realisations, each of them providing a different outcome ( $f_i$ ). The final outcome is an approximation of the correct value (expectation value  $\langle f \rangle$ ) with respective error bars, and the correct value is likely to be within those error bars  $\sigma^2$ . The expectation value  $\langle f \rangle$  is defined as

a mean value over the realisations  $f_i$  and the error bars can be computed as its standard deviation. The central limit theorem states that for large  $N$ ,  $\langle f \rangle \rightarrow f$ , where  $f$  is the true value of the solution to the problem. For very large  $N$ , in fact,  $\sigma^2(\langle f \rangle) \rightarrow 0$ .

It is possible to simulate radiation transport in matter both by using a deterministic and a MC approach.

---

### 2.8.1 Deterministic Methods: Solving Transport Equations

---

Simulating radiation transport in matter with deterministic methods consists in solving Boltzmann-type transport equations that treat the atomic and nuclear collisions altering the particle type and energy. NASA developed such a deterministic code for radiation protection in space applications. This code is called HZETRN [118]. The GSI Helmholtzzentrum für Schwerionenforschung is also developing a deterministic code for space applications called SpaceTRiP [119].

The relevant transport equations are derived based on the conservation principle for the flux density  $\phi_j(\vec{r}, \vec{\Omega}, E)$  of particles of type  $j$ :

$$\vec{\Omega} \cdot \vec{\nabla} \phi_j(\vec{r}, \vec{\Omega}, E) = \sum_k \int \int \sigma_{jk}(\vec{\Omega}, \vec{\Omega}', E, E') \phi_k(\vec{r}, \vec{\Omega}', E') dE' d\vec{\Omega}' - \sigma_j(E) \phi_j(\vec{r}, \vec{\Omega}, E), \quad (2.30)$$

where  $\phi_j(\vec{r}, \vec{\Omega}, E)$  is the flux of particles  $j$  having direction  $\Omega$  and energy  $E$ , and  $\phi_k(\vec{r}, \vec{\Omega}', E')$  the flux of particles  $k$  having direction  $\Omega'$  and energy  $E'$ .  $\sigma_j(E)$  is the total reaction cross-section describing the probability of a particle  $j$  with an energy  $E$  to interact with the medium,  $\sigma_{jk}(\vec{\Omega}, \vec{\Omega}', E, E')$  is the cross-section describing the probability for the process of a particle of type  $k$  moving in direction  $\vec{\Omega}'$  with an energy  $E'$  to produce a particle  $j$  with direction  $\vec{\Omega}$  and energy  $E$ . The cross-section to be used in Equation 2.30 are inclusive cross-sections.

---

### 2.8.2 Monte Carlo Methods: Single Particle Histories

---

On the other hand, also a MC approach can be used to simulate radiation transport in matter [120]. MC methods started to be used already towards the end of the 18<sup>th</sup> century with Buffon's needle problem. Nevertheless, a big step forward in the development of stochastic methods came with the Manhattan project (1939-1946) [121], where they were applied to the development of nuclear weapons. In particular, they were used to simulate neutron transport in matter.

Since the emission of radiation from atoms and its interaction with them is a natural stochastic process, it is possible to see a stochastic approach to the problem in two ways. It can be seen either as a rather straightforward stochastic simulation or as a process whose average behaviour can be described by mathematical equations whose solution can be obtained through MC methods.

Most radiation protection in space applications rely on the usage of MC codes such as FLUKA, Geant4, and PHITS. These MC codes were also used to simulate the experimental results presented in this work. Therefore, the focus from now on is put on MC methods. Radiation transport in matter in MC codes is simulated with single-particle histories.  $N$  particles are generated, one by one. Each particle has its history. The particle trajectories are divided into steps, which are defined as straight free-flight tracks between consecutive physics interactions. Pseudorandom numbers are translated into physical decisions that "Nature" would make when particles are moving around. The history of every particle is simulated until they exist in the system or has zero kinetic energy left. The decisions to be made (through the usage of pseudorandom numbers) are about the energy, type and direction of motion of the primary particle (for each of the  $N$  primary particles generated), the step length (for each step of each particle), the type of

collisions taking place, and the energy, type and direction of motion of the secondary particles possibly produced during the interaction.

A step is defined as a straight trajectory between two subsequent collisions. Therefore, deciding the step length equals deciding where the next collision takes place. The step length  $s$  is sampled from the following probability function:

$$p(s) = \mu e^{-\mu s}, \quad (2.31)$$

for homogenous media, and from:

$$p(s) = \mu(z) e^{-\int_0^s \mu(z') dz'}, \quad (2.32)$$

for inhomogeneous media.  $\mu$  is a property of the medium. It is proportional to the material density and it is proportional to the total reaction cross-section  $\sigma$ :

$$\mu = n\sigma = n \sum_i \sigma_i, \quad (2.33)$$

where  $n$  is the atomic density of the medium (see Equation 2.16), and  $\sigma_i$  are the cross-sections of each  $i$  competing process. Each process takes place with a probability  $\frac{\sigma_i}{\sigma}$ . For inhomogeneous media,  $\mu$  is a function of the material depth  $z$ ,  $\mu = \mu(z)$ . Nevertheless, also for homogenous media,  $\sigma$  is a function of the particle energy, that becomes lower at each interaction. Therefore,  $\sigma = \sigma(E) = \sigma(z)$  for every medium. Consequently,  $p(s)$  is a function of  $z$  as well, and needs to be recalculated at each step.

Once the step length is sampled, the process taking place is sampled according to  $\frac{\sigma_i}{\sigma}$ . If any secondary particles are produced during such interaction, the final state of the process, which is the energy and direction of motion of the secondary particle, is sampled from the double-differential cross-section of the secondary particle production  $\frac{d^2\sigma_p}{d\Omega dE}$ . After this, the direction of the primary particle is updated and the code goes on following the history of the primary particle, while the information about the produced secondary particles is stored somewhere, and they will be followed after the end of the history of the primary particle. Each of the secondary particles will have its history, and this is valid for any tertiary (or higher-order) particle produced.

Every single particle's history is a realisation. Therefore, the expectation values of the sampled quantities are computed as average over the single-particle histories with associated standard deviation.

### 2.8.3 The Need for Reliable Cross-Section Models

As seen in the previous sections, cross-sections are a key ingredient in both deterministic and MC simulations. On the one hand, for what concerns deterministic methods, total and double differential cross-sections are required in the Boltzmann-type equations (see Equation 2.30). On the other hand, in MC codes, reaction cross-sections are used to decide the step length and which of the competing processes occurs, and production cross-sections to determine the final state of a process, in particular, what secondary particles are produced. Double-differential production cross-sections contain additional information about the secondary particle energy and direction of motion. The codes make use of cross-section models (or parametrisations), and only in particular cases, e.g. slow neutron cross-sections, of experimental data tables. Parametrisations describing cross-sections are semi-empirical, meaning that both theory and experiments are involved in their development. It is therefore important to:

- understand what experimental cross-section data that are necessary to the parametrisation development are missing and
- understand which parametrisations work better for what systems and energies

This inter-dependence of MC codes, cross-section parametrisations, theory, and experimental data, is reported in Figure 2.19.

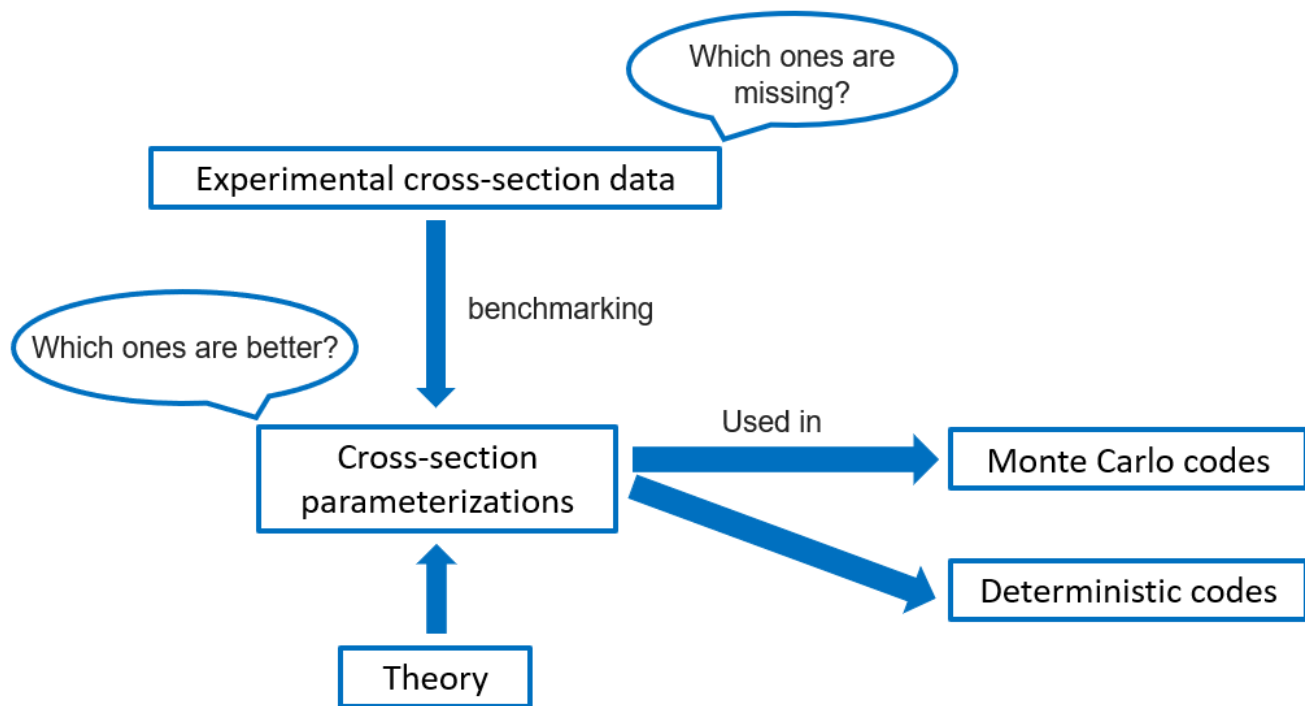


Figure 2.19: Representation of the inter-dependence of MC codes, cross-section models, theory, and experimental data.

## 2.9 Accelerator-Based Experiments

The simulation work performed for radiation protection in space has to be coupled with ground-based experimental activity. Particle accelerators, and in particular synchrotrons, are the only machines capable of delivering the high energies needed to understand the interaction of cosmic rays with matter. Accelerator-based experimental campaigns are needed for two main endpoints:

1. doing ground-based biological studies on the effects of heavy ions on biological targets such as cells and animals (biology experiments), and
2. performing meaningful experiments to determine absorbed dose attenuation properties of potential shielding materials, production of secondary radiation fields, and cross-sections (physics experiments) and comparing the results with MC simulations.

Biology experiments are key to reducing some of the uncertainties listed in Section 2.6.3. Physics experiments are key to improving MC codes and reducing uncertainties related to the secondary radiation field generated through the interaction of primary cosmic rays with structural and shielding materials. In this work, the focus is on the second endpoint. By comparing the results of MC simulations with experimental data, it is possible to study the accuracy of the physics models underlying the codes, among which are also cross-section parametrizations. The improvement of such models leads also to improvements in the risk calculations on which radiation protection of astronauts fully relies.

The more quantities are measured during an experiment, the more meaningful the comparison with MC simulations is. For instance, if the type, energy, and direction of motion of all the particles composing the secondary radiation field are measured, all these quantities can be compared with the outcome of

---

MC simulations. Nevertheless, it is not always feasible to perform such precise and complete experiments, as it requires a very large number of detectors, and most importantly, a very large number of beam time hours invested. Therefore, other experiments can be performed, which take very short and still provide meaningful data for the comparison with MC simulation outcomes. An example is absorbed dose measurements before and after a target of interest for space, which is what was performed for this work.

---

### 2.9.1 Facilities

Ion accelerators are the only machines on Earth able to reproduce the high-energy radiation fields of deep space. Thus, space radiation experiments are performed at these facilities. Among the most important in the field, there is the Joint Institute for Nuclear Research JINR in Dubna, the Helmholtzzentrum für Schwerionenforschung (GSI), the NASA Space Radiation Laboratory at Brookhaven National Laboratory, the Heavy Ion Medical Accelerator at the National Institute of Radiological Sciences in Chiba, Japan, and other accelerator facilities in Europe and Asia [45]. Focusing on the European facility, the SIS-18 synchrotron of GSI provides ion beams in the range of 80 to 2000 MeV  $u^{-1}$  for species from protons to uranium, which makes GSI the best European experimental facility to perform experimental research about radiation protection in space. Nevertheless, also medical facilities can be used for space application purposes, limiting the experiments to low-Z beams and energies not higher than a few hundreds of MeV  $u^{-1}$  (depending on the facility) [122].

---

### 2.9.2 Ion Beams of Interest for Space

In particular, the most important beams and energies to be used for radiation protection in space experimental campaigns can be deduced from Figures 2.7, 2.16 and 2.17. As explained in Section 2.7.2, high-Z ions contribute more to the dose equivalent behind thin shields, while low-Z ions behind thick shields. Both these exposure scenarios need to be taken into account because space explorers are supposed to experience both during the duration of a space mission. For instance, thick shields are supposed to be used on the spacecraft, especially in the sleeping quarters. On the other hand, during EVAs and *in situ* explorations, the space explorers will be only shielded with thin layers of material. Among low-Z ion beams, the most relevant are protons and helium ions, as their contribution together corresponds to 70% of the GCR BFO dose equivalent behind a 30 g  $cm^{-2}$  aluminium shield. In addition, protons are also the main constituent of SPEs. In the past, not many experimental campaigns have been performed by using proton and helium beams at energies of interest for space [11, 12, 123]. Concerning high-Z beams, it has been demonstrated [37] that the dose reduction of the complete heavy-ion component of GCRs behind thin shields is very similar to the dose reduction of 1 GeV  $u^{-1}$   $^{56}Fe$  behind the same shielding. The difference between the two is due to the hard component (kinetic energies greater than 1 GeV  $u^{-1}$ ) of the energy spectra of GCR heavy ions. Also, the GCR iron energy spectrum peaks around 1 GeV  $u^{-1}$  in solar maximum conditions, which have been demonstrated to be better for exploration scenarios [98]. Therefore, several accelerator-based experimental campaigns making use of 1 GeV  $u^{-1}$   $^{56}Fe$  beams, have been conducted in the past years [7, 8, 11–14, 124, 125].

The dose measurements performed within the current work include both high-Z (iron) and low-Z (protons and helium) ion beams. In particular, this work is a part of the ROSSINI3 and DEIMOS projects.

---

### 2.9.3 The ROSSINI3 Project

Among the many ground-based experimental campaigns conducted in the past decades, there are the ROSSINI projects, which aim at testing stable and manageable high-performance shielding materials. The

---

most recent of them was ROSSINI3 [15]. The project was funded by ESA and is a collaboration of Thales Alenia Space Italia, GSI Helmholtzzentrum für Schwerionenforschung, and the University of Torino. Two of the main branches of ROSSINI3 are the focus of this work. The first is the measurement of dose attenuation curves for  $1 \text{ GeV u}^{-1}$   $^{56}\text{Fe}$  and  $2 \text{ GeV}$  proton beams in structural and potential innovative and *in situ* shielding materials. Such curves have been then compared with the simulation results obtained with three of the main MC transport codes used for radiation protection in space. The second is an evaluation of the state-of-the-art experimentally measured reaction and fragment production cross-section data, alongside the semi-empirical parametrisations used to describe the dependence of such cross-sections on the projectile energy.

---

#### 2.9.4 The DEIMOS Project

---

Ideas for ground-based experiments for investigating the physics and biology of radiation protection in space are collected by ESA through its Continuously-Open Research Announcement Investigating biological effects of space radiation (ESA-CORA-IBER) [122]. The DEIMOS project is an experimental campaign funded by the ESA-CORA-IBER project. It aims at a deeper understanding of the nuclear interaction of high-energy light ions ( $^1\text{H}$  and  $^4\text{He}$ ) with materials of interest for radiation protection in space. The proton and helium GCR energy spectrum peaks around  $500 \text{ MeV u}^{-1}$ . Therefore, accelerator facilities other than GSI could be exploited for these dose measurements. In particular, the DEIMOS experimental campaigns are conducted at the Heidelberger Ionenstrahl-Therapiezentrum (HIT). The exact energies used for the experiments were  $480 \text{ MeV}$  for protons and  $430 \text{ MeV u}^{-1}$  for  $^4\text{He}$  ions since this is the maximum energy reachable at HIT.

---

## 3 Absorbed Dose Measurements

---

As seen in Section 2.2, the dangers due to space radiation are among the biggest hindrances to manned long-term deep-space exploration missions [3, 4, 95, 126], and currently, the most promising radiation protection strategy is passive shielding [4, 110, 111], despite its limitations [10, 108, 115]. Such a strategy needs to be tested at accelerator facilities before being used in space. Absorbed dose measurements for different materials can be performed relatively fast and effectively and allow a direct comparison of the dose values behind structural and potential shielding materials.

Ideally, measurements that also take into account possible synergistic effects of the complex space radiation field need a GCR simulator [45, 127]. However, this is important for biological experiments [128–131], while with materials, one could conceivably construct a GCR simulator by collecting single-beam data on the same target. In addition, “simple” accelerator-based experiments such as the one reported in this work, are necessary because their comparison to the outcome of MC simulations allows an understanding of the validity of the basic physics models underlying the MC codes (see Chapter 4).

Heavy ions such as iron are the main contributors to the dose equivalent due to GRCs behind thin shields [4] (see Figure 2.16), while light ions behind thick shields [105] (see Figure 2.17). Therefore, both iron and helium ions and protons were used for the absorbed dose measurements presented in this work. Innovative and *in situ* shielding materials for long-term deep-space missions were used in the experimental campaigns, alongside conventional structural and shielding materials for comparison.

The results presented in this Chapter and the following are part of the ROSSINI3 and DEIMOS projects. The experimental and MC results obtained with iron beams were published in F Luoni *et al.*, “Dose attenuation in innovative shielding materials for radiation protection in space: Measurements and simulations,” *accepted by Radiat. Res.*, 2022.

---

### 3.1 Materials and Methods

---

---

#### 3.1.1 Beams

---

The four different ion beams listed in Table 3.1 have been used to obtain the results presented in this section. The motivation behind the ion type choices is that both high ( $^{56}\text{Fe}$ ) and low-Z ions ( $^1\text{H}$  and  $^4\text{He}$ ) are important contributors to the GCR dose equivalent. The first behind thin and the second behind thick shields. The motivations behind the energy choices are the following:

- 1 GeV  $\text{u}^{-1}$   $^{56}\text{Fe}$ : this energy was selected as the GCR iron energy spectrum peaks around it in solar maximum conditions, which have been demonstrated to be better for exploration scenarios [98]. In addition, for the reasons explained in Section 2.9.2, this beam is a good proxy of GCRs behind thin shields.
- 2 GeV  $^1\text{H}$ : this energy is extremely high and still in a high-fluence region of the GCR hydrogen energy spectrum. The capability of GSI to accelerate ion beams to such high energies was exploited to study the interaction of such high-energy protons with matter.



Table 3.1: Beams used for the experimental campaigns of this work, listed in chronological order. Alongside the ion type, are reported details about the beam kinetic energy in  $\text{MeV u}^{-1}$ , the beam full-width-half-maximum (FWHM) in mm, the beam intensity in ions per spill, the facility where the experiments were performed, and the project of which the experiments were part.

Ion type	Energy	FWHM (mm)	Intensity (ions per spill)	Facility	Project
$^{56}\text{Fe}$	$1 \text{ GeV u}^{-1}$	$\approx 5 \text{ to } 10$	$1 \text{ to } 3 \times 10^7$	GSI (Cave A)	ROSSINI3
$^1\text{H}$	$2 \text{ GeV}$	$\approx 20$	$5 \times 10^8$	GSI (Cave M)	ROSSINI3
$^1\text{H}$	$480 \text{ MeV}$	$\approx 5$	$2 \times 10^8$	HIT	DEIMOS
$^4\text{He}$	$430 \text{ MeV u}^{-1}$	$\approx 5$	$4 \times 10^7$	HIT	DEIMOS

- $480 \text{ MeV } ^1\text{H}$ : the proton GCR energy spectrum peaks around  $500 \text{ MeV u}^{-1}$ . These measurements were part of the DEIMOS project that took place at HIT, where  $480 \text{ MeV}$  is the maximum energy to which  $^1\text{H}$  ions can be accelerated.
- $430 \text{ MeV u}^{-1} ^4\text{He}$ : also the helium GCR energy spectrum peaks around  $500 \text{ MeV u}^{-1}$ . Also in this case,  $430 \text{ MeV u}^{-1}$  is the maximum energy to which  $^4\text{He}$  ions can be accelerated at HIT.

Additionally,  $^1\text{H}$  and  $^4\text{He}$  ions are good to look at the build up caused by target fragments as explained in Section 2.5.4.

### 3.1.2 Target Materials

Traditional, innovative, and *in situ* shielding materials were used in this work, alongside structural spacecraft materials. In particular, the following target materials were irradiated during the experimental campaigns:

- HDPE: it was selected as reference material to compare the results with, as it has been considered the golden standard for a couple of decades [4, 6].
- LiH and  $\text{LiBH}_4$ : for the reasons discussed in Section 2.7.3, light materials are considered the best option for passive shielding purposes during deep-space missions [4–7, 9]. These lithium-base hydrides are lighter than HDPE, and therefore, they are expected to perform better than it.

In particular, LiH showed promising results in dose attenuation of  $^{56}\text{Fe}$  beams within the ROSSINI2 experimental campaigns [11, 12], which suggested that the follow-up ROSSINI3 campaign should focus more on lithium-based hydride materials.

Additionally,  $\text{LiBH}_4$  was selected as another promising lithium-based hydride because of its potential benefit for low-energy neutron capture by boron. Such property was, nevertheless, not deepened within these experimental campaigns. These lithium-based materials have also been the focus of attention of promising simulation campaigns [116]. The LiH used in this work was produced by the Alfa Aesar company with a purity of 97+% (CAS number: 7580-67-8) and the  $\text{LiBH}_4$  by Acros Organics with a purity of 95% (CAS: 16949-15-8).

- $\text{LiH}_p$  and  $\text{LiBH}_{4p}$  ( $\text{LiH}$  and  $\text{LiBH}_4$  embedded in a paraffin matrix):  $\text{LiH}$  and  $\text{LiBH}_4$  are chemically reacting with the moisture in the air and are, therefore, not suitable to be used in a pure form for shielding in space. Within this work, a certain amount of paraffin was mixed with the hydrides to make them more stable, and the resulting composite materials were also tested during the irradiations



Table 3.2: Aluminium 2024 average mass percentage composition.

Element	Mass contribution (%)	Element	Mass contribution (%)
Al	92.4	Mg	1.5
Si	0.5	Cr	0.1
Fe	0.5	Zn	0.25
Cu	4	Ti	0.15
Mn	0.6	Ni	0
V	0	Ag	0
Li	0		

and compared to pure LiH and LiBH<sub>4</sub>. The production and characterisation of the composite materials were carried out by the chemistry department of the University of Turin. Paraffin wax was selected to be mixed with hydrides, due to its high hydrogen content and relatively easy manufacturing processes.

LiH<sub>p</sub> and LiBH<sub>4p</sub> were produced using the highest possible hydride content that still guarantees sufficient mechanical and chemical stability of the samples. In particular, 50% hydride content in weight was used for LiH<sub>p</sub>, and 40% for LiBH<sub>4p</sub>.

The paraffin used in this work was produced by Sigma-Aldrich (Paraplast<sup>®</sup>, CAS: 145686-99-3). Also, both pure and composite lithium-based hydrides were embedded into vacuum seal plastic bags (areal density of 0.009 g cm<sup>-2</sup>) to keep them out of contact with air.

- Paraffin: pure paraffin was tested for comparison. These samples were prepared with a melting-cooling procedure performed in air, which was repeated until flat and parallel surfaces were obtained.
- Aluminium 2024, 2219 and 2195: three aluminium alloys generally used for structural components of space vehicles. They belong to the AA 2000 series (alloyed with copper), which is the most extensively used alloy family in aerospace structures due to its good mechanical properties.

Al2024 is commonly used in space applications, both on satellites and the International Space Station (ISS) Micrometeoroids and Debris Protection Systems. Al2219 is characterised by high fracture toughness, it is easily weldable and therefore widely used in space structures, e.g. the primary structure of the ISS pressurised modules.

Al2195 is one of the most complex grades in the aluminium-copper alloy family; it can be easily welded. This alloy is interesting because it is less dense than Al2219 thanks to its Li content and, at the same time, about 30% stronger. Al2195 has been already used in space, especially for rocket tanks, e.g. for the Space Shuttle external tank and Falcon9.

The average composition of the three aluminium alloys is given in Tables 3.2, 3.3, 3.4 in weight percentages.

- Li-poly batteries (stacked flat cellphone built-in Lithium polymer batteries without housing): they could potentially have a dual-use of energy sources and shields if placed around the habitable areas.
- Moon regolith: simulant of polar highland Moon regolith itself was tested as potential *in situ* shielding material. Polar highland regolith was chosen as the plans are for a future Moon base to be built near the Lunar south pole [133]. In particular, the Off Planet Research OPRH2N Near-Side Highland Lunar regolith simulant was used. Its composition is reported in Table 3.5, and it consists of sand

Table 3.3: Aluminium 2219 average mass percentage composition.

Element	Mass contribution (%)	Element	Mass contribution (%)
Al	92.295	Mg	0.02
Si	0.15	Cr	0
Fe	0.15	Zn	0.5
Cu	6.3	Ti	0.06
Mn	0.25	Zr	0.175
V	0.1	Ag	0
Li	0		

Table 3.4: Aluminium 2195 average mass percentage composition.

Element	Mass contribution (%)	Element	Mass contribution (%)
Al	93.4	Mg	0.525
Si	0.1	Cr	0
Fe	0.12	Zn	0.23
Cu	4	Ti	0.08
Mn	0	Zr	0.12
V	0	Ag	0.425
Li	1		

with grain diameter between 250 and 500  $\mu\text{m}$ . This customised diameter was chosen as the minimum to guarantee atomic and density uniformity during the irradiations without requiring special safety measures while handling the material (e.g. risk of inhalation of grains which are too small).

During the campaigns that made use of the 1 GeV  $\text{u}^{-1}$   $^{56}\text{Fe}$ -ion beam, it was irradiated into a PMMA container (later area of  $5 \times 7 \text{ cm}^2$  and length of 4 cm, walls 0.5 mm thick). A 1 mm-thick plexiglas wall was used to confine the Moon sand. Its relative position was changed at each irradiation so that thicker Moon layers could be placed.

During the light-ion campaigns (480 MeV  $^1\text{H}$  and 430 MeV  $\text{u}^{-1}$   $^4\text{He}$ -ion beams) it was irradiated in PMMA boxes with a lateral area of  $25 \times 25 \text{ cm}^2$  and a depth of 11 cm. One box was thinner (6 cm) to allow a finer resolution of significant depth ranges. Since the box walls perpendicular to the beam axis

Table 3.5: Highland Moon regolith simulant mass percentage composition. LOI stays for Low-Order Impurities.

Element	Mass contribution (%)	Element	Mass contribution (%)
$\text{SiO}_2$	47.89	$\text{Al}_2\text{O}_3$	27.06
$\text{TiO}_2$	0.52	$\text{FeO}$	3.68
$\text{MnO}$	0.06	$\text{MgO}$	2.84
$\text{CaO}$	14.19	$\text{Na}_2\text{O}$	2.43
$\text{K}_2\text{O}$	0.25	$\text{P}_2\text{O}_5$	0.2
LOI	0.88		

are 0.5 cm thick, the Moon regolith simulant thickness contained in the 11 cm-thick boxes is 10 cm, and in the 6 cm-thick box is 5 cm. Therefore, the 5 or 10 cm-thick Moon samples are interspersed with 1 cm of PMMA. Since the other walls of these boxes are 1 cm thick, the effective lateral area of the Moon regolith simulant was 23 (x axis) x ca. 23 (z axis) cm<sup>2</sup>.

- Si and SiO<sub>2</sub> (purity of 99 and 99.99%, respectively.): they were tested as main components of Moon regolith (see Table 3.5).
- PMMA: it was used as reference material for irradiations with 2 GeV <sup>1</sup>H because of its availability and because of its relatively similar atomic composition to PE.

For the targets where the full Bragg curve was measured, an increased curve resolution around the Bragg Peak area was obtained through fine steps (in depth) with a so-called range shifter (RS) [134] (see Section 3.1.3).

A complete list of the irradiated materials for each ion beam can be found in Tables 3.6, 3.7, and 3.8. Error bars for the areal densities of single irradiated targets were estimated through error propagation of the measured weight, thickness and area of the targets. They were then summed up to obtain the error associated with the areal density of the total irradiated thickness. It can be noticed that the amounts of lithium-based hydrides (both pure and composite) used for the irradiations are limited by the available amounts of material coming from the University of Turin. In addition, a maximum thickness of 3.096 g cm<sup>-2</sup> (corresponding to ca. 5 cm) was used for the case of the 2 GeV <sup>1</sup>H beam irradiations. The reason is that it had been estimated through preparatory MC simulations that, already for a 10 cm-thick target, the dose loss out of a 5 x 5 cm<sup>2</sup> area (slightly smaller than the LiH samples) would be 24%.

A material that was not used in this experimental campaign is water. Water has a potential shielding role for future missions as it is needed on the spacecraft for life support and could be kept in the walls with an additional shielding function. Nevertheless, the higher average mass number of water makes it perform less well than PE downstream of heavy-ion beams, as it was recently pointed out for 1 GeV u<sup>-1</sup> <sup>56</sup>Fe through MC simulations [135] and for 430 MeV u<sup>-1</sup> <sup>12</sup>C through experimental campaigns [11].

### 3.1.3 Experimental Setup

As reported in Table 3.1, the high-energy irradiations (1 GeV u<sup>-1</sup> <sup>56</sup>Fe and 2 GeV <sup>1</sup>H) were performed in GSI Cave A [136] and Cave M [137]. The lower-energy irradiations (480 MeV <sup>1</sup>H and 430 MeV u<sup>-1</sup> <sup>4</sup>He) at HIT. The setups consisted mainly of variable target thicknesses placed in between two large area parallel-plate ionisation chambers (ICs): the closest to the beam exit window is called IC1 and the other IC2. The active detector thickness is 2 x 10 mm in the IC2 and 2 x 5 mm in the IC1, with an active area of 26 x 26 cm<sup>2</sup>. It was filled with a gas mixture of 80% argon and 20% CO<sub>2</sub>. In Figure 3.1 a schematic description of the ICs is shown. The electrodes are represented with black lines. They are 6.7 mg cm<sup>-2</sup> thick and made of a nickel-coated polyester mesh (43% and 57% mass percentages, respectively). The outer foils are 25 µm thick and made of BoPET (Mylar).

The IC1 and IC2 were kept in the same position and the different targets were exchanged between subsequent irradiations. The IC1 operated as a reference monitor for normalisation. Therefore, the results are not affected by unavoidable fluctuations in the beam intensity. The charge readout of the ionisation chambers was realised with high-precision electrometers (model K6517, KEITHLEY), which guaranteed accuracy in the charge measurement to be below 1‰. The large area of the parallel-plate ionisation chambers laterally integrates almost the complete signal from the beam. Therefore, the sensitivity of the results to beam width and scattering effects is minimised. The distance between the IC2 and the targets is always minimised to avoid loss of signal. The same setup has been largely used in the past [11, 12, 85].

Table 3.6: List of the materials used for the 1 GeV  $u^{-1}$   $^{56}\text{Fe}$  beam irradiations, alongside their mass densities ( $\rho$ ), areas perpendicular to the beam line (A) and irradiated thicknesses (t) with associated uncertainties. The thicknesses are given in areal densities. The numbers in parentheses refer to the uncertainties of the values and apply to the least significant digits.

Material	$\rho$ (g cm $^{-3}$ )	A (cm $^2$ )	t (g cm $^{-2}$ ) <sup>a</sup>
LiH	0.5279(48)	33.20(51)	0.615(13), 1.231(16), 1.863(19), 2.481(26), 3.096(29), 3.710(31), 4.315(34), 4.937(37), 5.543(39), 6.149(41), 6.756(42), 7.359(44), 7.959(46), 8.559(47)
LiBH $_4$	0.5255(59)	33.20(51)	0.633(11), 1.264(18), 1.897(22), 2.525(27), 3.149(32), 3.758(34), 4.383(37), 5.003(39), 5.637(42), 6.261(45)
LiH $_p$	0.7844(50)	77.73(31)	0.733(13), 1.477(16), 2.227(21), 2.969(23), 3.718(25), 4.456(28), 5.216(30), 5.965(32), 6.731(34), 7.486(35), 8.232(37), 9.018(39), 9.721(40), 10.504(42), 11.267(45)
LiBH $_{4,p}$	0.7523(38)	28.23(19)	0.692(12), 1.277(17), 1.943(19), 2.627(24), 3.326(26), 4.003(28), 4.673(30), 5.353(31), 6.011(32)
Paraffin	0.9025(56)	93.48(55)	1.845(18), ... 34.06(17) <sup>b</sup>
HDPE	0.9270(93)	<sup>c</sup>	3.587(37), 4.811(49), 6.016(61), 6.962(70)
Al2024	2.690(55)	402(1)	2.261(18), 3.392(27)
Al2219	2.835(10)	72.00300(11)	2.026(10), 6.079(29), 8.105(38)
Al2195	2.705(28)	129.59(37)	3.646(31), 6.382(50)
Si	2.404(37)	79(2)	0.962(16), 1.923(30), 2.885(45), 3.846(59), 4.808(74), 5.769(88), 6.73(10)
SiO $_2$	2.213(32)	79(2)	0.885(13), 1.770(25), 2.656(38), 3.541(51), 4.426(63), 5.311(76), 6.196(89)
Moon regolith	1.35(8)	35.00(86)	0.243(28), 0.65(14), 1.32(15), 1.99(18), 2.66(22), 4.01(31), 5.62(41)
Li-poly batteries	2.27(57)	<sup>d</sup>	0.6883(29), 1.3899(64), 2.091(10), 2.789(14), 4.221(21), 6.545(31), 8.896(41), 11.933(53)

<sup>a</sup> The thicknesses of the pure and composite lithium-based hydrides include the thin plastic bags they were embedded in during the irradiations, as well as the thicknesses of the Moon regolith simulant include the plexiglas foil and PMMA walls of the box it was irradiated in.

<sup>b</sup> The whole Bragg curve was measured for paraffin in steps of 1.8 g cm $^{-2}$ . At the Bragg peak, the steps are smaller and realised with the HDPE foils of the range shifter.

<sup>c</sup> The HDPE target consists of two wedges shifted relatively to each other. Thus, the area of the target changes according to the overlap of the wedges. The wedges have an area of 246 cm $^2$  (minimum area) and an angle of 16°.

<sup>d</sup> The area of the Li-ion batteries varies from 39 to 59 cm $^2$ , depending on the battery.

Table 3.7: List of the materials used for the 2 GeV  $^1\text{H}$  beam irradiations, alongside their mass densities ( $\rho$ ), areas perpendicular to the beam line (A) and irradiated thicknesses (t) with associated uncertainties. The thicknesses are given in areal densities. The numbers in parentheses refer to the uncertainties of the values and apply to the least significant digits.

Material	$\rho$ (g cm $^{-3}$ )	A (cm $^2$ )	t (g cm $^{-2}$ )
LiH	0.5279(48)	33.20(51)	0.615(13), 1.231(16), 1.863(19), 3.096(29)
PMMA	1.183(11)	400.300(60) to 900(9)	0.7056(70), 1.877(13), 3.101(18), 8.813(33), 19.428(86), 25.190(97), 37.004(97)

Table 3.8: List of the materials used for the 480 MeV  $^1\text{H}$  and 430 MeV  $\text{u}^{-1}$   $^4\text{He}$  beam irradiations, alongside their mass densities ( $\rho$ ), areas perpendicular to the beam line (A) and irradiated thicknesses (t) with associated uncertainties. The thicknesses are given in areal densities. The numbers in parentheses refer to the uncertainties of the values and apply to the least significant digits.

Material	$\rho$ (g cm $^{-3}$ )	A (cm $^2$ )	t (g cm $^{-2}$ ) <sup>a</sup>
LiH	0.5279(48)	33.20(51)	0.615(13), 1.231(16), 1.863(19), 2.481(26), 3.096(29), 4.937(37), 6.756(42), 8.559(47)
HDPE	0.9340(96)	900(2)	<sup>a</sup>
Moon regolith	1.345(15) <sup>b</sup>	625(20) <sup>c</sup>	<sup>d</sup>

<sup>a</sup> The whole Bragg curve was measured in steps of either 4.7 or 9.4 g cm $^{-2}$ . Around the Bragg peak, the steps are smaller and realised with the HDPE foils of the range shifter.

<sup>b</sup> The uncertainty of the Moon regolith density reported in Table 3.6 is 0.08 g cm $^{-3}$ . This number was estimated by taking into account the difference between the compressed and uncompressed powder. Nevertheless, during the 480 MeV  $^1\text{H}$  and 430 MeV  $\text{u}^{-1}$   $^4\text{He}$  beam irradiations, the Moon regolith simulant was always irradiated as compressed. Therefore, the actual uncertainty of the density during the irradiations is estimated to be 0.015 g cm $^{-3}$ .

<sup>c</sup> The Moon regolith simulant was irradiated in PMMA boxes with a lateral area of 25 x 25 cm $^2$ . Nevertheless, the boxes were not filled until the end, therefore the large uncertainty.

<sup>d</sup> The whole Bragg curve was measured in steps of either 8.3(2) or 15.4(3) g cm $^{-2}$ . Around the Bragg peak, the steps are smaller and realised with the HDPE foils of the range shifter.

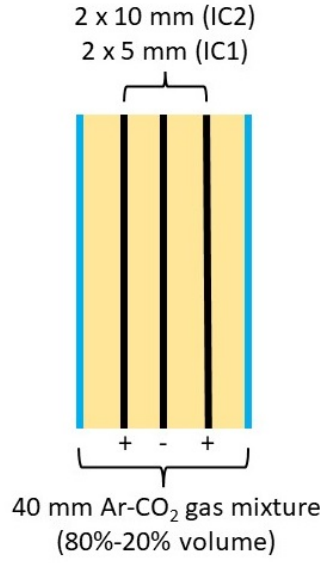


Figure 3.1: Details about the ionisation chambers used for the experimental campaigns.

For the case of the 2 GeV  $^1\text{H}$  beam, a third IC (IC3) was used as well. The IC3 is identical to the IC2. In particular, the IC3 was placed right before the target material, to measure the backscattered radiation. Since the IC3 was kept at a 0 cm distance from the target material, it was always repositioned between two subsequent irradiations. A similar setup has been used for high-energy protons also in the past [123].

Schematics of the experimental setups are reported in Figure 3.2.

The RS is composed of ten HDPE foils and plates with well-defined areal densities, each roughly doubling the previous one in thickness. Since it is remotely controlled, it allows quick changes of the amount of material in the beam line, varying from 62  $\mu\text{m}$  of HDPE up to 64 mm, in steps of ca. 60  $\mu\text{m}$ .

### 3.1.4 Data Analysis

The charge signals from the ICs were measured. The ratio of the charge signal from the two ionisation chambers ( $Q_2/Q_1$ ) was then computed and normalised to the same ratio obtained without any target ( $Q_{2,\text{no target}}/Q_{1,\text{no target}}$ ). This provides the change in the dose (reduction or enhance) due to the presence of the target:

$$\frac{D_2}{D_1} = \frac{Q_2/Q_1}{(Q_2/Q_1)_{\text{no target}}}. \quad (3.1)$$

Same was done for the backscattered dose measured with the IC3:

$$\frac{D_3}{D_1} = \frac{Q_3/Q_1}{(Q_3/Q_1)_{\text{no target}}}. \quad (3.2)$$

In this case, no target measurements were performed by leaving a few centimetres of air between the IC3 and the IC2.

### 3.1.5 Error Bars

Both error bars associated with the target areal density and the dose ratio were included in the analysis.

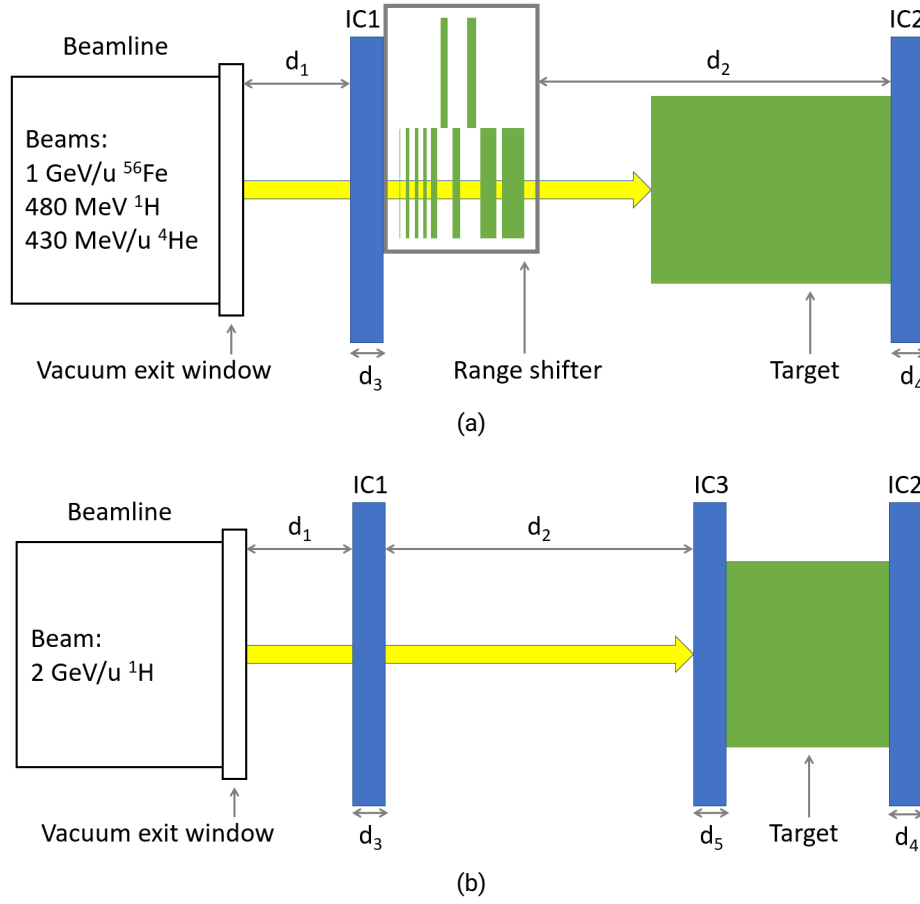


Figure 3.2: Panel (a): experimental setup used for 1 GeV  $\text{u}^{-1}$   $^{56}\text{Fe}$ , 480 MeV  $^1\text{H}$  and 430 MeV  $\text{u}^{-1}$   $^4\text{He}$  beam irradiations:  $d_3 = d_4 = 4$  cm,  $d_1$  and  $d_2$  are beam time dependent,  $d_1$  being about 15 cm for iron ions and 26.5 cm for protons and helium ions, and  $d_2$  about 1 m for iron ions and 135 cm for protons and helium ions. The distance between the target and the IC2 is also beam time dependent and varies between 0 and 2 cm. Panel (b): experimental setup used for 2 GeV  $^1\text{H}$  beam irradiations:  $d_3 = d_4 = d_5 = 4$  cm,  $d_1 = 13.5$  cm, and  $d_2 = 95.5$  cm. The distance between the target and the IC2 was 0 in this case.

### Areal Density Error Estimation

Uncertainties associated with the areal density of single targets (e.g. one HDPE slab) were computed through error propagation of the target thickness and volumetric density. The uncertainty associated with the volumetric density was in turn estimated through error propagation of the target mass and volume. For some samples, the volume was directly measured, e.g. Moon regolith simulant. For some others, it was computed from the target height, length, and width (e.g. HDPE slabs) or base radius and height (e.g. lithium-base hydrides). In these cases, the uncertainties associated with the single dimensions were propagated to compute the uncertainty associated with the volume. For each step, the following formula was used:

$$\Delta f = \sqrt{\sum_i \left( \frac{\partial f}{\partial x_i} \Delta x_i \right)^2}, \quad (3.3)$$

were  $f$  is either the target volume, volumetric density, or areal density,  $\Delta f$  is the error associated to  $f$ ,  $x_i$  are the variables  $f$  depends on, and  $\Delta x_i$  are the errors associated to the  $x_i$ . For each variable  $x_i$ , the  $\Delta x_i$  were estimated as the square addition of the uncertainties associated to the instrument used for the measurement ( $\Delta x_{i\text{instr}}$ ) and the statistical error obtained as the standard deviation of all the measurements taken of  $x_i$  ( $\Delta x_{i\text{stat}}$ ):

$$\Delta x_i = \sqrt{(\Delta x_{i\text{instr}})^2 + (\Delta x_{i\text{stat}})^2}. \quad (3.4)$$

The uncertainty associated with the total target areal density used for each irradiation (e.g. total HDPE areal density) was computed as the sum of the uncertainties of the areal densities of every single target placed in the beam line (e.g. each HDPE slab). The uncertainties, therefore, become bigger for larger target thicknesses.

---

### Absorbed Dose Error Estimation

---

For each material thickness, at least two measurement points were taken. The final data were computed as the arithmetic average of such values, and the associated statistical fluctuations as the standard deviation. The systematic component of the errors was evaluated as the statistical fluctuations (measured at different times of the experimental campaign) of the data obtained without target ( $(Q_2/Q_1)_{\text{no target}}$  or  $(Q_3/Q_1)_{\text{no target}}$ ). This systematic component accounts for the uncertainty related to the non-linearities of the readout electronics, e.g. slight offsets.

---

## 3.2 Results and Discussion

---

In this Section, the results obtained throughout the experimental campaigns are presented and discussed, starting from the data obtained with the iron beam and then going to the data obtained with the light-ion beams at low and high energy.

---

### 3.2.1 Iron Ions

---



---

#### Dose Attenuation Results

---

For the case of the 1 GeV  $\text{u}^{-1}$   $^{56}\text{Fe}$ -ion beam, the measured dose ratios decrease as a function of the target thickness. This is caused by the attenuation of the primary beam due to the fragmentation processes that the  $^{56}\text{Fe}$  ions undergo while traversing the target material. Since  $\text{LET} \propto Z^2$  (see Equation 2.8), the produced fragments have an LET lower than the  $^{56}\text{Fe}$  beam. In addition, the slowing down of the primary iron beam cannot compensate for the dose reduction due to the fragmentation. The analysis of the dose attenuation results has been performed as a function of the areal density of the targets ( $\text{g cm}^{-2}$ ), which is obtained by multiplying their mass density by their thickness. The more fragmentation per unit mass happens, the stronger the dose attenuation expected for the same areal density of different targets. Lighter materials such as lithium-based hydrides are expected to provide stronger dose attenuation because they have the lowest mass number  $A_T$  (see Section 2.7.3). Higher- $A_T$  materials such as aluminium or silicon are expected to be less effective for this purpose [115].

The dose ratios (see Equation 3.1) obtained for iron ions in all target materials used for the tests, are plotted in Figure 3.3. As expected, the dose reduction is stronger for lower- $A_T$  materials. LiH performs the best. The dose reduction obtained with  $\text{LiBH}_4$  and the chemically stable  $\text{LiH}_p$  are equal and are the best after LiH. This result is very interesting as it shows that a chemically stable material can be a better shield from high-Z GCRs than HDPE, which has been considered the gold standard for radiation protection



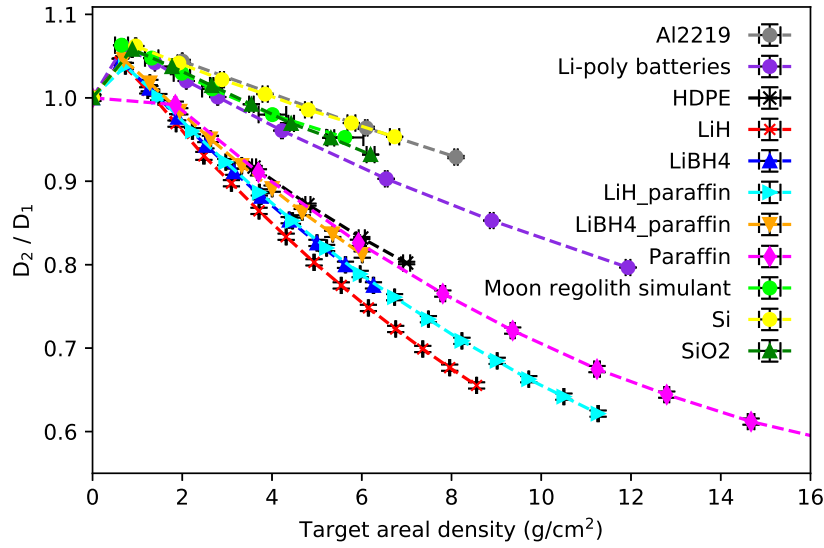


Figure 3.3:  $1 \text{ GeV u}^{-1} {}^{56}\text{Fe}$ -ion beam dose attenuation results for all tested materials up to  $16 \text{ g cm}^{-2}$ . The dashed lines simply connect the experimental points.

in space for the past couple of decades. Aluminium, the main structural material of spacecrafts, shows the worst shielding capabilities among the tested materials.  $\text{SiO}_2$  shows a dose reduction stronger than Si because of its lower mass number ( $A_{\text{O}} < A_{\text{Si}}$ ). The results obtained with the Moon regolith simulant and  $\text{SiO}_2$  are very similar as  $\text{SiO}_2$  is the main component of the Moon regolith simulant used (see Table 3.5). It should be noted that irradiating pure Moon regolith simulant was not possible because of its consistency (sand) and a thin-wall box made out of PE and PMMA was used as its container (see Section 3.1.2).

Concerning aluminium, only Al2219 alloy results are reported in Figure 3.3. Figure 3.4 reports a direct comparison between the three aluminium alloys used for these experimental campaigns. They show similar dose attenuation curves, but thanks to the high precision of the experimental setup, it was possible to resolve the small differences between them. These only small deviations prove that no big role is expected to be played by the type of aluminium alloy for what concerns radiation protection.

### Initial Dose Build Up

A small dose build up (see Section 2.5.4) can be seen for the very first  $\text{g cm}^{-2}$  of all target materials. The only exception is paraffin because the thinnest available target was too thick. After the build up equilibrium is reached (see Panel (b) of Figure 2.13), the dose attenuation due to projectile fragmentation takes over and the dose ratio starts to decrease.

Details of such build up were studied through MC simulations and are presented in Section 4.2.1.

### Paraffin Bragg Curve

The paraffin data reported in Figure 3.3 are only the initial points of the full Bragg curve that was measured and that is reported in Figure 3.5.

The apparent flat start of the curve hides an initial dose build up which was not possible to resolve due to the minimum available thickness of the paraffin targets.

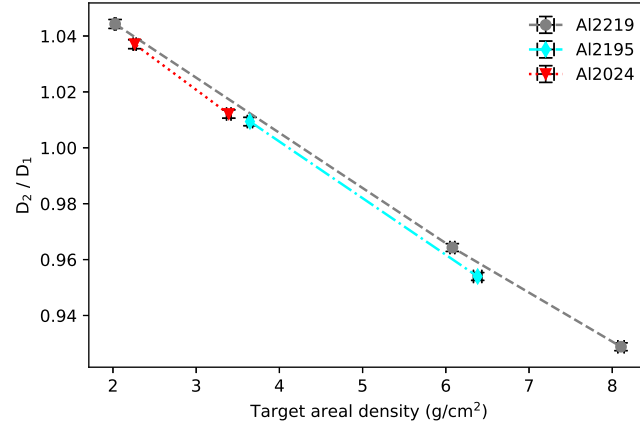


Figure 3.4: Dose attenuation results obtained with  $1 \text{ GeV u}^{-1} {}^{56}\text{Fe}$  ions for three different aluminium alloys generally used in space. The dashed lines simply connect the experimental points.

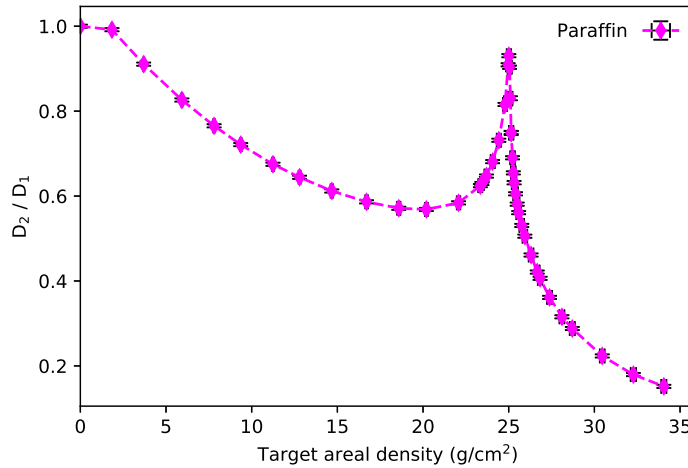


Figure 3.5: Full paraffin Bragg curve measured with  $1 \text{ GeV u}^{-1} {}^{56}\text{Fe}$  ions. The dashed lines simply connect the experimental points.

## Material Exchanges

Some irradiations were performed by exchanging the order of the targets only, without changing the material type or quantity. Pure LiH and LiBH<sub>4</sub> were used for this purpose, in combination with Al2219 and Al2195 alloys. The results of these exchange experiments are reported in Figure 3.6. They show that the dose attenuation is systematically higher (1% effect ca.) if the shielding material (LiH or LiBH<sub>4</sub>) is placed upstream of the structural material (aluminium). This does not change for different aluminium alloys, lithium-based hydrides, and different thicknesses. The reason for the difference might be that the combination of energy loss and fragmentation is slightly more beneficial for the configuration in which the shielding material is placed upstream of the aluminium. Nevertheless, since the difference is small, it is difficult to analyse and reproduce it through MC simulations. In a real case configuration, this would mean placing the shielding material outside the structural walls of the spacecraft.

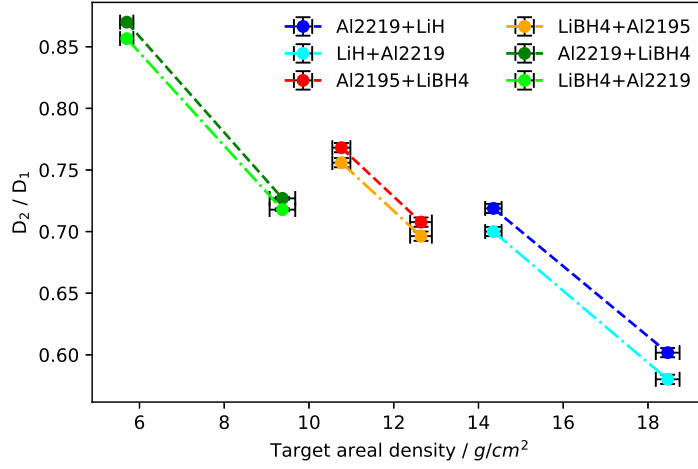


Figure 3.6: Dose attenuation results obtained merely by exchanging the relative order of aluminium (spacecraft structural material) and lithium-based hydrides (shielding material). The dashed lines simply connect the experimental points. All experimental results were obtained with a  $1 \text{ GeV u}^{-1} {}^{56}\text{Fe}$ -ion beam.

It was already known that the material order can have an impact on the shielding performance [108, 138]. Similar experiments were already performed by [138] with HDPE and aluminium but did not show such systematic results. The reason is probably that the smaller area of the EGG chamber used for those measurements could not guarantee the same experimental precision of the data presented in this work. It is very interesting to notice that the situation gets reversed for the case of dose equivalent. Placing the structural material (higher Z) outside of the shielding (lower Z) provides stronger dose equivalent attenuation [108]. In particular, this dose equivalent attenuation is much stronger than the few percentages observed in the present work. This highlights the need for studies involving the biological effectiveness of the shielding materials.

### 3.2.2 Light Ions

#### Lower-Energy Results

This section focuses on the results obtained with 480 MeV protons and 430 MeV  $\text{u}^{-1} {}^4\text{He}$  ions. For these beams, the materials used for dose measurements are HDPE, Moon regolith simulant, and LiH. While  ${}^4\text{He}$  ions undergo nuclear fragmentation processes in the materials, protons do not. They only slow down because of interactions with target electrons and nuclei and collide with target nuclei with consequent production of target fragments.

In Figures 3.7 and 3.8, the dose attenuation results are shown for 480 MeV proton and 430 MeV  $\text{u}^{-1} {}^4\text{He}$  beams. Figure 3.7 only reports HDPE and Moon regolith simulant results. Full Bragg curves were measured for these two materials. Due to the lack of material, only results for a maximum of  $11.2 \text{ g cm}^{-2}$  of LiH were measured. These data are reported in Figure 3.8, alongside HDPE and Moon simulant results.

In Figure 3.7, it can be seen that the results for the two different materials are almost identical in the

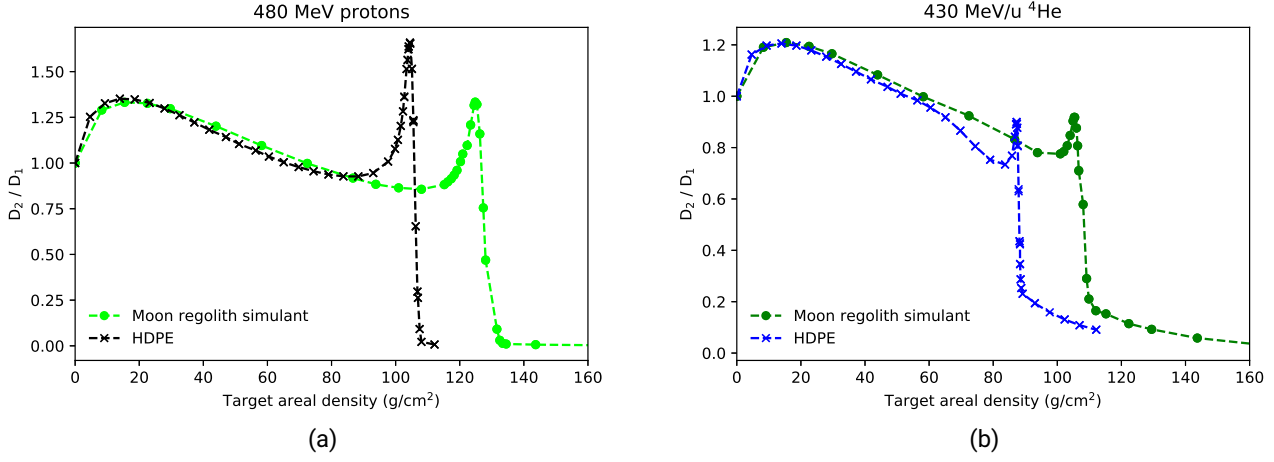


Figure 3.7: Bragg-curves experimental results obtained with 480 MeV protons (Panel (a)) and 430 MeV  $\text{u}^{-1}$   $^4\text{He}$  ions (Panel (b)) in HDPE and Moon regolith simulant. The dashed lines simply connect the experimental points.

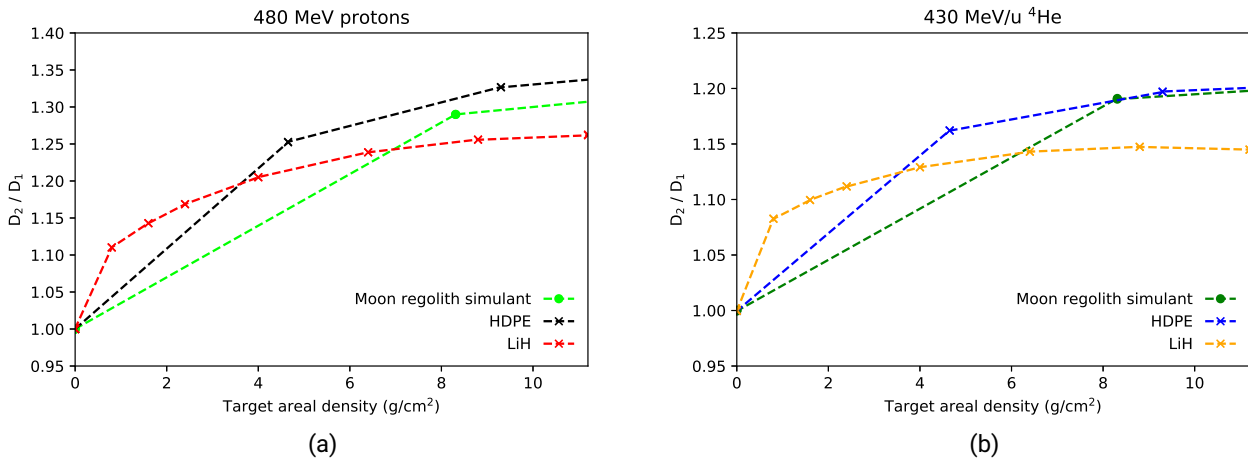


Figure 3.8: Experimental results obtained with 480 MeV protons (Panel (a)) and 430 MeV  $\text{u}^{-1}$   $^4\text{He}$  ions (Panel (b)) in HDPE, Moon regolith simulant, and LiH, up to the maximum irradiated LiH thickness ( $11.2 \text{ g cm}^{-2}$ ). HDPE and Moon regolith simulant data are the same as in Figure 3.7. The dashed lines simply connect the experimental points.

first part of the Bragg curves (until around  $70 \text{ g cm}^{-2}$ ) for both ion beams, and they differ in the Bragg peak region. This means that the production of secondary particles is quite similar in the two materials. It has to be considered though, that the Moon regolith simulant was irradiated inside PMMA boxes. Therefore, the results are not only pure Moon but Moon and PMMA mixed, Moon being the most abundant material. On the other hand, it can be seen in Figure 3.8, that the dose build up in LiH is weaker than in the other two materials for both beams.

The Bragg peaks of both protons and  $^4\text{He}$  ions are located at lower areal density for HDPE than for the Moon. The reason is that the stopping power is proportional to the density-normalised electron density:

$\frac{dE}{dx} \propto \frac{Z_T}{A_T}$ . Since  $(\frac{Z}{A})_{\text{HDPE}} > (\frac{Z}{A})_{\text{Moon regolith}}$ ,  $(\frac{dE}{dx})_{\text{HDPE}} > (\frac{dE}{dx})_{\text{Moon regolith}}$ . Therefore, for the same ion and energy  $R_{\text{HDPE}} < R_{\text{Moon regolith}}$ , where  $R$  is the particle range in  $\text{g cm}^{-2}$ . Also, the Bragg peak of protons in HDPE is higher than in the Moon regolith simulant. Nevertheless, the area under the proton Bragg peak is similar for the two materials. It is slightly larger for the Moon regolith simulant case. Therefore, the lower Bragg peak seems to be caused by the granular structure (sand) of the Moon regolith, which broadens the Bragg peak like an additional energy straggling [139].

In Figure 3.9, the same data of Figures 3.7 and 3.8 are plotted by grouping them by target material. The ranges of  $^4\text{He}$  ions are smaller because of the lower kinetic energy per nucleon of the beam. Also, the proton beam displays a higher dose build up effect. This happens because  $\frac{dE}{dx} \propto Z_p^2$ . The same  $D_1$  is therefore measured for more protons than helium ions. Overall, more primary ions undergo more nuclear collisions and generate more target fragments. Therefore, a higher dose build up is observed for the same dose  $D_1$ .

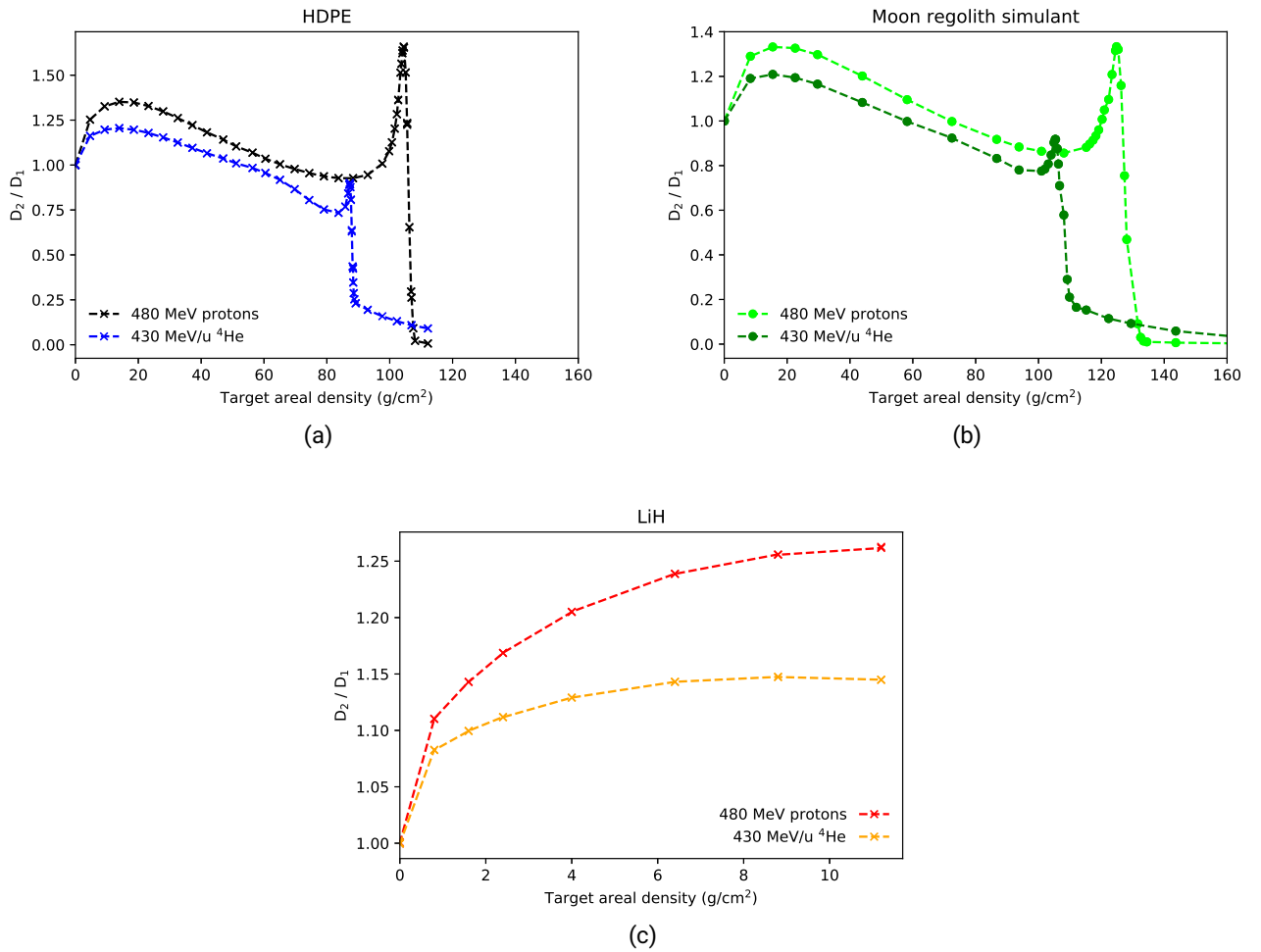


Figure 3.9: Same results of Figures 3.7 and 3.8 plotted by grouping them by target: HDPE data in Panel (a), Moon regolith simulant in Panel (b), and LiH in Panel (c). The dashed lines simply connect the experimental points.

## Higher-Energy Results

This section focuses on the results obtained with a 2 GeV proton beam at the GSI Cave M. For this beam, the materials used for dose measurements are PMMA and LiH. As stated in Section 3.1.2, PMMA was chosen as a reference material because of its availability and relatively similar atomic composition to PE. It is expected to see a higher dose build up for this beam than for 480 MeV protons because, as seen in Section 2.5.4, the build up is stronger in intensity for higher energies of the same ion beam. In addition, the build up is also expected to be longer in depth than for 480 MeV protons. The reason is that the higher energy of the primary beam translates into higher-energy secondary ions, which have in turn a larger range. In Figure 3.10, the results of dose ratio  $D_2/D_1$  obtained with 2 GeV protons in PMMA and LiH are reported.

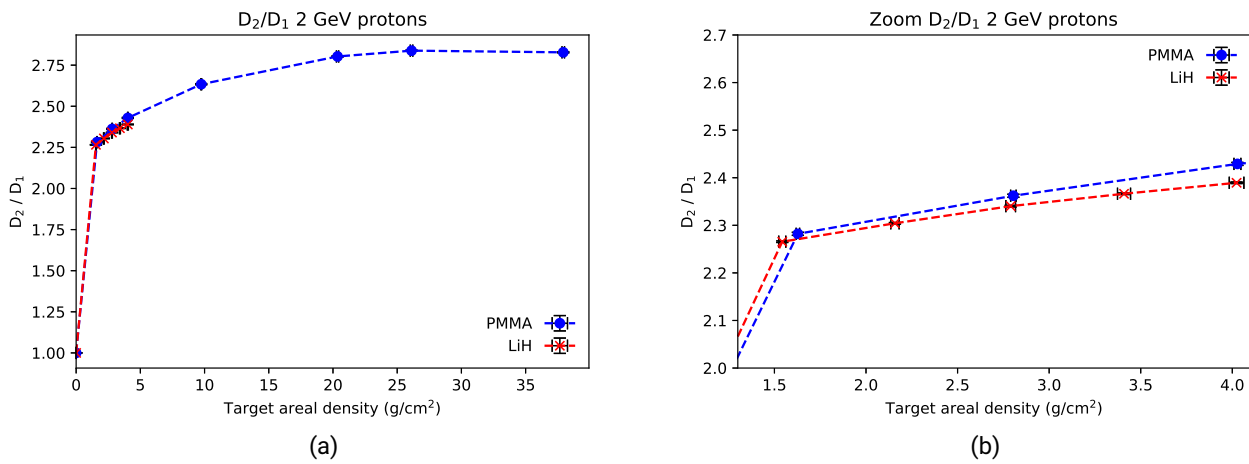


Figure 3.10: Panel (a): 2 GeV proton beam  $D_2/D_1$  experimental results. Panel (b): zoom-in the first  $4 \text{ g cm}^{-2}$ , which correspond to the maximum LiH thickness available. The dashed lines simply connect the experimental points.

As explained in Section 3.1.3, for this experimental campaign, a third IC was also used in front of the target material (see the schematic of the experiment in Panel (b) of Figure 3.2). The ratio between the dose measured with this chamber and the IC1 is called  $D_3/D_1$ . The results of this ratio for increasing material thicknesses are shown in Figure 3.11.

As it can be seen in Panels (a) of Figures 3.11 and 3.10, the dose build up results before ( $D_3/D_1$ ) and behind ( $D_2/D_1$ ) the target are extremely similar for PMMA and LiH. Nevertheless, the zoom-in reported in Panels (b) show that in both cases the results are consistently lower for LiH than for PMMA. This confirms what has already been seen for lower-energy beams. Therefore, it can be concluded that this material seems to be beneficial also from the point of view of slightly less dose build up for light-ion beams.

In literature, every proton with energy lower than the primary beam is commonly called a “secondary proton” since it cannot be distinguished if it is a target fragment or a primary proton whose energy has been degraded through collisions with the target. In the following, primary protons that undergo scattering reactions with the target ions will be called “primary protons” because, even if their kinetic energy is degraded, they are not formed during interactions with the target material. They are therefore beam ions. “Secondary protons” is the name that will be used for protons coming from the target material, namely, target fragments.

A further distinction between secondary protons (as defined above) can be made:

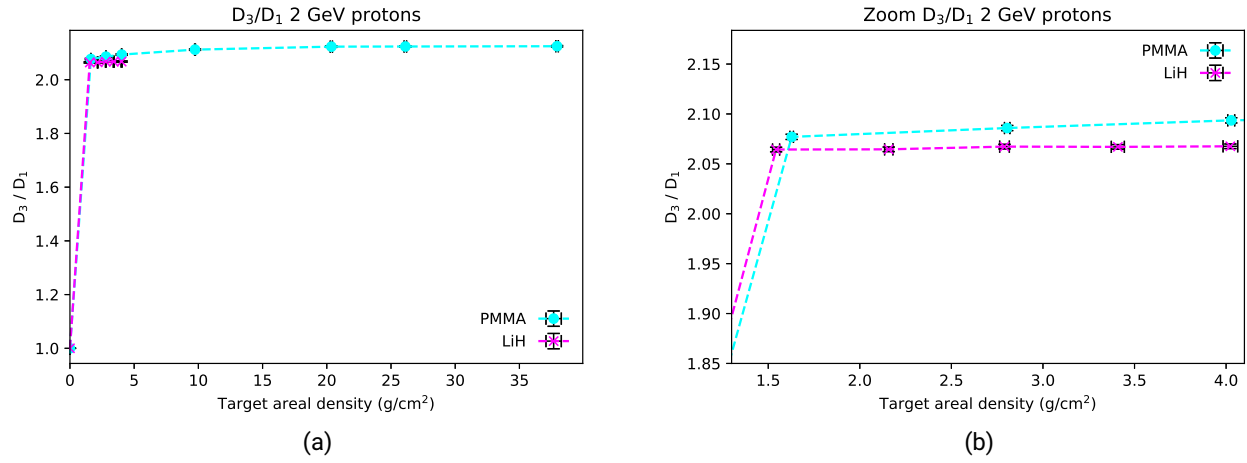


Figure 3.11: Panel (a): 2 GeV proton beam  $D_3/D_1$  experimental results. Panel (b): zoom-in the first  $4 \text{ g cm}^{-2}$ , which correspond to the maximum LiH thickness available. The dashed lines simply connect the experimental points.

- those directly knocked out by the primary protons (“knock-out protons”), whose angular distribution is strongly peaked towards the primary beam direction, and
- those generated within the nuclear evaporation de-excitation processes that target nuclei undergo after interacting with the primary beam (“evaporation protons”). Their angular distribution is isotropic.

Therefore, the dose release into the chambers is mainly due to the following particles:

1. IC1: primary protons only,
2. IC2: primary protons, knock-out secondary protons, lower-energy evaporation protons, and other secondary particles (e.g. electrons),
3. IC3: primary protons, evaporation protons, and other secondary particles (e.g. electrons).

The results obtained with the same material both for  $D_2/D_1$  and  $D_3/D_1$  are reported in Figure 3.12. The difference between the two sets of results is due to the additional contribution to  $D_2/D_1$  of slowed-down primary protons, knock-out secondary protons, and the different contributions of other secondary particles (e.g. electrons).

### 3.2.3 Lithium Hydride

As stated at the beginning of this chapter, within physics experiments (see Section 2.9), one could conceivably construct a GCR simulator by collecting single-beam data on the same target. In this work, results with four different ion beams of interest for GCR were collected for one same target, which is a candidate innovative shielding material for upcoming deep-space explorations: LiH. This is the material which performed the best for all the four ion beams used within the various experimental campaigns.

These results are reported in Figure 3.13. The absorbed dose results for one single material and several different beams of interest in space allow a more complete understanding of its properties. For the  $1 \text{ GeV u}^{-1}$

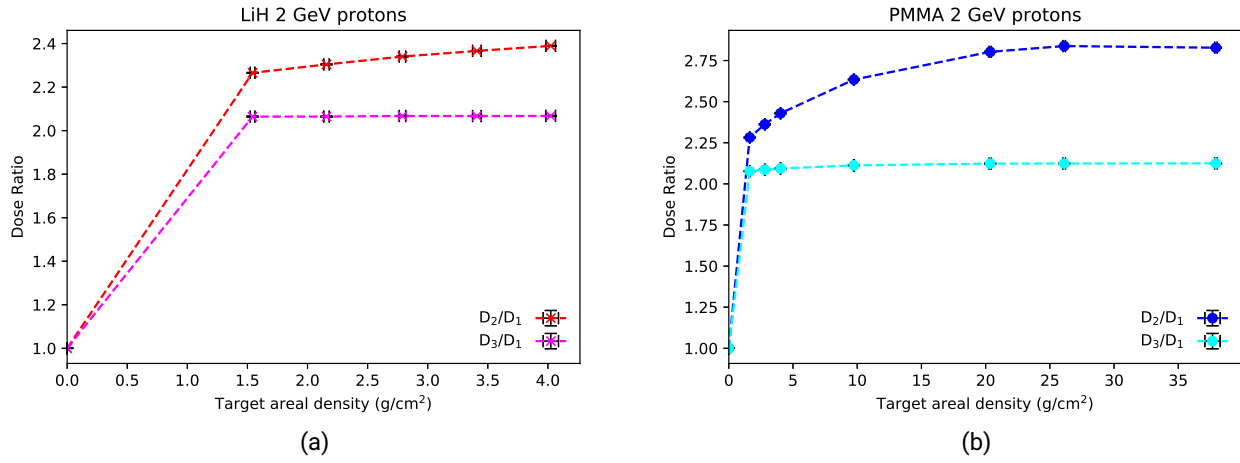


Figure 3.12: Panel (a): Comparison between  $D_2/D_1$  and  $D_3/D_1$  experimental results for LiH and the 2 GeV proton beam. Panel (b): Same as Panel (a), but for PMMA. The dashed lines simply connect the experimental points.

<sup>56</sup>Fe beam, the dose decreases after an initial short build up. This is due to the dominating fragmentation of the primary beam. For lower-Z beams, the dose keeps increasing for increasing LiH thickness. This dose build up is stronger for lighter ions and higher beam energies. The GCR spectrum is made of both light and heavy ions. Therefore, the overall absorbed dose behind LiH would result from a combination of this attenuation and build up effects.

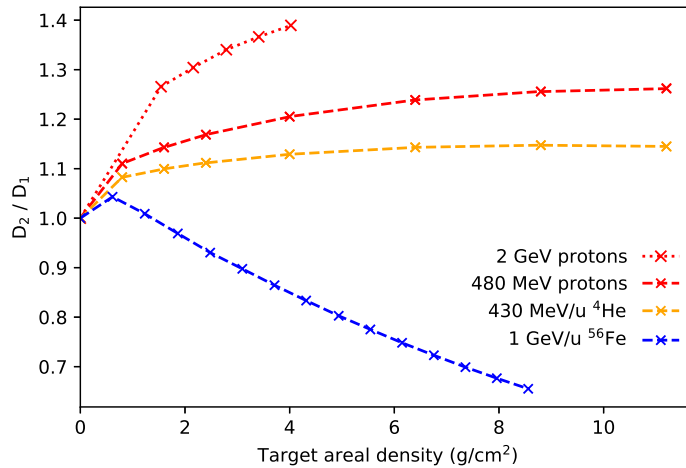


Figure 3.13: Results obtained with all the different ion beams for LiH. The dashed lines simply connect the experimental points.



---

### 3.3 Conclusions of Absorbed Dose Measurements

---

Absorbed dose measurements with  $1 \text{ GeV u}^{-1} {}^{56}\text{Fe}$ ,  $430 \text{ MeV u}^{-1} {}^4\text{He}$ , and 480 and  $2 \text{ GeV } {}^1\text{H}$ -ion beams were performed with well-established (PE), innovative (lithium-based hydrides) and potential *in situ* (Moon regolith) shielding materials for space exploration. Structural spacecraft materials (Al) and potential dual-use components (Li-poly batteries) were also tested for comparison. The iron beam was chosen because the GCR dose equivalent behind thin shields is dominated by the heavy-ion component of GCR (iron in particular), and the helium and proton beams because light-ions dominate such contribution behind thick shields.

A consistent dose attenuation is observed for the iron beam. The materials performing the best, and even better than PE, which is the gold standard for space exploration, are the lithium-based hydrides. As already found out in past experimental [11, 12] and simulation [116] campaigns, LiH is the best material for the dose attenuation endpoint. Second to it, there is the other lithium-based hydride tested in the experimental campaigns:  $\text{LiBH}_4$ . Nevertheless, these two hydrides are not chemically stable as they react with the moisture in the air. The addition of paraffin to them was proven to be effective to make mechanically and chemically stable promising composite shielding materials. Both the pure hydrides and their version chemically stabilised in a paraffin matrix performed better than PE. In particular, LiH-paraffin seems to combine the excellent dose attenuation properties of LiH with manageable chemical stability. The second-best performing materials after LiH, are  $\text{LiBH}_4$  and LiH-paraffin at the same level. This suggests a big potential of the chemically stable innovative material LiH-paraffin for its use in space radiation shielding applications.

Concerning the light-ion beam results, a consistent dose build up is observed. The dose build up is stronger and has a longer range for lighter ions and higher kinetic energies. A dose enhancement in the first centimetres of materials causes an inverse shielding, as the dose increases for increasing shielding thickness. Therefore, this phenomenon needs to be taken into account especially for high-energy light ions, as the range of such effect can become significant and affect the absorbed dose behind shielding thicknesses of interest in space missions. Once more, LiH resulted in the best material as the dose build up associated with it is the lowest among the tested materials.

Since the GCR spectrum is made both of light and heavy ions, the dose ratio due to the presence of the shielding materials in space will be a mixture of the dose attenuation of the heavy-ion contribution and the dose build up of the light ions.



---

## 4 Monte Carlo Simulations

---

As GCRs are a very difficult radiation environment to be reproduced on Earth, MC or deterministic transport codes are needed for risk assessment of exploration mission scenarios and shielding design. Therefore, as discussed in Section 2.9, it is necessary to validate the transport code simulation outcomes with results obtained from physics experiments performed at accelerator facilities. “Simple” single-ion beam accelerator-based experiments such as the one reported in Chapter 3 are important because their comparison to the outcome of simulations allows an understanding of the validity of the basic physics models underlying the transport codes.

The results of the experimental campaigns presented in Chapter 3 were compared to the predictions of some of the most commonly used MC codes for radiation protection in space applications, namely Geant4 [140], PHITS [141], and FLUKA [142–145].

The results presented in this Section are the outcome of a collaboration between GSI and Thales Alenia Space Italia in the framework of the ROSSINI3 project. Therefore, the Geant4 and PHITS simulations were performed by the Thales Alenia Space Italia team and the FLUKA simulations were carried out within the scope of this Thesis.

---

### 4.1 Materials and Methods

---

---

#### 4.1.1 Simulation Setup and Approximations

---

Simulations reproducing the ROSSINI3 experimental campaigns were carried out using the MC particle transport codes PHITS (version 3.20), Geant4 (version 10.6 patch-02) and FLUKA (version 2020.0.3, and flair version 2.3-0 [146]). The main goal was to keep the simulations as similar as possible to focus on the differences among the physics models.

---

#### Geometry

---

The simulation geometry reproduced the experimental setup: the air gaps and distances between the different setup components have been kept the same as during the experimental campaigns.

The simulations also included the plastic bags and the boxes into which the lithium-based hydrides and Moon were respectively irradiated. The beam was modelled with a Gaussian lateral profile of 0.8 cm FWHM (no angular divergence), the ICs as two 25  $\mu\text{m}$  Mylar walls filled with gas and no detailed internal electrode structures. Details about the ICs are not crucial since the dose ratios are normalised to the no target case. For the simulations, the number of generated primary ions has been selected high enough to decrease the statistical errors to less than 3% ( $10^4$  to  $10^5$  ions). The RS plates were precisely simulated, but the external RS structure was not included as it was not in the beam line.

Some Geant4 simulations were performed to check if it was necessary to include the geometry of the structures keeping the targets in place and the rest of the surrounding Cave structure. These simulation

---

runs proved that the addition of these elements did not make a difference in the results. Therefore, they were not added to the final simulations.

---

## Geant4

---

The following setup and approximations were used by the Thales Alenia Space Italia team for the Geant4 simulations.

The dose in the detector was calculated by summing up the energy deposition in the active region of the detector and dividing it by the mass of the region itself. The default electron range cut of 0.1 mm was used for the pure and composite lithium-based hydrides, and HDPE. It corresponds to an energy cut of 0.08 MeV in HDPE, and of 0.057 MeV in LiH. A 0.01 mm cut was used for electrons in the aluminium alloys, Si, SiO<sub>2</sub> and Moon regolith. It corresponds to an electron energy of 0.0325 MeV in aluminium, and of 0.03 MeV in Si.

The reference physics lists QGSP\_INCLXX, FTFP\_BERT, and QBBC\_EMY Geant4 physics lists were used for the simulations. QGSP\_INCLXX is an experimental physics list that uses the Quark-Gluon String model for high-energy hadronic interactions, and the Leige Intranuclear Cascade model for proton, neutron and pion induced reaction with low energies, instead of the Binary or Bertini Cascade models. It is recommended to be used for shielding applications [147]. FTFP\_BERT makes use of the FRITIOF String model for high-energy hadron interactions, and Bertini for low energies. It is recommended to be used for high-energy applications [147]. QBBC\_EMY is a list created *ad hoc* for space, radiation biology, and radiation protection applications. It includes combinations of Binary, Bertini, Quark-Gluon String, FRITIOF String and other models to reach high precision in the simulation of many hadron-ion and ion-ion interactions in a wide energy range [148]. This last list was chosen for the simulations because of the good agreement with the data presented in [12] and more generally in the energy range between 100 MeV u<sup>-1</sup> and 1.5 GeV u<sup>-1</sup> [148]. The reference physics lists QGSP\_BERT, QGSP\_BERT\_EMV, and FTFP\_INCLXX were also used to simulate the full paraffin Bragg curve for a deeper study of the differences among the lists themselves and the combination of the different models for different particles and energy ranges.

---

## PHITS

---

The following setup and approximations were used by the Thales Alenia Space Italia team for the PHITS simulations.

The T-Deposit tally was used to calculate the dose deposition. A  $1.0 \times 10^{-3}$  MeV energy cut was used for electrons, gammas, and positrons, while the production threshold for delta rays was set to 0.1 MeV. The transport of electrons, positrons, and photons was based on the EGS5 algorithm, while gamma decay residual nuclei transport was based on the EBITEM model. Landau Vavilov energy straggling option was selected for charged particles and nuclei. The Lynch formula based on the Molière theory was used for Coulomb diffusion, while JQMD-2.0 and SMM for nuclear reactions.

---

## FLUKA

---

In FLUKA, transport cuts for e<sup>±</sup> and γ were set to 0.1 MeV, like the delta ray production cut. This cut was chosen after running simulations with lower thresholds and reporting no significant differences in the results. Projectile and target electromagnetic-dissociation and coalescence processes were activated, and the FLUKA evaporation model used was “New evaporation with heavy frag”.

---

## 4.1.2 Data Analysis and Error Propagation

---

The dose ratios obtained for each simulated target thickness were divided by the dose ratio obtained for the no target case, as it was done with the experimental data:

$$\frac{D_2}{D_1} = \frac{(D_2/D_1)_{\text{target}}}{(D_2/D_1)_{\text{no target}}}. \quad (4.1)$$

Same for  $\frac{D_3}{D_1}$ . The doses were calculated in the active regions of the two ICs.

The errors were computed as follows:

$$\Delta\left(\frac{D_2}{D_1}\right) = \frac{D_2}{D_1} \sqrt{\left(\frac{\Delta((D_2/D_1)_{\text{target}})}{(D_2/D_1)_{\text{target}}}\right)^2 + \left(\frac{\Delta((D_2/D_1)_{\text{no target}})}{(D_2/D_1)_{\text{no target}}}\right)^2}. \quad (4.2)$$

Same for  $\Delta\left(\frac{D_3}{D_1}\right)$ .

---

## 4.2 Results and Discussion

---

---

### 4.2.1 Iron Ions

---

This Section focuses on the MC simulations performed to be compared to the experimental data obtained with the  $1 \text{ GeV u}^{-1} {}^{56}\text{Fe}$  beam and further analyse these results. The content of this Section was published in F Luoni *et al.*, “Dose attenuation in innovative shielding materials for radiation protection in space: Measurements and simulations,” *accepted by Radiat. Res.*, 2022.

---

#### Absorbed Dose Simulations

---

Monte Carlo predictions of the  $1 \text{ GeV u}^{-1} {}^{56}\text{Fe}$ -beam experimental results are reported in Figure 4.1 for the aluminium alloys and HDPE, Figure 4.2 for the lithium-based hydrides and their composites, and Figure 4.3 for pure Si,  $\text{SiO}_2$ , and Moon regolith. Error bars represent the statistical error due to the use of Monte Carlo approaches. PHITS reproduces well the results for aluminium and all the pure and composite lithium-based hydrides. On the other hand, PHITS overestimates the results for HDPE, Si,  $\text{SiO}_2$  and Moon regolith. FLUKA reproduces well the results for HDPE, all the pure and composite lithium-based hydrides and the Moon regolith. Nevertheless, it underestimates the results for the aluminium alloys, Si and  $\text{SiO}_2$ . FLUKA tends, therefore, to underestimate the results for the heaviest targets. The fit of the Moon results with FLUKA could be influenced by the presence of the PMMA/Plexiglas box involved in the setup. All the Geant4 physics lists used can reproduce well and give consistent results for the aluminium alloys and Si, which are the heaviest tested targets. For all the other cases, QGSP\_INCLXX is the list performing the best. QBBC\_EMY and FTFP\_BERT overestimate the results for HDPE, all the pure and composite lithium-based hydrides,  $\text{SiO}_2$  and Moon regolith. These results confirm the recommendation of using QGSP\_INCLXX for shielding applications. It should be also noted that QBBC\_EMY, which is the reference physics list recommended for medical and space applications, is not able to reproduce well the experimental data for any of the studied materials, but the aluminium alloys.

The differences obtained between different MC codes can be large, reaching 15% for the largest amount of  $\text{LiH}_p$ . This is due to the different hadronic physics underlying FLUKA, PHITS and different Geant4 physics lists, and in particular, to the different nuclear cross-section parametrisations employed in the codes.

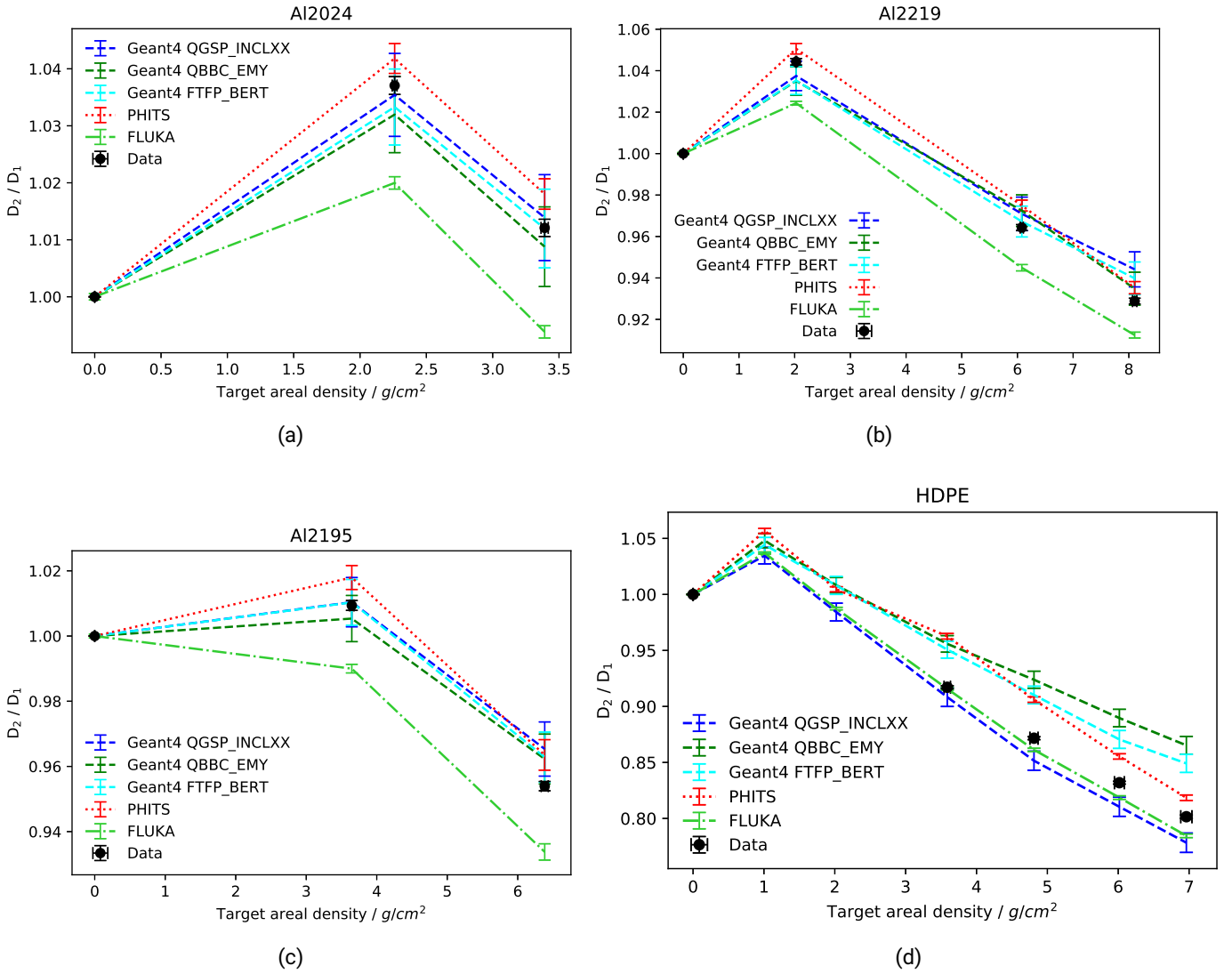


Figure 4.1: Comparison between experimental data and MC simulation results for the three tested aluminium alloys and for HDPE irradiated with the  $1 \text{ GeV } ^{56}\text{Fe}$  beam. The PHITS simulations were performed by Dr. Martina Giraudo and Claudio Cipriani. The Geant4 simulations were performed by Luca Bocchini.

These parametrisations are in fact, a crucial ingredient to Monte Carlo simulations [68, 72, 105, 149]. If a simulation overestimates the dose reduction, the nuclear fragmentation cross-section of the primary ions in the target material is overestimated. The opposite is valid for Monte Carlo simulations underestimating the experimentally measured dose attenuation. Geant4 QBBC\_EMY, for instance, underestimates the dose attenuation in HDPE and all lithium-based hydrides. Therefore, we can deduce that the underlying physics might underestimate the nuclear fragmentation cross-section of  $1 \text{ GeV } ^{56}\text{Fe}$  on  $^1\text{H}$  target nuclei. Since nuclear cross-section parametrisations are semi-empirical, they need cross-section measurement data to be validated. Chapter 5 goes into great detail in regard to the parametrisations and what cross-sections need to be measured.

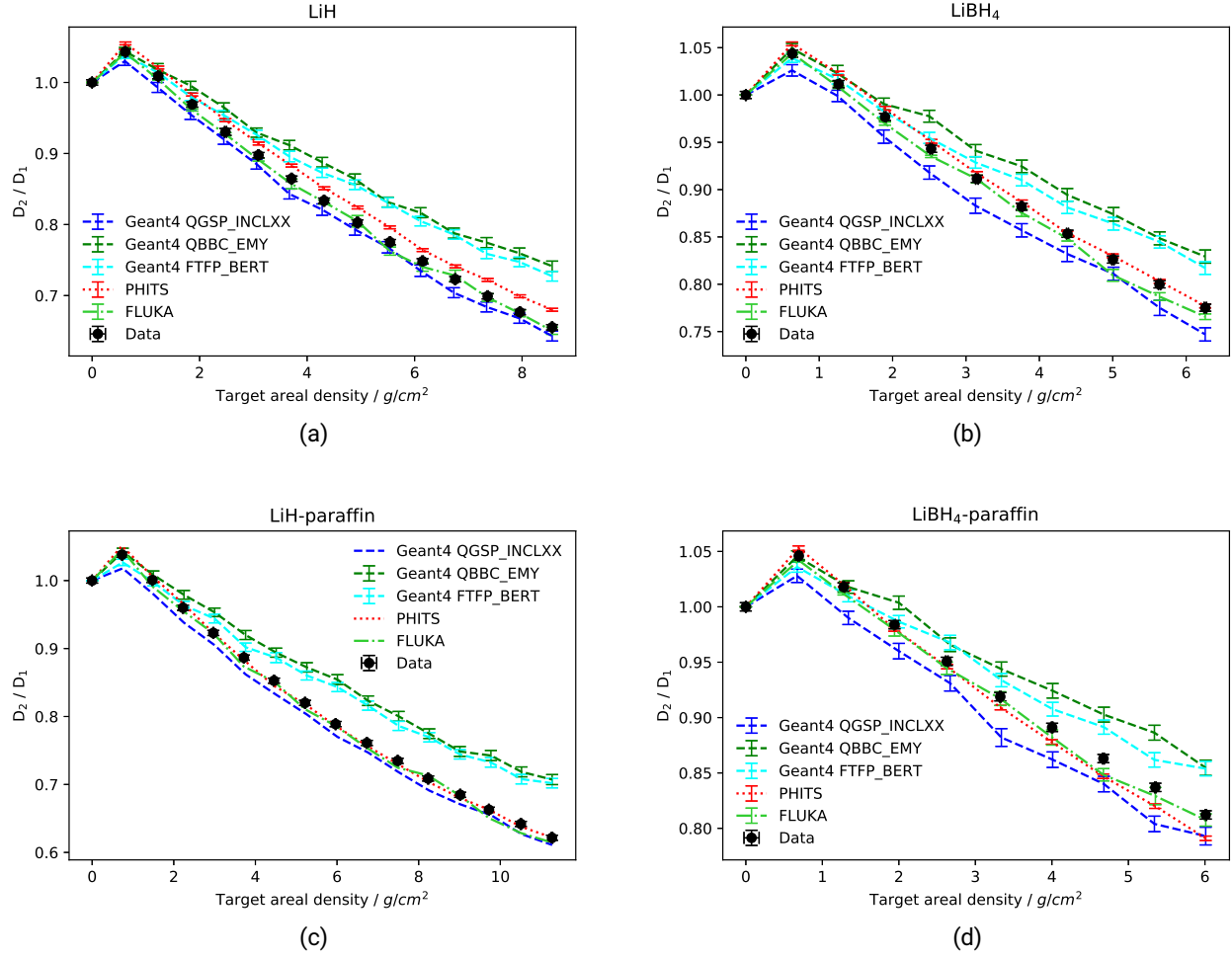


Figure 4.2: Comparison between experimental data and MC simulation results for the pure and composite lithium-based hydrides irradiated with the  $1 \text{ GeV } u^{-1} {}^{56}\text{Fe}$  beam. The PHITS simulations were performed by Dr. Martina Giraudo. The Geant4 simulations were performed by Luca Bocchini.

### Paraffin Bragg Curve Simulations

A full Bragg curve measurement has been carried out with paraffin. The first part of the curve can be found in Figure 3.3. The full curve and the Monte Carlo simulation results are reported in Figure 4.4. In Panel (b) of Figure 4.4, the results obtained with different Geant4 physics lists are reported. Several lists have been used to study the differences in the results introduced by changing the hadronic and electromagnetic models implemented in Geant4. Since QGSP\_INCLXX is the list performing the best, the results obtained with it are reported in Panel (a) of the same figure, alongside the PHITS and FLUKA results. It can be observed that FLUKA, PHITS and Geant4 QGSP\_INCLXX reproduce the fragmentation and tail regions well. PHITS, however, underestimates the range of the primaries, and Geant4 QGSP\_INCLXX overestimates the height of the Bragg peak. This overestimation is a sign of an underestimation of the nuclear fragmentation processes undergone by the primary Fe ions. In Panel (b), it can be observed that the results strongly depend on the reference physics list used. QGSP\_BERT\_EMY, QBBC\_EMY and QGSP\_BERT underestimate the Fe nuclear fragmentation processes much stronger than QGSP\_INCLXX and FTFP\_INCLXX. The latter though,

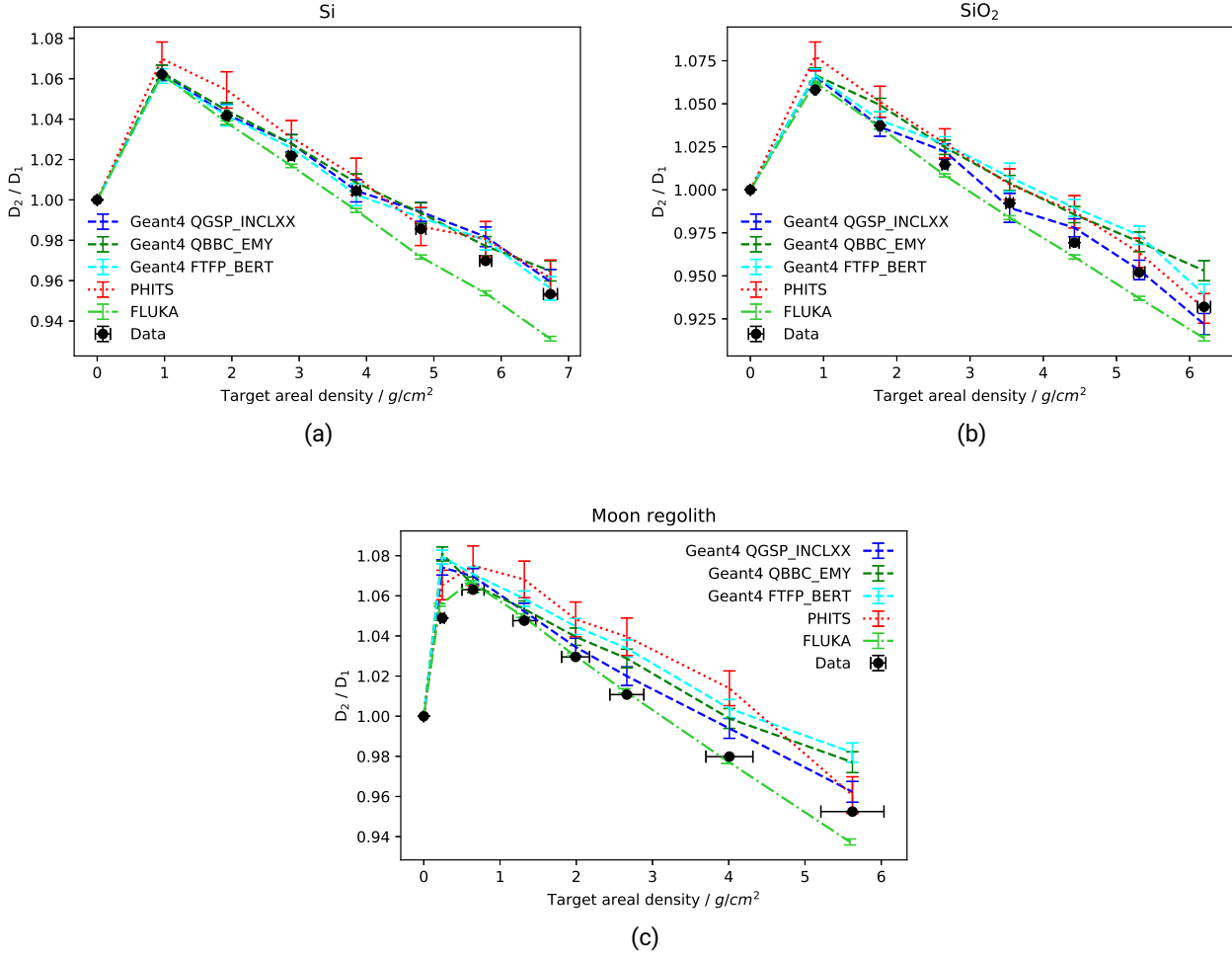


Figure 4.3: Comparison between experimental data and MC simulation results for Si, SiO<sub>2</sub> and highland Moon regolith irradiated with the 1 GeV u<sup>-1</sup> <sup>56</sup>Fe beam. The PHITS simulations were performed by Claudio Cipriani. The Geant4 simulations were performed by Luca Bocchini.

reproduce well the trend of the data before the Bragg peak and in the tail regions. QGSP\_BERT\_EMY and QGSP\_BERT make use of the Bertini Cascade model at low energies, and QBBC\_EMY for some interactions as well. On the other hand, QGSP\_INCLXX and FTFP\_INCLXX use the Leige Intranuclear Cascade model for proton, neutron and pion induced reactions at low energies. The differences among the lists look therefore mainly due to low-energy interactions.

### Initial Dose Build Up

MC simulations were performed with FLUKA to deepen the physical bases of the phenomenon. The results obtained for LiH and Al2219 are shown in Figure 4.5. The curves in magenta report the simulation results obtained when no delta electrons are generated. The electronic production threshold was set to 57 GeV, which is higher than the kinetic energy of the primary ions. The light green curve was instead generated by setting the electronic production threshold to 0.1 MeV. The outcome is that the dose build up observed for these experimental data is merely due to delta electrons. The target fragments generated through nuclear



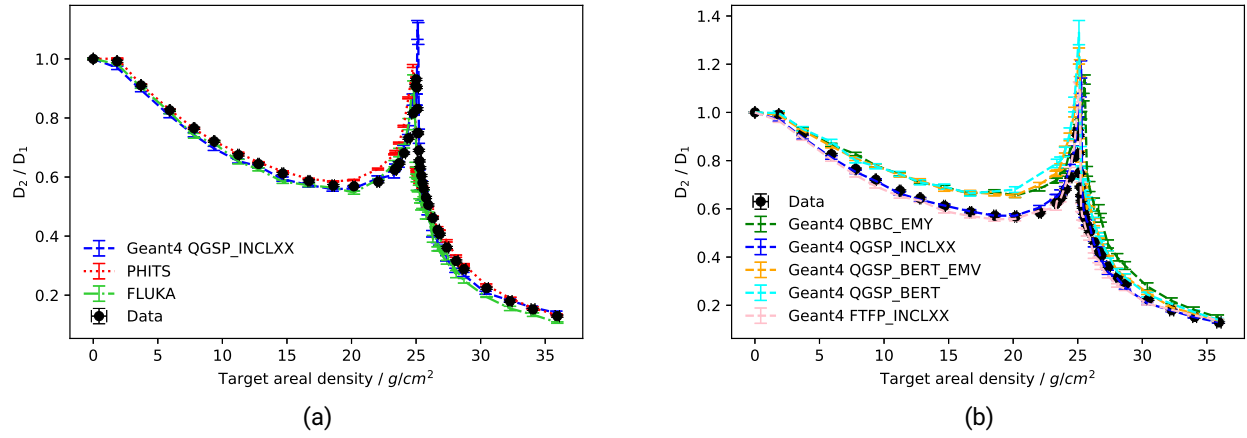


Figure 4.4: Comparison between experimental data and simulation results for paraffin irradiated with the  $1 \text{ GeV } u^{-1} {}^{56}\text{Fe}$  beam. In Panel (a) simulation results obtained with FLUKA, PHITS and Geant4 physics list QGSP\_INCLXX are reported. In Panel (b) results obtained with several Geant4 physics lists are shown. The PHITS simulations were performed by Dr. Martina Giraudo. The Geant4 simulations were performed by Luca Bocchini.

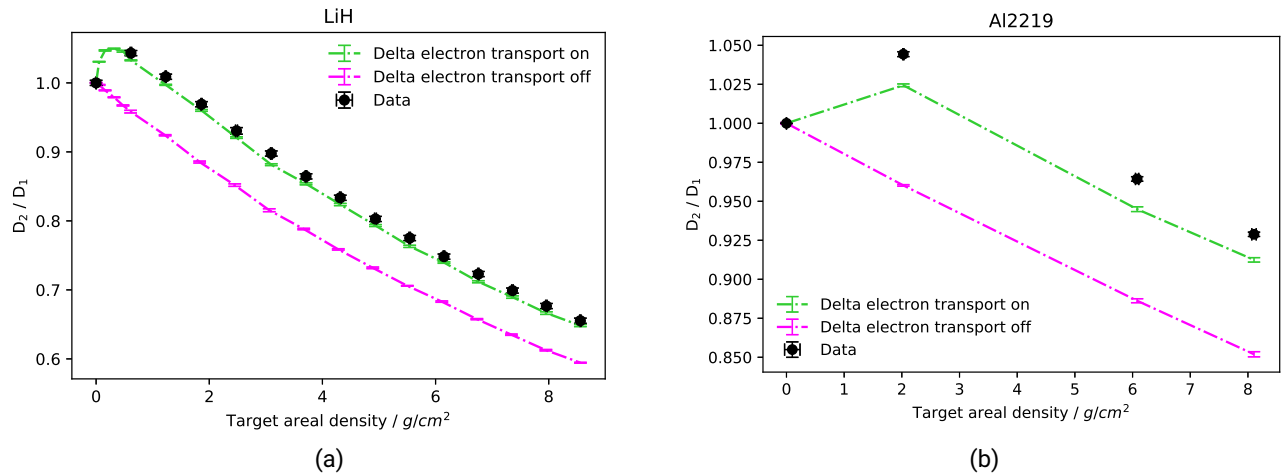


Figure 4.5: Comparison between the result of MC simulations performed with FLUKA for pure-LiH target (Panel (a)) and Al2219 (Panel (b)), including (light green) and excluding (magenta) the dose contribution of delta electrons. The experimental data were obtained through irradiation with the  $1 \text{ GeV } u^{-1} {}^{56}\text{Fe}$  beam and are the same as reported in Figure 3.3. The simulation results including the delta-electron contribution are the same as reported in Figure 4.2.

interactions between the iron ions and the target nuclei do not contribute to it. This is very different than what happens with light-ion beams (see Section 4.2.2).

## 4.2.2 Light Ions

This Section focuses on the MC simulations performed to be compared to the experimental data obtained with the 2 GeV proton beam and further analyse these results.

Monte Carlo predictions of the 2 GeV  $^1\text{H}$ -beam experimental results are reported in Figure 4.6 for  $D_2/D_1$  and Figure 4.7 for  $D_3/D_1$ . Error bars represent the statistical error due to the use of Monte Carlo approaches. For the  $D_3/D_1$  data, the error bars look larger because of the smaller range of  $D_3/D_1$  values included in the y-axes of the plots of Figure 4.7.

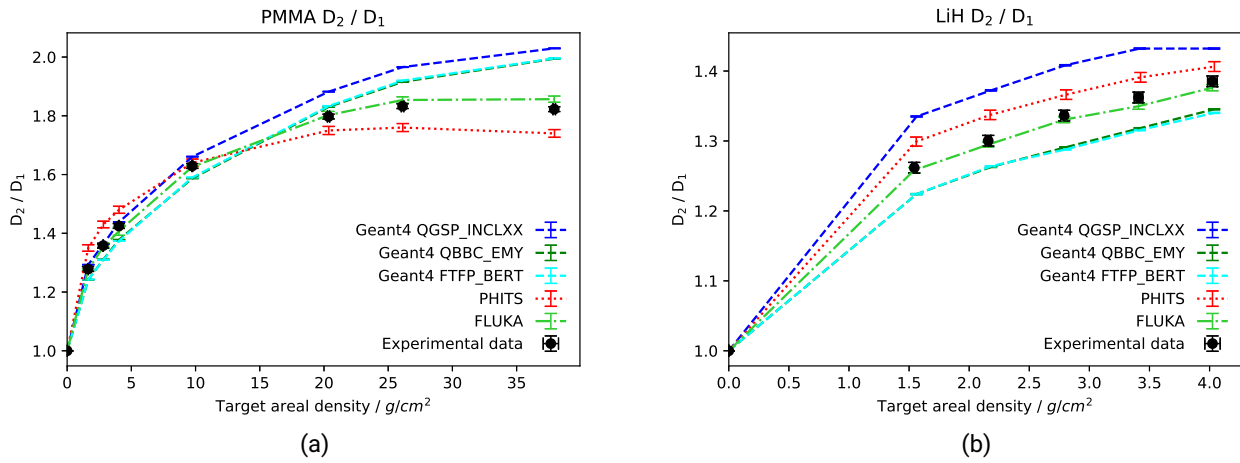


Figure 4.6: Comparison between  $D_2/D_1$  experimental data and MC simulation results for PMMA and LiH irradiated with the 2 GeV  $^1\text{H}$  beam. The PHITS simulations were performed by Dr. Martina Giraudo. The Geant4 simulations were performed by Luca Bocchini.

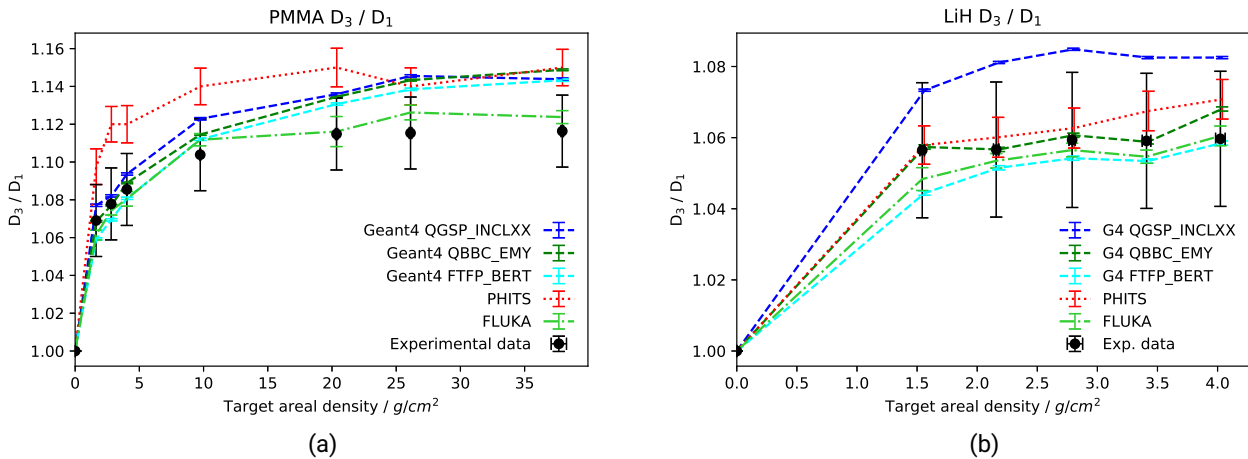


Figure 4.7: Comparison between  $D_3/D_1$  experimental data and MC simulation results for PMMA and LiH irradiated with the 2 GeV  $^1\text{H}$  beam. The PHITS simulations were performed by Dr. Martina Giraudo. The Geant4 simulations were performed by Luca Bocchini.

From Figure 4.6, it can be seen that FLUKA simulations fit the experimental data the best. PHITS

---

underestimates the dose build up for  $D_2/D_1$  in PMMA and overestimates it in LiH. This means that PHITS underestimates the production of knock-out secondary protons and, potentially, the electronic contribution to the build up in PMMA and overestimates them in LiH. The opposite is valid for the Geant4 QBBC\_EMY and FTFP\_BERT lists. Concerning QGSP\_INCLXX, it overestimates the build up for both materials.

Concerning the  $D_3/D_1$  results reported in Figure 4.7, FLUKA was found to be the best code for reproducing the experimental data for PMMA. All the other lists overestimate the build up of  $D_3/D_1$ , which means that they overestimate the evaporation nucleons emitted by the target and, potentially, the electronic contribution to the build up (see Section 4.2.2). PHITS overestimates the  $D_3/D_1$  results the most. Concerning LiH, only QGSP\_INCLXX overestimates the results. The other lists fit the results well (within error bars).

On the one hand, the results obtained with FLUKA are in agreement with the findings of Section 4.2.1. It was found to be the best code for light targets and both LiH and PMMA are low-Z targets. On the other hand, the results obtained with QGSP\_INCLXX are quite surprising, as it is the Geant4 list overall fitting the iron experimental data best. It overestimates both the knock-out of secondary protons ( $D_2/D_1$  results) and the production of evaporation nucleons ( $D_3/D_1$  results) and, potentially, the electronic contribution to the build ups. Therefore, it looks like the Leige Intranuclear Cascade model for low energies used in QGSP\_INCLXX reproduces well the results of a nuclear fragmentation interaction undergone by a high-energy heavy projectile such as iron, but not of a spallation reaction of a high-energy proton.

---

### Electronic Contribution to the Dose Build Up

---

MC simulations were performed with FLUKA to understand the impact of the electronic contribution to the build up. The results obtained for LiH and PMMA are shown in Figure 4.8. Also in this case, the curves in magenta report the simulation results obtained when no delta electrons are generated. The electronic production threshold was set to 3 GeV, which is higher than the kinetic energy of the primary protons. The light green curve was instead generated by setting the electronic production threshold to 0.1 MeV.

The outcome is that, as expected, only part of the dose build up observed for these experimental data is due to delta electrons, both for  $D_2/D_1$  and  $D_3/D_1$ .

The electronic contribution to  $D_2/D_1$  is  $\approx 40\%$  for thin material layers and decreases with increasing thickness, reaching  $\approx 20\%$  for the largest PMMA thickness. The range of electrons in such materials is, in fact, smaller than the range of protons. In particular, it was estimated with LISE++ [150] that the range of 2 GeV protons in LiH and PMMA is  $\approx 820 \text{ g cm}^{-2}$  and with the NIST database [151, 152] that the range of 2 GeV electrons is  $\approx 74 \text{ g cm}^{-2}$  in LiH and  $\approx 40 \text{ g cm}^{-2}$  in PMMA. Therefore, protons go on building up for longer ranges and the relative electronic contribution becomes smaller.

The electronic contribution to  $D_3/D_1$  is smaller. It ranges between  $\approx 20$  and  $\approx 30\%$  for LiH and it is  $\approx 30\%$  for thin layers of PMMA, reducing to between  $\approx 20$  and  $\approx 10\%$  for the thickest layers.

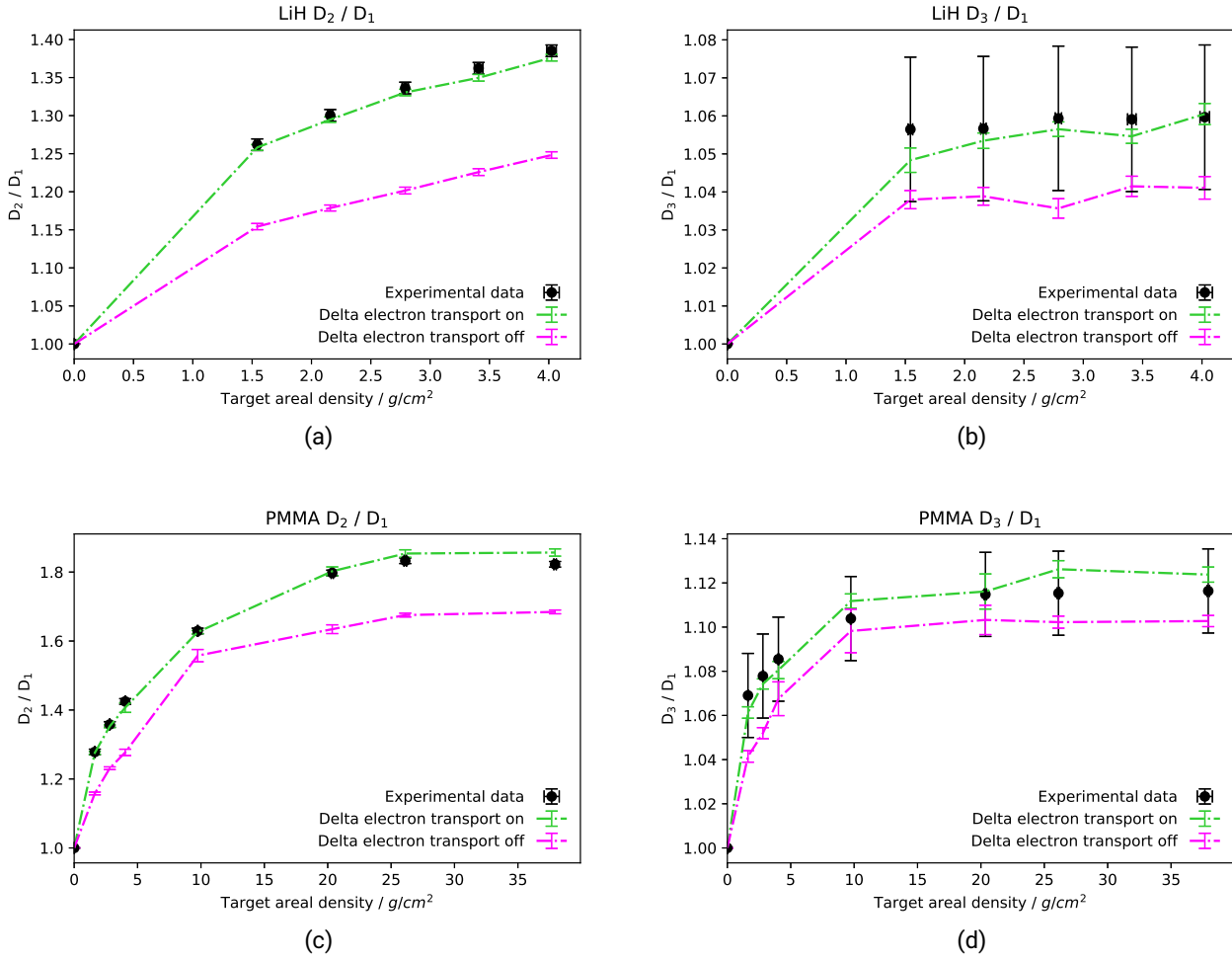


Figure 4.8: Comparison between the result of MC simulations performed with FLUKA for LiH (Panel (a)) and PMMA (Panel (b)), including (light green) and excluding (magenta) the dose contribution of delta electrons. The experimental data were obtained through irradiation with the 2 GeV  $^1\text{H}$  beam. The experimental data and simulation results including the delta-electron contribution the same as reported in Figures 4.7 and 4.6.

### 4.3 Conclusions of the Monte Carlo Simulations

The experimental data presented in Chapter 3 were compared with commonly used MC codes for space exploration simulations, i.e. FLUKA, PHITS, and Geant4. Three different Geant4 physics lists were used for all the simulations: QGSP\_INCLXX, Geant4 QBBC\_EMY, and FTFP\_BERT. For the case of the full paraffin Bragg curve measured with iron ions, a more complete comparison among Geant4 physics lists was performed by including also QGSP\_BERT, QGSP\_BERT\_EMV, and FTFP\_INCLXX.

Concerning the iron results, FLUKA resulted to be the best fit with the experimental data for hydrogen-rich materials (HDPE and lithium-based hydrides), while the worst fit for heavier materials such as the aluminium alloys, Si and  $\text{SiO}_2$ . In particular, FLUKA overestimates the fragmentation and, therefore, the dose attenuation of high-Z materials. For what concerns the paraffin Bragg curve, FLUKA can reproduce

---

well the first part of it, but it does not match the Bragg peak position and the tail as precisely as Geant4 QGSP\_INCLXX does. PHITS fits well the experimentally obtained dose ratios with the lithium-based hydride composites, pure  $\text{LiBH}_4$  and paraffin, but tends to underestimate the fragmentation and dose attenuation for all the other tested materials. The Geant4 physics lists results are compatible with each other for heavy targets such as aluminium and Si. These are also the cases in which the Geant4 results fit the data the best. In all the other cases, QGSP\_INCLXX is the best fit for the experimental data, while QBBC\_EMY and FTFP\_BERT underestimate the fragmentation. The more systematic comparison of the Geant4 lists performed for the paraffin Bragg curve showed a better fit for the lists making use of the Leige Intranuclear Cascade model for low energies (QGSP\_INCLXX and FTFP\_INCLXX). The list performing the best is QGSP\_INCLXX, confirming the recommendations of choosing it for shielding applications. The additional study made with FLUKA with LiH and Al2219 showed that the dose build up phenomenon is purely due to the generation of secondary electrons in the case of iron ions.

Concerning the high-energy proton results, FLUKA fits the experimental data best, which is in agreement with what was observed for iron ions, i.e. that FLUKA is the best fit for low-Z targets. Only LiH and PMMA were irradiated during the high-energy proton beam experimental campaign. Surprisingly, the Geant4 physics list QGSP\_INCLXX results are the worst fit for the experimental data for both targets and both the cases of  $D_2/D_1$  and  $D_3/D_1$  measurements.

Overall, the MC simulation results show significant and systematic differences among codes that are used for the same radiation protection purposes. This is mainly due to the need of optimising the current nuclear reaction cross-section models. This topic is discussed extensively in the following chapter.



---

## 5 Nuclear Cross-Section Databases

---

As the reader could understand from Section 2.8, realistic cross-sections are an essential ingredient to reliable deterministic and MC transport codes [72, 149]. In deterministic codes, they enter the transport equations (see Equation (2.30)). In MC codes, nuclear reaction cross-sections are involved in the sampling of the interaction distance of heavy-ions in matter - also called step length (see Equations 2.31, 2.32, and 2.33) - and nuclear production cross-sections are involved in the generation of secondary particles. Unfortunately, there are significant uncertainties in our understanding of nuclear interaction processes between different ions [153]. Several semi-empirical cross-section parametrisations have been developed over the past decades, and are used within MC codes. Nevertheless, none of them fit well the experimental data for all projectile-target systems. Therefore, a deep study of the state of the art of nuclear reaction and total fragment production cross-sections were included in the ROSSINI3 project. In particular, two data collections of experimentally measured reaction and fragment production cross-sections were generated within a collaboration between GSI, ESA and NASA. An up-to-date version of the data collections and a tool to generate cross-section plots can be found in the free and open-access web application accessible from GSI's official website [154]. The results obtained in this work can also be of usage for heavy-ion therapy applications [68], nuclear physics experiments and astrophysics [79].

A comprehensive overview of nuclear cross-section data relevant to radiation protection in space was published by Norbury *et al.* in 2012 [72]. In that work, the information related to the data concerned the systems of target and projectile for which the cross-section data were measured, the type of cross-section, and the kinetic energy range of the projectile. The present work aims at updating that collection and collecting further details about the data, such as the kinetic energy of the projectile, the measured cross-section values, and many more.

This chapter is divided into three sections: one describing the reaction cross-section database, one describing the fragment production cross-section database, and one the main features of the web application containing both databases.

---

### 5.1 Reaction Cross-Section Database

---

This work aims to give a broad overview of all nucleus-nucleus reaction cross-section data measured so far and to compare them with the most-commonly used parametrisations in transport codes. Through such a comprehensive study, recommendations are given on what cross-section data should be measured in future experiments and what formulae fit the existing data best for the most relevant systems to radiation protection in space. Most of the content of this section has been published in F Luoni *et al.*, “Total nuclear reaction cross-section database for radiation protection in space and heavy-ion therapy applications,” *New J. Phys.*, vol. 23, no. 101201, 2021. DOI: <https://doi.org/10.1088/1367-2630/ac27e1>.

---

#### 5.1.1 The Database

---

---

## Data

---

It was decided to focus on nucleus-nucleus reactions only. Therefore, reaction cross-section data measured for projectiles such as protons and neutrons are not reported. Only English peer-reviewed works have been included. A total of 1786 cross-section data from 103 publications [155–257] have been included in the database so far. In the cases in which old data were replaced by more accurate and later measurements, only the newest dataset was included (e.g. data from Ref. [258] were not reported as they were replaced with data from Ref. [179]). In Figure 5.1, the number of cross-section data reported in the database is plotted as a function of the projectile atomic number. A zoom on data points up to nickel projectiles is also reported, since heavier nuclei are only present in trace amounts in the GCR spectrum (see Section 2.3.2). Charge-changing cross-section data are shown in red and reaction cross-sections in green. Data collections

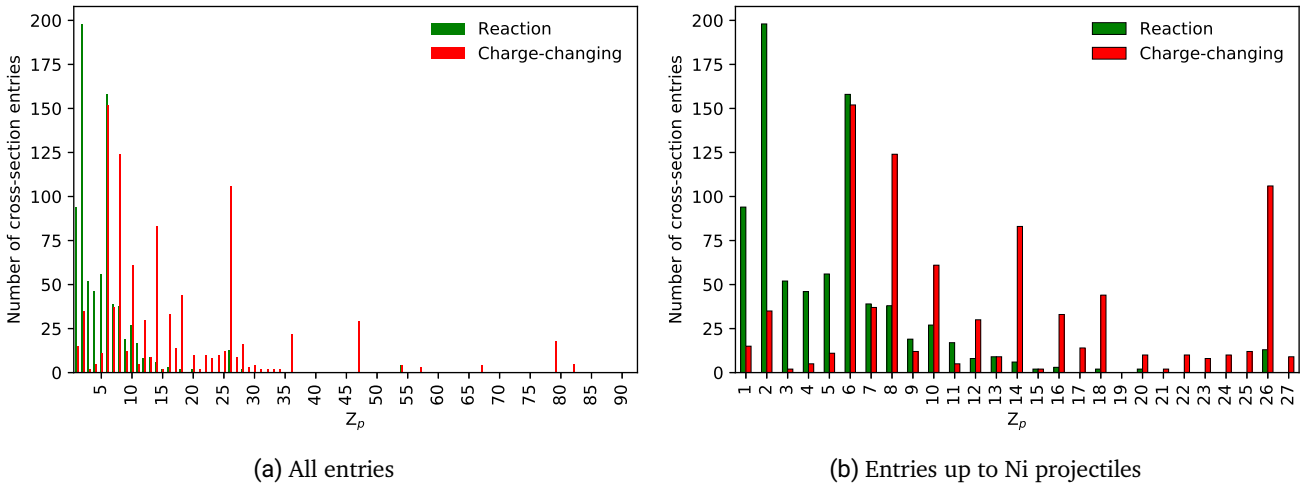


Figure 5.1: Number of cross-section data reported in the reaction cross-section database as a function of the atomic number of the projectile nucleus  $Z_p$ . Charge-changing cross-section entry numbers are shown in red and reaction in green. In Panel (a) all entries are shown, in Panel (b) only entries up to nickel projectiles.

for  $^4\text{He}$ ,  $^{12}\text{C}$  and  $^{56}\text{Fe}$  projectiles impinging on different targets are reported in Figures 5.2, 5.3, and 5.4, alongside predictions of one of the semi-empirical parametrisations (Kox-Shen model, see section 5.1.2) to guide the reader's eyes. Experimentally-measured cross-section data for composite targets (i.e. molecular targets, not made of one element only) were also included in the database. In Figure 5.5, data for different projectiles impinging on water targets are reported. Projectiles with high abundance contributions to the GCR spectrum (see Figure 2.7) were chosen.

---

## Database Structure

---

The database is available as a table with the following entrances:

- Projectile atomic number.
- Projectile mass number.



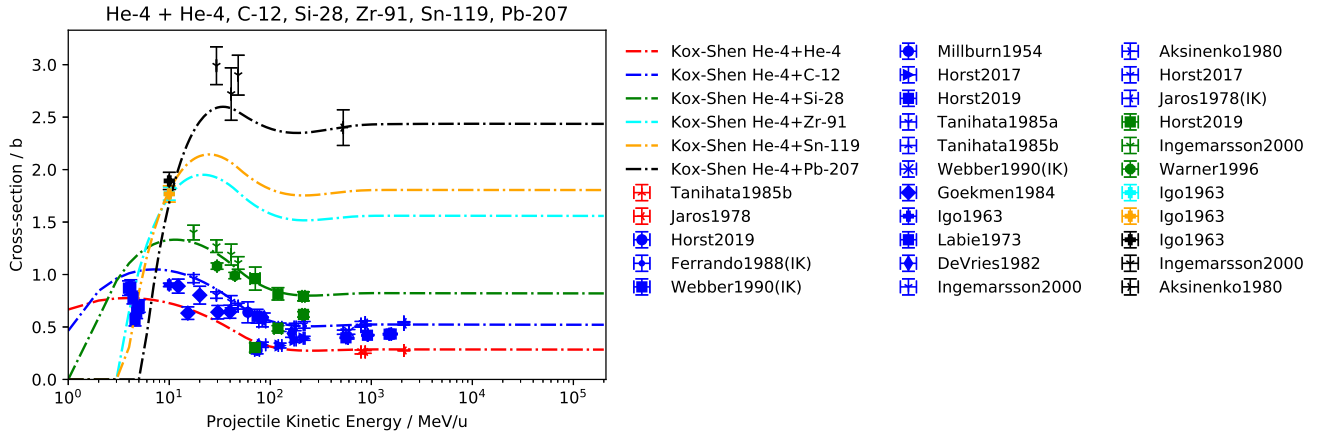


Figure 5.2: Data collection for  $^4\text{He}$  projectiles on different targets alongside the predictions of the Kox-Shen semi-empirical model (see section 5.1.2) to guide the reader's eyes. IK stands for Inverse Kinematic data (see Section 5.1.2). Different colours represent different targets. Both reaction and charge-changing cross-sections are plotted. The data are from references [156, 166, 167, 179, 180, 187, 188, 220, 229–232, 238, 251, 253].

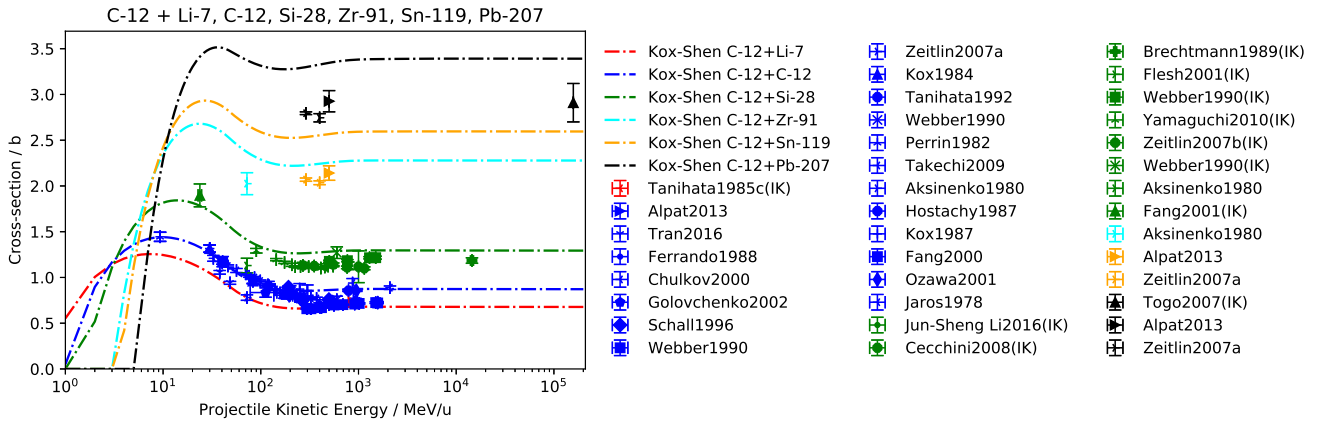


Figure 5.3: Same as Figure 5.2, but for  $^{12}\text{C}$  projectiles. The data are from references [161, 166, 168, 170, 181, 184, 186, 189, 203, 208, 209, 211, 218, 220, 223, 225, 226, 234–236, 238, 239, 242, 248, 249, 251].

- Target atomic number. For composite targets, the effective atomic number was computed as [259]:

$$Z_{\text{eff}} = \left( \sum_k f_k (Z_k)^{2.94} \right)^{\frac{1}{2.94}}, \quad (5.1)$$

where  $f_k$  is the fraction of the total number of electrons for the  $k$ -th element and  $Z_k$  is its atomic number.

- Target mass number. For compound materials, this is the sum of the single mass numbers of each element. If the target is just an element without specifications about the isotope (as it mostly is), it is reported with the standard atomic weight rounded to the closest integer (e.g. 64 for Cu).

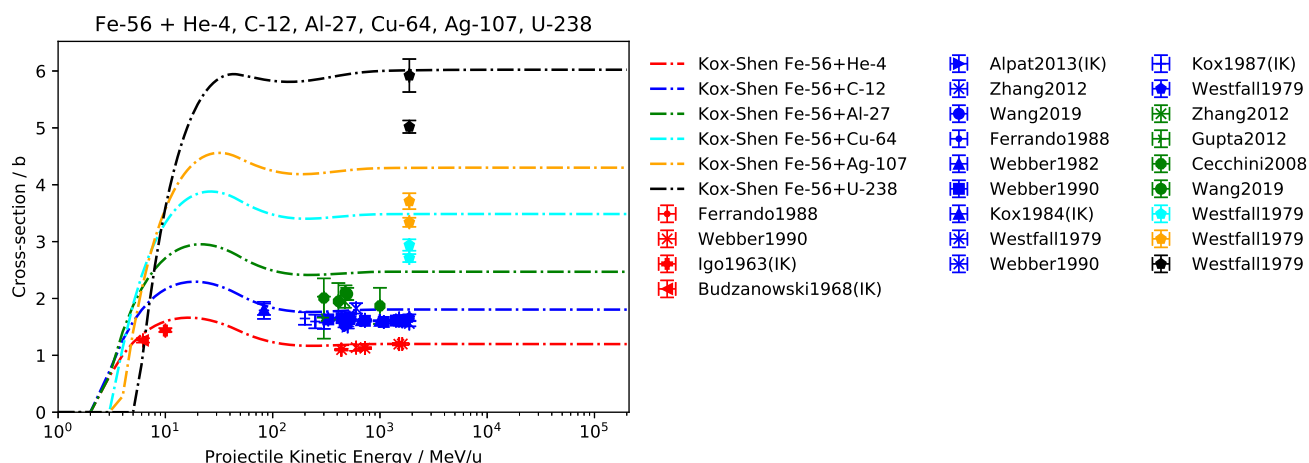


Figure 5.4: Same as Figure 5.2, but for  $^{56}\text{Fe}$  projectiles. For  $^{56}\text{Fe} + ^{64}\text{Cu}$ ,  $^{107}\text{Ar}$ ,  $^{238}\text{U}$ , both charge and mass-changing cross-section data were measured by Westfall *et al.* [174]. Therefore, two data points are reported for each system for the same energy. The data are from references [157, 161, 166, 170, 174, 178, 193, 196, 198, 220, 230, 235, 242].

- Target chemical formula.
- Target areal density ( $\text{g}/\text{cm}^2$ ). This is an important parameter to evaluate the quality of the data: the usage of thin targets provides better data as the projectile kinetic energy during the reaction is well defined and the probability of multiple reactions is low. However, the thinner the target is, the longer the beam time necessary to collect data with appropriate statistics is [105]. If more than one target was used, more than one value was reported.
- Projectile kinetic energy ( $\text{MeV}/u$ ). Many reaction cross-section data were measured in inverse kinematics (IK), which means that projectile and target have exchanged roles during the measurement. The passage from inverse to direct kinematics is straightforward since the reaction cross-section of e.g.  $220 \text{ MeV } u^{-1} ^{12}\text{C}$  (projectile) impinging on  $^{27}\text{Al}$  (target) is the same as the cross-section of  $220 \text{ MeV } u^{-1} ^{27}\text{Al}$  (projectile) on  $^{12}\text{C}$  (target). Having the same kinetic energy per nucleon means having the same velocity.
- Projectile kinetic energy lower uncertainty ( $\text{MeV}/u$ ).
- Projectile kinetic energy upper uncertainty ( $\text{MeV}/u$ ). These last two columns are almost always the same.
- Evaluation point of the projectile energy. The projectile energy reported in the publication can be either
  - the primary energy from the accelerator (e.g. identified as “out of the beam line” or “before the target”, depending on the authors’ definition), or
  - the energy at the centre of the target, especially for thick targets (e.g. identified as “in the centre of the target”).
- Cross-section type. The three main cross-section types are:
  - charge-changing (“cc”) - i.e. probability that the projectile nucleus loses at least one proton (this does not include neutron-removal reactions),

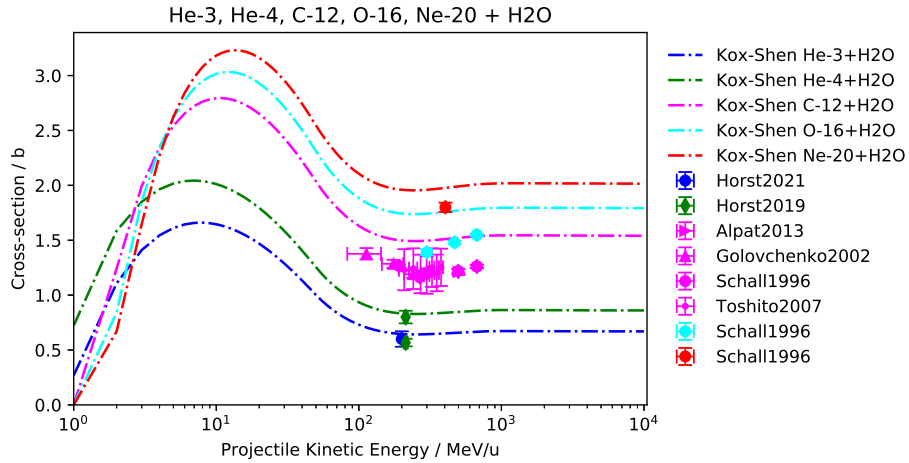


Figure 5.5: Data collections for  $^3\text{He}$ ,  $^4\text{He}$ ,  $^{12}\text{C}$ ,  $^{16}\text{O}$  and  $^{20}\text{Ne}$  projectiles on water alongside the predictions of the Kox-Shen semi-empirical model (see section 5.1.2) to guide the reader's eyes. Different colours represent different projectiles. Both reaction and charge-changing cross-sections are plotted. For  $^4\text{He} + \text{H}_2\text{O}$  both charge and mass-changing cross-section data were measured by Horst *et al.* [155, 156]. Mass-changing cross-sections were only measured by Horst *et al.* [156] for  $^3\text{He}$  and  $^4\text{He}$ . For all other projectiles, the data are charge-changing only. Therefore, the data points lie below the model predictions (see section 5.1.3). Data are from references [155, 156, 170, 211, 218].

- mass-changing (“mc”) - i.e. probability that the projectile loses at least one nucleon (this includes neutron-removal reaction channels), and
- reaction. It is to be noticed that it is more difficult to measure reaction/mass-changing cross-sections for heavy projectile nuclei. Therefore, the number of reaction cross-section data (green contributions in Figure 5.1) becomes lower with increasing projectile atomic number and mostly charge-changing cross-sections are available.

Since the definition of what the authors mean with a specific cross-section type depends on the publication, it is recommended to look into the specific work for a deeper understanding.

- Cross-section (mb): cross-section value reported in millibarn.
- Cross-section lower uncertainty (mb).
- Cross-section upper uncertainty (mb).
- Uncertainty type. This can be either:
  - both statistical and systematic, or
  - purely statistical. This is the case especially for older publications, as the reported uncertainties do not include systematic components due to e.g. instrument calibration. When using these data, it should be considered that the error bars are larger than they appear.
- First author of the publication.
- Year of the publication.

- DOI: unique Digital Object Identifier of the peer-reviewed publication.
- Experiment facility.
- Beamtime. If the month and the year of the experiment are reported in the publication, they are also reported in the database.
- Measurement method. Details about the detectors used to experimentally obtain the data have been added as well. It is recommended to refer to the publications for further details.
- Comments: other comments.
- Electromagnetic dissociation (EMD) cross-section (mb): they are only present in a few cases.
- EMD cross-section lower uncertainty (mb).
- EMD cross-section upper uncertainty (mb).

---

### 5.1.2 Parametrisations

---

Several semi-empirical parametrisations of reaction cross-sections were developed over the last forty years starting from the energy-dependent Bradt-Peters geometrical formula (Equation 2.17). The Kox [242], Shen [260], Kox-Shen [261], Tripathi [262, 263] with Horst optimisations for  $^4\text{He}$  projectiles [156], and Hybrid-Kurotama [264] parametrisations were re-implemented within this work with the aim of them being compared to the comprehensive data collection from the database. Details about the implementation are reported in the following sections. The Kox, Shen and Tripathi parametrisations are implemented in Geant4 [265], but none of them is set as default in any of the Geant4 physics lists. Nevertheless, they can be manually selected to be used. In the next Geant4 version the Kox and Shen parametrisations will be removed as they are obsolete. Hybrid-Kurotama is the default parametrisation used in PHITS (Kox-Shen and Tripathi are options). An empirically-modified version of Tripathi is implemented in FLUKA. The Horst optimisations for  $^4\text{He}$  were included in the last version of FLUKA [144]. The deterministic GSI in-house code SpaceTRiP [119] also makes use of Tripathi with Horst optimisations as default for total cross-sections. It is to be noted that EMD processes are not included in these parametrisations.

---

#### Kox Parametrisation

---

The phenomenological Kox parametrisation for reaction cross-sections was proposed in 1987 [242]:

$$\sigma_R = \pi R_{\text{int}}^2 \left( 1 - \frac{B}{E_{\text{cm}}} \right). \quad (5.2)$$

$B$  is the energy-independent Coulomb interaction barrier and  $R_{\text{int}}$  is the interaction radius, which has three components:

1.  $R_{\text{vol}}$ , which is similar to the Bradt-Peters interaction radius,
2.  $R_{\text{sur}}$  (“nuclear surface” contribution), which accounts for mass asymmetry (energy independent) and transparency, and
3. the neutron excess  $D$ , which in Ref. [242] is explained to be necessary only for projectile kinetic energies below  $200 \text{ MeV u}^{-1}$ .

$E_{\text{cm}}$  is the centre-of-mass energy of the system in MeV, which can be calculated as:

$$E_{\text{cm}} = E \frac{A_p A_T}{A_p + A_T}, \quad (5.3)$$

with  $E$  being the kinetic energy of the projectile in MeV  $\text{u}^{-1}$ . Equation 5.3 is not exact at high energies, but it is a good approximation because  $\frac{B}{E_{\text{cm}}} \xrightarrow{E \rightarrow \infty} 0$ .

In this work, the model was implemented as in Geant4, meaning as described in Ref. [242] with the following exceptions:

1. The neutron excess parameter  $D$  is applied to all kinetic energies, not only below 200 MeV  $\text{u}^{-1}$ .
2. The following functions have been used for the transparency parameter  $c$  instead of the values reported in Table III of Ref. [242]:

$$c = \left( -\frac{10}{1.5^5} + 2 \right) \left( \frac{x}{1.5} \right)^3 \quad \text{for } x < 1.5 \quad (5.4)$$

$$c = -\frac{10}{x^5} + 2 \quad \text{for } x \geq 1.5 \quad (5.5)$$

where  $x = \log_{10}(E)$ .

3. Equation 14 of Ref. [242] states that:

$$B = \frac{Z_T Z_p e^2}{r_C (A_T^{1/3} + A_p^{1/3})}. \quad (5.6)$$

Nevertheless, the correct expression for  $B$  is:

$$B = \frac{Z_T Z_p}{r_C (A_T^{1/3} + A_p^{1/3})}, \quad (5.7)$$

where  $r_C (= 1.3 \times 10^{-15} \text{ m})$  has to be inserted in femtometres.

4. As all the components of  $R$  ( $R_{\text{int}}$ ,  $R_{\text{vol}}$ ,  $R_{\text{sur}}$ ), also  $D$  should also be multiplied by  $r_0 (= 1.1 \times 10^{-15} \text{ m})$ . If  $r_0$  is always inserted in meters, the cross-section result is obtained in  $\text{m}^2$ .
5. A low-energy check was added, which automatically sets the cross-section to zero if  $E_{\text{cm}} \leq B$ .

---

### Shen Parametrisation

---

Since the Kox formula fails at reproducing the data for energies lower than 10 MeV  $\text{u}^{-1}$  and no values for  $c$  are given for  $E < 30 \text{ MeV u}^{-1}$  in Ref. [242], a new unified parametrisation based on the Kox formula was proposed by Shen *et al.* in 1989 [260]. The Shen cross-section formula is the same as Equation 5.2, but the  $B$  and  $R_{\text{int}}$  parameters are different. In particular,

$$B = 1.44 \frac{Z_T Z_p}{R_T + R_p + 3.2} - b \frac{R_T R_p}{R_T + R_p}, \quad (5.8)$$

where:

$$R_i = 1.12 A_i^{1/3} - 0.94 A_i^{-1/3} \quad i = (T, p) \quad (5.9)$$

and  $b = 1$ .  $i$  in Equation 5.9 can stand either for target ( $T$ ) or projectile ( $p$ ). Concerning  $R_{\text{int}}$ , the Shen model adds an energy-dependent term to it and changes the multiplication factor  $\alpha$  of the neutron excess term from 5 to 1. Nevertheless, it is pointed out in Ref. [260] that by using  $\alpha = 1$ , the cross-sections for heavy targets are underestimated. Also in this case,  $c$  from Equations 5.4 and 5.5 have been used, as well as the same low-energy check used for the Kox formula. The values of  $c$  given in Ref. [260] were not used because of the reasons pointed out in the following section.

---

### Kox-Shen Parametrisation

---

Recently [261], an updated version of the Shen parametrisation was proposed. In particular, it was pointed out that the transparency parameter  $c$  provided in Ref. [260] should not be used. It is not fully in agreement with what is reported in Ref. [242] (as it should be) and the energy scale of the  $c$  plot in Ref. [260] is inconsistent. Therefore, the following parametrisation was proposed:

$$c = \left( -\frac{10}{1.5^5} + 2 \right) \left( \frac{x}{1.38} \right)^3 + 0.0006 E \quad \text{for } E \leq 45 \text{ MeV u}^{-1} \quad (5.10)$$

$$c = 1.91 - 16 e^{-0.7274 E^{0.3493}} \cos(0.0849 E^{0.5904}) \quad \text{for } E > 45 \text{ MeV u}^{-1} \quad (5.11)$$

where  $E$  is the kinetic energy of the projectile in  $\text{MeV u}^{-1}$  and  $x = \log_{10}(E)$ . The expression valid for  $E > 45 \text{ MeV u}^{-1}$  had already been proposed in 1988 by Townsend and Wilson [266]. The expression for  $E \leq 45 \text{ MeV u}^{-1}$  is similar to the one developed for Geant4, but it has modifications that provide a smooth overlap with the Townsend and Wilson's part.

The other modification to the Shen parametrisation proposed in Ref. [261], is the use of  $\alpha = 5$  in the neutron-excess parameter, as in the Kox model. Therefore the name Kox-Shen model. Nevertheless, as explained in Ref. [260], the  $\alpha$  value that fits the experimental data best is 1. Therefore,  $\alpha = 1$  has been used in the implementation of this work.

---

### Tripathi Parametrisation

---

The Tripathi semi-empirical formula was first presented in 1996 [262]. Two publications followed in 1997 [267] and 1999 [263]. They respectively dealt with neutron projectiles and light systems, where “light systems” means that at least either projectile or target has mass number  $A \leq 4$ . The parametrisation for neutron projectiles [267] has not been included in the present work as neutron data are not part of the data collection. The other two parametrisations will be referred to as “Tripathi96” and “Tripathi99” in the following.

**Tripathi96 Parametrisation** The following form for the reaction cross-section was presented in Ref. [262]:

$$\sigma_R = \pi r_0^2 (A_p^{1/3} + A_T^{1/3} + \delta_E)^2 \left( 1 - \frac{B}{E_{\text{cm}}} \right) f, \quad (5.12)$$

where  $r_0 = 1.1 \text{ fm}$ ,  $B$  is the energy-dependent Coulomb barrier and  $f$  is a multiplication factor equal to 1 in all cases but for  $^1\text{H} + ^4\text{He}$  and  $^1\text{H} + ^{12}\text{C}$ , where it is supposed to be set to 27 and 3.5, respectively. Also in this case, Equation 5.3 is used for the computation of  $E_{\text{cm}}$ . In Geant4, the proper physical calculation for  $E_{\text{cm}}$  is implemented, while Equation 5.3 is used in PHITS.

The parameter  $\delta_E$  is defined as:

$$\delta_E = 1.85 S + 0.16 \frac{S}{E_{\text{cm}}^{1/3}} - C_E + \alpha \frac{(A_T - 2Z_T)Z_p}{A_T A_p}. \quad (5.13)$$

The last term is commonly called the neutron excess parameter and the multiplication factor is  $\alpha = 0.91$ .  $S$  is the mass asymmetry term and  $C_E$  is the parameter through which  $\delta_E$  accounts for the transparency and Pauli-blocking effects.  $C_E$  itself is energy-dependent and can be computed as:

$$C_E = D(1 + \exp(-E/T_1)) - 0.292 \exp(-E/792) \cos(0.229E^{0.453}), \quad (5.14)$$

where  $T_1 = 40$ ,  $E$  is the projectile kinetic energy in  $\text{MeV u}^{-1}$  and  $D$  is proportional to the density of the colliding system, scaled with respect to the density of the system  $^{12}\text{C} + ^{12}\text{C}$ :

$$D = 1.75 \frac{\rho_{A_p} + \rho_{A_T}}{\rho_{A_C} + \rho_{A_C}}. \quad (5.15)$$

More details can be found in Ref. [262]. Moreover, in Ref. [262] it is recommended to use:

- the single value  $D = 2.05$  for the proton - nucleus case
- the reduced value  $D/3$  for lithium nuclei
- the specific density-independent formula for the case of  $^4\text{He}$  projectiles, due to the small density compression:

$$D = 2.77 - 8.0 \times 10^{-3} A_T + 1.8 \times 10^{-5} A_T^2 - \frac{0.8}{1 + e^{\frac{250-E}{G}}}, \quad (5.16)$$

where  $G = 75$ . It is believed that there is a typo in the original publication [262] concerning the parentheses for  $D$ , since Equation 5.16 is consistent with the formula given for  $D$  in Ref. [263].

Tripathi96 has been implemented in the present work as described in Ref. [262], with a few modifications:

1. A different nuclear radius  $r_i$  has been used. The nuclear radius  $r_i$  is inside the Coulomb barrier parameter  $B$ . In Ref. [262] it is suggested to use:

$$r_i = 1.29 r_{\text{rms},i} \quad (5.17)$$

and to use data from Ref. [268] for  $r_{\text{rms},i}$ . This will be called “Wilson  $r_i$ ”. In particular, the  $r_{\text{rms},i}$  used for the present work is the arithmetic average of the data given in Ref. [268] for  $Z \leq 26$  and  $r_{\text{rms},i} = 0.84 A_i^{1/3} + 0.55$  for  $Z > 26$ . The formula for  $Z > 26$  is reported in Appendix A of Ref. [269]. Nevertheless, in Geant4 [147], the following formula is used to compute  $r_i$  of projectile and target nuclei:

$$r_i = \frac{1.29 \times 0.6 \times 1.36 \times 10^{-15} A_i^{1/3}}{r_0}. \quad (5.18)$$

In Figure 5.6, the radius computed as in Equation 5.18 is referred to as “G4  $r_i$ ”. It was observed that the Tripathi model is sensitive even to small changes of this parameter at low energies. It has been decided to use for  $r_i$  the same formula as implemented in Geant4 (Equation 5.18) after comparing all the low energy ( $\leq 10 \text{ MeV u}^{-1}$ ) cross-sections from the data collection with the results obtained either with Tripathi96 implemented with  $r_i$  from Equation 5.17 or Equation 5.18 (see Figure 5.6). The G4  $r_i$  does not fit the experimental data best for all systems. However, the decision of using it in the implementation comes from the following considerations. For the systems:  $^4\text{He} + ^{12}\text{C}$  (“Labie1973” dataset [180]),  $^4\text{He} + ^{27}\text{Al}$  (one data point),  $^4\text{He} + ^{56}\text{Fe}$  (two data points) and  $^4\text{He} + ^{237}\text{Np}$  (“Powers1966” dataset [250]), G4  $r_i$  fits the data best. For  $^4\text{He} + ^{181}\text{Ta}$  and  $^4\text{He} + ^{197}\text{Au}$ , the Wilson  $r_i$  applied to Tripathi96 fits the data best. For  $^{12}\text{C} + ^{12}\text{C}$ , both Wilson and G4  $r_i$  are compatible with the single data point. For the cases of  $^4\text{He} + ^{181}\text{Ta}$  and  $^4\text{He} + ^{197}\text{Au}$ , the measurements are only single data points, while for  $^4\text{He} + ^{237}\text{Np}$  there is a series of measurement points that systematically follow the cross-section increase in the Coulomb barrier energy region (see Figure 5.6). In PHITS, the Wilson radius is used.

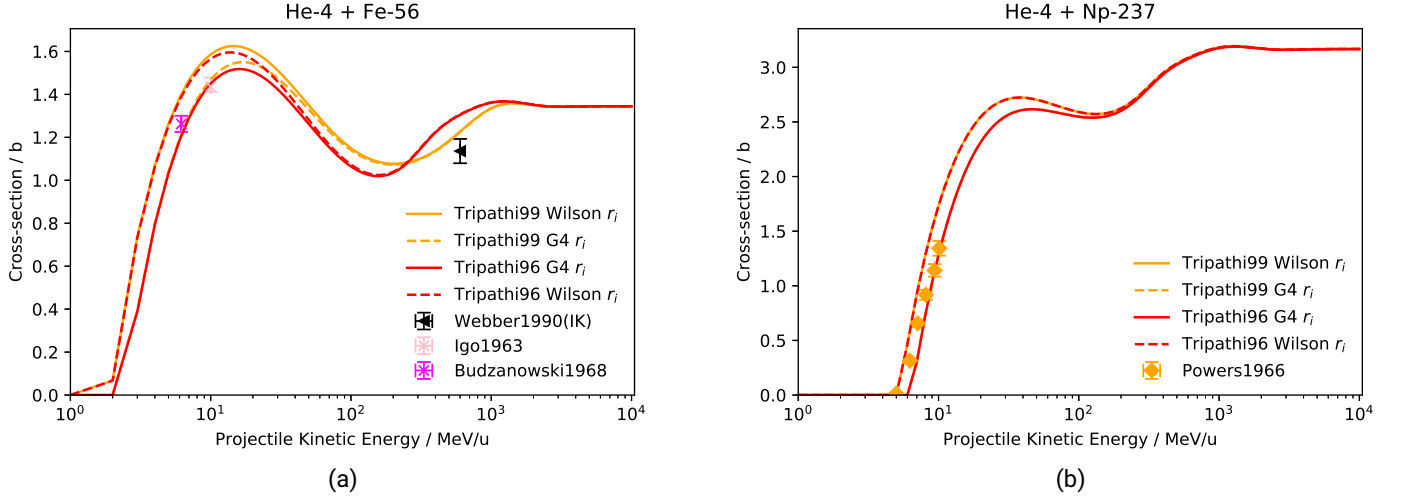


Figure 5.6: Dependence of Tripathi96 and Tripathi99 semi-empirical cross-section formulae on the nuclear radius for  $^4\text{He} + ^{56}\text{Fe}$  and  $^4\text{He} + ^{237}\text{Np}$ . Solid lines have been chosen for the version of the models that has been implemented within the present work. Data in Panel (a) are from references [178, 220, 230], in Panel (b) from reference [250].

2. Horst *et al.* optimisations [156] to Equation 5.16 are used to calculate  $D$  for  $^4\text{He} +$  targets from C to Si. Recently some charge- and mass-changing cross-section measurements with  $^4\text{He}$  were performed at therapeutic energies (70 - 220 MeV  $\text{u}^{-1}$ ) on  $^{12}\text{C}$ ,  $^{16}\text{O}$  and  $^{28}\text{Si}$  targets [156, 167]. Based on these data and the data by Ingemarsson *et al.* [179], an optimisation of Tripathi96 for the case of  $^4\text{He}$  projectiles on targets with masses between C and Si has been proposed being:

$$D = 2.2 - 8.0 \times 10^{-3} A_T + 1.8 \times 10^{-5} A_T^2 - \frac{0.3}{1 + e^{\frac{120-E}{G}}}. \quad (5.19)$$

where  $G = 50$ . These changes led to considerable improvements of  $^4\text{He}$  dose calculations [144, 270].

3. Low-energy check: once cross-sections are computed for all energies, any negative values are set to null. This procedure is implemented in Geant4 as well.

In Tripathi96 calculations performed for the present work, the lightest ion is always considered to be the projectile. This changes the choice of the  $D$  parameter to be used and the neutron excess parameter (last term of Equation 5.13). The same is done in Geant4 and PHITS.

**Tripathi99 Parametrisation** The Tripathi99 formula was implemented as presented in Ref. [263]:

$$\sigma_R = \pi r_0^2 (A_p^{1/3} + A_T^{1/3} + \delta_E)^2 \left( 1 - R_c \frac{B}{E_{\text{cm}}} \right) X_m. \quad (5.20)$$

The additional terms to Eqrespect 5.12 are the system-dependent Coulomb multiplier  $R_c$ , which allows one to keep the same formalism for light, medium and heavy nuclei, and the optical model multiplier  $X_m$ :

$$X_m = 1 - X_1 e^{-\frac{E}{X_1 S_L}}, \quad (5.21)$$



where  $X_1 = 5.2$  for the  $n+{}^4\text{He}$  system and

$$X_1 = 2.83 - 3.1 \times 10^{-2} A_T + 1.7 \times 10^{-4} A_T^2 \quad (5.22)$$

in all other cases, and

$$S_L = 1.2 + 1.6(1 - e^{-\frac{E}{15}}). \quad (5.23)$$

Differently from Tripathi96,  $T_1$  and  $G$  are system dependent in Tripathi99. The nuclear radius used in this case is the Wilson  $r_i$  (Equation 5.17), as recommended in Ref. [263]. Also in Geant4 and PHITS the Wilson  $r_i$  is used for Tripathi99. To be noticed is that the Geant4 radius would fit the experimental data better for all systems for which low-energy data were measured (see section 5.1.2 and Figure 5.6). From Ref. [263], the lightest particle is to be used as the projectile in the formulation. This is how the model is implemented in Geant4, PHITS and the present work. The model has been implemented as in Ref. [263], with a few modifications:

1. The centre-of-mass kinetic energy of the system  $E_{\text{cm}}$  is in MeV. We believe that the unit of measurement given for it in Ref. [263] (AMeV) is a typographical error.
2. In the Tripathi subroutine of PHITS,  $X_m = 1$  is used for every projectile ion but neutrons. Using  $X_m = 1$  instead of  $X_m$  from Equation 5.21 gives in fact, a better agreement with the original curves presented in Ref. [263] (the difference is appreciable for all figures from 3 to 20 of Ref. [263] but 4, 5 and 18). In addition, the curves were compared with the measured cross-sections from the database and in the majority of the cases, the use of  $X_m = 1$  gives better agreement with the data. Figure 5.7 shows how the use of  $X_m = 1$  instead of  $X_m$  from Equation 5.21, improves the fit of the model to the data and also to the curve reported in Ref. [263].

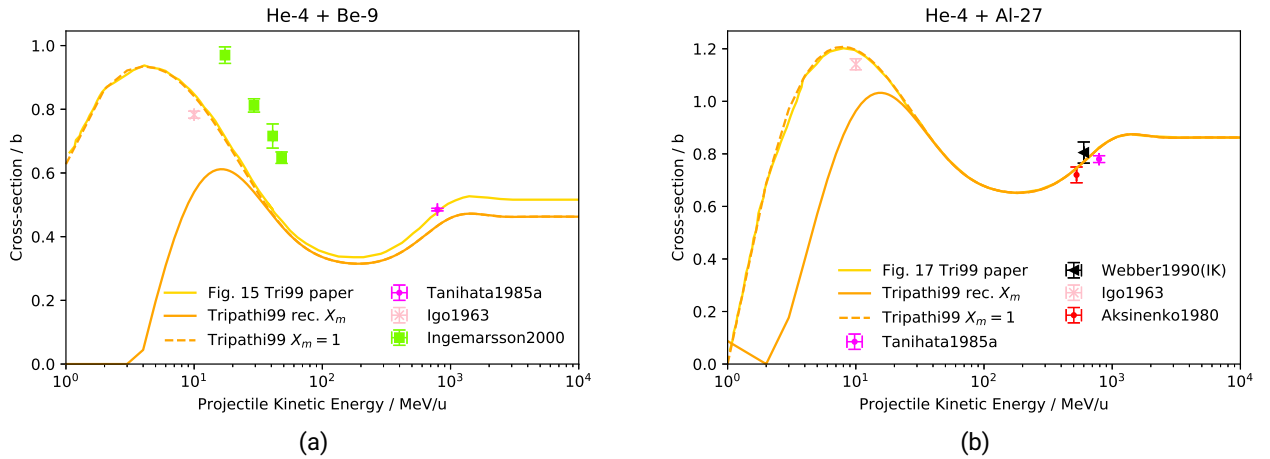


Figure 5.7: Comparison between the results of Tripathi99 for the systems  ${}^4\text{He}+{}^9\text{Be}$  and  ${}^4\text{He}+{}^{27}\text{Al}$ , obtained by using  $X_m = 1$  or  $X_m$  from Equation 5.21, which is recommended in Ref. [263] (“rec.  $X_m$ ”), and the curves presented in Ref. [263]. The experimental data from the database have been plotted as well. For the case of  $X_m$  from Equation 5.21, the low-energy check implemented in Geant4 has been used: below  $6 \text{ MeV u}^{-1}$ , if the first derivative of the cross-section as a function of the energy is negative (i.e. values becoming smaller with increasing energy) the cross-section values are set to zero. IK stands for Inverse Kinematic data. Data in Panel (a) are from references [179, 187, 230], in Panel (b) from references [187, 220, 230, 238].

Table 5.1: System-dependent values for  $T_1$  and  $D$  used in the Tripathi subroutine of PHITS and in the present work.

Projectile + Target	$T_1$	$D$
$^1\text{H} + ^3\text{He}$	58	1.70
$^1\text{H} + ^4\text{He}$	40	2.05
$^1\text{H} + ^6\text{Li}$	40	2.05
$^1\text{H} + ^7\text{Li}$	37	2.15
$^1\text{H} + (A_T > 7)$	40	2.05
$^2\text{H} + ^4\text{He}$	23	$1.65 + 0.22 / (1 + \exp \frac{500-E}{200})$

3. In the Tripathi subroutine of PHITS, optimised  $T_1$  and  $G$  parameters for a broader set of systems are specified. In particular, specific values are used for the cases of  $^1\text{H} + ^3\text{He}$ ,  $^4\text{He}$ ,  $^6\text{Li}$ ,  $^7\text{Li}$ ,  $^1\text{H} +$  targets with  $A_T > 7$  and  $^2\text{H} + ^4\text{He}$ . The values are presented in table 5.1. For  $^1\text{H} +$  other targets, the values used are the same as presented in the original work for  $^1\text{H} +$  any target. These additional optimisations have been implemented in the calculation of Tripathi99 for the present work.

In Geant4, in addition to the check for negative cross-section values, which is recommended in Ref. [263], an extra check was added for Tripathi99. At low energies (below  $6 \text{ MeV u}^{-1}$ ), if the first derivative of the cross-section as a function of the energy is negative (i.e. cross-section values becoming smaller with increasing energy) the cross-section values are set to null. This check is nevertheless not necessary if  $X_m = 1$  is used. For this reason, it has not been implemented within the current work.

### Hybrid-Kurotama Parametrisation

A semi-empirical parametrisation model called “Hybrid-Kurotama” was proposed in 2014 within Ref.[264]. It is based on the Black Sphere (“Kurotama” in Japanese) cross-section formula, extended to low energies by smoothly connecting it to the Tripathi parametrisation:

$$\sigma_R(E) = f_{\text{cut1}} \pi (a_p(E) + a_T(E))^2 + f_{\text{cut2}}(E) \sigma_{\text{Trip}}(E) \frac{\pi (a_p(E_{\text{cut}}) + a_T(E_{\text{cut}}))^2}{\sigma_{\text{Trip}}(E_{\text{cut}})}. \quad (5.24)$$

$a_p$  is the black-sphere radius of the projectile,  $a_T$  is the black-sphere radius of the target, and  $E$  is the projectile kinetic energy in  $\text{MeV u}^{-1}$ .  $E_{\text{cut}} = 400 \text{ MeV u}^{-1}$  in the case  $^4\text{He}$  is either the projectile or the target, otherwise  $E_{\text{cut}} = 115 \text{ MeV u}^{-1}$ .

$$f_{\text{cut1}} = \frac{1}{1 + e^{\frac{-E + E_{\text{cut}}}{d}}} \quad (5.25)$$

$$f_{\text{cut2}} = \frac{1}{1 + e^{\frac{E - E_{\text{cut}}}{d}}} \quad (5.26)$$

with  $d = 1 \text{ MeV u}^{-1}$ . It has been noticed that  $f_{\text{cut1}}$  and  $f_{\text{cut2}}$  were inverted in Ref.[264]. The values of the Tripathi parametrisation are renormalized so that they match the “Kurotama” value at  $E_{\text{cut}}$ . The Hybrid-Kurotama parametrisation has been implemented within this work in the same way it is in PHITS, i.e. using Tripathi99 (section 5.1.2) for  $\sigma_{\text{Trip}}$  in the case of “light” nucleus-nucleus systems ( $A \leq 4$  for at least either the projectile or the target) and Tripathi96 otherwise (section 5.1.2).

### 5.1.3 Mass-Changing Cross-Sections as Proxy of Nuclear Reaction Cross-Sections

Experimental cross-sections are often only estimates of the total reaction cross-sections. Since most nuclear fragmentation channels lead to loss of at least one proton, charge-changing cross-sections  $\sigma_{cc}$  are a good approximation of reaction cross-sections. However, the contribution of pure neutron-removal reactions (for example fragmentation of  $^{12}\text{C}$  into  $^{11}\text{C}$  or  $^{10}\text{C}$ ) is only taken into account in the mass-changing cross-section  $\sigma_{mc}$ . With the aim of studying for what colliding systems  $\sigma_{cc}$  can be used to validate total reaction cross-section models and for what systems  $\sigma_{mc}$  are required, the ratio  $\sigma_{cc}/\sigma_R$  was computed for a variety of colliding systems at  $1 \text{ GeV} \cdot \text{u}^{-1}$  (see Figure 5.8).  $\sigma_R$  was calculated with the Kox-Shen model (see Section 5.1.2), and the neutron-removal cross-section ( $\sigma_R - \sigma_{cc}$ ) was obtained from the parametrisation by Mei [79] as implemented in the program LISE++ [150]. From Figure 5.8, significant differences between

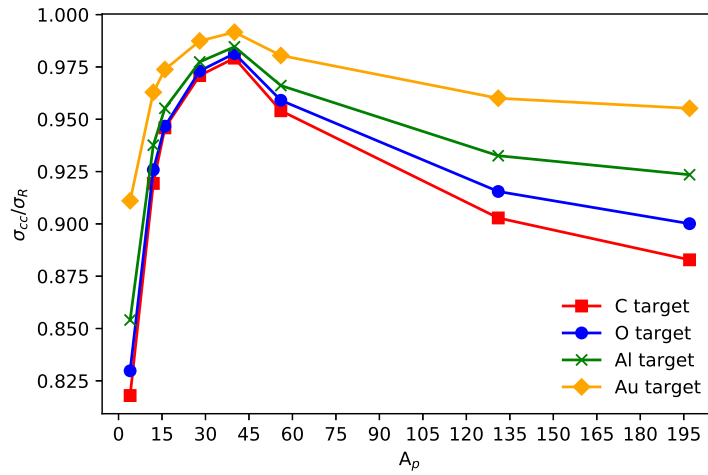


Figure 5.8: Ratio of charge-changing to total reaction cross-section  $\sigma_{cc}/\sigma_R$  as a function of the projectile mass number, computed for projectile kinetic energy  $1 \text{ GeV} \cdot \text{u}^{-1}$  and for different target materials. The total reaction cross-sections were calculated using the Kox-Shen model [261] and the neutron-removal cross-sections using the parametrisation by Mei *et al.* [79].

$\sigma_{cc}$  and  $\sigma_R$  can be observed for very low and very high- $A$  projectiles. The reason for it in the case of low  $A_p$  is that the number of possible fragmentation channels is limited and therefore, single neutron-removal has a high relative probability. On the other hand, for nuclei heavier than  $^{40}\text{Ca}$ , the higher the  $A_p$  is, the higher the nucleus neutron excess is. Therefore, also for very high- $A$  projectiles, neutron-removal reactions are probable. It can also be observed in Figure 5.8, that the difference between  $\sigma_{cc}$  and  $\sigma_R$  is more important for lighter targets. For them, peripheral collisions, which are the main cause for the removal of single nucleons, are more probable. These calculations are only an estimation of the real cross-section ratio, but measured data suggest that the ratio  $\sigma_{cc}/\sigma_R$  is even lower than expected, meaning that  $\sigma_{cc}$  and  $\sigma_R$  are more different than estimated in Figure 5.8. In Ref. [192], for instance, both mass and charge-changing cross-sections for the system  $^{20}\text{Ne} + ^{12}\text{C}$  at  $950 \text{ MeV} \cdot \text{u}^{-1}$  are reported and their ratio is 0.91, while it is expected to lay between 0.95 and 0.97.

In conclusion, since charge-changing cross-sections can have large deviations from reaction cross-sections, they were not used for the comparison of experimental data with parametrisations.

---

### 5.1.4 Comparison Between Data and Parametrisations

---

The primary systems of interest to radiation protection in space are:

$${}^4\text{He}, {}^{12}\text{C}, {}^{16}\text{O}, {}^{20}\text{Ne}, {}^{24}\text{Mg}, {}^{28}\text{Si}, {}^{56}\text{Fe} + {}^1\text{H}, {}^7\text{Li}, {}^{12}\text{C}, {}^{16}\text{O}, {}^{27}\text{Al}, {}^{28}\text{Si}. \quad (5.27)$$

The projectiles have been chosen because of their contribution to the GCR spectrum (see Section 2.3.2). Concerning the targets,  ${}^1\text{H}$  and  ${}^7\text{Li}$  was chosen because of its importance in innovative shielding materials for passive shielding in space (see Section 3.1.2),  ${}^1\text{H}$ ,  ${}^{12}\text{C}$  and  ${}^{16}\text{O}$  because they are among the main components of the human body.  ${}^{27}\text{Al}$  is the most important structural material spacecrafts are made of.  ${}^{28}\text{Si}$  is the main component of electronic devices and planetary regoliths.

${}^1\text{H}$  projectiles are not included in Equation (5.27) because the corresponding cross-section data were not included in the databases since  ${}^1\text{H}$  projectiles do not fragment. Therefore, in this study,  ${}^1\text{H}$  target data are not included since inverse kinematic data could not be plotted alongside them.

The plots shown in this Section can also be directly generated on the web application developed as part of the work (see section 5.3). In the past, the parametrisations presented in this work were often compared only to a limited data set [271, 272].

Inverse kinematics data are also reported in the plots. For example, for the case of  ${}^4\text{He} + {}^{56}\text{Fe}$  system, both reaction cross-section data measured using  ${}^4\text{He}$  projectiles and  ${}^{12}\text{C}$  targets and  ${}^{56}\text{Fe}$  on  ${}^4\text{He}$  were used. For this reason and since the reimplementation of each model uses the lightest nucleus as projectile, some plots are not reported because they would be identical to others. E.g.  ${}^{28}\text{Si} + {}^{12}\text{C}$  would be identical to  ${}^{12}\text{C} + {}^{28}\text{Si}$ .

---

## ${}^4\text{He}$ Results

---

In Figures 5.9 and 5.10, total reaction cross-section data of  ${}^4\text{He}$  projectiles impinging on the different targets listed in Equation 5.27 are extracted from the database and plotted alongside the predictions of the parametrisations presented in Section 5.1.2. The only exception is  ${}^1\text{H}$  targets because of the reasons explained above.

Some datasets are not compatible with each other. The Labie1973 data are probably not optimal for comparison since they do not include compound elastic scattering contributions, which have a resonance in this energy region. In addition, the fluctuations of the Gökmen1984 dataset are non-physical, and the data is not compatible with the Ingemarsson2000 dataset. Since Ingemarsson's data are more recent, they are likely to be more reliable. Since the single Igo1963 data point is old and lower than Ingemarsson2000, it is believed to underestimate the real cross-section value. The same considerations apply to the Warner1996 dataset (see  ${}^4\text{He} + {}^{28}\text{Si}$ ). The Horst2019, Horst2017 and DeVries1982 data are compatible with each other within error bars. It is to be noted that the Aksinenko1980 data (see  ${}^4\text{He} + {}^{27}\text{Al}$ ) are also believed to underestimate the real cross-section values. For all the targets but lithium, enough data points are available to check if the models fit the data well for low, mid and high energies.

All the models seem to be in reasonable agreement with the data points. Nevertheless, Tripathi99 and, consequently, Hybrid-Kurotama show a tendency to underestimate the data at low and intermediate energies. The only datasets that are well fitted by Hybrid-Kurotama at low energies are, indeed, the unreliable Igo1963 and Gökmen1984. The model that seems to fit the data best is Tripathi96, thanks to the optimisations recently proposed in Ref. [156]. Kox, Shen and Kox-Shen fit the data best at high energies (see  ${}^4\text{He} + {}^{12}\text{C}$ ).

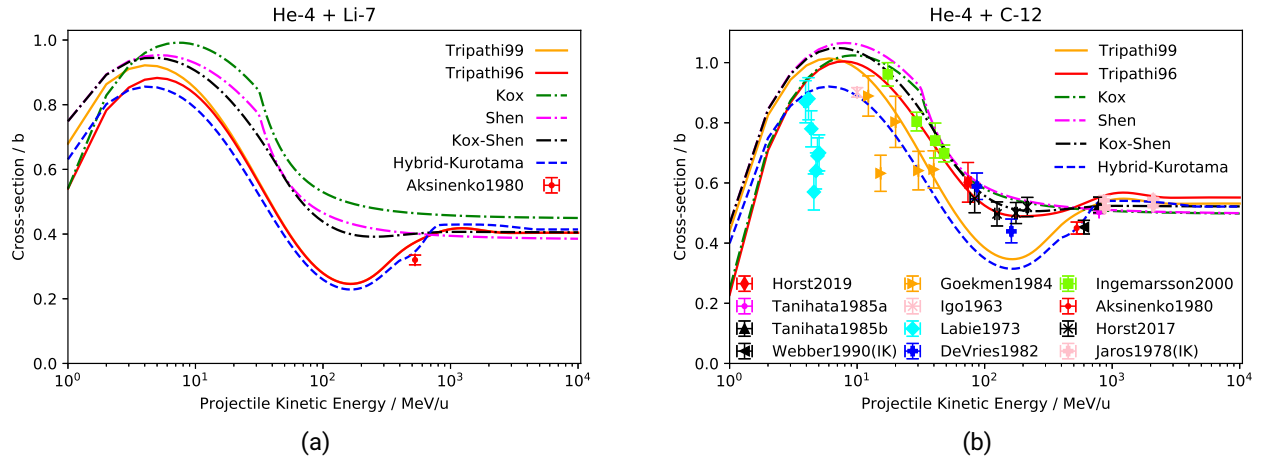


Figure 5.9: Comparison between parametrisation results and cross-section data for the following systems:  ${}^4\text{He} + {}^7\text{Li}$ ,  ${}^{12}\text{C}$ . IK stands for Inverse Kinematic data. To be noted that Tripathi96 is not the original model [262], but optimisations from Horst *et al.* [156] for  ${}^4\text{He}$  projectile are included. Data in Panel (a) are from reference [238], in Panel (b) from references [156, 167, 179, 180, 187, 188, 220, 229–231, 238, 251]. Error bar types of the Webber1990 and Igo1963 datasets are not specified to be only statistical or systematic as well. For Labie1973 and DeVries1982 they are only statistical. The rest are both statistical and systematic.

## **${}^{12}\text{C}$ Results**

Figures 5.11 and 5.12 report measured cross-section values extracted from the database for  ${}^{12}\text{C}$  projectiles on the targets of Equation 5.27 (but  ${}^1\text{H}$ ), alongside the parametrisation predictions. Starting from the  ${}^{12}\text{C} + {}^7\text{Li}$  system, the parametrisation fitting the single data point best is Hybrid-Kurotama.

From Figures 5.9 and 5.11, it can be noticed that the data points for the cases of  ${}^4\text{He}$  and  ${}^{12}\text{C}$  projectiles on  ${}^{12}\text{C}$  targets are many more than for most other systems. This is probably due to the importance of these two systems for heavy-ion therapy. This is an example of how the field of radiation protection in space can benefit from the research done for heavy-ion therapy [273]. Concerning the  ${}^{12}\text{C} + {}^{12}\text{C}$  system, the only data point that looks incompatible with the others in the low-energy range ( $\sim 70 \text{ MeV u}^{-1}$ ) is Aksinenko1980. It is smaller than the data from Takechi2009, Kox1987 and Hostachy1987. Since it is the oldest data point in this energy range, it is reasonable to believe that the results of Ref. [238] are not reliable. Therefore, it is not surprising that none of the models fit the Aksinenko1980 data point for the  ${}^{12}\text{C} + {}^{28}\text{Si}$  system as well. Coming to the mid-energy range ( $\sim 250 \text{ MeV u}^{-1}$ ), the Kox1987 data points are larger than both Takechi2009 and Hostachy1987 data. Therefore, it is believed that in this energy region the Kox1987 dataset is the most precise. For all the four systems, enough data points are available to check if the models fit the data well for all energy ranges.

All the models seem to be in reasonable agreement with the data. Nevertheless, Kox, Shen and Kox-Shen cannot reproduce the oscillation in the data (dip in the mid-energy region), which is parametrised by the cosine term in  $C_E$  in the Tripathi model, and, consequently, in the Hybrid-Kurotama model. Kox, Shen and Kox-Shen seem to fit the high-energy data best (see  ${}^{12}\text{C} + {}^{12}\text{C}$  and  ${}^{12}\text{C} + {}^{16}\text{O}$ ).

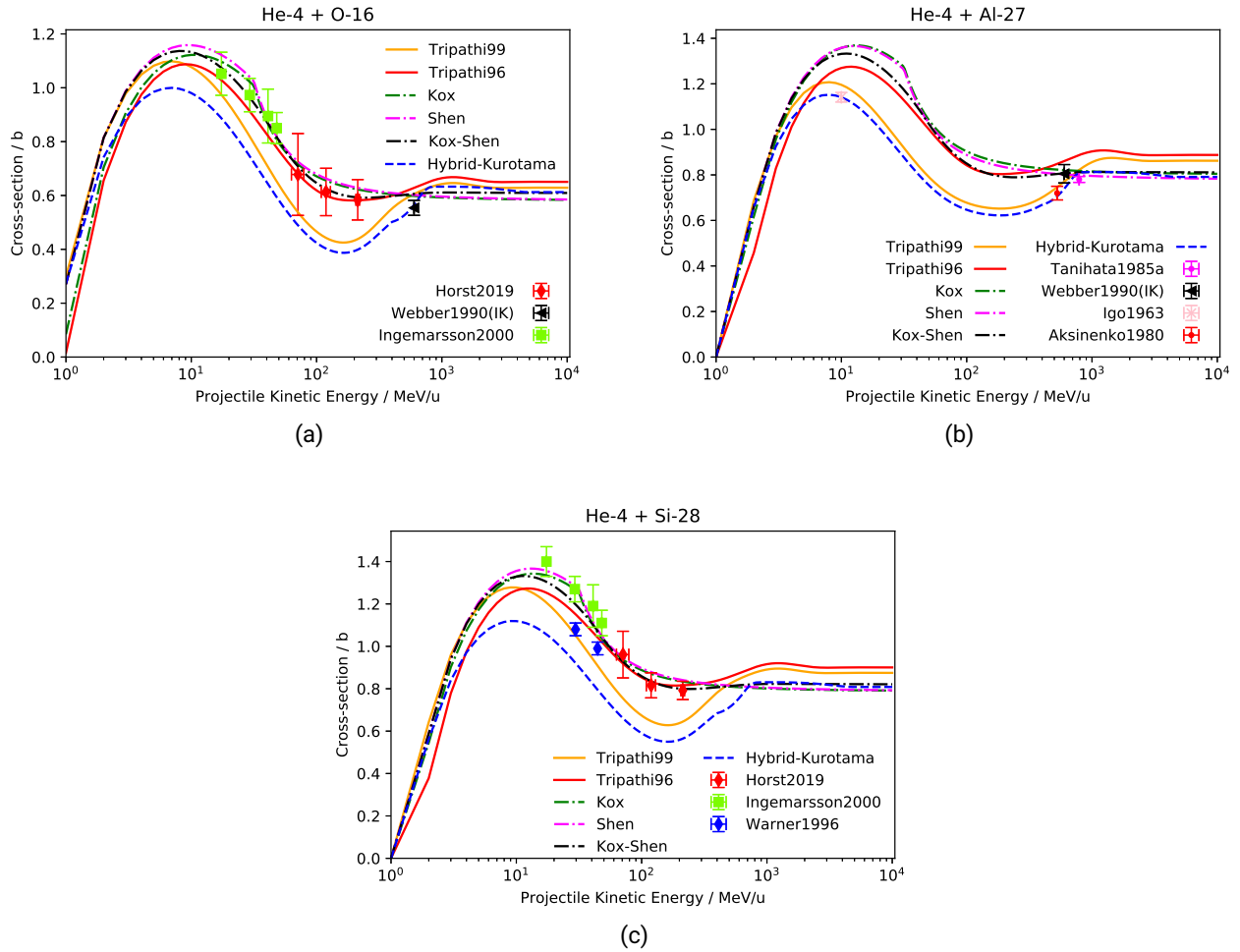


Figure 5.10: Comparison between parametrisation results and cross-section data for the following systems:  $^4\text{He} + ^{16}\text{O}$ ,  $^{27}\text{Al}$ ,  $^{28}\text{Si}$ . IK stands for Inverse Kinematic data. To be noted that Tripathi96 is not the original model [262], but optimisations from Horst *et al.* [156] for  $^4\text{He}$  projectile are included. Data in Panel (a) from references [156, 179, 220], in Panel (b) from references [187, 220, 230, 238], in Panel (c) from references [156, 179, 253]. Error bar types of the Webber1990 and Igo1963 datasets are not specified to be only statistical or systematic as well. The rest are both statistical and systematic.

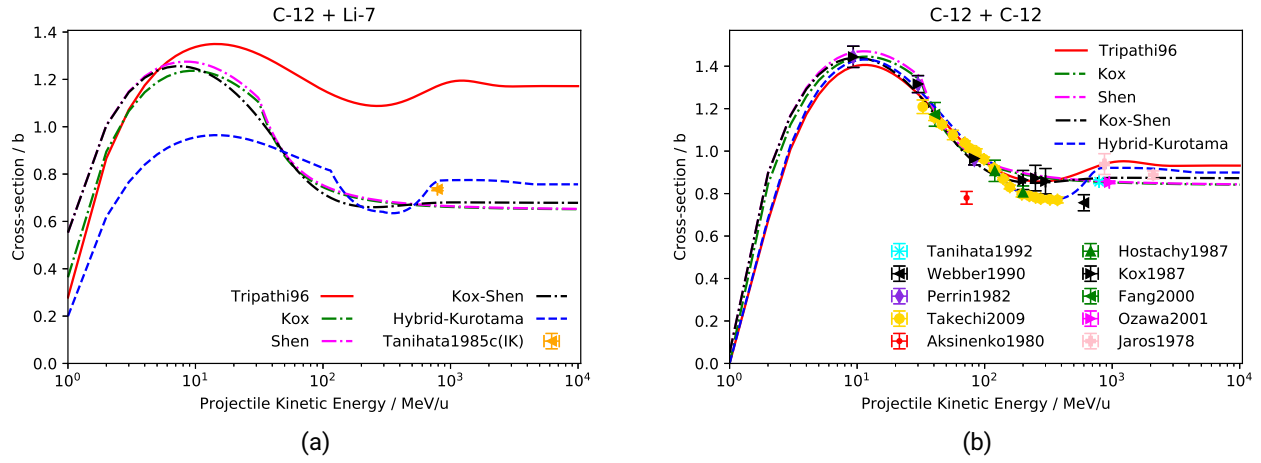


Figure 5.11: Comparison between parametrisation results and cross-section data for the following systems:  $^{12}\text{C} + ^7\text{Li}$ ,  $^{12}\text{C}$ . IK stands for Inverse Kinematic data. Data in Panel (a) are from references [189], in Panel (b) from references [186, 220, 234, 236, 238, 239, 242, 248, 249, 251]. Error bar types of the Webber1990 and Takechi2009 datasets are not specified to be only statistical or systematic too. Hostachy1987 error bars are only statistical. The rest are both statistical and systematic.

## **$^{16}\text{O}$ Results**

From Figure 5.13, it is clear that data are missing for  $^{16}\text{O}$  projectiles impinging on targets of interest for radiation protection in space. There is no data either for  $^7\text{Li}$ ,  $^{16}\text{O}$  or  $^{28}\text{Si}$  targets. There is only one data point for  $^{27}\text{Al}$ . There are not enough statistics to compare the model predictions to the data.

To be noted that  $^{16}\text{O} + ^{12}\text{C}$  is not reported since it would be the same plot as  $^{12}\text{C} + ^{16}\text{O}$ . As specified in Section 5.1.5, in every model the lightest nucleus is used as the projectile. In addition, since inverse kinematic data is included, both figures ( $^{12}\text{C} + ^{16}\text{O}$  and  $^{16}\text{O} + ^{12}\text{C}$ ) would show the same data as well.

## **$^{20}\text{Ne}$ Results**

In Figure 5.14, data for  $^{20}\text{Ne}$  projectiles extracted from the database are shown. Concerning  $^{20}\text{Ne} + ^{12}\text{C}$ , there are also very-low energy data, corresponding to the Coulomb barrier region. Also in this case, the Aksinenko1980 data point is smaller than the data points from the other datasets. At mid energies, three different measurements were performed around  $30 \text{ MeV u}^{-1}$ . They are compatible with each other within error bars. All the models seem to reproduce the data reasonably well, even if all of them predict lower values than the Shapira1982 data points in the Coulomb barrier. The data are, nevertheless, pretty old and characterised by large error bars.

For the case of  $^{20}\text{Ne} + ^{27}\text{Al}$ , there are not enough statistics to compare the model predictions to the data since all data were collected within the same measurement campaign. No experimental data have been measured for  $^{20}\text{Ne} + ^7\text{Li}$ ,  $^{16}\text{O}$  or  $^{28}\text{Si}$ .

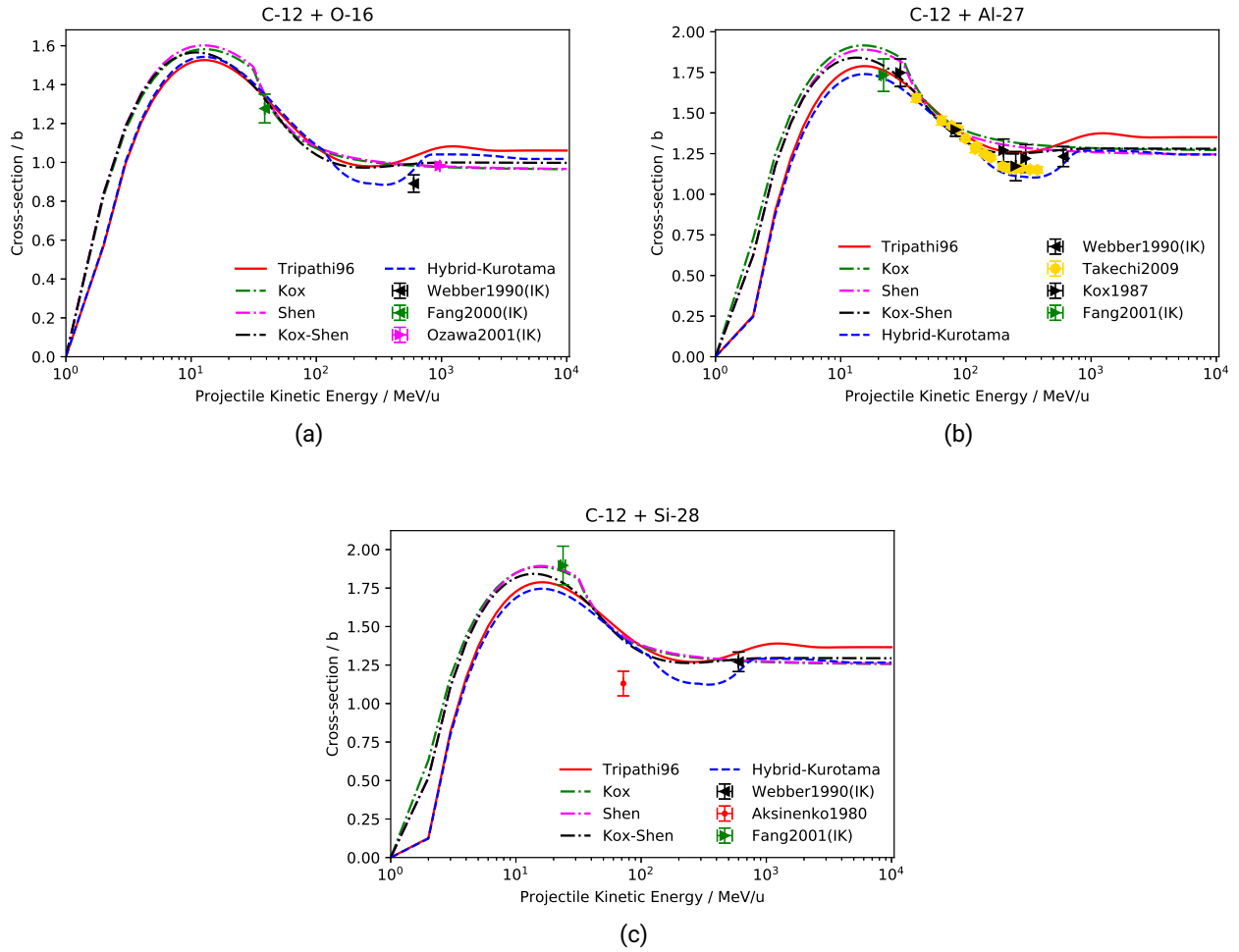


Figure 5.12: Comparison between parametrisation results and cross-section data for the following systems:  $^{12}\text{C} + ^{16}\text{O}$ ,  $^{12}\text{C} + ^{27}\text{Al}$ ,  $^{12}\text{C} + ^{28}\text{Si}$ . IK stands for Inverse Kinematic data. Data in Panel (a) from references [220, 248, 249], in Panel (b) from references [177, 220, 236, 242], in Panel (c) from references [177, 220, 238]. Error bar types of the Webber1990 and Takechi2009 datasets are not specified to be only statistical or systematic too. The rest are both statistical and systematic.



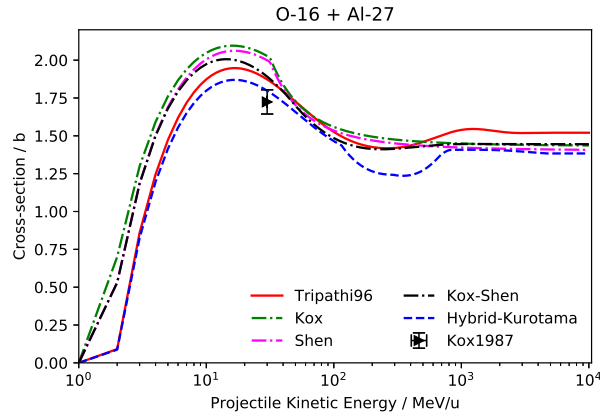


Figure 5.13: Comparison between parametrisation results and cross-section data for the following system:  $^{16}\text{O} + ^{27}\text{Al}$ . The data point is from reference [242]. Uncertainties are both statistical and systematic.

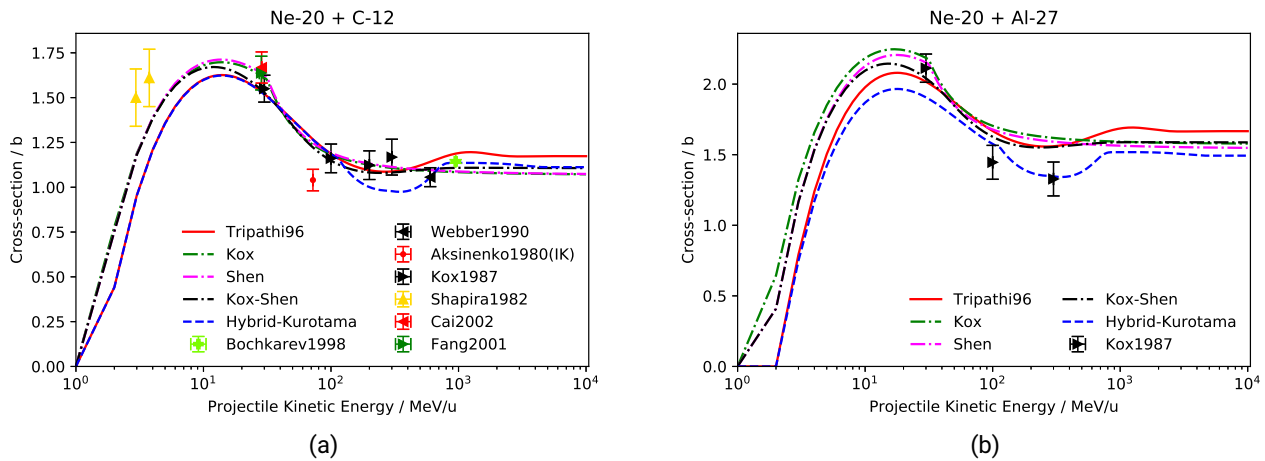


Figure 5.14: Comparison between parametrisation results and cross-section data for the following systems:  $^{20}\text{Ne} + ^{12}\text{C}$ ,  $^{27}\text{Al}$ . IK stands for Inverse Kinematic data. Data in Panel (a) are from references [175–177, 192, 220, 238, 242], in Panel (b) from reference [242]. Bochkarev1998 error bars are only statistical, while Webber1990 error bar type is not specified. The rest are both statistical and systematic.

## $^{24}\text{Mg}$ Results

Also for the case of  $^{24}\text{Mg}$ , very few experimental data have been measured. Only for the system  $^{24}\text{Mg} + ^{12}\text{C}$ , two data points were measured (see Figure 5.15). There are not enough statistics to compare the model predictions to the data.

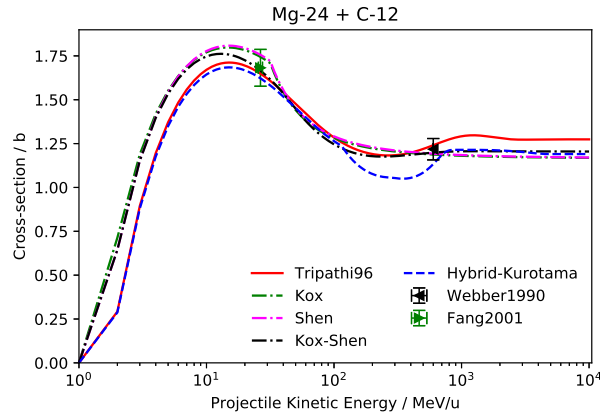


Figure 5.15: Comparison between parametrisation results and cross-section data for the following system:  $^{24}\text{Mg} + ^{12}\text{C}$ . Data are from references [177, 220]. The Webber1990 error bar type is not specified and Fang2001 are both statistical and systematic.

## $^{28}\text{Si}$ Results

No experimental data have been measured for  $^{28}\text{Si} + ^{27}\text{Al}$  or  $^{28}\text{Si} + ^{28}\text{Si}$ .  $^{28}\text{Si} + ^{12}\text{C}$  would be the same as Panel (c) of Figure 5.12, and it has already been pointed out that no data are there for the system  $^{16}\text{O} + ^{28}\text{Si}$ , and therefore for  $^{28}\text{Si} + ^{16}\text{O}$ . The only data points measured are for the system  $^{28}\text{Si} + ^7\text{Li}$  (see Figure 5.16). All parametrisations but Tripathi96 and Hybrid-Kurotama fit the data well.

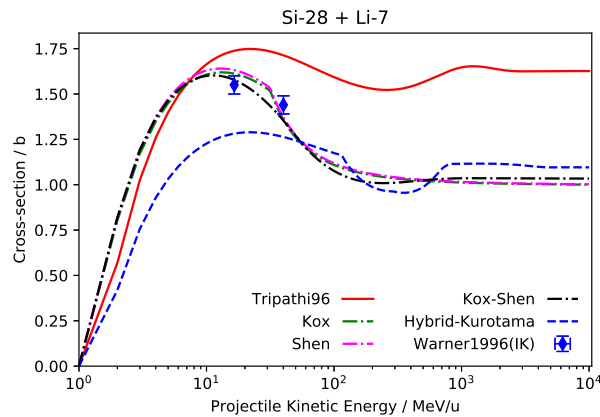


Figure 5.16: Comparison between parametrisation results and cross-section data for the following system:  $^{28}\text{Si} + ^7\text{Li}$ . Data are from reference [253]. Error bars are both statistical and systematic.

## $^{56}\text{Fe}$ Results

No data are available for  $^{56}\text{Fe} + ^{16}\text{O}$ ,  $^{27}\text{Al}$ ,  $^{28}\text{Si}$  (see Figure 5.17). Concerning the  $^{56}\text{Fe} + ^7\text{Li}$  system, all parametrisations fit the high-energy Westfall1979 data point, but Tripathi96. Because of the previous considerations about the Kox1987 dataset, it is difficult to make considerations for the  $^{56}\text{Fe} + ^{12}\text{C}$  system.

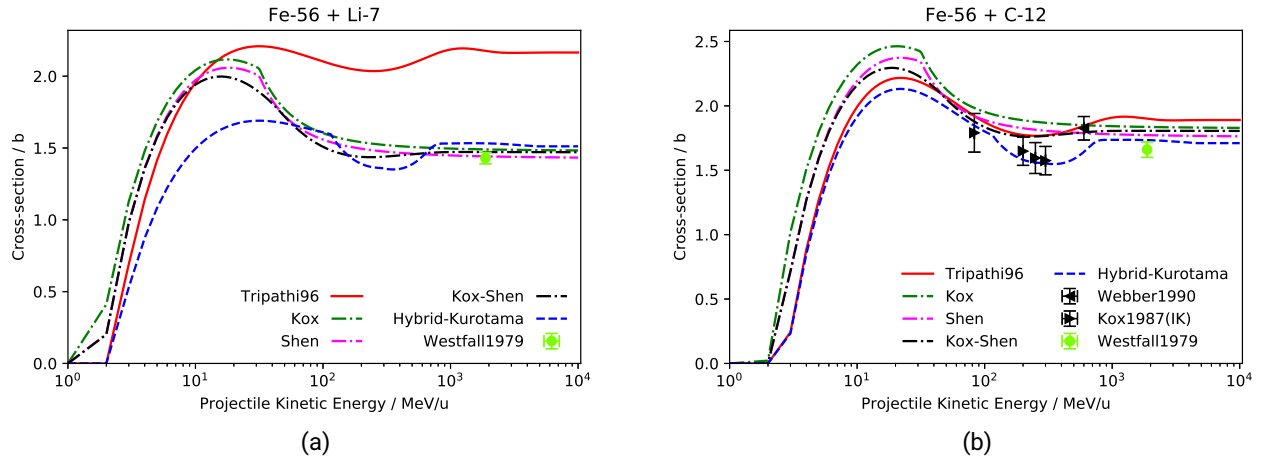


Figure 5.17: Comparison between parametrisation results and cross-section data for the following systems:  $^{56}\text{Fe} + ^7\text{Li}$ ,  $^{12}\text{C}$ . IK stands for Inverse Kinematic data. Data in Panel (a) are from reference [174] and data in Panel (b) from references [174, 220, 242]. Webber1990 error bar type is not specified, the rest are both statistical and systematic.

### 5.1.5 Discussion

#### The Kox1987 Dataset

If we take systems where also charge-changing cross-section data have been measured during experimental campaigns different to the Kox1987, and plot both reaction and charge-changing cross-sections together, we obtain Figure 5.18. It can be noticed that the charge-changing cross-sections are larger than the Kox1987 data. This is not physical since, by definition, reaction cross-sections are supposed to be larger than charge-changing cross-sections, as previously discussed in this Section. This provides additional evidence about the systematic underestimation of the reaction cross-section data by the Kox1987 dataset.

#### Projectile-Target Asymmetry Issue: the Neutron Excess Parameter

Due to the neutron-excess term, none of the parametrisations provides the same results in the case of a target-projectile exchange, unless they are characterised by the same neutron excess ( $A - 2Z$ ). In particular, the heavier the target nucleus is, the stronger the effect of the neutron-excess term becomes. This is a non-physical result, as reaction cross-sections should not depend on the reference system. Nevertheless, the heavier nucleus always plays the role of the target in the models. This was explicitly pointed out in Ref. [261], and it is implicit in the Tripathi parametrisations. As stated in Ref. [242, 260], the neutron excess parameter  $\alpha$  plays an important role at low energies ( $< 200 \text{ MeV u}^{-1}$ ). However, the parametrisations are structured in such a way that  $\alpha$  is likewise important at all energy ranges. Within this work, a careful study was conducted by making use of the experimental data from the database and the Kox-Shen model. It has been observed that with the multiplication factor of the neutron excess parameter being set to  $\alpha = 5$ , low-energy data are fitted best, while  $\alpha = 0$  fits them better at high energies. The recommended parameter in Ref. [260] is  $\alpha = 1$ , which is a good compromise if the condition is to keep  $\alpha$  constant at all energy values. Probably, an energy-dependent function modelling  $\alpha$  would be ideal.

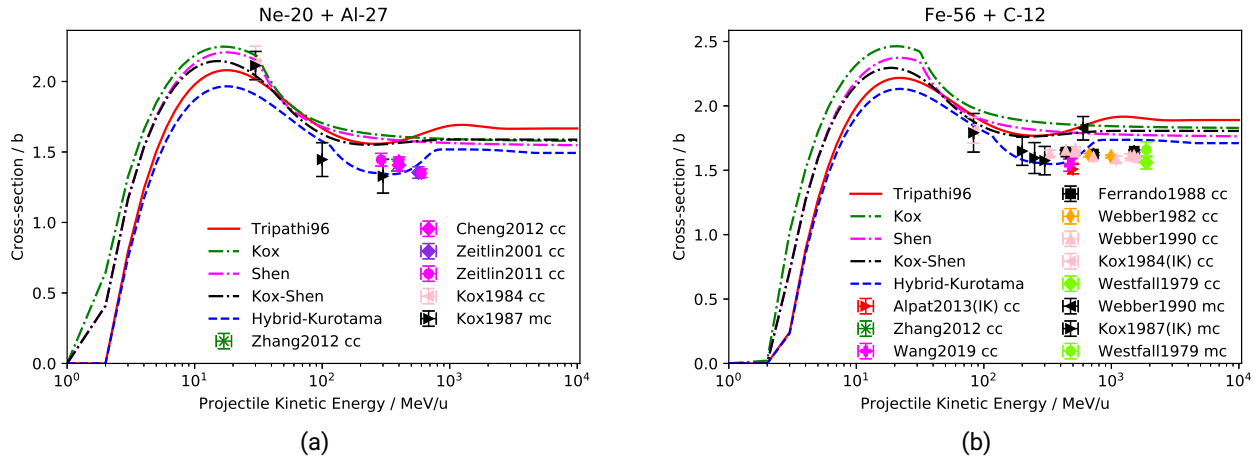


Figure 5.18: Comparison between Kox1987 mass and charge-changing cross-section data collected during different experimental campaigns for the following systems:  $^{20}\text{Ne} + ^{27}\text{Al}$  and  $^{56}\text{Fe} + ^{12}\text{C}$ . IK stands for Inverse Kinematic data, “cc” for charge-changing and “mc” for mass-changing cross-sections. Data in Panel (a) are from references [157, 182, 224, 228, 235, 242], in Panel (b) from references [157, 166, 170, 174, 196, 198, 220, 235, 242].

## High-Energy Data

For some systems, the parametrisations provide different results at high energies (see Figure 5.19). In particular, Tripathi96 tends to provide values higher than the other parametrisations at high energies and, for the case of heavy projectiles, Hybrid-Kurotama provides lower values. To quantify such effect, the relative differences were computed for several systems, between the maximum and minimum cross-section values provided by the different parametrisations at  $10 \text{ GeV u}^{-1}$ . The results for different projectiles (different colours) are reported in Figure 5.20 as a function of the target atomic number. It can be noticed that such relative deviations become systematically larger for heavier targets for all projectiles considered, and they tend to be larger for heavier projectiles (except for  $^4\text{He}$ ). Such differences underline uncertainties in the MC simulations since, for some systems, the results can strongly be influenced by the choice of the cross-section parametrisation.

## Considerations Involving the Absorbed Dose Measurements

As reported in Section 5.1.2, the Tripathi model is used in FLUKA MC simulations and the Hybrid-Kurotama in PHITS. Looking at the MC simulation results of Chapter 4, it can be seen in Figure 4.1 that PHITS underestimates the dose attenuation in HDPE, which means that it underestimates the reaction cross-section of  $^{56}\text{Fe} + ^{12}\text{C}$  or  $^1\text{H}$ . Concerning the system  $^{56}\text{Fe} + ^{12}\text{C}$ , it can be seen in Figure 5.17 that the Hybrid-Kurotama model at energies slightly lower than  $1 \text{ GeV u}^{-1}$  fits well the Kox1987 dataset. This is additional evidence that the dataset underestimates the real cross-section values. PHITS underestimates also the dose attenuation in the lithium-based hydrides. This could be due to an excessive depth of the Hybrid-Kurotama basin at intermediate energies. For what concerns FLUKA, it fits very well all the dose attenuation data with the lithium-based hydrides. Since Tripathi96 with  $D/3$  strongly overestimates the cross-section data, it is to be concluded that among the internal optimisations included in the implementation of the Tripathi parametrisation in FLUKA there is also the usage of  $D$  instead of  $D/3$  for the system  $^{56}\text{Fe} + ^7\text{Li}$  and, possibly,

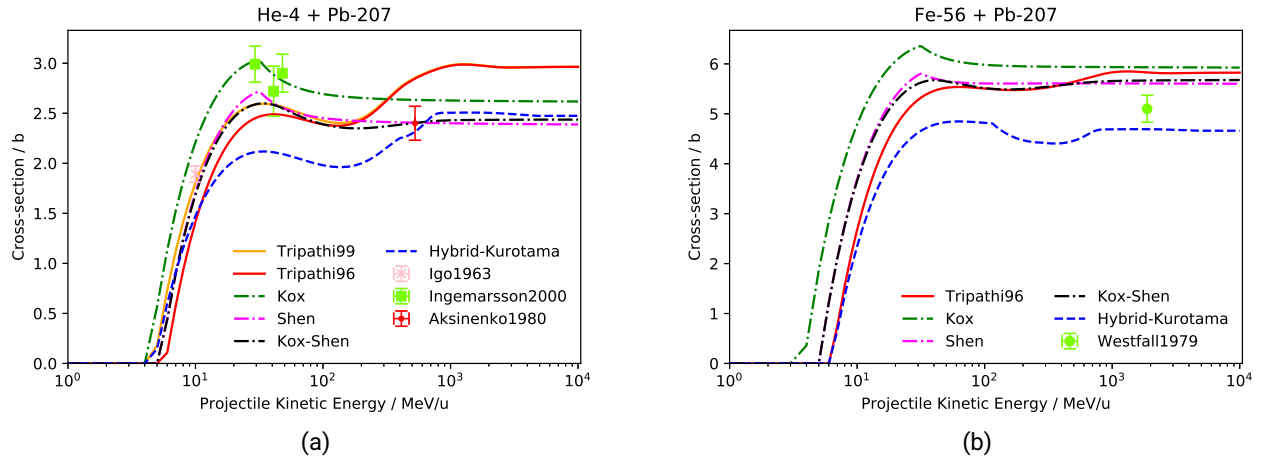


Figure 5.19: Comparison between parametrisation results and cross-section data for the following systems:  $^4\text{He} + ^{207}\text{Pb}$  and  $^{56}\text{Fe} + ^{207}\text{Pb}$ . Data in Panel (a) are from references [179, 230, 238], in Panel (b) from reference [174].

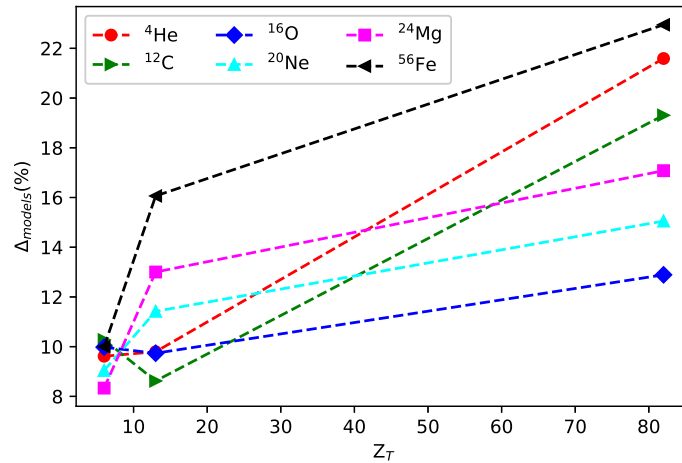


Figure 5.20: Relative differences between the maximum and minimum cross-section values predicted by the different parametrisations at  $10 \text{ GeV u}^{-1}$  (divided by the average value for all models) for different projectile nuclei as a function of the target atomic number. The dashed lines connect the points to guide the reader's eyes.

for all the cases involving lithium.

### 5.1.6 Proposed Optimisation of the Tripathi Parametrisation

Thanks to the large amount of data collected in this work, it was possible to optimise the Tripathi parametrisation so that it fits the data better. This parametrisation was chosen because it has many system-dependent parameters, which were adapted to fit the experimental data system by system.

## Tripathi96

Starting from the Tripathi96 parametrisation, the following modifications are proposed.

- The case of lithium projectile. As discussed in Section 2.7.3, lithium plays an important role in innovative passive shielding materials for radiation protection in space. Besides the fact that not many data have been measured at all with lithium, a comment about the Tripathi96 parametrisation for this element is added. The literature [262] recommends the usage of  $D/3$  instead of  $D$  for lithium projectiles for the Tripathi96 model calculations. However, Figure 5.21 reports a few examples that show that using  $D$  gives better agreement with the experimental data.

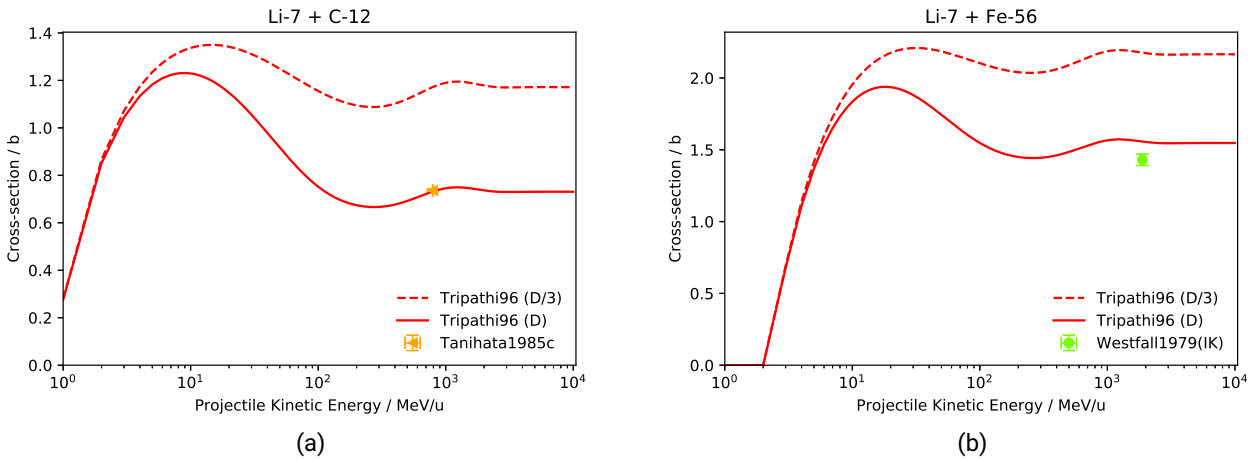


Figure 5.21: Tripathi96 computed both using  $D$  from Equation 5.15 (choice followed in the present work) and  $D/3$  (as recommended in Ref. [262]) for the following systems:  ${}^7\text{Li} + {}^{12}\text{C}$ ,  ${}^{56}\text{Fe}$ . IK stands for Inverse Kinematic data. Data in Panel (a) are from reference [189], in Panel (b) from reference [174].

In addition, optimisations were performed for all isotopes of lithium impinging on many different targets, by using the data collected in the database. Such optimisations are collected in Tab. 5.2. The parameters that were modified with respect to Ref. [262] are  $T_1$  (see Eq. 5.14) and the multiplication parameter of  $D$ , which was always set to 1.75 in Ref. [262] (see Eq. 5.15). By re-writing Equation 5.15 as:

$$D = d \frac{\rho_{A_p} + \rho_{A_T}}{\rho_{A_C} + \rho_{A_C}}, \quad (5.28)$$

the optimisations apply to the factor  $d$ . Such optimisations are reported in Tab. 5.2.

- Other projectiles. Optimisations for several other systems were performed by fitting Tripathi96 to the data collection (see Table 5.3). In particular, the focus was put on  ${}^9\text{Be}$ ,  ${}^{12}\text{C}$ ,  ${}^{16}\text{O}$ ,  ${}^{20}\text{Ne}$  and  ${}^{56}\text{Fe}$  on all the different targets from the database. Such ions were chosen because they contribute most to the GCR dose equivalent in free space (see Equation 5.27). Optimisations were performed also for  ${}^{27}\text{Al} + {}^{56}\text{Fe}$  since this is the projectile-target system that the parametrisation uses for  ${}^{56}\text{Fe} + {}^{27}\text{Al}$  (the lighter ion is always the projectile in the eyes of the model).

No optimisations could be performed for the case of  ${}^{24}\text{Mg}$  and  ${}^{28}\text{Si}$  projectiles, which are also important contributors to the GCR dose in free space since no mass-changing (reaction) cross-section data were

Table 5.2: Recommendations for parameters to be used for Li isotopes projectiles within Tripathi96. In Reference [262],  $T_1 = 40$ ,  $d = 1.75$ , and  $f = 1$  for all of the systems.

System	$T_1$	$d$	$f$	System	$T_1$	$d$	$f$
${}^6\text{Li} \rightarrow {}^9\text{Be}$	110	1.8	1.1	${}^7\text{Li} \rightarrow {}^9\text{Be}$	40	1.65	1
${}^{12}\text{C}$	110	1.75	1	${}^{27}\text{Al}$	40	1.8	1
${}^{27}\text{Al}$	110	1.9	1.05	${}^{28}\text{Si}$	40	1.6	1
${}^{28}\text{Si}$	110	1.8	0.95	${}^{56}\text{Fe}$	40	2	1
${}^{64}\text{Cu}$	100	1.8	1	${}^{64}\text{Cu}$	100	1.8	1
${}^8\text{Li} \rightarrow {}^9\text{Be}$	40	1.65	1	${}^9\text{Li} \rightarrow {}^{12}\text{C}$	40	1.8	1
${}^{28}\text{Si}$	80	1.8	0.93	${}^{27}\text{Al}$	40	1.9	1
${}^{64}\text{Cu}$	100	1.8	1	${}^{64}\text{Cu}$	100	1.8	1
${}^{11}\text{Li} \rightarrow {}^9\text{Be}$	40	1.3	1				
${}^{12}\text{C}$	40	1.35	1				
${}^{28}\text{Si}$	55	2.8	1.5				
${}^{64}\text{Cu}$	100	1.8	1				

Table 5.3: Recommendations for parameters to be used for different projectiles within Tripathi96. In Reference [262],  $T_1 = 40$ ,  $d = 1.75$ ,  $A = 0.292$ , and  $f = 1$  for all of the systems.

System	$T_1$	$d$	$A$	$f$	System	$T_1$	$d$	$A$	$f$
${}^{12}\text{C} \rightarrow {}^{12}\text{C}$	50	1.9	0.292	1	${}^9\text{Be} \rightarrow {}^9\text{Be}$	40	1.7	0.292	1
${}^{16}\text{O}$	40	2	0.292	1	${}^{12}\text{C}$	65	1.8	0.292	1
${}^{20}\text{Ne}$	30	2.7	0.292	1.4	${}^{27}\text{Al}$	40	1.8	0.292	1
${}^{22}\text{Na}$	80	2.1	0.292	1	${}^{56}\text{Fe}$	40	1.8	0.292	1
${}^{24}\text{Mg}$	55	1.9	0.292	1	${}^{64}\text{Cu}$	65	1.75	0.292	1
${}^{27}\text{Al}$	50	2	0.292	1	${}^{16}\text{O} \rightarrow {}^{27}\text{Al}$	25	1.75	0.292	1
${}^{28}\text{Si}$	70	1.9	0.292	1	${}^{64}\text{Cu}$	30	1.75	0.292	1
${}^{40}\text{Ca}$	50	2.2	0.292	1	${}^{20}\text{Ne} \rightarrow {}^{64}\text{Cu}$	60	1.75	0.292	1
${}^{56}\text{Fe}$	55	2.2	0.292	1					
${}^{64}\text{Cu}$	60	1.9	0.292	1					

measured. There are no available data for the system  ${}^{27}\text{Al} + {}^{28}\text{Si}$ . To be noted, for the specific case of  ${}^{12}\text{C} \rightarrow {}^{91}\text{Zr}$  no optimisation was proposed since there are only data from the Aksinenko1979 dataset, which was judged to be not reliable within the present work since it constantly underestimates the data for other systems (see Sec. 5.1.4).

For projectiles lighter than Li, optimisations are given for Tripathi99 later in this section.

### Tripathi99

The broad data collection allowed to carefully analyse all the nucleus-nucleus “light systems” for which cross-section data were measured. As a result, new parameters are recommended to be used for  ${}^2\text{H}$ ,  ${}^3\text{He}$  and  ${}^4\text{He}$  projectiles. All the recommendations are collected in Tables 5.4, 5.5 and 5.6. For the systems for which no data or only very high energy data are present, the parameters given in Ref. [263] remained unchanged.

Firstly, it is recommended to use  $\alpha = 5$  for the multiplication factor of the neutron excess parameter for  $Z_T > 54$ . Using  $\alpha = 0.91$  in fact, underestimates cross sections for very heavy targets. Concerning  $^2\text{H}$  and  $^3\text{He}$  systems, recommendations for  $R_C$  and  $T_1$  are given. In Fig. 5.22 are reported two examples of how the optimisations proposed in this work fit the experimental data better for  $^2\text{H} + ^{16}\text{O}$  and  $^2\text{H} + ^{56}\text{Fe}$ . For  $^3\text{He}$  no high-energy data were found in literature, so no changes in  $D$  were proposed. In Fig. 5.23 are reported two examples of how the optimised model fits the data for  $^3\text{He}$ :  $^3\text{He} + ^{28}\text{Si}$  and  $^3\text{He} + ^{207}\text{Pb}$ .

Concerning  $^4\text{He}$  projectiles, changes in  $R_C$ ,  $T_1$  and also  $A$  (see Eq. 5.14) are proposed. Changes in  $A$  were necessary only for  $^4\text{He}$  on  $^{12}\text{C}$  system. Recommendations are given about which Eq. to use between 5.15 and 5.19 and with what values for  $G$  and  $D_0$ . Among the other things, it can be noticed that a growth in  $D_0$  with the heavier targets gives a systematic better fit with the high-energy data. In Fig. 5.24 are reported two examples of how the optimisations proposed in this work fit the experimental data better for  $^4\text{He}$  on a medium-light ( $^{16}\text{O}$ ) and a heavy ( $^{207}\text{Pb}$ ) target.

Table 5.4: Recommendations of parameters to be used for  $^2\text{H}$  projectiles within Tripathi99, from Ref. [263] and this work. In the PHITS implementation, the parameters presented within Ref. [263] plus specific ones for  $^2\text{H} + ^4\text{He}$  are used. Systems that did not require any change with respect to the PHITS implementation (e.g.  $^2\text{H} + ^2\text{H}$ ,  $^4\text{He}$ ) are not reported. Exceptions to the rules are reported right under it (see  $^2\text{H} + ^{56}\text{Fe}$ ). When no specifications about the isotope are there, the recommendations are to be considered valid for every isotope of the element.

	Tripathi99 [263]		This work	
	$R_C$	$T_1$	$R_C$	$T_1$
$^2\text{H} + ^9\text{Be}, ^{16}\text{O}$	1	23	1	50
$^2\text{H} + ^{12}\text{C}$	6	23	1.5	50
$^2\text{H} + (12 \leq Z_T < 50)$	1	23	1	100
$^2\text{H} + ^{56}\text{Fe}$	1	23	0.6	100
$^2\text{H} + \text{Sn}, ^{136}\text{Xe}$	1	23	1	500
$^2\text{H} + ^{119}\text{Sn}$	1	23	1.2	500
$^2\text{H} + ^{159}\text{Tb}, ^{181}\text{Ta}, ^{197}\text{Au}$	1	23	1.2	500
$^2\text{H} + ^{207}\text{Pb}, ^{209}\text{Bi}$	1	23	1	500
$^2\text{H} + ^{232}\text{Th}$	1	23	1.4	500

With the optimisations presented in this section, the optimised Tripathi parametrisation fits the data best for all systems. Nevertheless, these optimisations should be tested by comparing the outcome of MC simulations against experimental results of e.g. absorbed dose curves, as it was done for the Horst  $D$  factor corrections [270].

## 5.1.7 Recommendations

### Parametrisations

All models can represent the trend of experimental data quite well, with the only exception that the Tripathi96  $D$  value should be used without dividing it by 3 for lithium projectiles. It is hard to make suggestions about what parametrisation should be used, especially because of the lack of data points for many systems, and the different results obtained for different systems. Table 5.7 collects the considerations



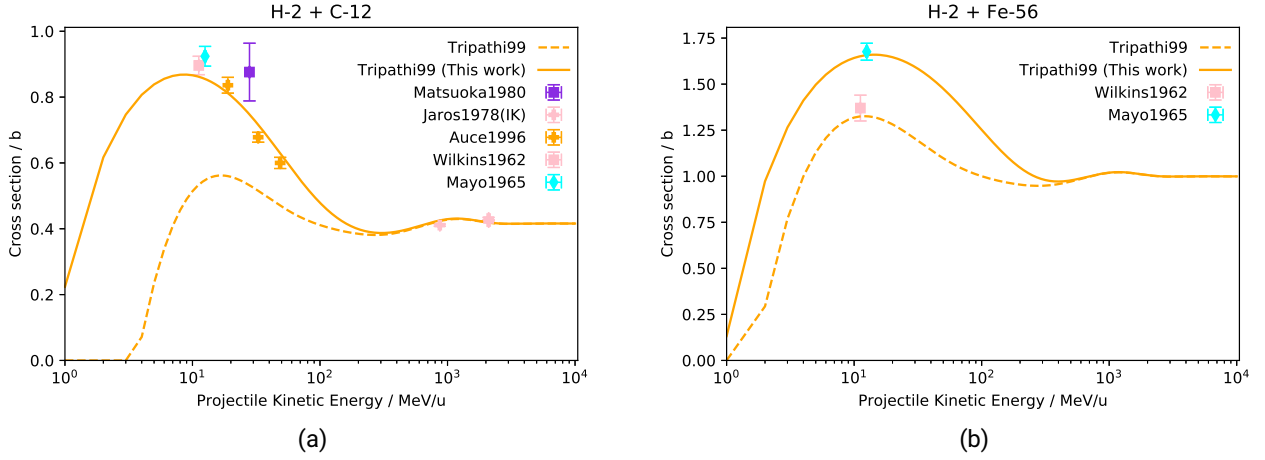


Figure 5.22: Comparison between the results obtained for  $^2\text{H}$  using Tripathi99 with the parameters reported in Ref. [263] and in this work (see Table 5.4). The experimental data from the database are plotted as well. For the case of  $^2\text{H} + ^{56}\text{Fe}$  the agreement is shifted from the Wilkins1962 set of data with the parameters from Ref. [263], to Mayo1965 with the parameters from this work. The reason is that Mayo1965 data are an upgraded version of Wilkins1962 data, which were found out to be an underestimation of the real values.

Table 5.5: Recommendations for parameters  $R_C$ ,  $T_1$ , and  $\alpha$  to be used for  $^3\text{He}$  projectiles in Tripathi99 [263]. The parameters from the original model are compared to the parameters recommended in this work. Systems that did not require any change in these parameters (e.g.  $^3\text{He} + ^{12}\text{C}$ ,  $^{27}\text{Al}$ ) are not reported.

	Tripathi99 [263]			This work		
	$R_C$	$T_1$	$\alpha$	$R_C$	$T_1$	$\alpha$
$^3\text{He} + ^9\text{Be}$	1	40	0.91	1	50	0.91
$^3\text{He} + ^{16}\text{O}$	1	40	0.91	1	50	0.91
$^3\text{He} + ^{28}\text{Si}$	1	40	0.91	1	65	0.91
$^3\text{He} + ^{40}\text{Ca}$	1	40	0.91	1	55	0.91
$^3\text{He} + ^{58}\text{Ni}$	1	40	0.91	0.6	60	0.91
$^3\text{He} + ^{60}\text{Ni}$	1	40	0.91	1	70	0.91
$^3\text{He} + ^{112}\text{Sn}$	1	40	0.91	1	90	0.91
$^3\text{He} + ^{116}\text{Sn}$	1	40	0.91	0.5	70	0.91
$^3\text{He} + ^{118}\text{Sn}$	1	40	0.91	0.5	75	0.91
$^3\text{He} + ^{120}\text{Sn}$	1	40	0.91	0.7	80	0.91
$^3\text{He} + ^{207}\text{Pb}$	1	40	0.91	1	50	5

that can be made out of the results presented in Section 5.1.4. Kox and Shen do not appear in Table 5.7 as the Kox-Shen parametrisation is the most recent update of both. Also, the Kox model tends to overestimate the importance of the neutron excess parameter, which makes it more error-prone when used for heavy-target systems. The Kox-Shen model does not appear for intermediate energies as it cannot reproduce the consistent drop in the datasets in this energy region. The Hybrid-Kurotama model is reported for high

Table 5.6: Recommendations of parameters to be used for  $^4\text{He}$  projectiles within Tripathi99, from Ref. [263] and this work. Eq. 5.16 comes from Ref. [262, 263], Eq. 5.19 from Ref. [156]. Systems that did not require any change to the parametrisation presented in Ref. [263] are not reported. When no specifications about the isotope are there, the recommendations are to be considered valid for every isotope of the element.

	Tripathi99 [263]						This work					
	$R_C$	$T_1$	$D$	$D_0$	$G$	$A$	$R_C$	$T_1$	$D$	$D_0$	$G$	$A$
$^4\text{He} + ^7\text{Li}$	1	40	Eq. 5.16	2.77	75	0.292	1	40	Eq. 5.16	2.95	75	0.292
$^4\text{He} + ^9\text{Be}$	1	25	Eq. 5.16	2.77	300	0.292	7	50	Eq. 5.19	2.2	50	1.4
$^4\text{He} + ^{12}\text{C}$	1	40	Eq. 5.16	2.77	75	0.292	3.5	50	Eq. 5.19	2.2	50	0.7
$^4\text{He} + ^{16}\text{O}$	1	40	Eq. 5.16	2.77	75	0.292	1	50	Eq. 5.19	2.4	50	0.292
$^4\text{He} + ^{20}\text{Ne}$	1	40	Eq. 5.16	2.77	75	0.292	1	40	Eq. 5.16	3	75	0.292
$^4\text{He} + ^{27}\text{Al}$	1	25	Eq. 5.16	2.77	300	0.292	1	20	Eq. 5.16	2.5	300	0.292
$^4\text{He} + ^{28}\text{Si}$	1	40	Eq. 5.16	2.77	75	0.292	1	50	Eq. 5.19	2.4	50	0.292
$^4\text{He} + ^{40}\text{Ca}$	1	40	Eq. 5.16	2.77	75	0.292	1	100	Eq. 5.16	2.77	75	0.292
$^4\text{He} + ^{48}\text{Ti}$	1	40	Eq. 5.16	2.77	75	0.292	1	40	Eq. 5.16	3	300	0.292
$^4\text{He} + ^{51}\text{V}, ^{52}\text{Cr}$	1	40	Eq. 5.16	2.77	75	0.292	1.2	40	Eq. 5.16	3	300	0.292
$^4\text{He} + ^{56}\text{Fe}$	1	40	Eq. 5.16	2.77	300	0.292	1.2	40	Eq. 5.16	3	300	0.292
$^4\text{He} + ^{59}\text{Co}$	1	40	Eq. 5.16	2.77	75	0.292	1.1	40	Eq. 5.16	3	300	0.292
$^4\text{He} + \text{Ni}$	1	40	Eq. 5.16	2.77	75	0.292	1.2	80	Eq. 5.16	3	300	0.292
$^4\text{He} + ^{64}\text{Cu}$	1	40	Eq. 5.16	2.77	75	0.292	1.2	80	Eq. 5.16	3.2	300	0.292
$^4\text{He} + ^{65}\text{Zn}$	1	40	Eq. 5.16	2.77	75	0.292	1.1	80	Eq. 5.16	3.2	300	0.292
$^4\text{He} + ^{91}\text{Zr}, ^{93}\text{Nb}, ^{96}\text{Mo}$	1	40	Eq. 5.16	2.77	75	0.292	1.1	80	Eq. 5.16	3.4	300	0.292
$^4\text{He} + ^{108}\text{Ag}$	1	40	Eq. 5.16	2.77	75	0.292	1	80	Eq. 5.16	3.4	300	0.292
$^4\text{He} + \text{Sn}$	1	40	Eq. 5.16	2.77	75	0.292	1.1	80	Eq. 5.16	3.4	300	0.292
$^4\text{He} + ^{181}\text{Ta}$	0.6	40	Eq. 5.16	2.77	75	0.292	1.1	80	Eq. 5.16	3.4	300	0.292
$^4\text{He} + ^{197}\text{Au}$	0.6	40	Eq. 5.16	2.77	75	0.292	1	80	Eq. 5.16	3.4	300	0.292
$^4\text{He} + ^{207}\text{Pb}, ^{209}\text{Bi}, ^{232}\text{Th}$	1	40	Eq. 5.16	2.77	75	0.292	1.1	75	Eq. 5.16	3.7	300	0.292
$^4\text{He} + ^{237}\text{Np}, ^{239}\text{Pu}$	1	40	Eq. 5.16	2.77	75	0.292	1.15	75	Eq. 5.16	3.7	300	0.292

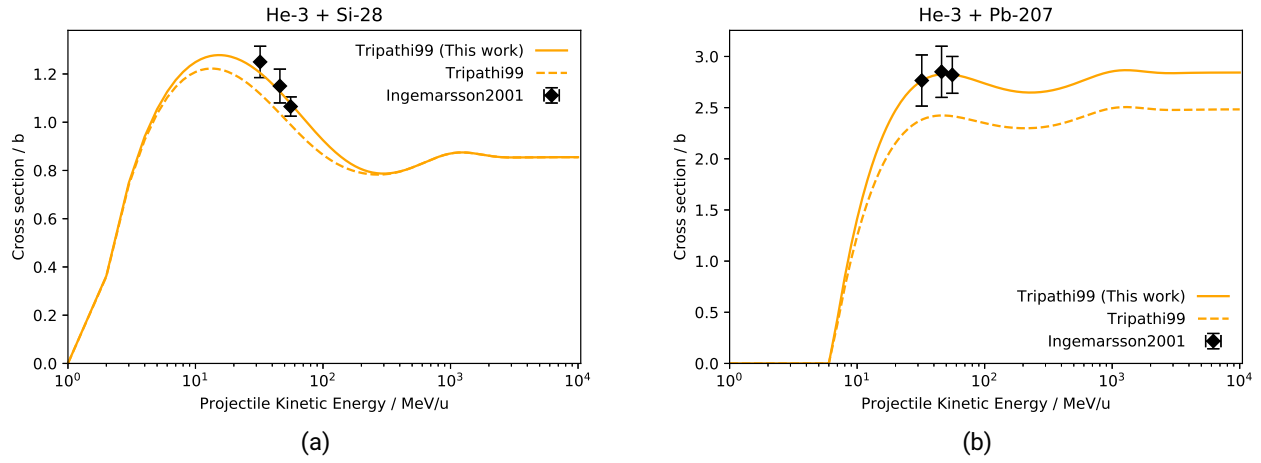


Figure 5.23: Comparison between the results obtained for  $^3\text{He}$  using Tripathi99 with the parameters reported in Ref. [263] and in this work (see Table 5.5). The experimental data from the database are plotted as well.

Table 5.7: Recommendations of parametrisations to be used for systems of interest for radiation protection in space for light and heavy systems and at different energy ranges.

System	Models fitting the best		
	Low energies ( $E \lesssim 30 \text{ MeV u}^{-1}$ )	Intermediate energies ( $30 \text{ MeV u}^{-1} \lesssim E \lesssim 500 \text{ MeV u}^{-1}$ )	High energies ( $E \gtrsim 500 \text{ MeV u}^{-1}$ )
All systems (including light)	Kox-Shen	Tripathi96 Hybrid-Kurotama	Kox-Shen Hybrid-Kurotama
Light systems			Tripathi99

energies, but underestimates the high-energy data for the case of heavy projectile and target systems. Since specific system-dependent optimisations were performed within this work for Tripathi96 and 99 to fit the collected data, the optimised Tripathi model presented in Section 5.1.6, fits the data best.

### Gaps in the Experimental Data

In literature, there are either no cross-section data (or not enough of them or they are non-reliable) for several important systems in the field of radiation protection in space. For instance, there are no data for  $^{16}\text{O}$ ,  $^{20}\text{Ne}$  and  $^{24}\text{Mg}$  impinging on any target of interest for space. Also, there are no data for the following systems:  $^{56}\text{Fe} + ^{16}\text{O}$ ,  $^{27}\text{Al} + ^{28}\text{Si}$ ,  $^{28}\text{Si} + ^{27}\text{Al}$ , and  $^{28}\text{Si} + ^{28}\text{Si}$ . Since cross-section measurements on oxygen targets are difficult to perform, inverse kinematic measurements using  $^{16}\text{O}$  beams on various solid targets (e.g. carbon, aluminium, silicon, iron) could be very efficient to fill some of the gaps. High-energy ( $> 1 \text{ GeV u}^{-1}$ ) data are available for almost none of the systems in Equation 5.27, meaning that the models cannot be validated at such energies. This is very important since different parametrisations model the high-energy cross-section values very differently (see Figure 5.20). High-energy cross-sections are relevant when it comes to cosmic radiation transport through matter, and poor knowledge of them can lead to large

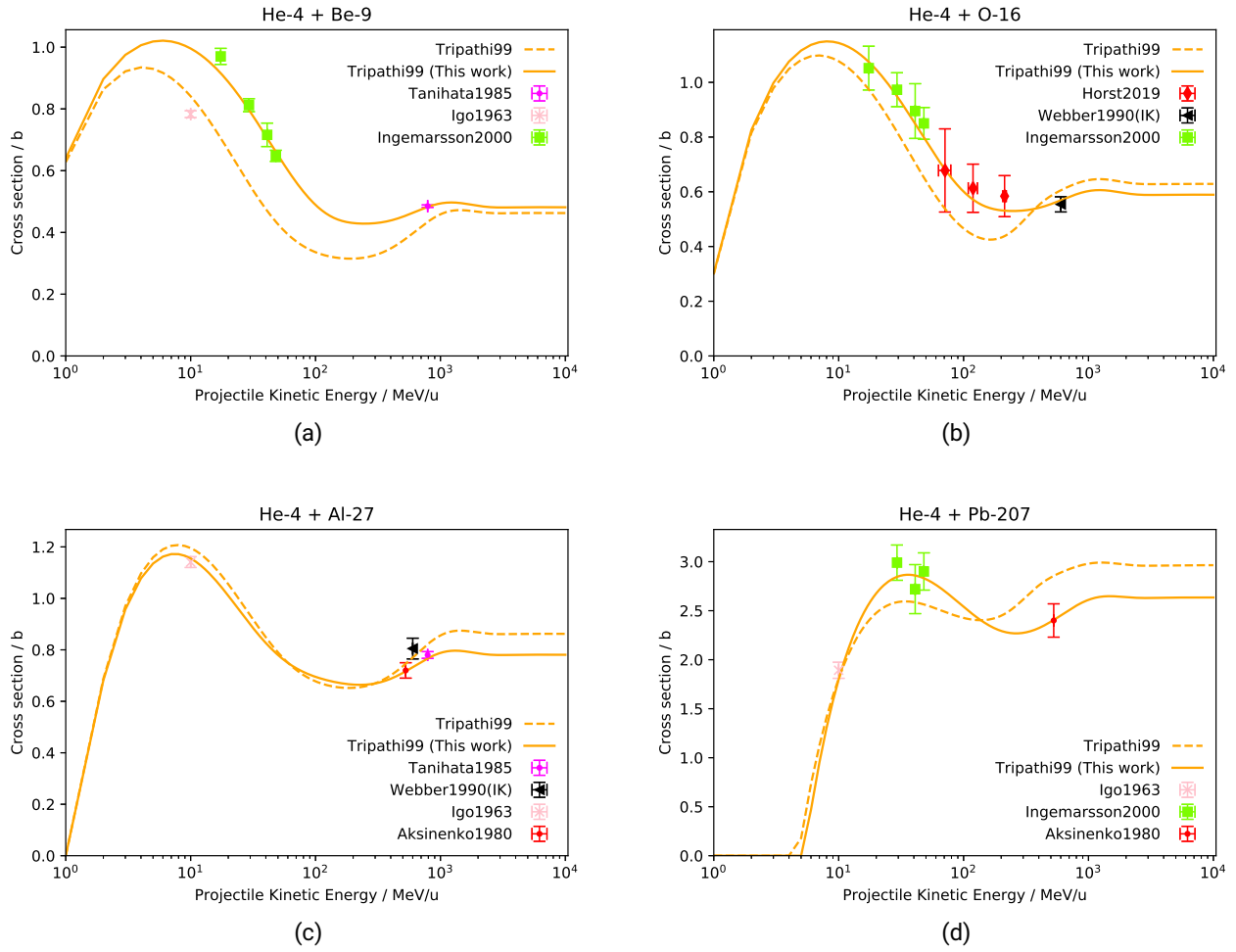


Figure 5.24: Comparison between the results obtained for  $^4\text{He}$  using Tripathi99 with the parameters reported in Ref. [263] and in this work (see Table 5.6). The experimental data from the database are plotted as well.

simulation errors. Therefore, high-energy cross-sections are the most important to be measured to improve simulation capabilities.

---

## 5.2 Fragment Production Cross-Section Database

---

This data collection aims to give a broad overview of all the total inclusive fragment production cross-section data measured so far. A study of both elemental and isotopic fragment production cross-sections is included in this work. At the end, considerations about the experimental gaps for space radiation shielding applications are reported.

---

### 5.2.1 The Database

---

---

#### Data

---

Also in this case, only data from English-written peer-reviewed publications were included in the data collection. A total of 7536 fragment production cross-section data from 69 peer-reviewed publications [157–163, 165–170, 174, 182, 198, 200, 201, 203, 209, 211, 213, 214, 217, 224, 227, 228, 274–315] have been included in the database so far.

As explained in Section 2.5.2, production cross-sections can be inclusive or exclusive, elemental or isotopic, total or differential. Since total inclusive cross-sections are the easiest to be measured, more data are available in the literature. Therefore, the database created within this work only contains total inclusive fragment production cross-section data, both elemental and isotopic.

In figure 5.25, the number of cross-section data reported in the fragment production cross-section database is plotted as a function of the atomic number of the projectile nucleus. A zoom on the data until nickel is reported in Panel (b), as those are the most relevant projectiles for radiation protection in space purposes. Elemental cross-section numbers are shown in blue and isotopic in cyan. By comparing

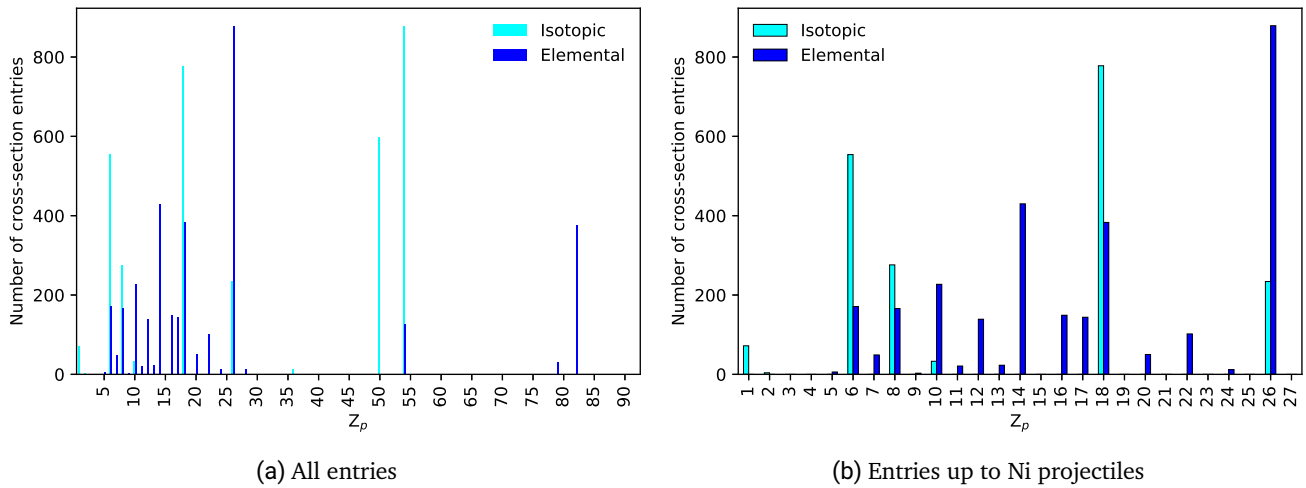


Figure 5.25: Number of cross-section data reported in the production cross-section database as a function of the atomic number of the projectile nucleus  $Z_p$ . Elemental cross-section entry numbers are shown in blue and isotopic in cyan. In Panel (a) all entries are shown, in Panel (b) only entries up to nickel projectiles.

Figures 5.1 and 5.25, it can be noticed that fragment production cross-sections were measured for fewer projectiles, as many  $Z_p$  have no data associated with them. The measurement of fragment production

---

cross-sections requires, in fact, a greater experimental effort than total reaction cross-sections. Nevertheless, for the systems for which data were measured, more data than for reaction cross-sections are reported. One nuclear reaction generates many fragments (multiplicity). In particular, the higher the  $Z_p$  is, the more different projectile fragments can be generated. Also, in most cases for which isotopic cross-sections were also measured, the number of isotopic cross-section data is higher because many isotopic cross-sections are associated with one elemental cross-section, as more than one isotope corresponds to one element.

As a general consideration, there are fewer publications for fragment production cross-section data (69) than for reaction cross-section data (103). This is because production cross-section data are harder to be measured as they require more detectors and statistics, therefore more beam time. Nevertheless, within such publications, more fragment production cross-section data can be found (7552) than reaction cross-sections (1786). For each nuclear reaction, several different fragments can be produced. Additionally, the heavier the projectile is, the greater the number of fragments that are produced. This is even more true for isotopic cross-sections. Therefore, the fragment production cross-section data in this second database are more than the reaction cross-section data in the first database even if the number of publications is considerably smaller.

---

## Database Structure

---

Also this database is available as a table. The columns of the table are the following (an explanation is reported only for columns that are different to the reaction database):

- Projectile atomic number.
- Projectile mass number.
- Target chemical formula.
- Target mass number.
- Projectile kinetic energy (MeV/u).
- Fragment atomic number.
- Fragment mass number. This was set to 0 in case the cross-section is elemental since all the mass numbers of the element are included.
- Cross-section (mb).
- Cross-section error (mb).
- First author of the publication.
- Year of the publication.
- DOI: unique Digital Object Identifier of the peer-reviewed publication.
- Comments.

## 5.2.2 Elemental Cross-Sections

In the following are reported the elemental cross-section data for the most relevant systems for radiation protection in space applications (see Equation 5.27).

For  $^4\text{He}$  projectiles, no elemental cross-section data were measured. Only hydrogen and helium fragments can be produced. Therefore, isotopic cross-sections are more relevant for this projectile (see Section 5.2.3). Also, no data for oxygen or silicon targets were measured for any of the projectiles of interest. Solely for iron projectiles, lithium target data are present in the literature.

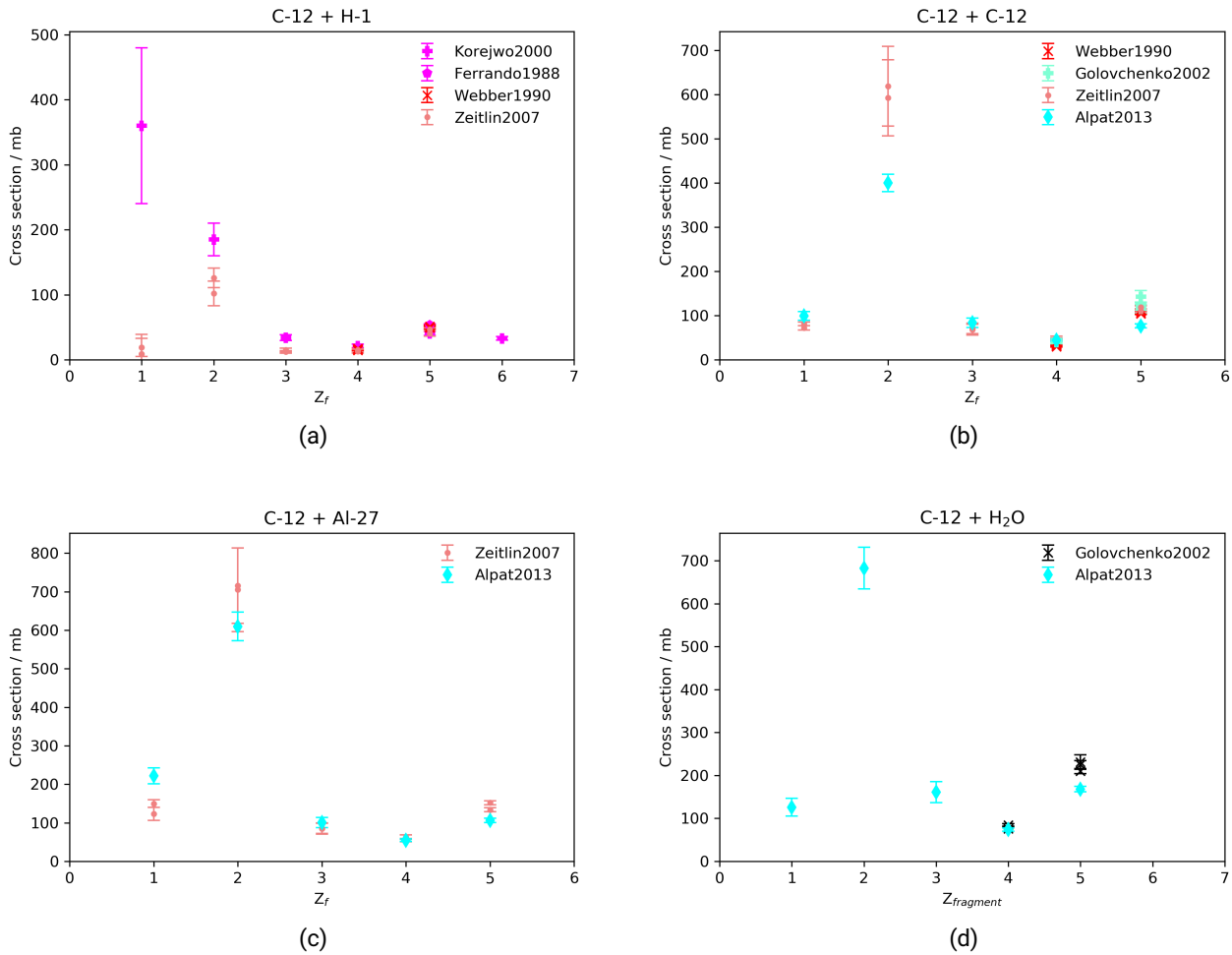


Figure 5.26: Total inclusive elemental fragment production cross-section data as a function of the fragment atomic number  $Z_f$  for the following systems:  $^{12}\text{C} + ^1\text{H}$ ,  $^{12}\text{C}$ ,  $^{27}\text{Al}$ ,  $\text{H}_2\text{O}$ . Data in Panel (a) are from references [166, 225, 300, 305], data in Panel (b) from references [170, 211, 225, 305], data in Panel (c) from references [170, 225], and data in Panel (d) from references [170, 211].

The  $^{12}\text{C}$  projectiles data are reported in Figure 5.26. Only data for  $^1\text{H}$ ,  $^{12}\text{C}$ , and  $^{27}\text{Al}$  targets are reported, as data for  $^7\text{Li}$ ,  $^{16}\text{O}$  or  $^{28}\text{Si}$  are not present literature. Only for the case of  $^{12}\text{C}$  projectiles, elemental cross-sections were measured on water. Since water is the main component of human body, such data are reported in Panel (d) of Figure 5.26. Probably, water target data are only present in the literature for  $^{12}\text{C}$  projectiles because of the importance of such cross-sections in heavy-ion therapy. This is another example

of how the field of radiation protection in space can benefit of the research done for heavy-ion therapy [273]. A different combination of colour and symbol was used for different datasets. For each of them, the first author and year of the peer-reviewed publication from which the data were extracted, are reported. It can be noticed that the probability of producing helium fragments is much higher than that of the other elements. The reason for this is that the binding energy per nucleon of  $^4\text{He}$  is very high (double-magic nucleus). Therefore,  $^{12}\text{C}$  has a high cross-section for the so-called three- $\alpha$  process, where it breaks into three  $\alpha$  nuclei.

The  $^{16}\text{O}$ ,  $^{20}\text{Ne}$ ,  $^{24}\text{Mg}$  and  $^{28}\text{Si}$  projectile data are reported in Figures 5.27, 5.28, 5.29, and 5.30. For these systems, only data for  $^1\text{H}$ ,  $^{12}\text{C}$ , and  $^{27}\text{Al}$  targets are present in literature.

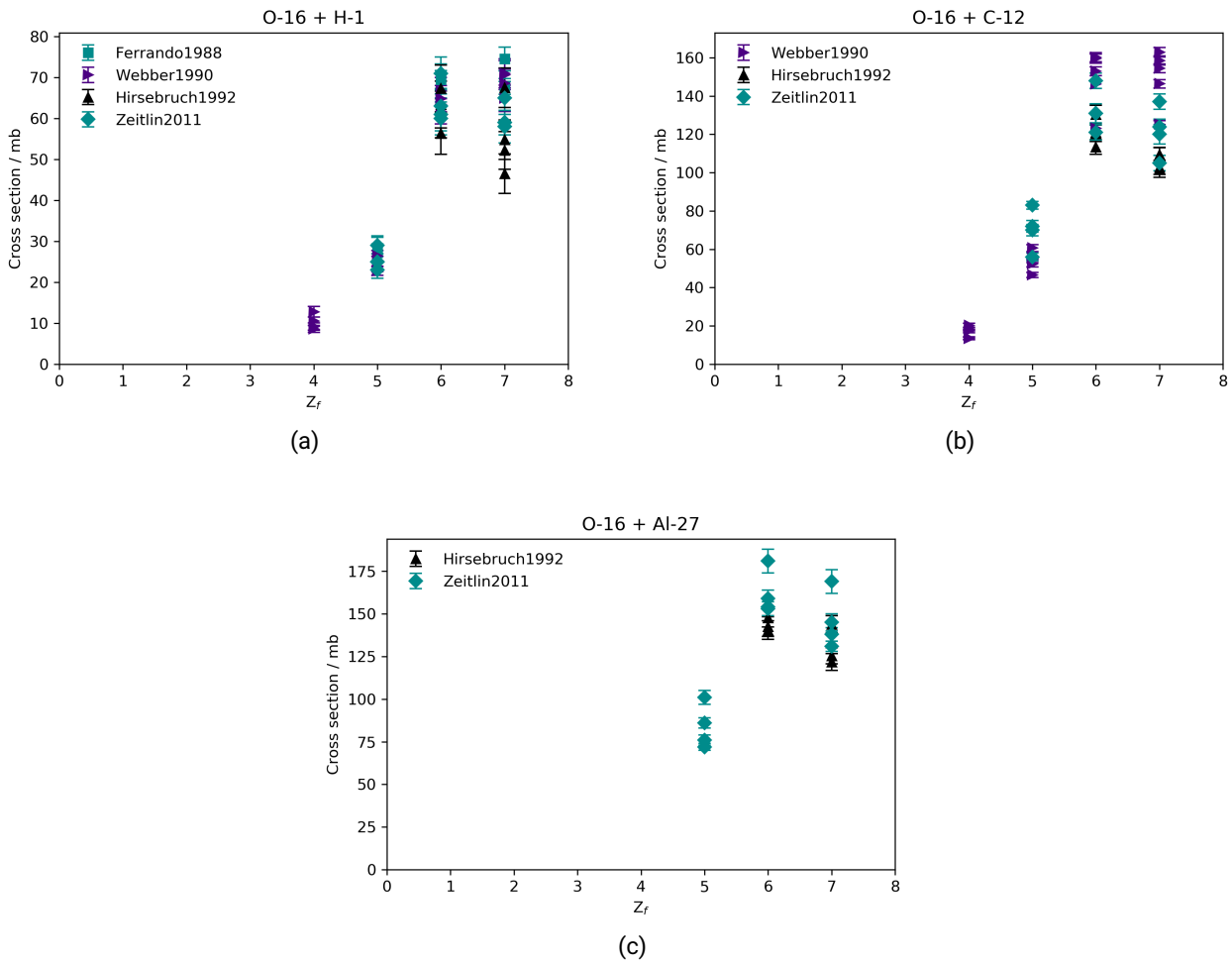


Figure 5.27: Total inclusive elemental fragment production cross-section data as a function of the fragment atomic number  $Z_f$  for the following system:  $^{16}\text{O} + ^1\text{H}$ ,  $^{12}\text{C}$ ,  $^{27}\text{Al}$ . Data in Panel (a) are from references [166, 213, 228, 305], in Panel (b) from references [213, 228, 305], and in Panel (c) from references [213, 228].

For the case of  $^{20}\text{Ne}$  projectiles, Zeitlin *et al.* measured helium production cross-sections. As for the case of  $^{12}\text{C}$  projectiles, the double-magic nuclear property of  $\alpha$  nuclei makes these cross-section values much larger than the production of any other element. Nevertheless, the helium production cross-section is less large than the cross-section of the production of other fragment elements in the case of  $^{20}\text{Ne}$  projectiles



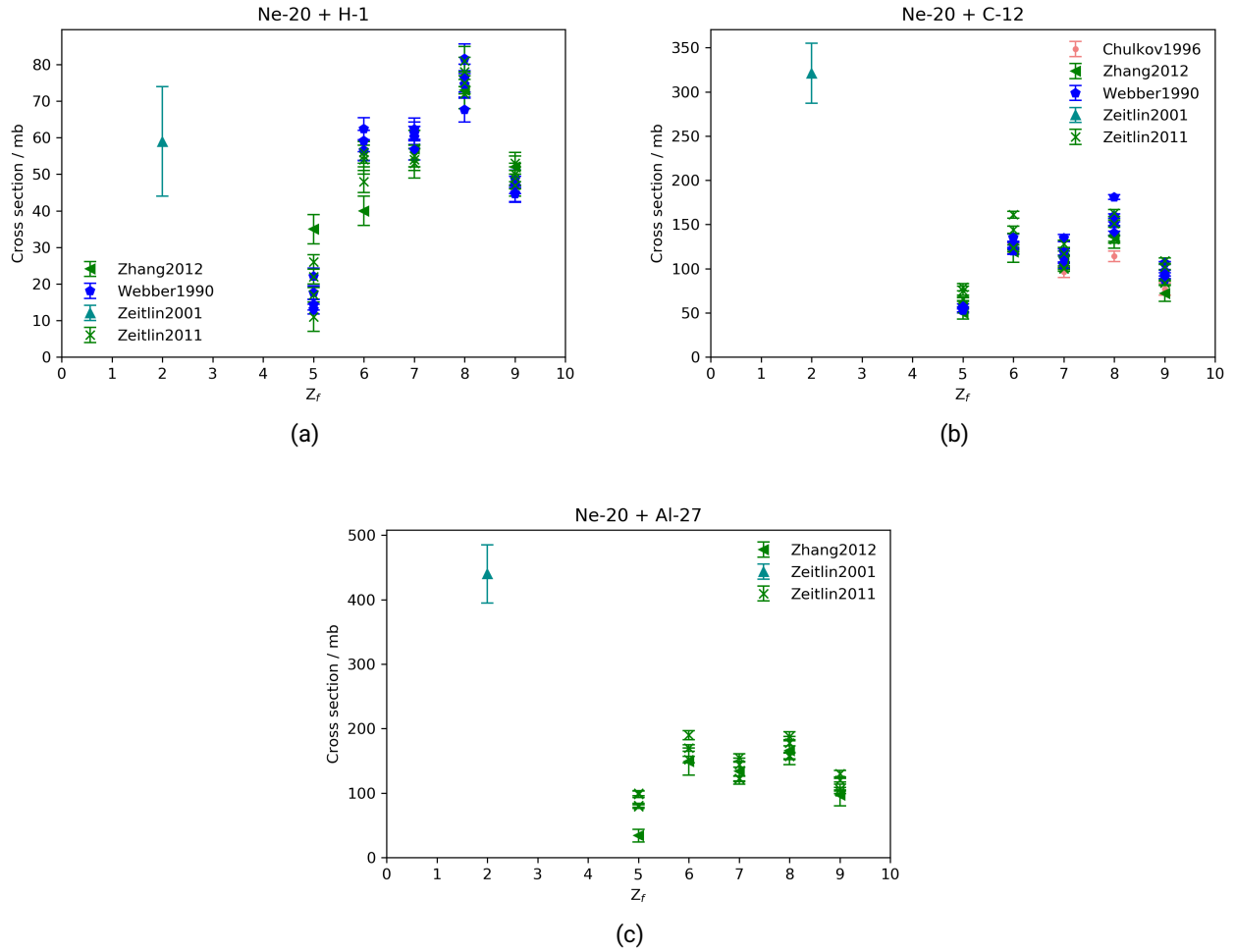


Figure 5.28: Total inclusive elemental fragment production cross-section data as a function of the fragment atomic number  $Z_f$  for the following systems:  $^{20}\text{Ne} + ^1\text{H}$ ,  $^{12}\text{C}$ ,  $^{27}\text{Al}$ . Data in Panel (a) are from references [157, 224, 228, 305], data in Panel (b) from references [157, 224, 228, 289, 305], and in Panel (c) from [157, 224, 228].

than  $^{12}\text{C}$ .  $^{20}\text{Ne}$  ions do not undergo the three- $\alpha$  process of  $^{12}\text{C}$  projectiles.

The  $^{56}\text{Fe}$  projectiles data are reported in Figure 5.31. Data for  $^1\text{H}$ ,  $^7\text{Li}$ ,  $^{12}\text{C}$ , and  $^{27}\text{Al}$  targets are reported, as no data for  $^{16}\text{O}$  or  $^{28}\text{Si}$  were measured.

For all projectiles heavier than  $^{12}\text{C}$ , only fragments with  $Z_f \geq 4$  could be resolved during the measurements, except for the production of helium ( $Z_f = 2$ ) from  $^{20}\text{Ne}$  projectiles, and of lithium ( $Z_f = 3$ ) from  $^{56}\text{Fe} + ^{27}\text{Al}$  reactions. It becomes, in fact, more challenging to resolve the production of light ions when heavier projectiles come into the picture.

Because of peripheral collisions, which cause the loss of a few nucleons only, the cross-section values become higher the closer the  $Z_f$  gets to  $Z_p$ . The only exceptions are the production cross-sections of helium fragments, which are very high due to high binding energy per nucleon of  $^4\text{He}$ , and the production cross-sections of nitrogen and fluorine, which tend to be lower due to the drop in the binding energy per nucleon for the nuclei of the stable isotopes of these two elements. Also, the OES effect can be observed for almost all systems.

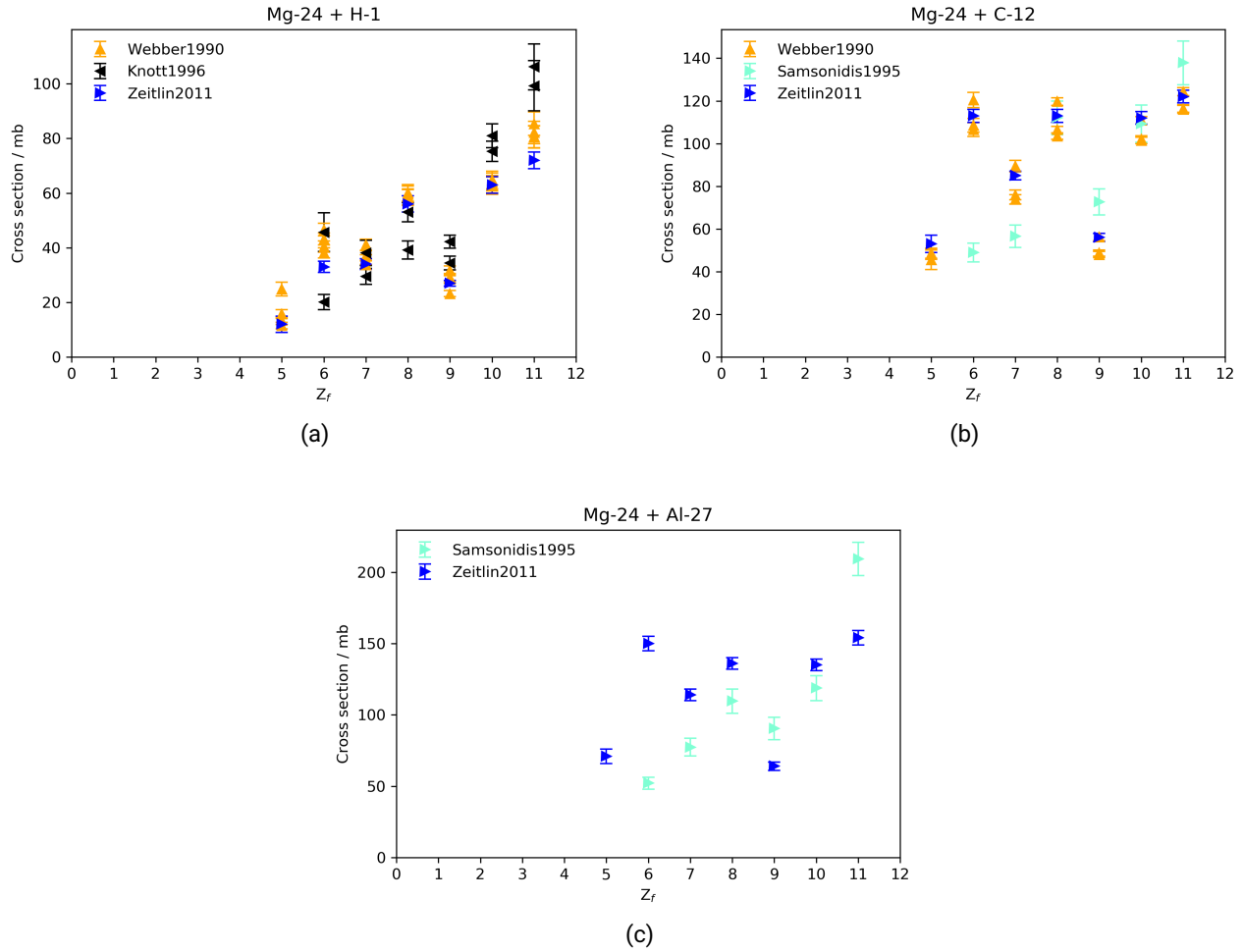


Figure 5.29: Total inclusive elemental fragment production cross-section data as a function of the fragment atomic number  $Z_f$  for the following systems:  $^{24}\text{Mg} + ^1\text{H}$ ,  $^{12}\text{C}$ ,  $^{27}\text{Al}$ . Data in Panel (a) are from references [228, 305, 308], data in Panel (b) from references [217, 228, 305], and in Panel (c) from [217, 228].

### 5.2.3 Isotopic Cross-Sections

In this Section, the focus is put on isotopic cross-sections, for which not only the atomic number of the fragment  $Z_f$  is measured but also its mass number  $A_f$ . In Figures 5.32, 5.33, 5.34, and 5.35, the isotopic cross-section data for the most relevant systems for radiation protection in space applications (see Equation 5.27) are reported. The plots show cross-section data as a function of  $A_f$  and different colours are used for different elements ( $Z_f$ ). At times, more than one data point is present for a single fragment isotope. The reason is that data at different projectile kinetic energies were measured.

Concerning  $^4\text{He}$  projectiles, only data on  $^{12}\text{C}$  and specifically for the production of  $^3\text{He}$  were measured at four different energies, which are of interest for heavy-ion therapy applications. No data for the production of other fragments were measured.

For  $^{12}\text{C}$  projectiles, data on  $^1\text{H}$ ,  $^{12}\text{C}$ ,  $^{16}\text{O}$ , and  $^{27}\text{Al}$  targets were measured. Since  $^{12}\text{C}$  is an ion of interest also for therapy applications, more cross-section measurements were performed. Several isotopes of all

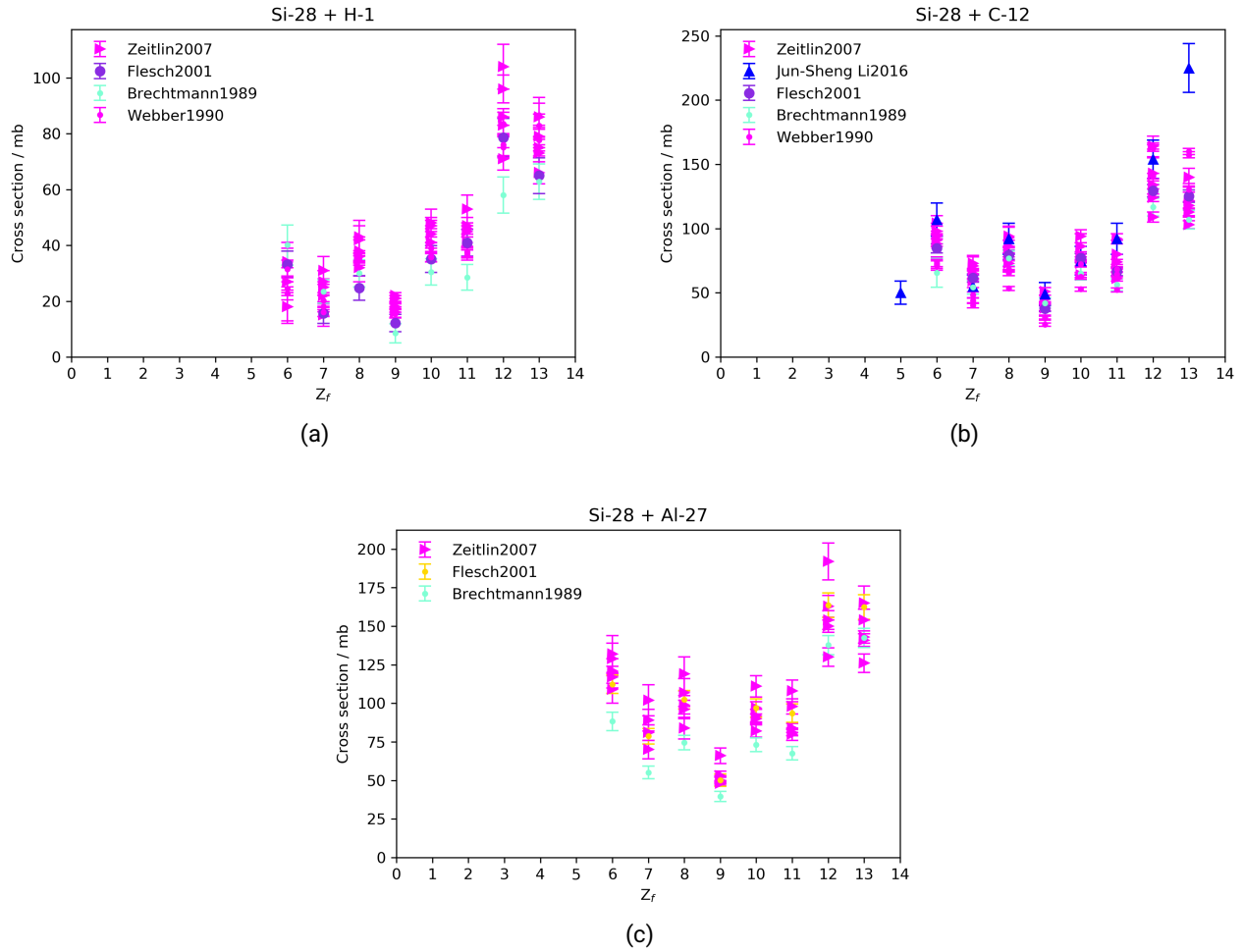


Figure 5.30: Total inclusive elemental fragment production cross-section data as a function of the fragment atomic number  $Z_f$  for the following systems:  $^{28}\text{Si} + ^1\text{H}$ ,  $^{12}\text{C}$ ,  $^{27}\text{Al}$ . Data in Panel (a) are from references [203, 209, 226, 305], in Panel (b) from references [168, 203, 209, 226, 305], and in Panel (c) from references [203, 209, 226].

elements from hydrogen to carbon were covered during such measurements. Many different projectile kinetic energies were used for fragments with  $Z_f = 1, 2$ . Cross-sections for the production of hydrogen and helium are higher than cross-sections for the production of heavier elements. The cross-sections for the production of elements with  $Z_f = 1, 2$  are much lower (around a factor of 5) for  $^1\text{H}$  targets than for the others.

For the system  $^{12}\text{C} + ^1\text{H}$ , data for  $Z_f = 1, 2$  come from four different experiments [277, 286, 300, 304] at very different energies, from 95 to about 3000  $\text{MeV u}^{-1}$ , and data for heavier fragments come from one experiment only [301]. It is hard to reveal both heavy and light fragments with the same set of detectors. The data collected at 95  $\text{MeV u}^{-1}$  [277] are of interest for therapy, the others for space applications.

For the system  $^{12}\text{C} + ^{12}\text{C}$ , data come more or less in equal amounts for energies of interest for therapy and space applications. During some experiments, all fragments were detected [277, 286, 304], but during others, only the production of either heavy or light fragments was measured.

As already pointed out, using  $^{16}\text{O}$  as target is not trivial. Therefore, only one experiment made mea-

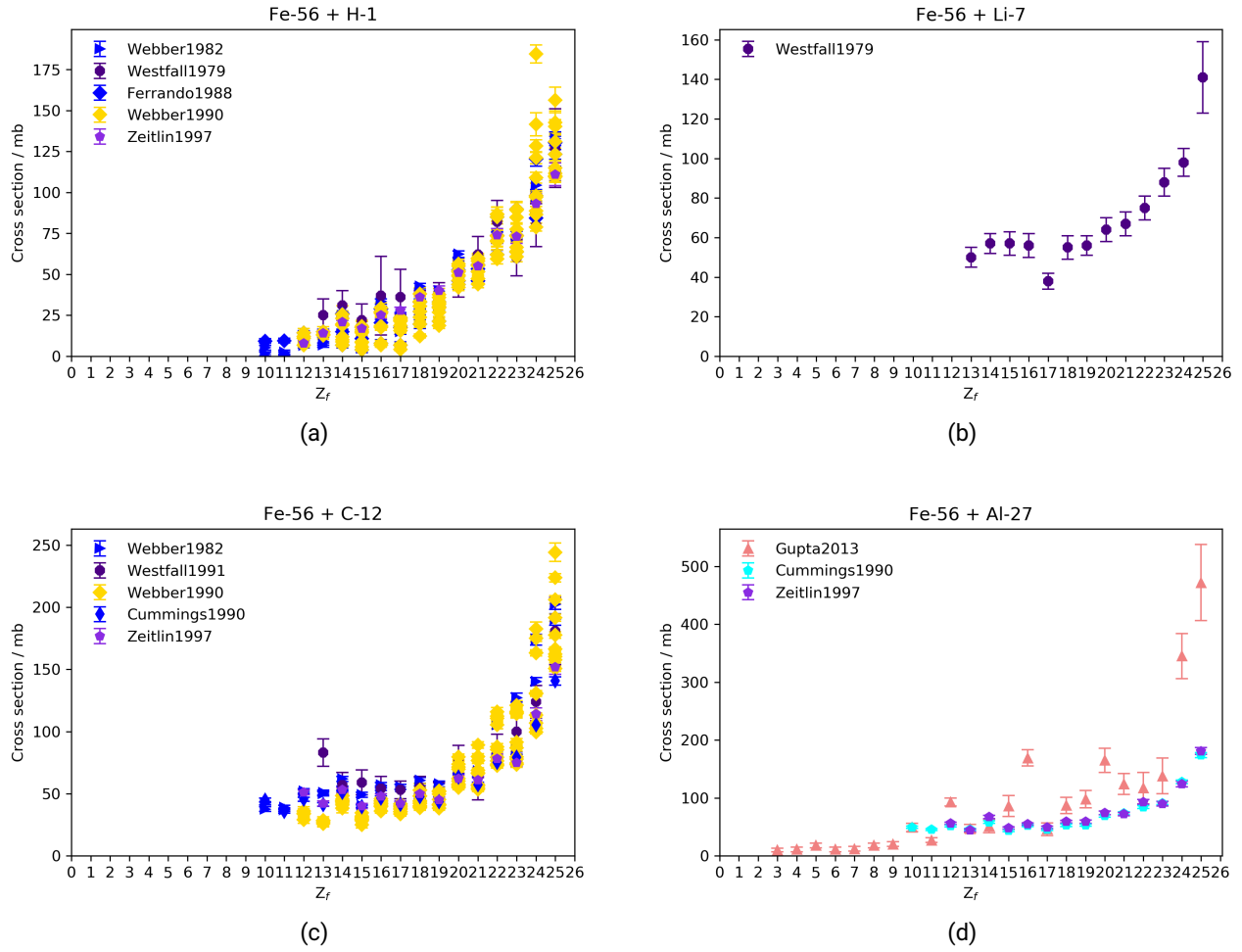


Figure 5.31: Total inclusive elemental fragment production cross-section data as a function of the fragment atomic number  $Z_f$  for the following systems:  $^{56}\text{Fe} + ^1\text{H}$ ,  $^{56}\text{Fe} + ^7\text{Li}$ ,  $^{56}\text{Fe} + ^{12}\text{C}$ ,  $^{56}\text{Fe} + ^{27}\text{Al}$ . Data in Panel (a) are from references [166, 174, 198, 285, 305, 309], data in Panel (b) from [174], in Panel (c) from [174, 198, 285, 305, 307, 309], and data in Panel (d) from [285, 299, 307, 309].

measurements of isotopic fragment production cross-sections for  $^{12}\text{C} + ^{16}\text{O}$  [277]. The energy is  $95 \text{ MeV u}^{-1}$ , which is of interest mainly for therapy. All fragments were resolved.

Also for the case of  $^{12}\text{C} + ^{27}\text{Al}$ , all fragments were resolved and both low ( $95 \text{ MeV u}^{-1}$ ) [277] and high energies ( $1.05$  and  $2.1 \text{ GeV u}^{-1}$ ) [286, 304] were covered.

Concerning  $^{16}\text{O}$  projectiles, fewer data are available than for  $^{12}\text{C}$  projectiles. Nevertheless, since  $^{16}\text{O}$  has been thought to be used for therapy applications [316], data at therapy energies were also measured [296, 297, 303]. Nevertheless, high-energy data were also measured [286, 304]. Also for  $^{16}\text{O}$  projectiles, in most cases, either light or heavy fragments were resolved during one experiment. Therefore, hydrogen and helium data were not taken for the same energies as for the rest. In the case of  $^{16}\text{O} + ^{27}\text{Al}$ , production data for  $Z_f = 1, 2$  were taken at high energies ( $2100 \text{ MeV u}^{-1}$ ) and for heavier fragments at low energies ( $100 \text{ MeV u}^{-1}$ ). For all other cases, the situation is reversed.

It can be noticed that, for both cases of  $^{12}\text{C}$  and  $^{16}\text{O}$  projectiles, the production cross-section values of light fragments become higher for heavier targets. In addition, differently from the other systems studied,

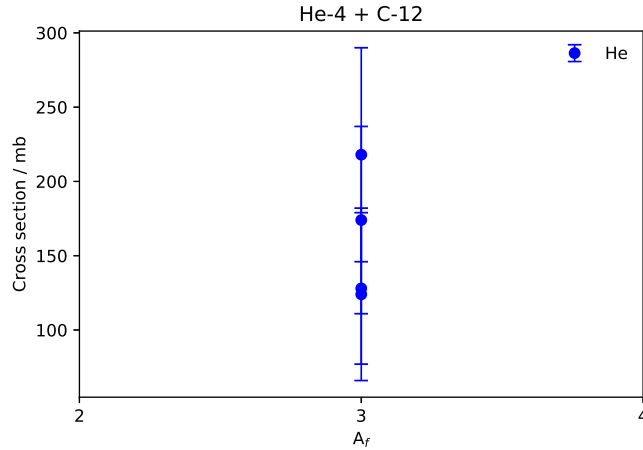


Figure 5.32: Total inclusive isotopic fragment production cross-section data as a function of the fragment mass number  $A_f$  for the following systems:  ${}^4\text{He} + {}^{12}\text{C}$ . Data are from reference [167] at energies of 83.5, 125 and 176  $\text{MeV u}^{-1}$ .

the OES is very pronounced for the systems  ${}^{16}\text{O} + {}^1\text{H}$ ,  ${}^{12}\text{C}$ , especially for  $Z_f = 1, 2, 6$ .

It is more difficult to perform isotopic cross-section measurements for  ${}^{56}\text{Fe}$  projectiles because many more fragments are produced. In fact, data for  ${}^{56}\text{Fe} + {}^1\text{H}$  (Panel (a) of Figure 5.35) are from one experimental campaign only [312] and the same is valid for data for  ${}^{56}\text{Fe} + {}^{12}\text{C}$  (Panel (b) [306]). Nevertheless, a wide range of fragments were covered in both cases, especially for the system  ${}^{56}\text{Fe} + {}^1\text{H}$ . The projectile kinetic energy for the system  ${}^{56}\text{Fe} + {}^1\text{H}$  is  $1 \text{ GeV u}^{-1}$ , and for  ${}^{56}\text{Fe} + {}^{12}\text{C}$   $600 \text{ MeV u}^{-1}$ , both of interest for space applications.

Since data at various energies were collected for  ${}^4\text{He}$  and  ${}^{12}\text{C}$  projectiles, plots showing only the cross-section data for the production of one specific fragment as a function of the projectile kinetic energy were generated. The focus was put on light fragments, as more data at different energies were collected and because of their relative importance in radiation protection in space [105]. The plots are shown in Figures 5.36, 5.37, 5.38, and 5.39. Data from Olson1983 [304] were excluded by all plots containing data from Lindstrom1975 [286] as they simply reproduce them perfectly. For all cases plotted in the four Figures, the data seem to decrease as the projectile kinetic energy increases, with the exception of the production of  ${}^2\text{H}$  and  ${}^3\text{H}$  for the system  ${}^{12}\text{C} + {}^1\text{H}$  (see Figure 5.37).

## 5.2.4 Discussion and Recommendations

### Elemental Cross-Sections

Concerning elemental cross-sections, no data for oxygen or silicon targets were measured for any of the projectiles of interest. Solely for iron projectiles, lithium target data are present in the literature.

The lack of oxygen target data is probably due to the technical difficulties in using a gaseous target. Nevertheless, it is possible to measure such cross-sections by using a composite target such as water and subtracting the hydrogen contribution. This same method is often used to measure cross-sections for hydrogen targets with a combination of graphite (pure C) and  $\text{CH}_2$  targets. For oxygen target data, a combination of graphite,  $\text{CH}_2$ , and water targets could be exploited.

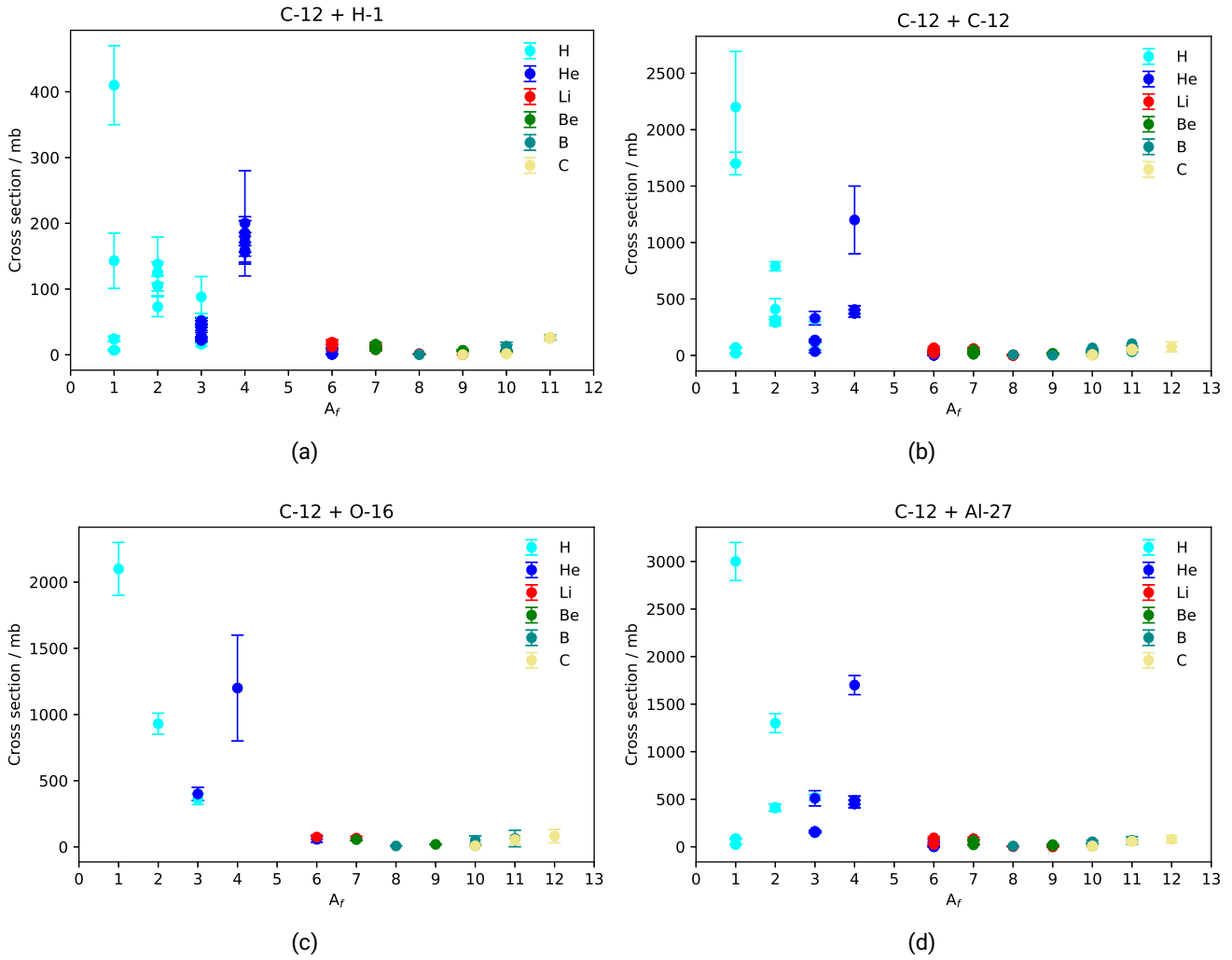


Figure 5.33: Total inclusive isotopic fragment production cross-section data as a function of the fragment mass number  $A_f$  for the following systems:  $^{12}\text{C} + ^1\text{H}$ ,  $^{12}\text{C}$ ,  $^{16}\text{O}$ ,  $^{27}\text{Al}$ . Data in Panel (a) are from references [277, 286, 300, 301, 304], in Panel (b) from [220, 277, 278, 286, 288, 296, 302, 304], in Panel (c) from [277], and in Panel (d) from [277, 286, 304].

Concerning silicon target data, they are important to be measured because of the consistent amount of electronic devices surrounding the spacecraft habitat. It is therefore recommended that they are measured. The same is valid for lithium targets because of the lithium content of innovative shielding materials such as the ones tested in this work (see Chapter 3).

### Isotopic Cross-Sections

Also for isotopic cross-sections, almost no  $^4\text{He}$  projectiles data were measured, except for  $^3\text{He}$  production data for the system  $^4\text{He} + ^{12}\text{C}$ , which is of interest for therapy applications. This is a very important gap in such data because of the relative importance of such ions in the GCR contribution behind thick shields [105]. Therefore, it is recommended that this gap is filled in future experimental campaigns. Data measured using  $^{20}\text{Ne}$ ,  $^{24}\text{Mg}$ , and  $^{28}\text{Si}$  projectiles are missing and recommended to be measured.

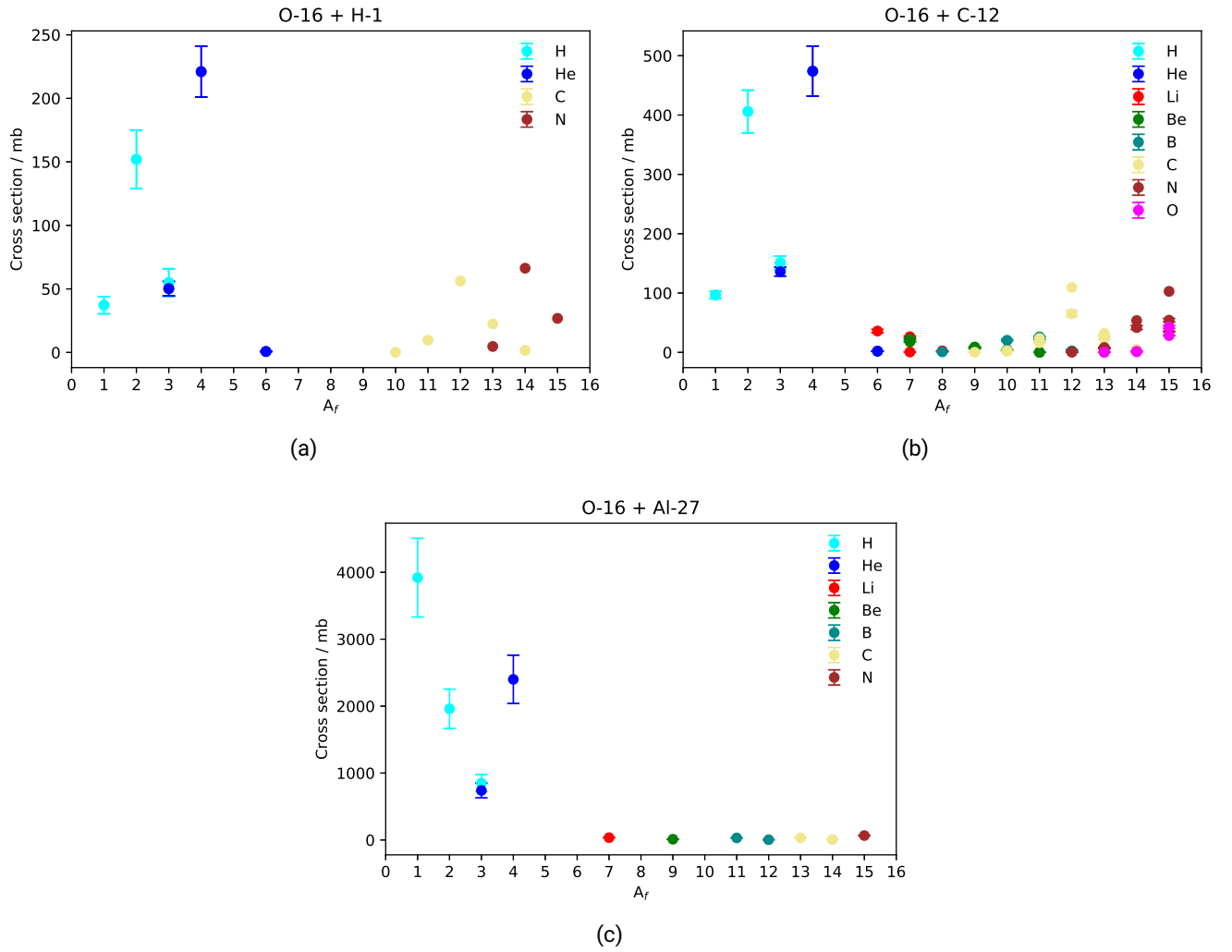


Figure 5.34: Total inclusive isotopic fragment production cross-section data as a function of the fragment mass number  $A_f$  for the following systems:  $^{16}\text{O} + ^1\text{H}$ ,  $^{12}\text{C}$ ,  $^{27}\text{Al}$ . Data in Panel (a) are from references [286, 296], in Panel (b) from [286, 296, 297], and in Panel (c) from references [303, 304].

Also for the case of isotopic cross-sections, data on lithium, oxygen, and silicon targets are missing, except for the system of interest for therapy  $^{12}\text{C} + ^{16}\text{O}$ , where data only at energies of interest for therapy and not space ( $95 \text{ MeV u}^{-1}$ ) were measured. Therefore, data with these targets are recommended to be measured. For all the elemental and isotopic cross-sections listed, the focus is recommended to be put on high energies.

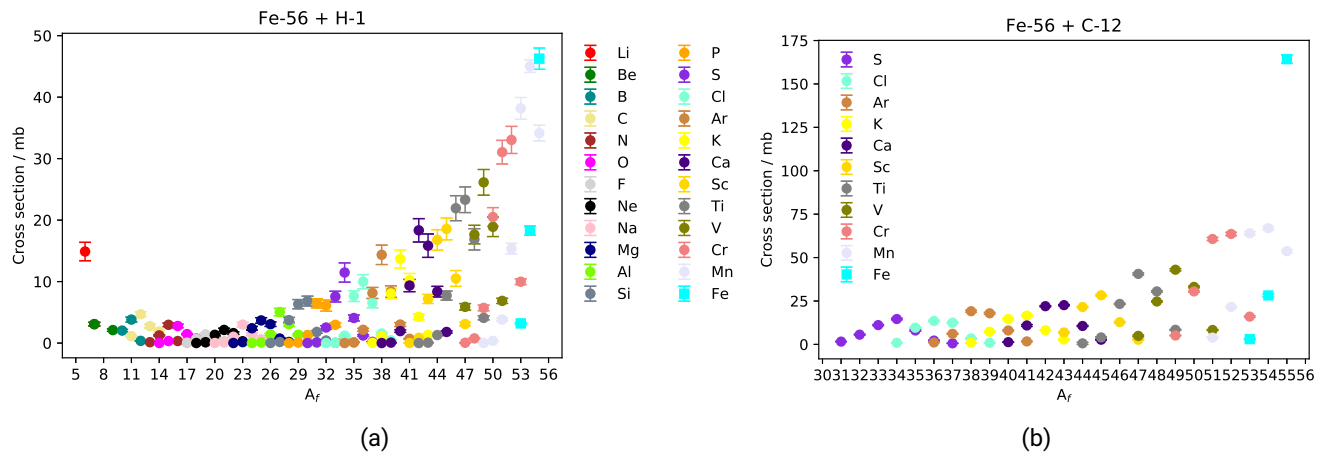


Figure 5.35: Total inclusive isotopic fragment production cross-section data as a function of the fragment mass number  $A_f$  for the following systems:  $^{56}\text{Fe} + ^1\text{H}$ ,  $^{12}\text{C}$ . Data in Panel (a) are from reference [312] and in Panel (b) from [306].

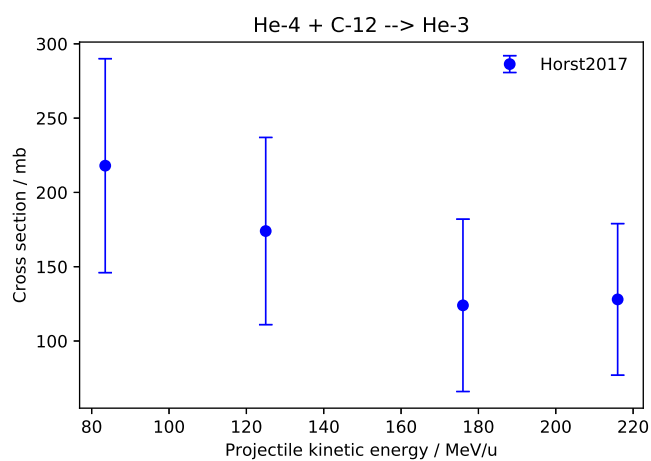


Figure 5.36: Total inclusive isotopic production cross-section data as a function of the projectile kinetic energy for the following reaction:  $^4\text{He} + ^{12}\text{C} \rightarrow ^3\text{He}$ . Data are from reference [167].



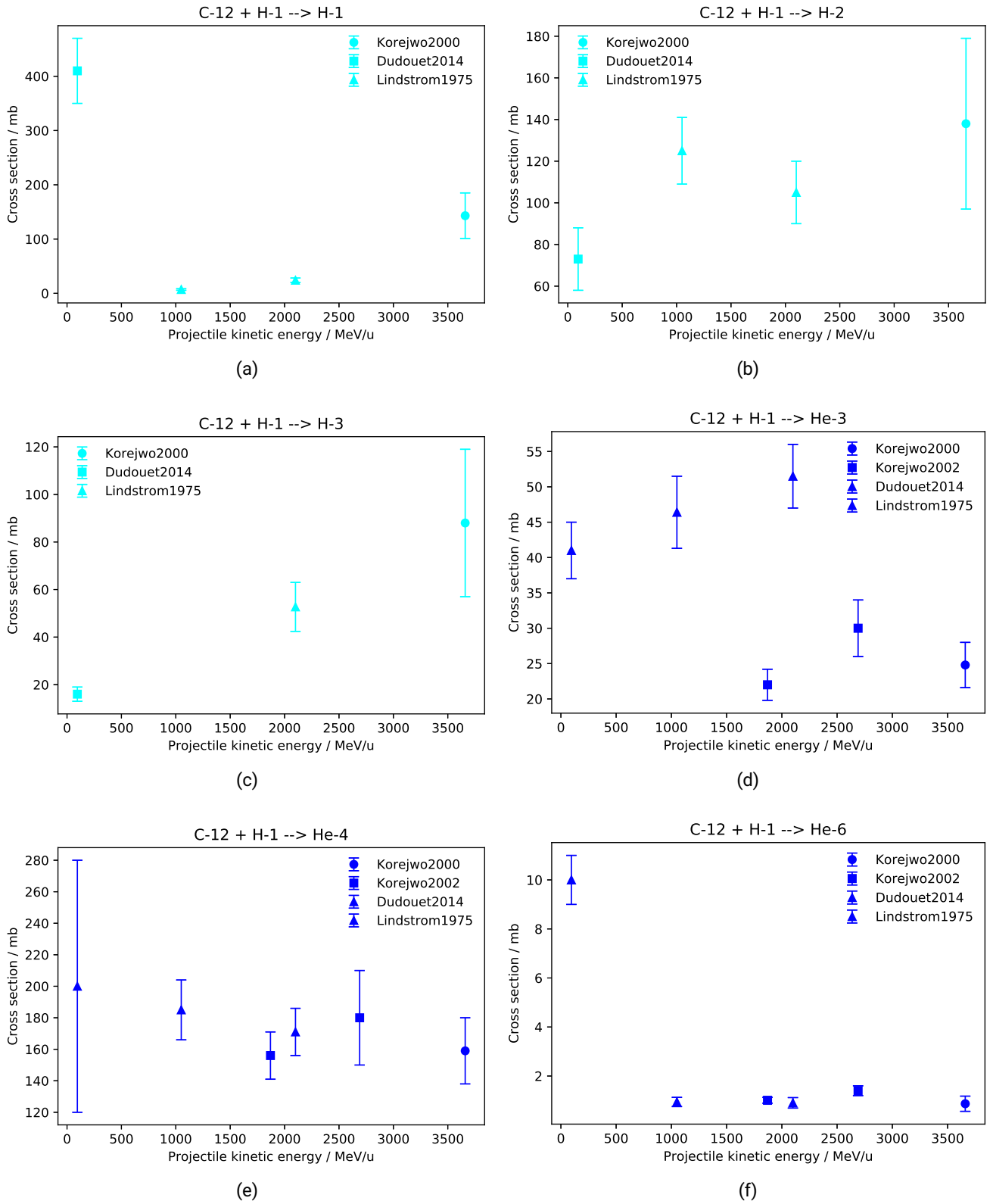


Figure 5.37: Total inclusive isotopic fragment production cross-section data as a function of the projectile kinetic energy for the following reactions:  $^{12}\text{C} + ^1\text{H} \rightarrow ^1\text{H}$ ,  $^{12}\text{C} + ^1\text{H} \rightarrow ^2\text{H}$ ,  $^{12}\text{C} + ^1\text{H} \rightarrow ^3\text{H}$ ,  $^{12}\text{C} + ^1\text{H} \rightarrow ^3\text{He}$ ,  $^{12}\text{C} + ^1\text{H} \rightarrow ^4\text{He}$ ,  $^{12}\text{C} + ^1\text{H} \rightarrow ^6\text{He}$ . Data are from references [277, 286, 300, 301].

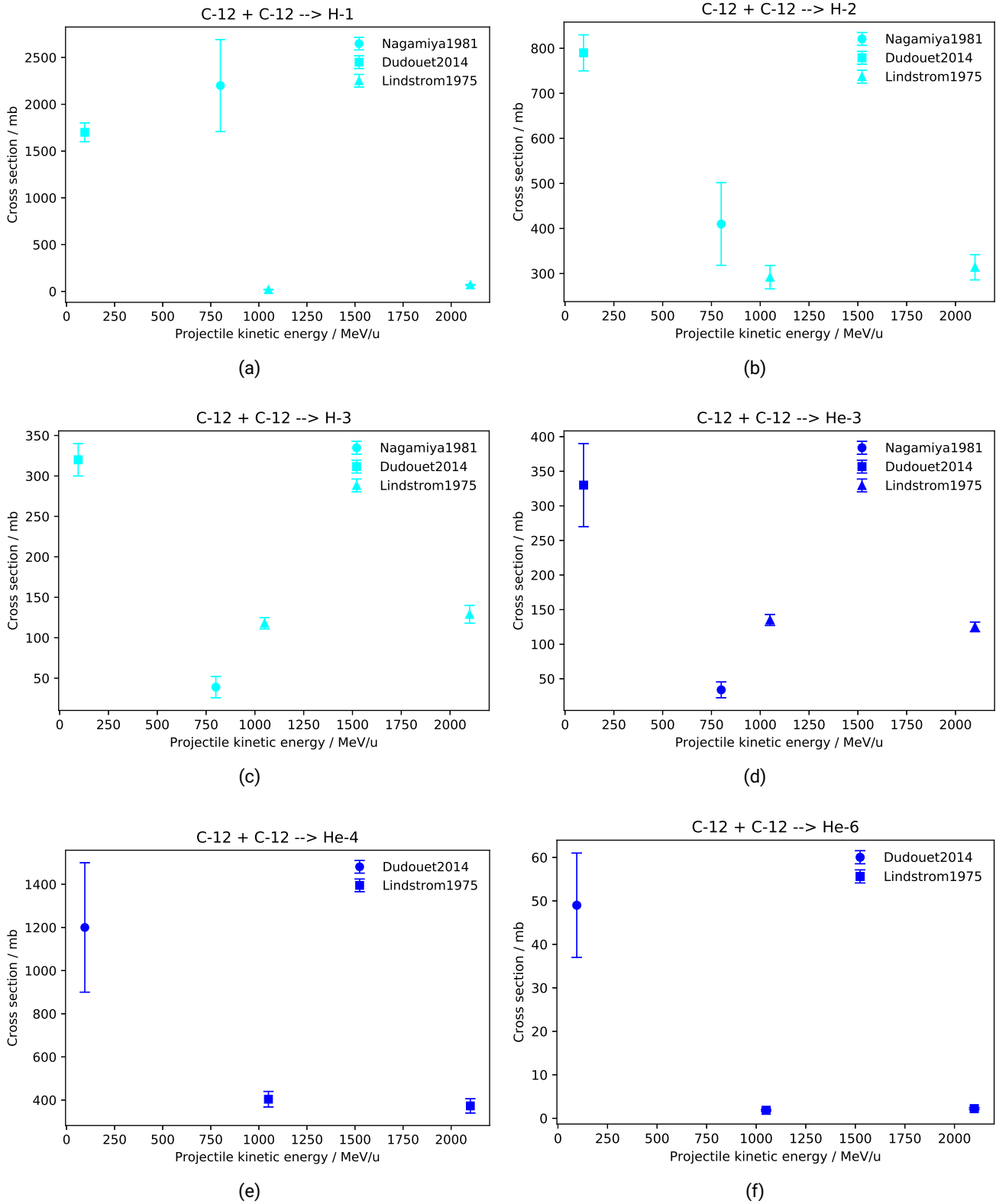


Figure 5.38: Total inclusive isotopic fragment production cross-section data as a function of the projectile kinetic energy for the following reactions:  $^{12}\text{C} + ^{12}\text{C} \rightarrow \text{H-1}$ ,  $^{12}\text{C} + ^{12}\text{C} \rightarrow \text{H-2}$ ,  $^{12}\text{C} + ^{12}\text{C} \rightarrow \text{H-3}$ ,  $^{12}\text{C} + ^{12}\text{C} \rightarrow \text{He-3}$ ,  $^{12}\text{C} + ^{12}\text{C} \rightarrow \text{He-4}$ ,  $^{12}\text{C} + ^{12}\text{C} \rightarrow \text{He-6}$ . Data are from references [277, 286, 302].

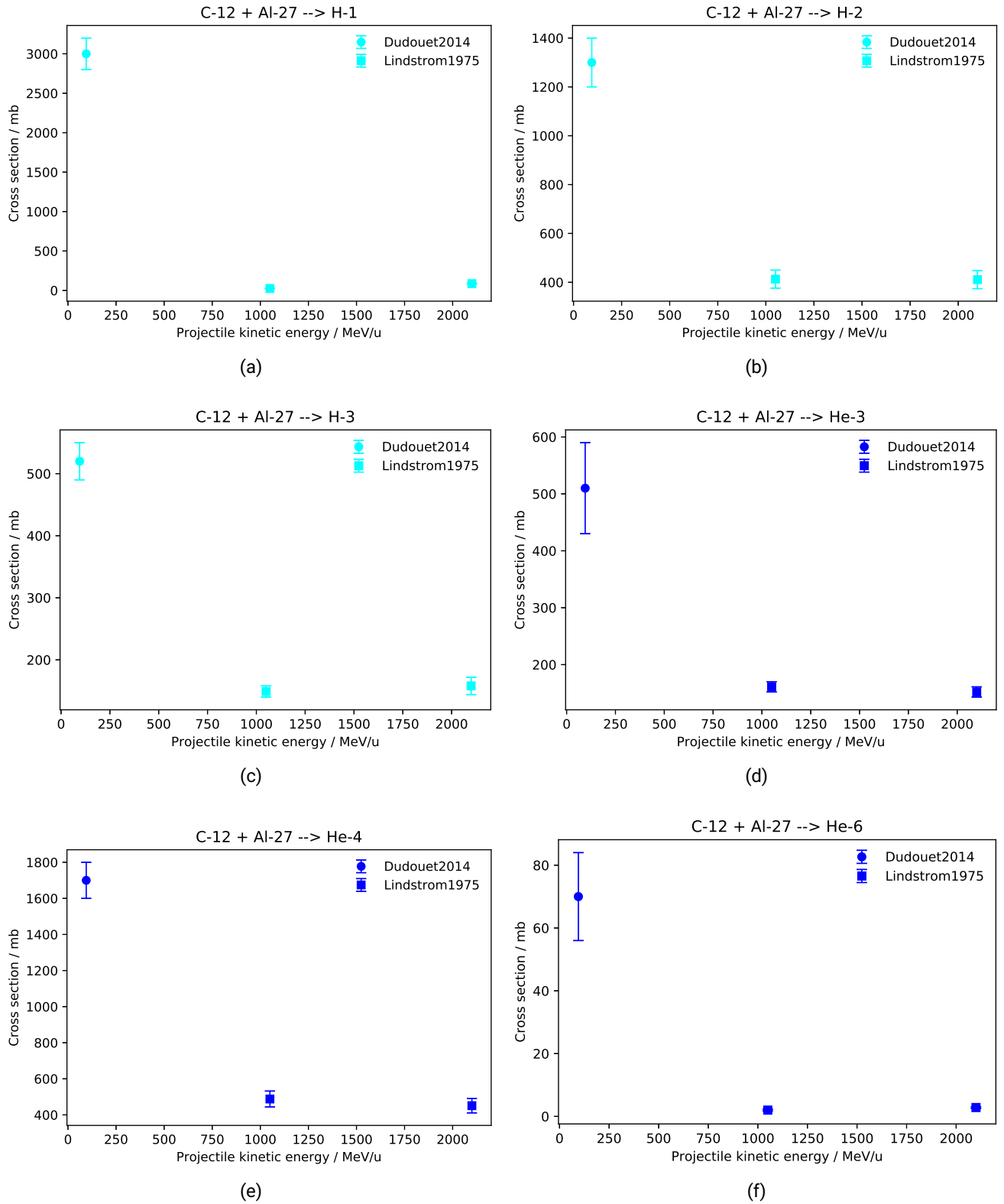


Figure 5.39: Total inclusive isotopic fragment production cross-section data as a function of the projectile kinetic energy for the following reactions:  $^{12}\text{C} + ^{27}\text{Al} \rightarrow ^1\text{H}, ^2\text{H}, ^3\text{H}, ^3\text{He}, ^4\text{He}, ^6\text{He}$ . Data are from references [277, 286].

---

## 5.3 Web Application

---

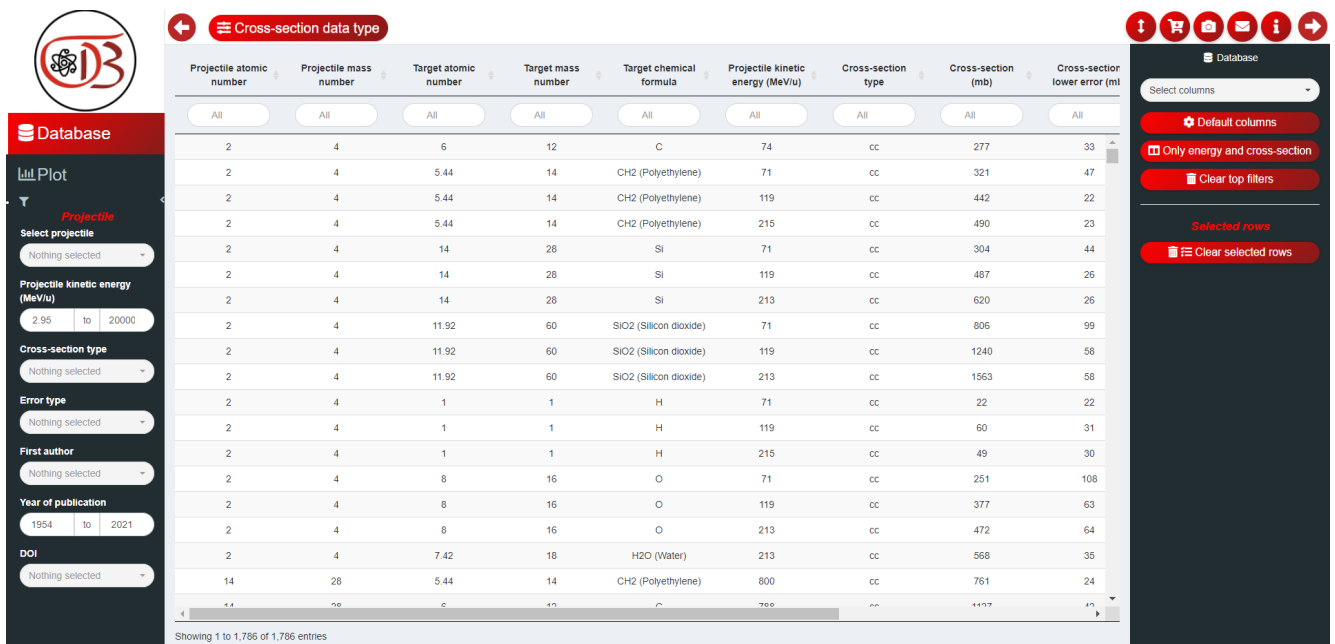
A web application was developed for the users to access the databases. From the link [154], the user can access the database web application itself, the user manual, the reaction cross-section database publication where the database is explained, and the email address of the responsible team.

In the web application (see Figure 5.40), the user can select the database of interest between reaction and fragment production cross-section databases, by selecting it to heading “Cross-section data type”. Once selected the database, two tabs navigate the user to the related sections. The first section is a display of the data (“Database” section). In the second section, the user can directly plot the cross-section data as a function of the projectile kinetic energy (“Plot” section). For the reaction cross-section database, it is possible to also plot the parametrisations described in Section 5.1.2, either alone or alongside the data from the database. The database and plot sections are independent of each other. They are equipped with filters and settings. The filters allow the user to select the data and, eventually, the parametrisations of interest. Through the settings, the visual properties of the data collection and of any generated plots can be adjusted. It is possible to download the database (entire or only the data of interest) and the plots. It is also possible to send feedback about the databases or the app and report eventual bugs to the responsible team, send data and the generated plots to a desired email address without downloading them first, send some data that do not appear in the databases to the responsible team so that they addition can be assessed.

As already mentioned, the plot section allows the user also to plot parametrisations only. In this case, the target can be any isotope, element or self-defined molecule. Atomic and mass numbers of such compound targets are computed as described in section 5.1.1. The cross-sections of projectiles impinging on compound targets are computed as:

$$\sigma = \sum_i n_i(\sigma_i), \quad (5.29)$$

where  $n_i$  is the number of atoms of the element  $i$  in the molecule and  $\sigma_i$  is the reaction cross-section of the projectile with the element.  $\sigma_i$  is computed taking into account the natural isotopic abundances of the element  $i$ .



(a)



(b)

Figure 5.40: Screenshots of the web application. Panel (a) is from the data section of the total reaction cross-section database, without any filters applied. Panel (b) is from the plot section of the total reaction cross-section database, for the system  $^{12}\text{C} + ^{12}\text{C}$ , including only mass-changing cross-section data and all parametrisation.

---

## 5.4 Conclusions of the Cross-Section Databases and Future Work

---

Human space exploration relies on deterministic and stochastic transport codes, and nucleus-nucleus cross-sections are a key ingredient to them. Therefore, nuclear reaction and fragment production cross-section databases for nucleus-nucleus systems were generated as a result of a GSI-ESA-NASA collaboration in the framework of the ROSSINI3 project. Chapter 5 focused on presenting the two data collections generated (reaction cross-section database) or expanded starting from the work of colleagues (fragment production cross-section database) in the framework of this thesis work. The reaction cross-section database contains 1786 data from 103 publications. The fragment production cross-section database contains 7536 data from 69 publications. Both were made open-access and can be found at [154].

---

### 5.4.1 Reaction Cross-Section Database

---

The reaction cross-section database [68] is made of charge-changing and reaction cross-section data. The reaction data were compared to the parametrisations implemented in the MC codes most commonly used for radiation protection in space applications, namely the Kox, Shen, Kox-Shen, Tripathi, and Hybrid Kurotama parametrisations.

The comparison between data and parametrisations allowed to highlight some problems in some of the available datasets, point out limitations in the parametrisations such as the projectile-target asymmetry issue and the large differences at high energies and give recommendations about which parametrisations fit the data best depending on the system and energy region and what are the gaps in the currently available cross-section data. In particular, the Kox-Shen model is the best at reproducing the data at low energies and high energies for most systems, Tripathi96 can reproduce the data trend at intermediate energies, and Hybrid-Kurotama works well at intermediate and high energies. Concerning light systems, Tripathi99 can reproduce the high-energy trend of the data well.

Additionally, the lack of data in the high-energy ( $> 1 \text{ GeV u}^{-1}$ ) region, where the models show significant differences, leads to large uncertainties in transport simulations. Therefore, it is recommended to measure such high-energy data for the systems listed in Equation 5.27. Particular attention should be paid to:

- helium projectiles because of their relative contribution to dose equivalent behind thick shields [105] and
- lithium targets, because lithium-based hydrides are promising innovative shielding materials in space and nearly no cross-section data are available in the literature.

Also, the data from the database were used to optimise the Tripathi model. Therefore, this optimised version of the Tripathi model is the parametrisation fitting the existing sets of data best. Nevertheless, this optimised model should be validated by comparing the outcome of MC simulations with and without its implementation to accelerator-based data, such as absorbed dose measurements [270].

---

### 5.4.2 Fragment Production cross-section database

---

The fragment production cross-section database is made of elemental and isotopic cross-section data. The data for systems of interest for space are reported. Elemental cross-section data are missing for:

- lithium (but for iron projectiles), oxygen, and silicon targets,
- very light fragments ( $Z_f \leq 3$ ) for projectiles heavier than carbon.

---

Concerning isotopic cross-sections, data are missing for:

- helium projectiles,
- lithium, oxygen, and silicon targets,
- the system  $^{56}\text{Fe} + ^{27}\text{Al}$ ,
- low-Z fragments for iron projectiles,
- energies of interest for space for the systems  $^4\text{He} + ^{12}\text{C}$  and  $^{12}\text{C} + ^{16}\text{O}$ .

In both cases, such literature gaps should be covered. In addition, a study was conducted on the energy dependence of isotopic cross-sections for the cases in which data of isotopic cross-sections at different energies are available in the literature.

Future developments include comparing these data to the parametrisations most commonly used for radiation protection in space applications, namely EPAX3, FRACS, SPACS, NUCFRG3, and RAADFRG.





---

## 6 Conclusions and Future Work

---

The damages caused by GCRs represent a main obstacle to deep-space exploration and passive shielding is currently the most promising radiation protection strategy. This thesis work focused on accelerator-based experimental campaigns performed with standard, innovative, and potential *in situ* shielding materials [132], the comparison of these results with the most commonly used MC transport codes, and a revision of the available nuclear cross-section data and parametrisations used in these codes to model them [68].

The experimental campaigns were performed in the framework of the ESA project ROSSINI3 [15] and the GSI project DEIMOS, with beams of interest for radiation protection in space, namely 1 GeV  $u^{-1}$   $^{56}\text{Fe}$ , 2 GeV  $^1\text{H}$ , 480 MeV  $^1\text{H}$ , and 430 MeV  $u^{-1}$   $^4\text{He}$ . On the one hand,  $^{56}\text{Fe}$  is the main contributor to dose equivalent behind thin shields. [4, 37]. On the other hand, light ions such as  $^1\text{H}$  and  $^4\text{He}$  are the main contributors behind thick shields. The target materials used for the experimental campaigns are structural spacecraft materials such as aluminium, standard shielding materials such as PE, innovative shielding materials such as lithium-based hydrides, potential dual-use components i.e. Li-poly batteries, and *in situ* shielding materials such as Moon regolith. Lithium-based hydrides had already shown promising absorbed dose attenuation results both through experiments and simulation campaigns. Nevertheless, they are not chemically stable as they react with the moisture in the air. Therefore, composite materials were produced by adding a stabilising paraffin matrix to the pure hydrides and they were tested within this work. The irradiations with  $^{56}\text{Fe}$  showed a consistent dose attenuation for all the target materials. The materials performing the best are the lithium-based hydrides. In particular, the measurements confirmed that LiH is the best material among the ones investigated in this work concerning heavy-ion dose attenuation. Both the pure hydrides and their version chemically stabilised in a paraffin matrix performed better than PE. Among them, LiH-paraffin seems to combine the excellent dose attenuation properties of LiH with manageable chemical stability. This suggests a big potential of the chemically stable innovative material LiH-paraffin for its use in space radiation shielding applications. On the other hand, the irradiations with the light ions showed a consistent dose build-up, which is stronger for lighter ions and higher energies. This dose enhancement in the first centimetres of materials causes an inverse shielding, as the dose increases because of the presence of the shielding material. Since the GCR spectrum is made of both light and heavy ions, the dose ratio due to the presence of the shields in space will be a mixture of the dose attenuation of the heavy-ion contribution and the dose build-up of the light ions.

Future developments of such experimental campaigns include testing the biological effectiveness of the most promising materials through biological experiments with cells and animals. In particular, a GCR simulator should be used to take into account possible synergistic effects of the complex space radiation field. Also, measurements characterising the full secondary particle spectra behind the shields would be very useful, especially to be benchmarked with MC codes. In particular, for physics experiments, one could conceivably construct a GCR simulator by collecting single-beam data on the same target, both from literature and from new experiments. This is similar to what was done in this work for LiH, but using even more ions and energies.

The results obtained during the experimental campaigns were then compared to the simulation results of some of the most commonly used MC codes for radiation protection in space applications, namely FLUKA, PHITS, and Geant4. The Geant4 and PHITS simulations were performed by the Thales Alenia Space

---

Italia team and the FLUKA simulations were carried out within the scope of this Thesis. Overall, the MC simulation results showed significant and systematic differences among codes that are used for the same radiation protection purposes. These differences are mainly due to the different nuclear cross-section models used. Therefore, a comprehensive data collection was generated within this work as a GSI-ESA-NASA collaboration and was made available as open-access online [154], where the data can be downloaded and plotted.

As a result of a systematic study of the systems of interest for radiation protection in space, gaps in the experimental data were pointed out. For several systems, no data are present in the literature at any energy range. These gaps are therefore recommended to be filled. Particular attention should be focused on  $^4\text{He}$  projectiles because of their relevance to dose equivalent behind thick shields in space and to lithium targets, as no data are present in literature and lithium-based hydrides are promising innovative candidate shielding materials for space missions.

The study also included a systematic comparison between the data and the semi-empirical parametrisations implemented in the MC codes used for space. This highlighted the need for high-energy data as the parametrisation predictions differ largely at high-energies, leading to high uncertainties in the outcome of MC codes depending on the parametrisation used. Also, no single parametrisation appears to reproduce well the experimental data for all systems and energy regions. Thanks to the comprehensive data collection generated in this work, an optimisation of the Tripathi (both Tripathi96 and 99) model was performed. Tripathi was chosen because of the high number of free parameters, which were changed system by system to fit the data at best. In the future, these optimisations should be tested by implementing them into MC codes and comparing the simulation outcome with experimental results of e.g. absorbed dose curves. Future developments also include the usage of one optimal cross-section parametrisation in all MC codes, as the preparation of space exploration missions from the radiation protection point of view fully relies on them.

This work went, therefore, through three different aspects of the field of passive shielding from space radiation. Firstly, it added both heavy and light-ion experimental data on many materials of interest for space, including the promising innovative lithium-based hydrides. Secondly, it provided a complete benchmark of MC codes with these data and considerations about the nuclear cross-section models implemented in the codes were drawn. Lastly, a comprehensive nuclear reaction and production cross-section data collection was developed, which allowed the highlighting of gaps in the experimental data and the systematic comparison of the data with the most commonly used parametrisations in MC codes.

---

## Bibliography

---

- [1] “The global exploration roadmap,” International Space Exploration Coordination Group, Tech. Rep., 2018.
- [2] <https://imagine.gsfc.nasa.gov/Images/science/abund2.gif>.
- [3] J. Chancellor, G. Scott, and J. Sutton, “Space Radiation: The Number One Risk to Astronaut Health beyond Low Earth Orbit,” *Life*, 2014. DOI: <https://doi.org/10.3390/life4030491>.
- [4] M Durante and F. Cucinotta, “Physical basis of radiation protection in space travel,” *Rev. Mod. Phys.*, vol. 83, pp. 1245–1281, 4 2011. DOI: 10.1103/RevModPhys.83.1245. [Online]. Available: <https://link.aps.org/doi/10.1103/RevModPhys.83.1245>.
- [5] J Miller, C Zeitlin, F. Cucinotta, L Heilbronn, D Stephens, and J. Wilson, “Benchmark studies of the effectiveness of structural and internal materials as radiation shielding for the international space station,” *Radiat. Res.*, vol. 159, no. 3, pp. 381–390, 2003, ISSN: 0033-7587. DOI: 10.1667/0033-7587(2003)159[0381:BSOTE0]2.0.CO;2.
- [6] M. Shavers *et al.*, “Implementation of alara radiation protection on the iss through polyethylene shielding augmentation of the service module crew quarters,” *Adv. Space Res.*, vol. 34, no. 6, pp. 1333–1337, 2004, ISSN: 0273-1177. DOI: <https://doi.org/10.1016/j.asr.2003.10.051>.
- [7] C Zeitlin, S. Guetersloh, L. Heilbronn, and J. Miller, “Measurements of materials shielding properties with 1 GeV/nuc  $^{56}\text{Fe}$ ,” *Nucl. Instrum. Methods Phys. Res. B*, vol. 252, no. 2, pp. 308–318, 2006, ISSN: 0168-583X. DOI: <https://doi.org/10.1016/j.nimb.2006.08.011>. [Online]. Available: <https://www.sciencedirect.com/science/article/pii/S0168583X06008809>.
- [8] C Zeitlin *et al.*, “Shielding experiments with high-energy heavy ions for spaceflight applications,” *New J. Phys.*, vol. 10, no. 7, p. 075 007, 2008. DOI: 10.1088/1367-2630/10/7/075007. [Online]. Available: <https://doi.org/10.1088/1367-2630/10/7/075007>.
- [9] S Guetersloh *et al.*, “Polyethylene as a radiation shielding standard in simulated cosmic-ray environments,” *Nucl. Instrum. Methods Phys. Res. B*, vol. 252, no. 2, pp. 319–332, 2006, ISSN: 0168-583X. DOI: <https://doi.org/10.1016/j.nimb.2006.08.019>. [Online]. Available: <https://www.sciencedirect.com/science/article/pii/S0168583X06008822>.
- [10] J Barthel and N Sarigul-Klijn, “Radiation production and absorption in human spacecraft shielding systems under high charge and energy galactic cosmic rays: Material medium, shielding depth, and byproduct aspects,” *Acta Astronaut.*, vol. 144, pp. 254–262, 2018, ISSN: 0094-5765. DOI: <https://doi.org/10.1016/j.actaastro.2017.12.040>.
- [11] M Girauo *et al.*, “Accelerator-Based Tests of Shielding Effectiveness of Different Materials and Multilayers using High-Energy Light and Heavy Ions,” *Radiat. Res.*, vol. 190, no. 5, pp. 526–537, Aug. 2018, ISSN: 0033-7587. DOI: <https://doi.org/10.1667/RR15111.1>.
- [12] C Schuy *et al.*, “Experimental Assessment of Lithium Hydride’s Space Radiation Shielding Performance and Monte Carlo Benchmarking,” *Radiat. Res.*, vol. 191, no. 2, pp. 154–161, Nov. 2018, ISSN: 0033-7587. DOI: <https://doi.org/10.1667/RR15123.1>.

- 
- [13] L. Castellanos *et al.*, “Thick-target yields of secondary ions and neutrons for validation of radiation transport codes,” in *2017 IEEE Aerospace Conference*, 2017, pp. 1–10. doi: 10.1109/AERO.2017.7943575.
- [14] D Boscolo *et al.*, “Characterization of the secondary neutron field produced in a thick aluminum shield by 1 gev/u  $^{56}\text{Fe}$  ions using tld-based ambient dosimeters,” *Front. Phys.*, vol. 8, p. 365, 2020, ISSN: 2296-424X. doi: 10.3389/fphy.2020.00365. [Online]. Available: <https://www.frontiersin.org/article/10.3389/fphy.2020.00365>.
- [15] ROSSINI3 team, “Tasi-sd-ros3-tno-0432 rossini3 final report,” ESA *et al.*, Tech. Rep., 2021.
- [16] M Giraudo and C Lobascio, “Developments in passive shielding for human explorations missions: the ROSSINI study,” in *40th COSPAR Scientific Assembly*, vol. 40, Jan. 2014, F2.2-30-14, F2.2-30-14.
- [17] C Schuy *et al.*, “Status of the rossini project at gsi,” Tech. Rep., 2012.
- [18] C Schuy, M. Rovituso, R. Pleskac, C. La Tessa, and M. Durante, “The rossini project at gsi,” Tech. Rep., 2014, p. 248.
- [19] Department of Nuclear Safety and Security INTERNATIONAL ATOMIC ENERGY AGENCY, *Iaea safety glossary*, 2006.
- [20] F Takahashi, “Icru report 51,” Japan, Tech. Rep. JAERI-Conf-95-007, 1995.
- [21] “Unsear 2008 report vol. i,” United Nations Scientific Committee on the Effects of Atomic Radiation, Tech. Rep., 2008.
- [22] “Icrp, 2007. the 2007 recommendations of the international commission on radiological protection. icrp publication 103,” The International Commission on Radiological Protection, Tech. Rep., 2007, pp. 2–4.
- [23] “Icru report 60: Fundamental quantities and units for ionizing radiation,” International commission on radiation units and measurements, Tech. Rep., 1998.
- [24] G Iliakis, E Mladenov, and V Mladenova, “Necessities in the processing of dna double strand breaks and their effects on genomic instability and cancer,” *Cancers*, vol. 11, no. 11, 2019, ISSN: 2072-6694. doi: <https://doi.org/10.3390/cancers11111671>.
- [25] M Krämer and G Kraft, “Calculations of heavy-ion track structure,” *Radiat. Environ. Biophys.*, vol. 33, no. 2, pp. 91–109, 1994, ISSN: 1432-2099. doi: 10.1007/BF01219334.
- [26] M Krämer and M Durante, “Ion beam transport calculations and treatment plans in particle therapy,” *Eur. Phys. J. D*, vol. 60, no. 1, pp. 195–202, 2010, ISSN: 1434-6079. doi: <https://doi.org/10.1140/epjd/e2010-00077-8>.
- [27] M. Krämer, <http://bio.gsi.de/DOCS/trax.html>.
- [28] R Katz, S. C. Sharma, and M Homayoonfar, *Topics in radiation dosimetry*. 1972, p. 317.
- [29] M Belli *et al.*, “Inactivation and mutation induction in v79 cells by low energy protons: Re-evaluation of the results at the Inl facility,” *Int. J. Radiat. Biol.*, vol. 63, no. 3, pp. 331–337, 1993, ISSN: 0955-3002. doi: <https://doi.org/10.1080/09553009314550441>.
- [30] F. A. Cucinotta, J. W. Wilson, M. R. Shavers, and R. Katz, “Effects of track structure and cell inactivation on the calculation of heavy ion mutation rates in mammalian cells,” *Int. J. Radiat. Biol.*, vol. 69, no. 5, pp. 593–600, 1996, ISSN: 0955-3002. doi: <https://doi.org/10.1080/095530096145607>.

- 
- [31] H Nikjoo, S. Uehara, W. E. Wilson, M. Hoshi, and D. T. Goodhead, "Track structure in radiation biology: Theory and applications," *Int. J. Radiat. Biol.*, vol. 73, no. 4, pp. 355–364, 1998. doi: 10.1080/095530098142176. eprint: <https://doi.org/10.1080/095530098142176>. [Online]. Available: <https://doi.org/10.1080/095530098142176>.
- [32] D. Schardt, T. Elsässer, and D. Schulz-Ertner, "Heavy-ion tumor therapy: Physical and radiobiological benefits," *Rev. Mod. Phys.*, vol. 82, no. 1, p. 383, 2010. doi: <https://doi.org/10.1103/RevModPhys.82.383>.
- [33] E. J. Hall and A. J. Giaccia, *Radiobiology for the radiologist*. Hagerstown, Md. : Medical Dept., Harper & Row, 1973. [Online]. Available: <https://search.library.wisc.edu/catalog/999539825402121>.
- [34] United Nations Scientific Committee on the Effects of Atomic Radiation, "Unsear 2010 report vol. i: Sources and effects of ionizing radiation. volume i," United Nations, Tech. Rep., 2010.
- [35] "Icrp, 1977. recommendations of the icrp. icrp publication 26.," The International Commission on Radiological Protection, Tech. Rep., 1977, p. 1.
- [36] *Human research roadmap*, <https://humanresearchroadmap.nasa.gov/>.
- [37] M. Durante, "Space radiation protection: Destination mars," *Life Sci. Space Res.*, vol. 1, pp. 2–9, 2014, ISSN: 2214-5524. doi: <https://doi.org/10.1016/j.lssr.2014.01.002>. [Online]. Available: <https://www.sciencedirect.com/science/article/pii/S2214552414000042>.
- [38] P. Carlson, "Discovery of cosmic rays," *AIP Conf. Proc.*, vol. 1516, no. 1, pp. 9–16, 2013. doi: 10.1063/1.4792532. [Online]. Available: <https://aip.scitation.org/doi/abs/10.1063/1.4792532>.
- [39] R. McGuire, T. Von Rosenvinge, and F. McDonald, "The composition of solar energetic particles," *Astrophys. J.*, vol. 301, pp. 938–961, 1986. [Online]. Available: <https://adsabs.harvard.edu/pdf/1986ApJ...301..938M>.
- [40] R. Tripathi, J. Wilson, F. Badavi, and G De Angelis, "A characterization of the moon radiation environment for radiation analysis," *Adv. Space Res.*, vol. 37, no. 9, pp. 1749–1758, 2006, Space Life Sciences: Flight Measurements, Calibration of Detectors and Environmental Models for Radiation Analysis, ISSN: 0273-1177. doi: <https://doi.org/10.1016/j.asr.2006.03.016>. [Online]. Available: <https://www.sciencedirect.com/science/article/pii/S0273117706001384>.
- [41] E. Cliver, "The 1859 space weather event: Then and now," *Adv. Space Res.*, vol. 38, no. 2, pp. 119–129, 2006, The Great Historical Geomagnetic Storm of 1859: A Modern Look, ISSN: 0273-1177. doi: <https://doi.org/10.1016/j.asr.2005.07.077>. [Online]. Available: <https://www.sciencedirect.com/science/article/pii/S0273117705010215>.
- [42] J. W. Wilson *et al.*, "Shielding from solar particle event exposures in deep space," *Radiat. Meas.*, vol. 30, no. 3, pp. 361–382, 1999, ISSN: 1350-4487. doi: [https://doi.org/10.1016/S1350-4487\(99\)00063-3](https://doi.org/10.1016/S1350-4487(99)00063-3). [Online]. Available: <https://www.sciencedirect.com/science/article/pii/S1350448799000633>.
- [43] J. W. Cronin, "Cosmic rays: The most energetic particles in the universe," in *More Things in Heaven and Earth: A Celebration of Physics at the Millennium*, B. Bederson, Ed. New York, NY: Springer New York, 1999, pp. 278–290, ISBN: 978-1-4612-1512-7.



- 
- [44] F. A. Cucinotta, H. Nikjoo, and D. T. Goodhead, "The Effects of Delta Rays on the Number of Particle-Track Traversals per Cell in Laboratory and Space Exposures," *Radiat. Res.*, vol. 150, no. 1, pp. 115–119, Jul. 1998, ISSN: 0033-7587. DOI: 10.2307/3579651. eprint: <https://meridian.allenpress.com/radiation-research/article-pdf/150/1/115/2143379/3579651.pdf>. [Online]. Available: <https://doi.org/10.2307/3579651>.
- [45] J. W. Norbury, W. Schimmerling, T. C. Slaba, *et al.*, "Galactic cosmic ray simulation at the nasa space radiation laboratory," *Life Sci. Space Res.*, vol. 8, pp. 38–51, 2016, ISSN: 2214-5524. DOI: <https://doi.org/10.1016/j.lssr.2016.02.001>.
- [46] C Zeitlin *et al.*, "Measurements of energetic particle radiation in transit to mars on the mars science laboratory," *Science*, vol. 340, no. 6136, pp. 1080–1084, 2013. DOI: 10.1126/science.1235989. eprint: <https://www.science.org/doi/pdf/10.1126/science.1235989>. [Online]. Available: <https://www.science.org/doi/abs/10.1126/science.1235989>.
- [47] G. Horneck *et al.*, "Humex, a study on the survivability and adaptation of humans to long-duration exploratory missions, part ii: Missions to mars," *Adv. Space Res.*, vol. 38, no. 4, pp. 752–759, 2006, ISSN: 0273-1177. DOI: <https://doi.org/10.1016/j.asr.2005.06.072>.
- [48] S. Avdeev *et al.*, "Eye light flashes on the mir space station," *Acta Astronaut.*, vol. 50, no. 8, pp. 511–525, 2002, ISSN: 0094-5765. DOI: [https://doi.org/10.1016/S0094-5765\(01\)00190-4](https://doi.org/10.1016/S0094-5765(01)00190-4).
- [49] W. G. Sannita, L. Narici, and P. Picozza, "Positive visual phenomena in space: A scientific case and a safety issue in space travel," *Vision Res.*, vol. 46, no. 14, pp. 2159–2165, 2006, ISSN: 0042-6989. DOI: <https://doi.org/10.1016/j.visres.2005.12.002>.
- [50] V. Bidoli *et al.*, "Study of cosmic rays and light flashes on board space station mir: The sileye experiment," *Adv. Space Res.*, vol. 25, no. 10, pp. 2075–2079, 2000, ISSN: 0273-1177. DOI: [https://doi.org/10.1016/S0273-1177\(99\)01017-0](https://doi.org/10.1016/S0273-1177(99)01017-0).
- [51] M. Casolino *et al.*, "Dual origins of light flashes seen in space," *Nature*, vol. 422, no. 6933, pp. 680–680, 2003, ISSN: 1476-4687. DOI: <https://doi.org/10.1038/422680a>.
- [52] G. Reitz, T. Berger, and D. Matthiae, "Radiation exposure in the moon environment," *Planet. Space Sci.*, vol. 74, no. 1, pp. 78–83, 2012, Scientific Preparations For Lunar Exploration, ISSN: 0032-0633. DOI: <https://doi.org/10.1016/j.pss.2012.07.014>. [Online]. Available: <https://www.sciencedirect.com/science/article/pii/S0032063312002085>.
- [53] B. Ehresmann *et al.*, "Charged particle spectra measured during the transit to mars with the mars science laboratory radiation assessment detector (msl/rad)," *Life Sci. Space Res.*, vol. 10, pp. 29–37, 2016, ISSN: 2214-5524. DOI: <https://doi.org/10.1016/j.lssr.2016.07.001>. [Online]. Available: <https://www.sciencedirect.com/science/article/pii/S2214552416300050>.
- [54] J. W. Wilson, M. S. Cloudsley, F. A. Cucinotta, R. K. Tripathi, J. E. Nealy, and G. De Angelis, "Deep space environments for human exploration," *Adv. Space Res.*, vol. 34, no. 6, pp. 1281–1287, 2004, ISSN: 0273-1177. DOI: <https://doi.org/10.1016/j.asr.2003.10.052>.
- [55] L. W. Townsend *et al.*, "Estimates of carrington-class solar particle event radiation exposures on mars," *Acta Astronaut.*, vol. 69, no. 7, pp. 397–405, 2011, ISSN: 0094-5765. DOI: <https://doi.org/10.1016/j.actaastro.2011.05.020>. [Online]. Available: <https://www.sciencedirect.com/science/article/pii/S0094576511001585>.

- 
- [56] L. W. Townsend, J. A. Anderson, A. M. Adamczyk, and C. M. Werneth, "Estimates of carrington-class solar particle event radiation exposures as a function of altitude in the atmosphere of mars," *Acta Astronaut.*, vol. 89, pp. 189–194, 2013, ISSN: 0094-5765. doi: <https://doi.org/10.1016/j.actaastro.2013.04.010>. [Online]. Available: <https://www.sciencedirect.com/science/article/pii/S0094576513001227>.
- [57] S. McKenna-Lawlor, P. Gonçalves, A. Keating, G. Reitz, and D. Matthiä, "Overview of energetic particle hazards during prospective manned missions to mars," *Planet. Space Sci.*, vol. 63-64, pp. 123–132, 2012, Advances in Planetary Atmospheres and Exploration, ISSN: 0032-0633. doi: <https://doi.org/10.1016/j.pss.2011.06.017>. [Online]. Available: <https://www.sciencedirect.com/science/article/pii/S0032063311002030>.
- [58] L. W. Townsend *et al.*, "Extreme solar event of ad775: Potential radiation exposure to crews in deep space," *Acta Astronaut.*, vol. 123, pp. 116–120, 2016, Special Section: Selected Papers from the International Workshop on Satellite Constellations and Formation Flying 2015, ISSN: 0094-5765. doi: <https://doi.org/10.1016/j.actaastro.2016.03.002>. [Online]. Available: <https://www.sciencedirect.com/science/article/pii/S0094576515303301>.
- [59] <https://www.grc.nasa.gov/www/k-12/airplane/atmosmrm.html>.
- [60] H. Bethe, "Zur theorie des durchgangs schneller korpuskularstrahlen durch materie," *Annalen der Physik*, vol. 397, no. 3, pp. 325–400, 1930, ISSN: 0003-3804. doi: <https://doi.org/10.1002/andp.19303970303>.
- [61] F. Bloch, "Zur bremsung rasch bewegter teilchen beim durchgang durch materie," *Annalen der Physik*, vol. 408, no. 3, pp. 285–320, 1933, ISSN: 0003-3804. doi: <https://doi.org/10.1002/andp.19334080303>.
- [62] E. Fermi, "The ionization loss of energy in gases and in condensed materials," *Phys. Rev.*, vol. 57, no. 6, p. 485, 1940. doi: <https://doi.org/10.1103/PhysRev.57.485>.
- [63] G Kraft, M Scholz, and U Bechthold, "Tumor therapy and track structure," *Radiat. Environ. Biophys.*, vol. 38, no. 4, pp. 229–237, 1999, ISSN: 1432-2099. doi: <https://doi.org/10.1007/s004110050163>.
- [64] H Bichsel, "Shell corrections in stopping powers," *Phys. Rev. A*, vol. 65, p. 052 709, 5 2002. doi: <https://doi.org/10.1103/PhysRevA.65.052709>. [Online]. Available: <https://link.aps.org/doi/10.1103/PhysRevA.65.052709>.
- [65] W. H. Barkas, W. Birnbaum, and F. M. Smith, "Mass-ratio method applied to the measurement of l-meson masses and the energy balance in pion decay," *Phys. Rev.*, vol. 101, pp. 778–795, 2 1956. doi: <https://doi.org/10.1103/PhysRev.101.778>. [Online]. Available: <https://link.aps.org/doi/10.1103/PhysRev.101.778>.
- [66] W. H. Barkas, J. N. Dyer, and H. H. Heckman, "Resolution of the  $\Sigma^-$ -mass anomaly," *Phys. Rev. Lett.*, vol. 11, pp. 138–138, 3 1963. doi: <https://doi.org/10.1103/PhysRevLett.11.138>. [Online]. Available: <https://link.aps.org/doi/10.1103/PhysRevLett.11.138>.
- [67] *Microdosimetry ICRU report 36*. International Commission on Radiation Units and Measurements; Bethesda, MD (United States), 1983.
- [68] F Luoni *et al.*, "Total nuclear reaction cross-section database for radiation protection in space and heavy-ion therapy applications," *New J. Phys.*, vol. 23, no. 101201, 2021. doi: <https://doi.org/10.1088/1367-2630/ac27e1>.

- 
- [69] R Serber, “Nuclear reactions at high energies,” *Phys. Rev.*, vol. 72, pp. 1114–1115, 11 1947. doi: 10.1103/PhysRev.72.1114. [Online]. Available: <https://link.aps.org/doi/10.1103/PhysRev.72.1114>.
- [70] NASA, United States, Tech. Rep., 1984.
- [71] H. Bradt and B Peters, “The Heavy Nuclei of the Primary Cosmic Radiation,” *Phys. Rev.*, vol. 77, pp. 54–70, 1 1950. doi: 10.1103/PhysRev.77.54. [Online]. Available: <https://link.aps.org/doi/10.1103/PhysRev.77.54>.
- [72] J. Norbury *et al.*, “Nuclear data for space radiation,” *Radiat. Meas.*, vol. 47, no. 5, pp. 315–363, 2012, issn: 1350-4487. doi: <https://doi.org/10.1016/j.radmeas.2012.03.004>. [Online]. Available: <http://www.sciencedirect.com/science/article/pii/S1350448712000686>.
- [73] G. Rudstam, “Systematics of spallation yields,” *Z. Naturforschung A*, vol. 21, no. 7, pp. 1027–1041, 1966. doi: doi:10.1515/zna-1966-0724. [Online]. Available: <https://doi.org/10.1515/zna-1966-0724>.
- [74] R. Silberberg and C. H. Tsao, “Partial Cross-Sections in High-Energy Nuclear Reactions, and Astrophysical Applications. I. Targets With  $Z \leq 28$ ,” *Astrophys. J., Suppl. Ser.*, vol. 25, pp. 315–333, 1973, issn: 0067-0049.
- [75] B. Mei, “Universal odd-even staggering in isotopic fragmentation and spallation cross sections,” *Phys. Rev. C*, vol. 100, p. 054619, 5 2019. doi: 10.1103/PhysRevC.100.054619. [Online]. Available: <https://link.aps.org/doi/10.1103/PhysRevC.100.054619>.
- [76] K. Sümmerer, “Improved empirical parametrization of fragmentation cross sections,” *Physical Review C*, vol. 86, no. 1, p. 014601, 2012. doi: <https://doi.org/10.1103/PhysRevC.86.014601>.
- [77] A. Adamczyk *et al.*, “Nucfrg3: Light ion improvements to the nuclear fragmentation model,” *Nucl. Instrum. Methods Phys. Res. A*, vol. 678, pp. 21–32, 2012, issn: 0168-9002. doi: <https://doi.org/10.1016/j.nima.2012.02.021>. [Online]. Available: <https://www.sciencedirect.com/science/article/pii/S0168900212001842>.
- [78] C. Schmitt, K.-H. Schmidt, and A. Kelić-Heil, “Spacs: A semi-empirical parameterization for isotopic spallation cross sections,” *Phys. Rev. C*, vol. 90, p. 064605, 6 2014. doi: <https://doi.org/10.1103/PhysRevC.90.064605>.
- [79] B. Mei, “Improved empirical parameterization for projectile fragmentation cross sections,” *Phys. Rev. C*, vol. 95, p. 034608, 3 2017. doi: 10.1103/PhysRevC.95.034608. [Online]. Available: <https://link.aps.org/doi/10.1103/PhysRevC.95.034608>.
- [80] C. M. Werneth *et al.*, “Relativistic abrasion-ablation de-excitation fragmentation (raadfrg) model,” *Nucl. Instrum. Methods Phys. Res. B*, vol. 502, pp. 118–135, 2021, issn: 0168-583X. doi: <https://doi.org/10.1016/j.nimb.2021.06.016>.
- [81] C. FA, P. I, P. AL, and K. MH, “Nuclear interactions in heavy ion transport and event-based risk models,” *Radiat Prot Dosimetry*, vol. 143(2-4), pp. 384–90, 2011. doi: 10.1093/rpd/ncq512.
- [82] E Haettner, H Iwase, M Krämer, G Kraft, and D Schardt, “Experimental study of nuclear fragmentation of 200 and 400 MeV/u  $^{12}\text{C}$  ions in water for applications in particle therapy,” *Phys. Med. Biol.*, vol. 58, no. 23, pp. 8265–8279, 2013. doi: 10.1088/0031-9155/58/23/8265. [Online]. Available: <https://doi.org/10.1088/0031-9155/58/23/8265>.



- 
- [83] D Schardt, T Elsässer, and D Schulz-Ertner, “Heavy-ion tumor therapy: Physical and radiobiological benefits,” *Rev. Mod. Phys.*, vol. 82, pp. 383–425, 1 2010. doi: 10.1103/RevModPhys.82.383. [Online]. Available: <https://link.aps.org/doi/10.1103/RevModPhys.82.383>.
- [84] C. Carlsson and G. Carlsson, “Proton dosimetry with 185 mev protons,” *Health Phys.*, vol. 33, no. 5, pp. 481–484, 1977.
- [85] T Pfuhl, F Horst, C Schuy, and U Weber, “Dose build-up effects induced by delta electrons and target fragments in proton bragg curves—measurements and simulations,” *Phys. Med. Biol.*, vol. 63, no. 17, p. 175 002, 2018. doi: 10.1088/1361-6560/aad8fc. [Online]. Available: <https://doi.org/10.1088/1361-6560/aad8fc>.
- [86] United Nations Scientific Committee on the Effects of Atomic Radiation, “Unscar 2000 report vol. i: Sources and effects of ionizing radiation,” United Nations, Tech. Rep., 2000.
- [87] M. Durante and C. Bruno, “Impact of rocket propulsion technology on the radiation risk in missions to mars,” *Eur. Phys. J. D*, vol. 60, no. 1, pp. 215–218, 2010, ISSN: 1434-6079. doi: 10.1140/epjd/e2010-00035-6. [Online]. Available: <https://doi.org/10.1140/epjd/e2010-00035-6>.
- [88] “Report no. 132 – radiation protection guidance for activities in low-earth orbit,” National Council on Radiation Protection and Measurements, Tech. Rep., 2000.
- [89] “Icrp, 1991. 1990 recommendations of the international commission on radiological protection. icrp publication 60.,” The International Commission on Radiological Protection, Tech. Rep., 1991, p. 2.
- [90] F. A. Cucinotta *et al.*, “Space radiation and cataracts in astronauts,” *Radiat. Res.*, vol. 156, no. 5, pp. 460–466, 2001, ISSN: 0033-7587. doi: [https://doi.org/10.1667/0033-7587\(2001\)156\[0460:SRACIA\]2.0.CO;2](https://doi.org/10.1667/0033-7587(2001)156[0460:SRACIA]2.0.CO;2).
- [91] L. T. Chylack Jr *et al.*, “Nasa study of cataract in astronauts (nasca). report 1: Cross-sectional study of the relationship of exposure to space radiation and risk of lens opacity,” *Radiat. Res.*, vol. 172, no. 1, pp. 10–20, 2009, ISSN: 0033-7587. doi: <https://doi.org/10.1667/RR1580.1>.
- [92] F. Cucinotta, M.-H. Y.Kim, and L. Chappell, “Space radiation cancer risk projections and uncertainties – 2012,” NASA, Tech. Rep., 2013.
- [93] E. National Academies of Sciences and Medicine, “Space radiation and astronaut health: Managing and communicating cancer risks,” Tech. Rep., 2021.
- [94] D. Boscolo and M. Durante, “Dose limits and countermeasures for mitigating radiation risk in moon and mars exploration,” *Physics*, vol. 4, no. 1, pp. 172–184, 2022, ISSN: 2624-8174. doi: <https://doi.org/10.3390/physics4010013>.
- [95] F. Cucinotta, M.-H. Kim, L. Chappell, and J. Huff, “How safe is safe enough? radiation risk for a human mission to mars,” *PloS one*, vol. 8, no. 10, e74988, 2013. doi: <https://doi.org/10.1371/journal.pone.0074988>.
- [96] F. A. Cucinotta, W. Schimmerling, E. A. Blakely, and T. K. Hei, “A proposed change to astronaut exposures limits is a giant leap backwards for radiation protection,” *Life Sci. Space Res.*, vol. 31, pp. 59–70, 2021, ISSN: 2214-5524. doi: <https://doi.org/10.1016/j.lssr.2021.07.005>.
- [97] “Report no. 153 – information needed to make radiation protection recommendations for space missions beyond low-earth orbit,” National Council on Radiation Protection and Measurements, Tech. Rep., 2006.

- 
- [98] M. I. Dobynde, Y. Y. Shprits, A. Y. Drozdov, J. Hoffman, and J. Li, "Beating 1 sievert: Optimal radiation shielding of astronauts on a mission to mars," *Space Weather*, vol. 19, no. 9, e2021SW002749, 2021, e2021SW002749 2021SW002749. DOI: <https://doi.org/10.1029/2021SW002749>.
- [99] V. Choutko, H. Hofer, and S. C. C. Ting, "The ams experiment and magnet faraday cage for human space exploration," 2004.
- [100] J. Hoffman, P. Fisher, and O. Batishchev, "Use of superconducting magnet technology for astronaut radiation protection," Tech. Rep., 2005.
- [101] P. Spillantini, "Active shielding for long duration interplanetary manned missions," *Adv. Space Res.*, vol. 45, no. 7, pp. 900–916, 2010, Life Sciences in Space, ISSN: 0273-1177. DOI: <https://doi.org/10.1016/j.asr.2010.01.025>. [Online]. Available: <https://www.sciencedirect.com/science/article/pii/S0273117710000621>.
- [102] M.-H. Y. Kim, M. J. Hayat, A. H. Feiveson, and F. A. Cucinotta, "Prediction of frequency and exposure level of solar particle events," *Health Phys.*, vol. 97, no. 1, 2009, ISSN: 0017-9078. DOI: 10.1097/01.HP.0000346799.65001.9c.
- [103] S. Hu, M.-H. Y. Kim, G. E. McClellan, and F. A. Cucinotta, "Modeling the acute health effects of astronauts from exposure to large solar particle events," *Health Phys.*, vol. 96, no. 4, pp. 465–476, 2009, ISSN: 0017-9078. DOI: 10.1097/01.HP.0000339020.92837.61.
- [104] A. Posner, "Up to 1-hour forecasting of radiation hazards from solar energetic ion events with relativistic electrons," *Space Weather*, vol. 5, no. 5, 2007. DOI: <https://doi.org/10.1029/2006SW000268>. [Online]. Available: <https://agupubs.onlinelibrary.wiley.com/doi/abs/10.1029/2006SW000268>.
- [105] J. Norbury *et al.*, "Are Further Cross Section Measurements Necessary for Space Radiation Protection or Ion Therapy Applications? Helium Projectiles," *Front. Phys.*, vol. 8, p. 409, 2020. DOI: <https://doi.org/10.3389/fphy.2020.565954>.
- [106] T. Slaba and S. Blattnig, "GCR environmental models I: Sensitivity analysis for GCR environments," *Space Weather*, vol. 12, no. 4, pp. 217–224, 2014. DOI: <https://doi.org/10.1002/2013SW001025>. eprint: <https://agupubs.onlinelibrary.wiley.com/doi/pdf/10.1002/2013SW001025>. [Online]. Available: <https://agupubs.onlinelibrary.wiley.com/doi/abs/10.1002/2013SW001025>.
- [107] L. H. Heilbronn, T. B. Borak, L. W. Townsend, P.-E. Tsai, C. A. Burnham, and R. A. McBeth, "Neutron yields and effective doses produced by galactic cosmic ray interactions in shielded environments in space," *Life Sci. Space Res.*, vol. 7, pp. 90–99, 2015, ISSN: 2214-5524. DOI: <https://doi.org/10.1016/j.lssr.2015.10.005>.
- [108] F. Horst, D. Boscolo, M. Durante, F. Luoni, C. Schuy, and U. Weber, "Thick shielding against galactic cosmic radiation: A monte carlo study with focus on the role of secondary neutrons," *Life Sci. Space Res.*, vol. 33, pp. 58–68, 2022, ISSN: 2214-5524. DOI: <https://doi.org/10.1016/j.lssr.2022.03.003>. [Online]. Available: <https://www.sciencedirect.com/science/article/pii/S2214552422000141>.
- [109] S. A. Walker, L. W. Townsend, and J. W. Norbury, "Heavy ion contributions to organ dose equivalent for the 1977 galactic cosmic ray spectrum," *Adv. Space Res.*, vol. 51, no. 9, pp. 1792–1799, 2013, ISSN: 0273-1177. DOI: <https://doi.org/10.1016/j.asr.2012.12.011>.
- [110] National Research Council *et al.*, *Managing space radiation risk in the new era of space exploration*. National Academies Press, 2008.

- 
- [111] S. Washburn, S. Blattnig, R. Singleterry, and S. Westover, "Active magnetic radiation shielding system analysis and key technologies," *Life Sci. Space Res.*, vol. 4, pp. 22–34, 2015, ISSN: 2214-5524. DOI: <https://doi.org/10.1016/j.lssr.2014.12.004>. [Online]. Available: <https://www.sciencedirect.com/science/article/pii/S2214552414000686>.
- [112] E. N. Khalili, "Lunar structures generated and shielded with on-site materials," *J. Aerosp. Eng.*, vol. 2, no. 3, pp. 119–129, 1989, ISSN: 0893-1321. DOI: [https://doi.org/10.1061/\(ASCE\)0893-1321\(1989\)2:3\(119\)](https://doi.org/10.1061/(ASCE)0893-1321(1989)2:3(119)).
- [113] J. Miller *et al.*, "Lunar soil as shielding against space radiation," *Radiat. Meas.*, vol. 44, no. 2, pp. 163–167, 2009, ISSN: 1350-4487. DOI: <https://doi.org/10.1016/j.radmeas.2009.01.010>.
- [114] B. Ehresmann *et al.*, "Natural radiation shielding on mars measured with the msl/rad instrument," *J. Geophys. Res. Planets*, vol. 126, no. 8, e2021JE006851, 2021, ISSN: 2169-9097. DOI: <https://doi.org/10.1029/2021JE006851>.
- [115] T. C. Slaba, A. A. Bahadori, B. D. Reddell, R. C. Singleterry, M. S. Cloudsley, and S. R. Blattnig, "Optimal shielding thickness for galactic cosmic ray environments," *Life Sci. Space Res.*, vol. 12, pp. 1–15, 2017, ISSN: 2214-5524. DOI: <https://doi.org/10.1016/j.lssr.2016.12.003>.
- [116] M. Naito *et al.*, "Investigation of shielding material properties for effective space radiation protection," *Life Sci. Space Res.*, vol. 26, pp. 69–76, 2020, ISSN: 2214-5524. DOI: <https://doi.org/10.1016/j.lssr.2020.05.001>. [Online]. Available: <https://www.sciencedirect.com/science/article/pii/S2214552420300377>.
- [117] M. H. Kalos and P. A. Whitlock, *Monte carlo methods*. John Wiley & Sons, 2009.
- [118] J. W. Wilson *et al.*, "Transport methods and interactions for space radiations," Springer, 1993, pp. 187–786.
- [119] M Kraemer, E Scifoni, M Giraudo, and M Durante, "Towards a space-trip: A space radiation version of the trip98 code," GSI-FAIR Scientific Report 2017, Tech. Rep., 2018, p.289. DOI: 10.15120/GSI-2017-01856.
- [120] R. Y. Rubinstein and D. P. Kroese, *Simulation and the Monte Carlo method*. John Wiley & Sons, 2016.
- [121] <https://hackaday.com/2015/09/11/fermiac-the-computer-that-advanced-the-manhattan-project/>.
- [122] [https://www.esa.int/Science\\_Exploration/Human\\_and\\_Robotic\\_Exploration/Research](https://www.esa.int/Science_Exploration/Human_and_Robotic_Exploration/Research).
- [123] D. Mancusi *et al.*, "Comparison of aluminum and lucite for shielding against 1 gev protons," *Adv. Space Res.*, vol. 40, no. 4, pp. 581–585, 2007, ISSN: 0273-1177. DOI: <https://doi.org/10.1016/j.asr.2006.11.033>.
- [124] C La Tessa, S Guetersloh, L Heilbronn, J Miller, L Sihver, and C Zeitlin, "Fragmentation of 1 gev/nucleon iron ions in thick targets relevant for space exploration," *Adv. Space Res.*, vol. 35, no. 2, pp. 223–229, 2005, Space Life Sciences: Ground-Based Iron-Ion Biology and Physics, Including Shielding, ISSN: 0273-1177. DOI: <https://doi.org/10.1016/j.asr.2005.02.007>. [Online]. Available: <https://www.sciencedirect.com/science/article/pii/S0273117705001730>.
- [125] C Lobascio *et al.*, "Accelerator-based tests of radiation shielding properties of materials used in human space infrastructures," *Health Phys.*, vol. 94, no. 3, 2008, ISSN: 0017-9078. DOI: 10.1097/01.HP.0000288560.21906.4e.

- 
- [126] A. Kennedy, "Biological effects of space radiation and development of effective countermeasures," *Life Sci. Space Res.*, vol. 1, pp. 10–43, 2014, ISSN: 2214-5524. doi: <https://doi.org/10.1016/j.lssr.2014.02.004>. [Online]. Available: <https://www.sciencedirect.com/science/article/pii/S2214552414000108>.
- [127] C Schuy, U Weber, and M Durante, "Hybrid active-passive space radiation simulation concept for gsi and the future fair facility," *Front. Phys.*, p. 337, 2020, ISSN: 2296-424X. doi: <https://doi.org/10.3389/fphy.2020.00337>.
- [128] L. C. Simonsen, T. C. Slaba, P. Guida, and A. Rusek, "Nasa's first ground-based galactic cosmic ray simulator: Enabling a new era in space radiobiology research," *PLoS Biol.*, vol. 18, no. 5, pp. 1–32, 2020. doi: <https://doi.org/10.1371/journal.pbio.3000669>.
- [129] M Zaider and H. H. Rossi, "The synergistic effects of different radiations," *Radiat. Res.*, pp. 732–739, 1980, ISSN: 0033-7587. doi: <https://doi.org/10.2307/3575352>.
- [130] G. K. Y. Lam, "The survival response of a biological system to mixed radiations," *Radiat. Res.*, vol. 110, no. 2, pp. 232–243, 1987, ISSN: 0033-7587. doi: <https://doi.org/10.2307/3576901>.
- [131] Y. Furusawa, M. Aoki, and M. Durante, "Simultaneous exposure of mammalian cells to heavy ions and x-rays," *Adv. Space Res.*, vol. 30, no. 4, pp. 877–884, 2002, ISSN: 0273-1177. doi: [https://doi.org/10.1016/S0273-1177\(02\)00409-X](https://doi.org/10.1016/S0273-1177(02)00409-X).
- [132] F Luoni *et al.*, "Dose attenuation in innovative shielding materials for radiation protection in space: Measurements and simulations," *accepted by Radiat. Res.*, 2022.
- [133] L. Shekhtman, *Nasa's artemis base camp on the moon will need light, water, elevation*, 2021. [Online]. Available: <https://www.nasa.gov/feature/goddard/2021/nasa-s-artemis-base-camp-on-the-moon-will-need-light-water-elevation>.
- [134] Y. Simeonov *et al.*, "3d range-modulator for scanned particle therapy: Development, monte carlo simulations and experimental evaluation," *Phys. Med. Biol.*, vol. 62, no. 17, pp. 7075–7096, 2017. doi: [10.1088/1361-6560/aa81f4](https://doi.org/10.1088/1361-6560/aa81f4). [Online]. Available: <https://doi.org/10.1088/1361-6560/aa81f4>.
- [135] Z. Wu *et al.*, "Comparison of the radiation shielding properties of wall materials for the manned spacecraft for future china space exploration missions," *J. Korean Phys. Soc.*, vol. 75, no. 9, pp. 666–671, 2019, ISSN: 1976-8524. doi: <https://doi.org/10.3938/jkps.75.666>.
- [136] F Luoni *et al.*, "Beam monitor calibration for radiobiological experiments with scanned high energy heavy ion beams at fair," *Front. Phys.*, vol. 8, 2020, ISSN: 2296-424X. doi: <https://doi.org/10.3389/fphy.2020.568145>.
- [137] M. Lis *et al.*, "A facility for the research, development, and translation of advanced technologies for ion-beam therapies," *J. Instrum.*, vol. 16, no. 03, T03004, 2021. doi: <https://doi.org/10.1088/1748-0221/16/03/T03004>.
- [138] M Durante, "Physical and biomedical countermeasures for space radiation risk," *Z. Med. Phys.*, vol. 18, no. 4, pp. 244–252, 2008, ISSN: 0939-3889. doi: <https://doi.org/10.1016/j.zemedi.2008.06.010>. [Online]. Available: <https://www.sciencedirect.com/science/article/pii/S0939388908000846>.
- [139] T. P. Ringbaek *et al.*, "Modulation power of porous materials and usage as ripple filter in particle therapy," *Phys. Med. Biol.*, vol. 62, no. 7, p. 2892, 2017, ISSN: 0031-9155. doi: <https://doi.org/10.1088/1361-6560/aa5c28>.

- 
- [140] S Agostinelli *et al.*, “Geant4—a simulation toolkit,” *Nucl. Instrum. Methods Phys. Res. A*, vol. 506, no. 3, pp. 250–303, 2003, issn: 0168-9002. doi: [https://doi.org/10.1016/S0168-9002\(03\)01368-8](https://doi.org/10.1016/S0168-9002(03)01368-8). [Online]. Available: <https://www.sciencedirect.com/science/article/pii/S0168900203013688>.
- [141] H. Iwase, K. Niita, and T. Nakamura, “Development of general-purpose particle and heavy ion transport monte carlo code,” *Journal of Nuclear Science and Technology*, vol. 39, no. 11, pp. 1142–1151, 2002. doi: 10.1080/18811248.2002.9715305. eprint: <https://doi.org/10.1080/18811248.2002.9715305>. [Online]. Available: <https://doi.org/10.1080/18811248.2002.9715305>.
- [142] A Ferrari, P. Sala, A Fasso, J Ranft, U Siegen, *et al.*, *Fluka: A multi-particle transport code*, Stanford Linear Accelerator Center (SLAC), 2005.
- [143] T. Böhlen *et al.*, “The fluka code: Developments and challenges for high energy and medical applications,” *Nucl. Data Sheets*, vol. 120, pp. 211–214, 2014, issn: 0090-3752. doi: <https://doi.org/10.1016/j.nds.2014.07.049>. [Online]. Available: <https://www.sciencedirect.com/science/article/pii/S0090375214005018>.
- [144] G Aricò *et al.*, “Developments of the nuclear reaction and fragmentation models in FLUKA for ion collisions at therapeutic energies,” *CERN Proc.*, vol. 1, F. Cerutti, A. Ferrari, T. Kawano, F. Salvat-Pujol, and P. Talou, Eds., pp. 321–326, 2019.
- [145] G Arico’ *et al.*, <http://www.fluka.org/fluka.php>.
- [146] V Vlachoudis *et al.*, “Flair: A powerful but user friendly graphical interface for fluka,” in *Proc. Int. Conf. on Mathematics, Computational Methods & Reactor Physics (M&C 2009)*, Saratoga Springs, New York, vol. 176, 2009.
- [147] *Geant4 physics reference manual, release 10.6*, Geant4 Collaboration, 2017. [Online]. Available: <http://geant4-userdoc.web.cern.ch/geant4-userdoc/UsersGuides/PhysicsReferenceManual/fo/PhysicsReferenceManual.pdf>.
- [148] A. V. Ivantchenko, V. N. Ivanchenko, J.-M. Q. Molina, and S. L. Incerti, “Geant4 hadronic physics for space radiation environment,” *Int. J. Radiat. Biol.*, vol. 88, no. 1-2, pp. 171–175, 2012. doi: 10.3109/09553002.2011.610865. [Online]. Available: <https://doi.org/10.3109/09553002.2011.610865>.
- [149] L. Townsend, F. Cucinotta, and L. Heilbronn, “Nuclear model calculations and their role in space radiation research,” *Adv. Space Res.*, vol. 30, no. 4, pp. 907–916, 2002, issn: 0273-1177. doi: [https://doi.org/10.1016/S0273-1177\(02\)00405-2](https://doi.org/10.1016/S0273-1177(02)00405-2). [Online]. Available: <https://www.sciencedirect.com/science/article/pii/S0273117702004052>.
- [150] M. Kuchera, O. Tarasov, D Bazin, B Sherril, and K. Tarasova, “LISE++ software updates and future plans,” *J. Phys. Conf. Ser.*, vol. 664, no. 7, p. 072029, 2015. doi: 10.1088/1742-6596/664/7/072029. [Online]. Available: <https://doi.org/10.1088/1742-6596/664/7/072029>.
- [151] <https://physics.nist.gov/PhysRefData/Star/Text/ESTAR.html>.
- [152] M. Berger, J. Coursey, M. Zucker, and J. Chang, *Stopping-power & range tables for electrons, protons, and helium ions, nist standard reference database 124*, 2017. doi: <https://dx.doi.org/10.18434/T4NC7P>.
- [153] Z.-W. Lin, “Determination of important nuclear fragmentation processes for human space radiation protection,” *Phys. Rev. C*, vol. 75, no. 3, p. 034609, 2007. doi: <https://doi.org/10.1103/PhysRevC.75.034609>.



- 
- [154] <https://www.gsi.de/fragmentation>.
- [155] F Horst, D Schardt, H Iwase, C Schuy, M Durante, and U Weber, “Physical characterization of  $^3\text{He}$  ion beams for radiotherapy and comparison with  $^4\text{He}$ ,” *Phys. Med. Biol.*, vol. 66, no. 095009, 2021. doi: <https://doi.org/10.1088/1361-6560/abef88>. [Online]. Available: <http://iopscience.iop.org/article/10.1088/1361-6560/abef88>.
- [156] F Horst *et al.*, “Measurement of  $^4\text{He}$  charge- and mass-changing cross sections on H, C, O, and Si targets in the energy range 70-220 MeV/u for radiation transport calculations in ion-beam therapy,” *Phys. Rev. C*, vol. 99, p. 014603, 1 2019. doi: 10.1103/PhysRevC.99.014603. [Online]. Available: <https://link.aps.org/doi/10.1103/PhysRevC.99.014603>.
- [157] D.-H. Zhang, J.-X. Cheng, S Kodaira, and N Yasuda, “Projectile fragmentation of 388 AMeV  $^{20}\text{Ne}$  in polyethylene, carbon and aluminum targets,” *Nucl. Instrum. Methods Phys. Res. B*, vol. 286, pp. 238–242, 2012, Proceedings of the Sixteenth International Conference on Radiation Effects in Insulators (REI), ISSN: 0168-583X. doi: <https://doi.org/10.1016/j.nimb.2012.01.058>. [Online]. Available: <http://www.sciencedirect.com/science/article/pii/S0168583X12001036>.
- [158] S. Hirzebruch, E Becker, G Hüntrup, T Streibel, E Winkel, and W Heinrich, “Charge-changing interactions of  $^{197}\text{Au}$  at 10 GeV/nucleon in collisions with targets from H to Pb,” *Phys. Rev. C*, vol. 51, pp. 2085–2090, 4 1995. doi: 10.1103/PhysRevC.51.2085. [Online]. Available: <https://link.aps.org/doi/10.1103/PhysRevC.51.2085>.
- [159] S. Hirzebruch, G Rusch, E Winkel, and W Heinrich, “Response of BP-1 to  $^{197}\text{Au}$  heavy ions at 11.3 GeV/nucleon,” *Nucl. Instrum. Methods Phys. Res. B*, vol. 74, no. 4, pp. 519–522, 1993, ISSN: 0168-583X. doi: [https://doi.org/10.1016/0168-583X\(93\)95950-A](https://doi.org/10.1016/0168-583X(93)95950-A). [Online]. Available: <http://www.sciencedirect.com/science/article/pii/0168583X9395950A>.
- [160] A Ozawa *et al.*, “Charge-changing cross sections of  $^{30}\text{Ne}$ ,  $^{32,33}\text{Na}$  with a proton target,” *Phys. Rev. C*, vol. 89, p. 044602, 4 2014. doi: 10.1103/PhysRevC.89.044602. [Online]. Available: <https://link.aps.org/doi/10.1103/PhysRevC.89.044602>.
- [161] S Cecchini *et al.*, “Fragmentation cross sections of  $\text{Fe}^{26+}$ ,  $\text{Si}^{14+}$  and  $\text{C}^{6+}$  ions of 0.3-10 AGeV on polyethylene, CR39 and aluminum targets,” *Nucl. Phys. A*, vol. 807, no. 3, pp. 206–213, 2008, ISSN: 0375-9474. doi: <https://doi.org/10.1016/j.nuclphysa.2008.03.017>. [Online]. Available: <http://www.sciencedirect.com/science/article/pii/S0375947408004417>.
- [162] N Matsuoka *et al.*, “Deuteron break-up in the fields of nuclei at 56 MeV,” *Nucl. Phys. A*, vol. 345, no. 1, pp. 1–12, 1980, ISSN: 0375-9474. doi: [https://doi.org/10.1016/0375-9474\(80\)90409-1](https://doi.org/10.1016/0375-9474(80)90409-1). [Online]. Available: <http://www.sciencedirect.com/science/article/pii/0375947480904091>.
- [163] L Giot *et al.*, “Isotopic production cross sections of the residual nuclei in spallation reactions induced by  $^{136}\text{Xe}$  projectiles on proton at 500 AMeV,” *Nucl. Phys. A*, vol. 899, pp. 116–132, 2013, ISSN: 0375-9474. doi: <https://doi.org/10.1016/j.nuclphysa.2012.12.119>. [Online]. Available: <http://www.sciencedirect.com/science/article/pii/S0375947412004423>.
- [164] C Paradela *et al.*, “Isotopic production cross sections of residual nuclei in the spallation reaction  $^{136}\text{Xe}(200\text{ AMeV}) + p$ ,” *Phys. Rev. C*, vol. 95, p. 044606, 4 2017. doi: 10.1103/PhysRevC.95.044606. [Online]. Available: <https://link.aps.org/doi/10.1103/PhysRevC.95.044606>.

- 
- [165] J Alcantara-Nunez, J Benlliure, C Paradela, *et al.*, “Isotopic yields of spallation residues produced in  $^{136}\text{Xe}$ -induced reactions on deuterium at 500 AMeV,” *Phys. Rev. C*, vol. 92, p. 024607, 2 2015. DOI: 10.1103/PhysRevC.92.024607. [Online]. Available: <https://link.aps.org/doi/10.1103/PhysRevC.92.024607>.
- [166] P Ferrando *et al.*, “Measurement of  $^{12}\text{C}$ ,  $^{16}\text{O}$ , and  $^{56}\text{Fe}$  charge changing cross sections in helium at high energy, comparison with cross sections in hydrogen, and application to cosmic-ray propagation,” *Phys. Rev. C*, vol. 37, pp. 1490–1501, 4 1988. DOI: 10.1103/PhysRevC.37.1490. [Online]. Available: <https://link.aps.org/doi/10.1103/PhysRevC.37.1490>.
- [167] F Horst, C Schuy, U Weber, K. Brinkmann, and K Zink, “Measurement of charge- and mass-changing cross sections for  $^4\text{He}+^{12}\text{C}$  collisions in the energy range 80-220 MeV/u for applications in ion beam therapy,” *Phys. Rev. C*, vol. 96, p. 024624, 2 2017. DOI: 10.1103/PhysRevC.96.024624. [Online]. Available: <https://link.aps.org/doi/10.1103/PhysRevC.96.024624>.
- [168] J.-S. Li, D.-H. Zhang, J.-X. Cheng, S. Kodaira, and N. Yasuda, “Fragmentation cross sections of 788 AMeV  $^{28}\text{Si}$  on carbon and polyethylene targets,” *Chin. J. Phys.*, vol. 54, no. 2, pp. 314–317, 2016, ISSN: 0577-9073. DOI: <https://doi.org/10.1016/j.cjph.2016.05.003>. [Online]. Available: <http://www.sciencedirect.com/science/article/pii/S0577907316302271>.
- [169] R Gupta and A Kumar, “Fragmentation cross-section of 600 AMeV  $\text{Si}^{14+}$  ions in thick polyethylene target,” *Eur. Phys. J. A*, vol. 49, no. 8, p. 98, 2013, ISSN: 1434-601X. DOI: 10.1140/epja/i2013-13098-3. [Online]. Available: <https://doi.org/10.1140/epja/i2013-13098-3>.
- [170] B Alpat *et al.*, “Total and Partial Fragmentation Cross-Section of 500 MeV/nucleon Carbon Ions on Different Target Materials,” *IEEE Trans Nucl Sci*, vol. 60, no. 6, pp. 4673–4682, 2013, ISSN: 1558-1578. DOI: 10.1109/TNS.2013.2284855.
- [171] A Ozawa *et al.*, “Interaction cross sections and radii of light nuclei,” *Nucl. Phys. A*, vol. 608, no. 1, pp. 63–76, 1996, ISSN: 0375-9474. DOI: [https://doi.org/10.1016/0375-9474\(96\)00241-2](https://doi.org/10.1016/0375-9474(96)00241-2). [Online]. Available: <http://www.sciencedirect.com/science/article/pii/0375947496002412>.
- [172] A Ozawa *et al.*, “Interaction cross-sections and radii of  $^{11}\text{C}$  and  $^{12}\text{N}$  and effective deformation parameters in light mirror nuclei,” *Nucl. Phys. A*, vol. 583, pp. 807–810, 1995, Nucleus-Nucleus Collisions, ISSN: 0375-9474. DOI: [https://doi.org/10.1016/0375-9474\(94\)00763-D](https://doi.org/10.1016/0375-9474(94)00763-D). [Online]. Available: <http://www.sciencedirect.com/science/article/pii/037594749400763D>.
- [173] A Ozawa *et al.*, “Interaction cross sections and radii of the mass number  $A=17$  isobar ( $^{17}\text{N}$ ,  $^{17}\text{F}$ , and  $^{17}\text{Ne}$ ),” *Phys. Lett. B*, vol. 334, no. 1, pp. 18–22, 1994, ISSN: 0370-2693. DOI: [https://doi.org/10.1016/0370-2693\(94\)90585-1](https://doi.org/10.1016/0370-2693(94)90585-1). [Online]. Available: <http://www.sciencedirect.com/science/article/pii/0370269394905851>.
- [174] G. Westfall, L. Wilson, P. Lindstrom, H. Crawford, D. Greiner, and H. Heckman, “Fragmentation of relativistic  $^{56}\text{Fe}$ ,” *Phys. Rev. C*, vol. 19, pp. 1309–1323, 4 1979. DOI: 10.1103/PhysRevC.19.1309. [Online]. Available: <https://link.aps.org/doi/10.1103/PhysRevC.19.1309>.
- [175] D Shapira, J. Ford, and J. del Campo, “Reactions of  $^{20}\text{Ne}$  with  $^{12}\text{C}$ ,” *Phys. Rev. C*, vol. 26, pp. 2470–2486, 6 1982. DOI: 10.1103/PhysRevC.26.2470. [Online]. Available: <https://link.aps.org/doi/10.1103/PhysRevC.26.2470>.

- 
- [176] X. Cai *et al.*, “Existence of a proton halo in  $^{23}\text{Al}$  and its significance,” *Phys. Rev. C*, vol. 65, p. 024 610, 2 2002. doi: 10.1103/PhysRevC.65.024610. [Online]. Available: <https://link.aps.org/doi/10.1103/PhysRevC.65.024610>.
- [177] D. Fang *et al.*, “Evidence for a proton halo in  $^{27}\text{P}$  through measurements of reaction cross-sections at intermediate energies,” *Eur. Phys. J. A*, vol. 12, no. 3, pp. 335–339, 2001, issn: 1434-601X. doi: 10.1007/s100500170011. [Online]. Available: <https://doi.org/10.1007/s100500170011>.
- [178] A Budzanowski *et al.*, “Total reaction cross section and elastic scattering of 24.7 MeV alpha particles in the region of  $A = 60$  nuclei,” *Nucl. Phys. A*, vol. 106, no. 1, pp. 21–34, 1967, issn: 0375-9474. doi: [https://doi.org/10.1016/0375-9474\(67\)90825-1](https://doi.org/10.1016/0375-9474(67)90825-1). [Online]. Available: <http://www.sciencedirect.com/science/article/pii/0375947467908251>.
- [179] A Ingemarsson *et al.*, “New results for reaction cross sections of intermediate energy  $\alpha$ -particles on targets from  $^9\text{Be}$  to  $^{208}\text{Pb}$ ,” *Nucl. Phys. A*, vol. 676, no. 1, pp. 3–31, 2000, issn: 0375-9474. doi: [https://doi.org/10.1016/S0375-9474\(00\)00200-1](https://doi.org/10.1016/S0375-9474(00)00200-1). [Online]. Available: <http://www.sciencedirect.com/science/article/pii/S0375947400002001>.
- [180] E Labie, J Lega, P Leleux, and P. Macq, “Total reaction cross section of  $\alpha$ -particles on carbon between 15.8 and 20.1 MeV,” *Nucl. Phys. A*, vol. 205, no. 1, pp. 81–89, 1973, issn: 0375-9474. doi: [https://doi.org/10.1016/0375-9474\(73\)90121-8](https://doi.org/10.1016/0375-9474(73)90121-8). [Online]. Available: <http://www.sciencedirect.com/science/article/pii/0375947473901218>.
- [181] V Togo *et al.*, “Fragmentation studies of high-energy ions using CR39 nuclear track detectors,” *Nucl. Instrum. Methods. Phys. Res. A*, vol. 580, no. 1, pp. 58–61, 2007, Proceedings of the 10 th International Symposium on Radiation Physics, issn: 0168-9002. doi: <https://doi.org/10.1016/j.nima.2007.05.017>. [Online]. Available: <http://www.sciencedirect.com/science/article/pii/S0168900207008625>.
- [182] J.-X. Cheng *et al.*, “The fragmentation of  $^{20}\text{Ne}$  at 400 AMeV,” *Chinese Phys. C*, vol. 36, no. 1, pp. 37–42, 2012. doi: 10.1088/1674-1137/36/1/006. [Online]. Available: <https://doi.org/10.1088/1674-1137/36/1/006>.
- [183] G. Bisheva *et al.*, “Cross sections of deuteron interaction with aluminium at 710 MeV,” *Phys. Lett. B*, vol. 24, no. 10, pp. 533–536, 1967, issn: 0370-2693. doi: [https://doi.org/10.1016/0370-2693\(67\)90420-0](https://doi.org/10.1016/0370-2693(67)90420-0). [Online]. Available: <http://www.sciencedirect.com/science/article/pii/0370269367904200>.
- [184] D. Tran *et al.*, “Charge-changing cross-section measurements of  $^{12-16}\text{C}$  at around 45 AMeV and development of a Glauber model for incident energies 10–2100 AMeV,” *Phys. Rev. C*, vol. 94, p. 064 604, 6 2016. doi: 10.1103/PhysRevC.94.064604. [Online]. Available: <https://link.aps.org/doi/10.1103/PhysRevC.94.064604>.
- [185] T Yamaguchi *et al.*, “Scaling of Charge-Changing Interaction Cross Sections and Point-Proton Radii of Neutron-Rich Carbon Isotopes,” *Phys. Rev. Lett.*, vol. 107, p. 032 502, 3 2011. doi: 10.1103/PhysRevLett.107.032502. [Online]. Available: <https://link.aps.org/doi/10.1103/PhysRevLett.107.032502>.
- [186] I Tanihata *et al.*, “Determination of the density distribution and the correlation of halo neutrons in  $^{11}\text{Li}$ ,” *Phys. Lett. B*, vol. 287, no. 4, pp. 307–311, 1992, issn: 0370-2693. doi: [https://doi.org/10.1016/0370-2693\(92\)90988-G](https://doi.org/10.1016/0370-2693(92)90988-G). [Online]. Available: <http://www.sciencedirect.com/science/article/pii/037026939290988G>.



- 
- [187] I Tanihata *et al.*, “Measurements of interaction cross sections and radii of He isotopes,” *Phys. Lett. B*, vol. 160, no. 6, pp. 380–384, 1985, ISSN: 0370-2693. DOI: [https://doi.org/10.1016/0370-2693\(85\)90005-X](https://doi.org/10.1016/0370-2693(85)90005-X). [Online]. Available: <http://www.sciencedirect.com/science/article/pii/037026938590005X>.
- [188] I Tanihata, “Nuclear physics using unstable nuclear beams,” *Hyperfine Interact.*, vol. 21, no. 1, pp. 251–264, 1985, ISSN: 1572-9540. DOI: 10.1007/BF02061988. [Online]. Available: <https://doi.org/10.1007/BF02061988>.
- [189] I Tanihata *et al.*, “Measurements of Interaction Cross Sections and Nuclear Radii in the Light *p*-Shell Region,” *Phys. Rev. Lett.*, vol. 55, pp. 2676–2679, 24 1985. DOI: 10.1103/PhysRevLett.55.2676. [Online]. Available: <https://link.aps.org/doi/10.1103/PhysRevLett.55.2676>.
- [190] I Tanihata *et al.*, “Measurement of interaction cross sections using isotope beams of Be and B and isospin dependence of the nuclear radii,” *Phys. Lett. B*, vol. 206, no. 4, pp. 592–596, 1988, ISSN: 0370-2693. DOI: [https://doi.org/10.1016/0370-2693\(88\)90702-2](https://doi.org/10.1016/0370-2693(88)90702-2). [Online]. Available: <http://www.sciencedirect.com/science/article/pii/0370269388907022>.
- [191] T Kobayashi, “Projectile fragmentation of exotic nuclear beams,” *Nucl. Phys. A*, vol. 538, pp. 343–352, 1992, ISSN: 0375-9474. DOI: [https://doi.org/10.1016/0375-9474\(92\)90784-H](https://doi.org/10.1016/0375-9474(92)90784-H). [Online]. Available: <http://www.sciencedirect.com/science/article/pii/037594749290784H>.
- [192] O. Bochkarev *et al.*, “Evidence for a neutron skin in  $^{20}\text{N}$ ,” *Eur. Phys. J. A*, vol. 1, no. 1, pp. 15–17, 1998, ISSN: 1434-601X. DOI: 10.1007/s100500050026. [Online]. Available: <https://doi.org/10.1007/s100500050026>.
- [193] R Gupta, A Kumar, G Giacomelli, L Patrizii, and V Togo, “Calibration of CR39 detectors with new system for Fe26+ ion beam and measurement of total charge changing cross-section in Al target,” *Radiat. Meas.*, vol. 47, no. 10, pp. 1023–1029, 2012, ISSN: 1350-4487. DOI: <https://doi.org/10.1016/j.radmeas.2012.07.007>. [Online]. Available: <http://www.sciencedirect.com/science/article/pii/S1350448712002132>.
- [194] R Gupta and A Kumar, “Response of CR39 detector to 5 AGeV Si14+ ions and measurement of total charge changing cross-section,” *Radiat. Phys. Chem.*, vol. 92, pp. 8–13, 2013, ISSN: 0969-806X. DOI: <https://doi.org/10.1016/j.radphyschem.2013.07.012>. [Online]. Available: <http://www.sciencedirect.com/science/article/pii/S0969806X13004490>.
- [195] D. Greiner *et al.*, “Uranium nuclear reactions at 900 MeV/nucleon,” *Phys. Rev. C*, vol. 31, pp. 416–420, 2 1985. DOI: 10.1103/PhysRevC.31.416. [Online]. Available: <https://link.aps.org/doi/10.1103/PhysRevC.31.416>.
- [196] L.-H. Wang *et al.*, “Projectile fragment emission in the fragmentation of  $^{56}\text{Fe}$  on Al, C, and CH<sub>2</sub> targets,” *Nucl. Sci. Tech.*, vol. 30, no. 12, p. 186, 2019, ISSN: 2210-3147. DOI: 10.1007/s41365-019-0704-1. [Online]. Available: <https://doi.org/10.1007/s41365-019-0704-1>.
- [197] P Napolitani *et al.*, “Measurement of the complete nuclide production and kinetic energies of the system  $^{136}\text{Xe}$ +hydrogen at 1 GeV per nucleon,” *Phys. Rev. C*, vol. 76, p. 064609, 6 2007. DOI: 10.1103/PhysRevC.76.064609. [Online]. Available: <https://link.aps.org/doi/10.1103/PhysRevC.76.064609>.
- [198] W. Webber and D. Brautigam, “Fragmentation of Fe-56 nuclei on CH<sub>2</sub>, carbon, and hydrogen targets - Individual charge changing and total cross sections,” *Astrophys. J.*, vol. 260, pp. 894–908, Sep. 1982. DOI: 10.1086/160308.
-

- 
- [199] W. Binns *et al.*, “Systematics of the release of residual nuclei from relativistic nucleus-nucleus interactions,” *Phys. Rev. C*, vol. 36, pp. 1870–1885, 5 1987. doi: 10.1103/PhysRevC.36.1870. [Online]. Available: <https://link.aps.org/doi/10.1103/PhysRevC.36.1870>.
- [200] C Brechtmann and W Heinrich, “Measurements of elemental fragmentation cross section for relativistic heavy ions using CR39 plastic nuclear track detectors,” *Nucl. Instrum. Methods Phys. Res. B*, vol. 29, no. 4, pp. 675–679, 1988, ISSN: 0168-583X. doi: [https://doi.org/10.1016/0168-583X\(88\)90475-2](https://doi.org/10.1016/0168-583X(88)90475-2). [Online]. Available: <http://www.sciencedirect.com/science/article/pii/0168583X88904752>.
- [201] C Brechtmann and W Heinrich, “Fragmentation cross sections of  $^{32}\text{S}$  at 0.7, 1.2 and 200 GeV/nucleon,” *Z. Phys.*, vol. 331, no. 4, pp. 463–472, 1988, ISSN: 0939-7922. doi: 10.1007/BF01291905. [Online]. Available: <https://doi.org/10.1007/BF01291905>.
- [202] C. Brechtmann and W. Heinrich, “Fragmentation cross sections of  $^{16}\text{O}$  at 60 and 200 GeV/nucleon,” *Z. Phys.*, vol. 330, no. 4, pp. 407–416, 1988, ISSN: 0939-7922. doi: 10.1007/BF01290126. [Online]. Available: <https://doi.org/10.1007/BF01290126>.
- [203] C Brechtmann, W Heinrich, and E. Benton, “Fragmentation cross sections of  $^{28}\text{Si}$  at 14.5 GeV/nucleon,” *Phys. Rev. C*, vol. 39, pp. 2222–2226, 6 1989. doi: 10.1103/PhysRevC.39.2222. [Online]. Available: <https://link.aps.org/doi/10.1103/PhysRevC.39.2222>.
- [204] T Brohm *et al.*, “Total charge-changing cross sections of stable and neutron-deficient secondary projectiles around  $A = 60$ ,” *Nucl. Phys. A*, vol. 585, no. 3, pp. 565–576, 1995, ISSN: 0375-9474. doi: [https://doi.org/10.1016/0375-9474\(94\)00507-J](https://doi.org/10.1016/0375-9474(94)00507-J). [Online]. Available: <http://www.sciencedirect.com/science/article/pii/037594749400507J>.
- [205] C. Chen *et al.*, “Interactions in hydrogen of relativistic neon to nickel projectiles: Total charge-changing cross sections,” *Phys. Rev. C*, vol. 49, pp. 3200–3210, 6 1994. doi: 10.1103/PhysRevC.49.3200. [Online]. Available: <https://link.aps.org/doi/10.1103/PhysRevC.49.3200>.
- [206] D. Cheshire *et al.*, “Fragmentation cross sections of 2.1-GeV/nucleon  $^{12}\text{C}$  and  $^{16}\text{O}$  ions,” *Phys. Rev. D*, vol. 10, pp. 25–31, 1 1974. doi: 10.1103/PhysRevD.10.25. [Online]. Available: <https://link.aps.org/doi/10.1103/PhysRevD.10.25>.
- [207] W. Christie *et al.*, “Fragmentation of 1.2 GeV per nucleon  $^{139}\text{La}$ ,” *Phys. Rev. C*, vol. 48, pp. 2973–2983, 6 1993. doi: 10.1103/PhysRevC.48.2973. [Online]. Available: <https://link.aps.org/doi/10.1103/PhysRevC.48.2973>.
- [208] L. Chulkov *et al.*, “Total charge-changing cross sections for neutron-rich light nuclei,” *Nucl. Phys. A*, vol. 674, no. 3, pp. 330–342, 2000, ISSN: 0375-9474. doi: [https://doi.org/10.1016/S0375-9474\(00\)00168-8](https://doi.org/10.1016/S0375-9474(00)00168-8). [Online]. Available: <http://www.sciencedirect.com/science/article/pii/S0375947400001688>.
- [209] F Flesch, G Iancu, W Heinrich, and H Yasuda, “Projectile fragmentation of silicon ions at 490 AMeV,” *Radiat. Meas.*, vol. 34, no. 1, pp. 237–240, 2001, Proceedings of the 20th International Conference on Nuclear Tracks in Solids, ISSN: 1350-4487. doi: [https://doi.org/10.1016/S1350-4487\(01\)00158-5](https://doi.org/10.1016/S1350-4487(01)00158-5). [Online]. Available: <http://www.sciencedirect.com/science/article/pii/S1350448701001585>.

- 
- [210] A. Golovchenko *et al.*, “Total charge-changing and partial cross-section measurements in the reaction of 110 MeV/u  $^{12}\text{C}$  with paraffin,” *Radiat. Meas.*, vol. 34, no. 1, pp. 297–300, 2001, Proceedings of the 20th International Conference on Nuclear Tracks in Solids, ISSN: 1350-4487. DOI: [https://doi.org/10.1016/S1350-4487\(01\)00171-8](https://doi.org/10.1016/S1350-4487(01)00171-8). [Online]. Available: <http://www.sciencedirect.com/science/article/pii/S1350448701001718>.
- [211] A. Golovchenko *et al.*, “Total charge-changing and partial cross-section measurements in the reactions of  $\sim 110 - 250$  MeV/nucleon  $^{12}\text{C}$  in carbon, paraffin, and water,” *Phys. Rev. C*, vol. 66, p. 014609, 1 2002. DOI: 10.1103/PhysRevC.66.014609. [Online]. Available: <https://link.aps.org/doi/10.1103/PhysRevC.66.014609>.
- [212] Y. He and P. Price, “Nuclear and electromagnetic fragmentation of 2.25-TeV  $^{197}\text{Au}$  nuclei,” *Z. Phys.*, vol. 348, no. 2, pp. 105–109, 1994, ISSN: 0939-7922. DOI: 10.1007/BF01289597. [Online]. Available: <https://doi.org/10.1007/BF01289597>.
- [213] S. Hirzebruch, W. Heinrich, K. Tolstov, A. Kovalenko, and E. Benton, “Fragmentation cross sections of  $^{16}\text{O}$  between 0.9 and 200 GeV/nucleon,” *Phys. Rev. C*, vol. 46, pp. 1487–1494, 4 1992. DOI: 10.1103/PhysRevC.46.1487. [Online]. Available: <https://link.aps.org/doi/10.1103/PhysRevC.46.1487>.
- [214] G. Iancu, F. Flesch, and W. Heinrich, “Nuclear fragmentation cross-sections of 400 AMeV  $^{36}\text{Ar}$  and  $^{40}\text{Ar}$  in collisions with light and heavy target nuclei,” *Radiat. Meas.*, vol. 39, no. 5, pp. 525–533, 2005, ISSN: 1350-4487. DOI: <https://doi.org/10.1016/j.radmeas.2004.10.011>. [Online]. Available: <http://www.sciencedirect.com/science/article/pii/S1350448704002483>.
- [215] B. Nilsen, C. Waddington, J. Cummings, T. Garrard, and J. Klarmann, “Fragmentation cross sections of relativistic  $^{84}_{36}\text{Kr}$  and  $^{109}_{47}\text{Ag}$  nuclei in targets from hydrogen to lead,” *Phys. Rev. C*, vol. 52, pp. 3277–3290, 6 1995. DOI: 10.1103/PhysRevC.52.3277. [Online]. Available: <https://link.aps.org/doi/10.1103/PhysRevC.52.3277>.
- [216] P. Price and Y. He, “Behavior of nuclear projectile fragments produced in collisions of 14.5 AGeV  $^{28}\text{Si}$  with Pb and Cu targets,” *Phys. Rev. C*, vol. 43, pp. 835–848, 2 1991. DOI: 10.1103/PhysRevC.43.835. [Online]. Available: <https://link.aps.org/doi/10.1103/PhysRevC.43.835>.
- [217] D. Sampsonidis *et al.*, “Fragmentation cross sections of  $^{16}\text{O}$ ,  $^{24}\text{Mg}$ , and  $^{32}\text{S}$  projectiles at 3.65 GeV/nucleon,” *Phys. Rev. C*, vol. 51, pp. 3304–3308, 6 1995. DOI: 10.1103/PhysRevC.51.3304. [Online]. Available: <https://link.aps.org/doi/10.1103/PhysRevC.51.3304>.
- [218] I. Schall *et al.*, “Charge-changing nuclear reactions of relativistic light-ion beams ( $5 \leq Z \leq 10$ ) passing through thick absorbers,” *Nucl. Instrum. Methods Phys. Res. B*, vol. 117, no. 3, pp. 221–234, 1996, ISSN: 0168-583X. DOI: [https://doi.org/10.1016/0168-583X\(96\)00325-4](https://doi.org/10.1016/0168-583X(96)00325-4). [Online]. Available: <http://www.sciencedirect.com/science/article/pii/0168583X96003254>.
- [219] T. Toshito, K. Kodama, L. Sihver, *et al.*, “Measurements of total and partial charge-changing cross sections for 200- to 400-MeV/nucleon  $^{12}\text{C}$  on water and polycarbonate,” *Phys. Rev. C*, vol. 75, p. 054606, 5 2007. DOI: 10.1103/PhysRevC.75.054606. [Online]. Available: <https://link.aps.org/doi/10.1103/PhysRevC.75.054606>.
- [220] W. Webber, J. Kish, and D. Schrier, “Total charge and mass changing cross sections of relativistic nuclei in hydrogen, helium, and carbon targets,” *Phys. Rev. C*, vol. 41, pp. 520–532, 2 1990. DOI: 10.1103/PhysRevC.41.520. [Online]. Available: <https://link.aps.org/doi/10.1103/PhysRevC.41.520>.

- 
- [221] W. Webber *et al.*, “Production Cross Sections of Fragments from Beams of 400 – 650 MeV per Nucleon  $^9\text{Be}$ ,  $^{11}\text{B}$ ,  $^{12}\text{C}$ ,  $^{14}\text{N}$ ,  $^{15}\text{N}$ ,  $^{16}\text{O}$ ,  $^{20}\text{Ne}$ ,  $^{22}\text{Ne}$ ,  $^{56}\text{Fe}$ , and  $^{58}\text{Ni}$  Nuclei Interacting in a Liquid Hydrogen Target. I. Charge Changing and Total Cross Sections,” *ApJ*, vol. 508, no. 2, pp. 940–948, 1998. doi: 10.1086/306445. [Online]. Available: <https://doi.org/10.1086/306445>.
- [222] W. Webber *et al.*, “Measurement of charge changing and isotopic cross sections at  $\sim 600$  MeV/nucleon from the interactions of  $\sim 30$  separate beams of relativistic nuclei from  $^{10}\text{B}$  to  $^{55}\text{Mn}$  in a liquid hydrogen target,” *Phys. Rev. C*, vol. 58, pp. 3539–3552, 6 1998. doi: 10.1103/PhysRevC.58.3539. [Online]. Available: <https://link.aps.org/doi/10.1103/PhysRevC.58.3539>.
- [223] T Yamaguchi *et al.*, “Energy-dependent charge-changing cross sections and proton distribution of  $^{28}\text{Si}$ ,” *Phys. Rev. C*, vol. 82, p. 014609, 1 2010. doi: 10.1103/PhysRevC.82.014609. [Online]. Available: <https://link.aps.org/doi/10.1103/PhysRevC.82.014609>.
- [224] C Zeitlin, A Fukumura, L Heilbronn, Y Iwata, J Miller, and T Murakami, “Fragmentation cross sections of 600 MeV/nucleon  $^{20}\text{Ne}$  on elemental targets,” *Phys. Rev. C*, vol. 64, p. 024902, 2 2001. doi: 10.1103/PhysRevC.64.024902. [Online]. Available: <https://link.aps.org/doi/10.1103/PhysRevC.64.024902>.
- [225] C Zeitlin *et al.*, “Fragmentation cross sections of 290 and 400 MeV/nucleon  $^{12}\text{C}$  beams on elemental targets,” *Phys. Rev. C*, vol. 76, p. 014911, 1 2007. doi: 10.1103/PhysRevC.76.014911. [Online]. Available: <https://link.aps.org/doi/10.1103/PhysRevC.76.014911>.
- [226] C Zeitlin *et al.*, “Fragmentation cross sections of  $^{28}\text{Si}$  at beam energies from 290A to 1200A MeV,” *Nucl. Phys. A*, vol. 784, no. 1, pp. 341–367, 2007, issn: 0375-9474. doi: <https://doi.org/10.1016/j.nuclphysa.2006.10.088>. [Online]. Available: <http://www.sciencedirect.com/science/article/pii/S0375947406007767>.
- [227] C Zeitlin *et al.*, “Fragmentation cross sections of medium-energy  $^{35}\text{Cl}$ ,  $^{40}\text{Ar}$ , and  $^{48}\text{Ti}$  beams on elemental targets,” *Phys. Rev. C*, vol. 77, p. 034605, 3 2008. doi: 10.1103/PhysRevC.77.034605. [Online]. Available: <https://link.aps.org/doi/10.1103/PhysRevC.77.034605>.
- [228] C Zeitlin *et al.*, “Fragmentation of  $^{14}\text{N}$ ,  $^{16}\text{O}$ ,  $^{20}\text{Ne}$ , and  $^{24}\text{Mg}$  nuclei at 290 to 1000 MeV/nucleon,” *Phys. Rev. C*, vol. 83, p. 034909, 3 2011. doi: 10.1103/PhysRevC.83.034909. [Online]. Available: <https://link.aps.org/doi/10.1103/PhysRevC.83.034909>.
- [229] A Gökmen, H Breuer, A. Mignerey, B. Glagola, K Kwiatkowski, and V. Viola, “Fragment mass, energy, and angular distributions for the  $^{12}\text{C}(^4\text{He}, \text{heavy ion})$  reaction between 49 and 159 MeV,” *Phys. Rev. C*, vol. 29, pp. 1595–1605, 5 1984. doi: 10.1103/PhysRevC.29.1595. [Online]. Available: <https://link.aps.org/doi/10.1103/PhysRevC.29.1595>.
- [230] G Igo and B. Wilkins, “Alpha-Particle Reaction Cross Sections at 40 MeV,” *Phys. Rev.*, vol. 131, pp. 1251–1253, 3 1963. doi: 10.1103/PhysRev.131.1251. [Online]. Available: <https://link.aps.org/doi/10.1103/PhysRev.131.1251>.
- [231] R. De Vries *et al.*, “Dominance of nucleon-nucleon interactions in  $\alpha + ^{12}\text{C}$  total reaction cross sections,” *Phys. Rev. C*, vol. 26, pp. 301–303, 1 1982. doi: 10.1103/PhysRevC.26.301. [Online]. Available: <https://link.aps.org/doi/10.1103/PhysRevC.26.301>.
- [232] G. Millburn, W Birnbaum, W. Crandall, and L Schecter, “Nuclear Radii from Inelastic Cross-Section Measurements,” *Phys. Rev.*, vol. 95, pp. 1268–1278, 5 1954. doi: 10.1103/PhysRev.95.1268. [Online]. Available: <https://link.aps.org/doi/10.1103/PhysRev.95.1268>.



- 
- [233] O. Bilaniuk, V. Tokarevskii, V. Bulkin, L. Dubar, O. Nemets, and L. Slyusarenko, "Deuteron and alpha-particle total reaction cross sections for nuclei with  $A \sim 50$ ," *J. Phys. G*, vol. 7, no. 12, pp. 1699–1712, 1981. doi: 10.1088/0305-4616/7/12/020. [Online]. Available: <https://doi.org/10.1088/0305-4616/7/12/020>.
- [234] C Perrin *et al.*, "Direct Measurement of the  $^{12}\text{C} + ^{12}\text{C}$  Reaction Cross Section between 10 and 83 MeV/Nucleon," *Phys. Rev. Lett.*, vol. 49, pp. 1905–1909, 26 1982. doi: 10.1103/PhysRevLett.49.1905. [Online]. Available: <https://link.aps.org/doi/10.1103/PhysRevLett.49.1905>.
- [235] S Kox *et al.*, "Direct measurements of heavy-ion total reaction cross sections at 30 and 83 MeV/nucleon," *Nucl. Phys. A*, vol. 420, no. 1, pp. 162–172, 1984, ISSN: 0375-9474. doi: [https://doi.org/10.1016/0375-9474\(84\)90663-8](https://doi.org/10.1016/0375-9474(84)90663-8). [Online]. Available: <http://www.sciencedirect.com/science/article/pii/0375947484906638>.
- [236] M Takechi *et al.*, "Reaction cross sections at intermediate energies and Fermi-motion effect," *Phys. Rev. C*, vol. 79, p. 061 601, 6 2009. doi: 10.1103/PhysRevC.79.061601. [Online]. Available: <https://link.aps.org/doi/10.1103/PhysRevC.79.061601>.
- [237] G Singh and P. Jain, "Electromagnetic dissociation of relativistic heavy-ions in emulsion," *Z. Phys.*, vol. 344, no. 1, pp. 73–80, 1992, ISSN: 0939-7922. doi: 10.1007/BF01291023. [Online]. Available: <https://doi.org/10.1007/BF01291023>.
- [238] V. Aksinenko *et al.*, "Streamer chamber study of the cross sections and multiplicities in nucleus-nucleus interactions at the incident momentum of 4.5 GeV/c per nucleon," *Nucl. Phys. A*, vol. 348, no. 4, pp. 518–534, 1980, ISSN: 0375-9474. doi: [https://doi.org/10.1016/0375-9474\(80\)90269-9](https://doi.org/10.1016/0375-9474(80)90269-9). [Online]. Available: <http://www.sciencedirect.com/science/article/pii/0375947480902699>.
- [239] J. Hostachy *et al.*, "Elastic scattering of  $^{12}\text{C}$  on  $^{12}\text{C}$  at  $E/A = 120$  MeV/u and 200 MeV/u," *Phys. Lett. B*, vol. 184, no. 2, pp. 139–143, 1987, ISSN: 0370-2693. doi: [https://doi.org/10.1016/0370-2693\(87\)90557-0](https://doi.org/10.1016/0370-2693(87)90557-0). [Online]. Available: <http://www.sciencedirect.com/science/article/pii/0370269387905570>.
- [240] M Fukuda *et al.*, "Neutron halo in  $^{11}\text{Be}$  studied via reaction cross sections," *Phys. Lett. B*, vol. 268, no. 3, pp. 339–344, 1991, ISSN: 0370-2693. doi: [https://doi.org/10.1016/0370-2693\(91\)91587-L](https://doi.org/10.1016/0370-2693(91)91587-L). [Online]. Available: <http://www.sciencedirect.com/science/article/pii/037026939191587L>.
- [241] M Fukuda *et al.*, "Density distribution of  $^8\text{B}$  studied via reaction cross sections," *Nucl. Phys. A*, vol. 656, no. 2, pp. 209–228, 1999, ISSN: 0375-9474. doi: [https://doi.org/10.1016/S0375-9474\(99\)00308-5](https://doi.org/10.1016/S0375-9474(99)00308-5). [Online]. Available: <http://www.sciencedirect.com/science/article/pii/S0375947499003085>.
- [242] S Kox *et al.*, "Trends of total reaction cross sections for heavy ion collisions in the intermediate energy range," *Phys. Rev. C*, vol. 35, pp. 1678–1691, 5 1987. doi: 10.1103/PhysRevC.35.1678. [Online]. Available: <https://link.aps.org/doi/10.1103/PhysRevC.35.1678>.
- [243] M. Saint-Laurent *et al.*, "Total cross sections of reactions induced by neutron-rich light nuclei," *Z. Phys.*, vol. 332, no. 4, pp. 457–465, 1989, ISSN: 0939-7922. doi: 10.1007/BF01292431. [Online]. Available: <https://doi.org/10.1007/BF01292431>.
- [244] T Suzuki *et al.*, "Neutron Skin of Na Isotopes Studied via Their Interaction Cross Sections," *Phys. Rev. Lett.*, vol. 75, pp. 3241–3244, 18 1995. doi: 10.1103/PhysRevLett.75.3241. [Online]. Available: <https://link.aps.org/doi/10.1103/PhysRevLett.75.3241>.

- 
- [245] T Suzuki *et al.*, “Nuclear radii of  $^{14}\text{Be}$  and  $^{17,19}\text{B}$ ,” *AIP Conf. Proc.*, vol. 455, no. 1, pp. 84–89, 1998. doi: 10.1063/1.57311. eprint: <https://aip.scitation.org/doi/pdf/10.1063/1.57311>. [Online]. Available: <https://aip.scitation.org/doi/abs/10.1063/1.57311>.
- [246] M. Obuti *et al.*, “Interaction cross section and interaction radius of the  $^8\text{B}$  nucleus,” *Nucl. Phys. A*, vol. 609, no. 1, pp. 74–90, 1996, ISSN: 0375-9474. doi: [https://doi.org/10.1016/0375-9474\(96\)00267-9](https://doi.org/10.1016/0375-9474(96)00267-9). [Online]. Available: <http://www.sciencedirect.com/science/article/pii/S0375947496002679>.
- [247] B Blank *et al.*, “Total interaction and proton-removal cross-section measurements for the proton-rich isotopes  $^7\text{Be}$ ,  $^8\text{B}$ , and  $^9\text{C}$ ,” *Nucl. Phys. A*, vol. 624, no. 2, pp. 242–256, 1997, ISSN: 0375-9474. doi: [https://doi.org/10.1016/S0375-9474\(97\)81837-4](https://doi.org/10.1016/S0375-9474(97)81837-4). [Online]. Available: <http://www.sciencedirect.com/science/article/pii/S0375947497818374>.
- [248] D. Fang *et al.*, “Measurements of total reaction cross sections for some light nuclei at intermediate energies,” *Phys. Rev. C*, vol. 61, p. 064311, 6 2000. doi: 10.1103/PhysRevC.61.064311. [Online]. Available: <https://link.aps.org/doi/10.1103/PhysRevC.61.064311>.
- [249] A Ozawa *et al.*, “Measurements of interaction cross sections for light neutron-rich nuclei at relativistic energies and determination of effective matter radii,” *Nucl. Phys. A*, vol. 691, no. 3, pp. 599–617, 2001, ISSN: 0375-9474. doi: [https://doi.org/10.1016/S0375-9474\(01\)00563-2](https://doi.org/10.1016/S0375-9474(01)00563-2). [Online]. Available: <http://www.sciencedirect.com/science/article/pii/S0375947401005632>.
- [250] J. Powers, N. Wogman, and J. Cobble, “Mass Distribution in the Fission of  $\text{Np}^{237}$  and  $\text{Pu}^{239}$  by Intermediate-Energy Helium Ions,” *Phys. Rev.*, vol. 152, pp. 1096–1102, 3 1966. doi: 10.1103/PhysRev.152.1096. [Online]. Available: <https://link.aps.org/doi/10.1103/PhysRev.152.1096>.
- [251] J Jaros *et al.*, “Nucleus-nucleus total cross sections for light nuclei at 1.55 and 2.89 GeV/c per nucleon,” *Phys. Rev. C*, vol. 18, pp. 2273–2292, 5 1978. doi: 10.1103/PhysRevC.18.2273. [Online]. Available: <https://link.aps.org/doi/10.1103/PhysRevC.18.2273>.
- [252] S. Neumaier *et al.*, “Small-angle proton elastic scattering from the neutron-rich isotopes  $^6\text{He}$  and  $^8\text{He}$ , and from  $^4\text{He}$ , at 0.7 GeV in inverse kinematics,” *Nucl. Phys. A*, vol. 712, no. 3, pp. 247–268, 2002, ISSN: 0375-9474. doi: [https://doi.org/10.1016/S0375-9474\(02\)01274-5](https://doi.org/10.1016/S0375-9474(02)01274-5). [Online]. Available: <http://www.sciencedirect.com/science/article/pii/S0375947402012745>.
- [253] R. Warner *et al.*, “Total reaction and 2n-removal cross sections of 20-60 A MeV  $^{4,6,8}\text{He}$ ,  $^{6-9,11}\text{Li}$ , and  $^{10}\text{Be}$  on Si,” *Phys. Rev. C*, vol. 54, pp. 1700–1709, 4 1996. doi: 10.1103/PhysRevC.54.1700. [Online]. Available: <https://link.aps.org/doi/10.1103/PhysRevC.54.1700>.
- [254] A Ingemarsson *et al.*, “Reaction cross sections of intermediate energy  $^3\text{He}$ -particles on targets from  $^9\text{Be}$  to  $^{208}\text{Pb}$ ,” *Nucl. Phys. A*, vol. 696, no. 1, pp. 3–30, 2001, ISSN: 0375-9474. doi: [https://doi.org/10.1016/S0375-9474\(01\)01116-2](https://doi.org/10.1016/S0375-9474(01)01116-2). [Online]. Available: <https://www.sciencedirect.com/science/article/pii/S0375947401011162>.
- [255] A Auce *et al.*, “Reaction cross sections for 38, 65, and 97 mev deuterons on targets from  $^9\text{Be}$  to  $^{208}\text{Pb}$ ,” *Phys. Rev. C*, vol. 53, pp. 2919–2925, 6 1996. doi: 10.1103/PhysRevC.53.2919. [Online]. Available: <https://link.aps.org/doi/10.1103/PhysRevC.53.2919>.
- [256] B Wilkins and G Igo, “Total reaction cross sections for 22.4 ev deuterons,” Tech. Rep., 1962. [Online]. Available: <https://escholarship.org/uc/item/23x9v996>.

- 
- [257] S Mayo, W Schimmerling, M. Sametband, and R. Eisberg, “Reaction cross sections for 26.5 mev deuterons,” *Nucl. Phys.*, vol. 62, no. 3, pp. 393–400, 1965, issn: 0029-5582. doi: [https://doi.org/10.1016/0029-5582\(65\)90487-6](https://doi.org/10.1016/0029-5582(65)90487-6). [Online]. Available: <https://www.sciencedirect.com/science/article/pii/0029558265904876>.
- [258] A Auce *et al.*, “Reaction cross sections for 75-190 mev alpha particles on targets from  $^{12}\text{C}$  to  $^{208}\text{Pb}$ ,” *Phys. Rev. C*, vol. 50, pp. 871–879, 2 1994. doi: 10.1103/PhysRevC.50.871. [Online]. Available: <https://link.aps.org/doi/10.1103/PhysRevC.50.871>.
- [259] W Mayneord, “The significance of the röntgen,” *Unio Internationalis Contra Cancrum*, vol. 2, 271–282, 1937.
- [260] W. qing Shen, B. Wang, J. Feng, W. long Zhan, Y. tai Zhu, and E. pu Feng, “Total reaction cross section for heavy-ion collisions and its relation to the neutron excess degree of freedom,” *Nucl. Phys. A*, vol. 491, no. 1, pp. 130–146, 1989, issn: 0375-9474. doi: [https://doi.org/10.1016/0375-9474\(89\)90209-1](https://doi.org/10.1016/0375-9474(89)90209-1). [Online]. Available: <http://www.sciencedirect.com/science/article/pii/0375947489902091>.
- [261] L Sihver, M Lantz, and A Kohama, “Improved parametrization of the transparency parameter in Kox and Shen models of total reaction cross sections,” *Phys. Rev. C*, vol. 89, p. 067602, 6 2014. doi: 10.1103/PhysRevC.89.067602. [Online]. Available: <https://link.aps.org/doi/10.1103/PhysRevC.89.067602>.
- [262] R. Tripathi, F. Cucinotta, and J. Wilson, “Accurate universal parameterization of absorption cross sections,” *Nucl. Instrum. Methods Phys. Res. B*, vol. 117, no. 4, pp. 347–349, 1996, issn: 0168-583X. doi: [https://doi.org/10.1016/0168-583X\(96\)00331-X](https://doi.org/10.1016/0168-583X(96)00331-X). [Online]. Available: <http://www.sciencedirect.com/science/article/pii/0168583X9600331X>.
- [263] R. Tripathi, F. Cucinotta, and J. Wilson, “Accurate universal parameterization of absorption cross sections III – light systems,” *Nucl. Instrum. Methods Phys. Res. B*, vol. 155, no. 4, pp. 349–356, 1999, issn: 0168-583X. doi: [https://doi.org/10.1016/S0168-583X\(99\)00479-6](https://doi.org/10.1016/S0168-583X(99)00479-6). [Online]. Available: <http://www.sciencedirect.com/science/article/pii/S0168583X99004796>.
- [264] L Sihver *et al.*, “Current status of the “Hybrid Kurotama model” for total reaction cross sections,” *Nucl. Instrum. Methods Phys. Res. B*, vol. 334, pp. 34–39, 2014, issn: 0168-583X. doi: <https://doi.org/10.1016/j.nimb.2014.04.021>. [Online]. Available: <http://www.sciencedirect.com/science/article/pii/S0168583X14005230>.
- [265] J. Wellisch, I. Corneliu, B. Trieu, P. Truscott, and G. Folger, “Ion transport simulation using geant4 hadronic physics,” CERN, Tech. Rep., 2005.
- [266] L. Townsend and J. Wilson, “Comment on “trends of total reaction cross sections for heavy ion collisions in the intermediate energy range”,” *Phys. Rev. C*, vol. 37, pp. 892–893, 2 1988. doi: 10.1103/PhysRevC.37.892. [Online]. Available: <https://link.aps.org/doi/10.1103/PhysRevC.37.892>.
- [267] R. Tripathi, J. Wilson, and F. Cucinotta, “Accurate universal parameterization of absorption cross sections II — neutron absorption cross sections,” *Nucl. Instrum. Methods Phys. Res. B*, vol. 129, no. 1, pp. 11–15, 1997, issn: 0168-583X. doi: [https://doi.org/10.1016/S0168-583X\(97\)00121-3](https://doi.org/10.1016/S0168-583X(97)00121-3). [Online]. Available: <http://www.sciencedirect.com/science/article/pii/S0168583X97001213>.

- 
- [268] H De Vries, C. De Jager, and C De Vries, “Nuclear charge-density-distribution parameters from elastic electron scattering,” *At. Data Nucl. Data Tables*, vol. 36, no. 3, pp. 495–536, 1987, ISSN: 0092-640X. DOI: [https://doi.org/10.1016/0092-640X\(87\)90013-1](https://doi.org/10.1016/0092-640X(87)90013-1). [Online]. Available: <http://www.sciencedirect.com/science/article/pii/0092640X87900131>.
- [269] R. Tripathi, F. Cucinotta, and J. Wilson, “Medium modified nucleon–nucleon cross sections in a nucleus,” *Nucl. Instrum. Methods Phys. Res. B*, vol. 152, no. 4, pp. 425–431, 1999, ISSN: 0168-583X. DOI: [https://doi.org/10.1016/S0168-583X\(99\)00181-0](https://doi.org/10.1016/S0168-583X(99)00181-0). [Online]. Available: <http://www.sciencedirect.com/science/article/pii/S0168583X99001810>.
- [270] F Horst, “Measurement of nuclear reaction cross sections for applications in radiotherapy with protons, helium and carbon ions,” Ph.D. dissertation, Justus Liebig University Gießen, 2020. [Online]. Available: <http://geb.uni-giessen.de/geb/volltexte/2020/15052/>.
- [271] L Sihver *et al.*, “A comparison of total reaction cross section models used in particle and heavy ion transport codes,” *Adv. Space Res.*, vol. 49, no. 4, pp. 812–819, 2012, ISSN: 0273-1177. DOI: <https://doi.org/10.1016/j.asr.2011.11.029>. [Online]. Available: <https://www.sciencedirect.com/science/article/pii/S0273117711007897>.
- [272] T. T. Boehlen *et al.*, “Benchmarking nuclear models of fluka and geant4 for carbon ion therapy,” *Phys. Med. Biol.*, vol. 55, no. 19, p. 5833, 2010, ISSN: 0031-9155. DOI: <https://doi.org/10.1088/0031-9155/55/19/014>.
- [273] W Tinganelli, F Luoni, and M Durante, “What can space radiation protection learn from radiation oncology?” *Life sci. Space res.*, vol. 30, pp. 82–95, 2021, ISSN: 2214-5524. DOI: <https://doi.org/10.1016/j.lssr.2021.06.002>.
- [274] R. Schneider *et al.*, “Production and identification of  $^{100}\text{Sn}$ ,” *Z. Phys., A Hadrons nucl.*, vol. 348, no. 4, pp. 241–242, 1994, ISSN: 0939-7922. DOI: [10.1007/BF01305875](https://doi.org/10.1007/BF01305875). [Online]. Available: <https://doi.org/10.1007/BF01305875>.
- [275] V. Föhr *et al.*, “Experimental study of fragmentation products in the reactions  $^{112}\text{Sn} + ^{112}\text{Sn}$  and  $^{124}\text{Sn} + ^{124}\text{Sn}$  at 1A gev,” *Phys. Rev. C*, vol. 84, p. 054605, 5 2011. DOI: [10.1103/PhysRevC.84.054605](https://doi.org/10.1103/PhysRevC.84.054605). [Online]. Available: <https://link.aps.org/doi/10.1103/PhysRevC.84.054605>.
- [276] X. H. Zhang *et al.*, “Projectile fragmentation reactions of  $^{40}\text{Ar}$  at 57 MeV/nucleon,” *Phys. Rev. C*, vol. 85, p. 024621, 2 2012. DOI: [10.1103/PhysRevC.85.024621](https://doi.org/10.1103/PhysRevC.85.024621). [Online]. Available: <https://link.aps.org/doi/10.1103/PhysRevC.85.024621>.
- [277] J. Dudouet *et al.*, “Zero-degree measurements of  $^{12}\text{C}$  fragmentation at 95 MeV/nucleon on thin targets,” *Phys. Rev. C*, vol. 89, p. 064615, 6 2014. DOI: [10.1103/PhysRevC.89.064615](https://doi.org/10.1103/PhysRevC.89.064615). [Online]. Available: <https://link.aps.org/doi/10.1103/PhysRevC.89.064615>.
- [278] T. Ogawa, T. Sato, S. Hashimoto, D. Satoh, S. Tsuda, and K. Niita, “Energy-dependent fragmentation cross sections of relativistic  $^{12}\text{C}$ ,” *Phys. Rev. C*, vol. 92, p. 024614, 2 2015. DOI: [10.1103/PhysRevC.92.024614](https://doi.org/10.1103/PhysRevC.92.024614). [Online]. Available: <https://link.aps.org/doi/10.1103/PhysRevC.92.024614>.
- [279] B. Blank *et al.*, “New neutron-deficient isotopes from  $^{78}\text{Kr}$  fragmentation,” *Phys. Rev. C*, vol. 93, p. 061301, 6 2016. DOI: [10.1103/PhysRevC.93.061301](https://doi.org/10.1103/PhysRevC.93.061301). [Online]. Available: <https://link.aps.org/doi/10.1103/PhysRevC.93.061301>.
- [280] J. L. Rodríguez-Sánchez *et al.*, “Knockout and fragmentation reactions using a broad range of tin isotopes,” *Phys. Rev. C*, vol. 96, p. 034303, 3 2017. DOI: [10.1103/PhysRevC.96.034303](https://doi.org/10.1103/PhysRevC.96.034303). [Online]. Available: <https://link.aps.org/doi/10.1103/PhysRevC.96.034303>.



- 
- [281] D. Pérez-Loureiro *et al.*, “Neutron-rich fragments produced by in-flight fission of  $^{238}\text{U}$ ,” *Phys. Rev. C*, vol. 99, p. 054606, 5 2019. doi: 10.1103/PhysRevC.99.054606. [Online]. Available: <https://link.aps.org/doi/10.1103/PhysRevC.99.054606>.
- [282] Y. P. Viyogi *et al.*, “Fragmentations of  $^{40}\text{Ar}$  at 213 mev/nucleon,” *Phys. Rev. Lett.*, vol. 42, pp. 33–36, 1 1979. doi: 10.1103/PhysRevLett.42.33. [Online]. Available: <https://link.aps.org/doi/10.1103/PhysRevLett.42.33>.
- [283] J.-S. Li *et al.*, “Fragmentation cross section of 800 a · mev silicon ions on polyethylene target,” *J. Surf. Investig.*, vol. 10, no. 4, pp. 826–828, 2016, issn: 1819-7094. doi: 10.1134/S1027451016040303. [Online]. Available: <https://doi.org/10.1134/S1027451016040303>.
- [284] T. Gorbinet *et al.*, “Study of the reaction mechanisms of  $^{136}\text{Xe} + \text{p}$  and  $^{136}\text{Xe} + ^{12}\text{C}$  at 1 A GeV with inverse kinematics and large-acceptance detectors,” *Eur. Phys. J. A*, vol. 55, no. 1, p. 11, 2019, issn: 1434-601X. doi: 10.1140/epja/i2019-12683-8. [Online]. Available: <https://doi.org/10.1140/epja/i2019-12683-8>.
- [285] L.-C. Wang *et al.*, “Fragmentation cross sections of  $^{56}\text{Fe}$  at 471 amev on al, c, and  $\text{ch}_2$  targets,” *Acta Phys. Pol. B*, vol. 43, no. 8, pp. 1769–1782, 2012.
- [286] P. Lindstrom, “ISOTOPE PRODUCTION CROSS SECTIONS FROM THE FRAGMENTATION OF  $^{16}\text{O}$  AND  $^{12}\text{C}$  AT RELATIVISTIC ENERGIES,” Lawrence Berkeley National Laboratory, Tech. Rep., 1975. [Online]. Available: <https://escholarship.org/uc/item/0w02k5nz>.
- [287] C. Tull, “Relativistic heavy ion fragmentation at hiss,” Lawrence Berkeley National Laboratory, Tech. Rep. LBL-29718, 1990. [Online]. Available: <https://escholarship.org/uc/item/2tv8q4sg>.
- [288] C. A. Bertulani and G. Baur, “Electromagnetic processes in relativistic heavy ion collisions,” *Phys. Rep.*, vol. 163, no. 5, pp. 299–408, 1988, issn: 0370-1573. doi: [https://doi.org/10.1016/0370-1573\(88\)90142-1](https://doi.org/10.1016/0370-1573(88)90142-1). [Online]. Available: <https://www.sciencedirect.com/science/article/pii/0370157388901421>.
- [289] L. Chulkov *et al.*, “Interaction cross sections and matter radii of  $a = 20$  isobars,” *Nucl. Phys. A*, vol. 603, no. 2, pp. 219–237, 1996, issn: 0375-9474. doi: [https://doi.org/10.1016/0375-9474\(96\)00160-1](https://doi.org/10.1016/0375-9474(96)00160-1). [Online]. Available: <https://www.sciencedirect.com/science/article/pii/0375947496001601>.
- [290] C. Brechtmann, H. Drechsel, J. Beer, and W. Heinrich, “Cross sections for the production of fragments with  $z \geq 8$  by fragmentation of  $9 \leq z \leq 26$  nuclei,” *Int. j. radiat. appl. instrum. D*, vol. 12, no. 1, pp. 361–364, 1986, Special Volume Solid State Nuclear Track Detectors, issn: 1359-0189. doi: [https://doi.org/10.1016/1359-0189\(86\)90609-6](https://doi.org/10.1016/1359-0189(86)90609-6). [Online]. Available: <https://www.sciencedirect.com/science/article/pii/1359018986906096>.
- [291] M. Caamaño *et al.*, “Production cross-sections and momentum distributions of fragments from neutron-deficient  $^{36}\text{Ar}$  at 1.05A GeV,” *Nucl. Phys. A*, vol. 733, no. 3, pp. 187–199, 2004, issn: 0375-9474. doi: <https://doi.org/10.1016/j.nuclphysa.2004.01.070>. [Online]. Available: <https://www.sciencedirect.com/science/article/pii/S0375947404000880>.
- [292] H.-H. Ao *et al.*, “Fragmentation cross section of 800 a mev silicon ions on carbon target,” *Phys. Procedia*, vol. 80, pp. 46–49, 2015, 26th International Conference on Nuclear Tracks in Solids (ICNTS26) Kobe, Japan 15th – 19th September 2014, issn: 1875-3892. doi: <https://doi.org/10.1016/j.phpro.2015.11.091>. [Online]. Available: <https://www.sciencedirect.com/science/article/pii/S1875389215016089>.

- 
- [293] D. Pérez-Loureiro *et al.*, “Production of neutron-rich nuclei in fragmentation reactions of sn-132 projectiles at relativistic energies,” *Phys. Lett. B*, vol. 703, no. 5, pp. 552–556, 2011, ISSN: 0370-2693. DOI: <https://doi.org/10.1016/j.physletb.2011.08.037>. [Online]. Available: <https://www.sciencedirect.com/science/article/pii/S0370269311009853>.
- [294] J. Kurcewicz *et al.*, “Discovery and cross-section measurement of neutron-rich isotopes in the element range from neodymium to platinum with the frs,” *Phys. Lett. B*, vol. 717, no. 4, pp. 371–375, 2012, ISSN: 0370-2693. DOI: <https://doi.org/10.1016/j.physletb.2012.09.021>. [Online]. Available: <https://www.sciencedirect.com/science/article/pii/S0370269312009689>.
- [295] D.-H. Zhang, L.-C. Wang, Y.-J. Li, S. Kodaira, and N. Yasuda, “Projectile fragmentation of 471 A MeV  $^{56}\text{Fe}$  in polyethylene, carbon and aluminum targets,” *Radiat. Meas.*, vol. 50, pp. 56–60, 2013, 25th ICNTS, ISSN: 1350-4487. DOI: <https://doi.org/10.1016/j.radmeas.2012.06.014>. [Online]. Available: <https://www.sciencedirect.com/science/article/pii/S1350448712001837>.
- [296] L. Sihver *et al.*, “Projectile fragment emission angles in fragmentation reactions of light heavy ions in the energy region <200 mev/nucleon: Experimental study,” *Radiat. Meas.*, vol. 48, pp. 73–81, 2013, ISSN: 1350-4487. DOI: <https://doi.org/10.1016/j.radmeas.2012.08.006>. [Online]. Available: <https://www.sciencedirect.com/science/article/pii/S1350448712002569>.
- [297] S. Momota *et al.*, “Production of projectile-like fragments at intermediate energies,” *Nucl. Phys. A*, vol. 701, no. 1, pp. 150–155, 2002, 5th International Conference on Radioactive Nuclear Beams, ISSN: 0375-9474. DOI: [https://doi.org/10.1016/S0375-9474\(01\)01564-0](https://doi.org/10.1016/S0375-9474(01)01564-0). [Online]. Available: <https://www.sciencedirect.com/science/article/pii/S0375947401015640>.
- [298] S. Cecchini *et al.*, “Fragmentation cross sections of 158agev pb ions in various targets measured with cr39 nuclear track detectors,” *Nucl. Phys. A*, vol. 707, no. 3, pp. 513–524, 2002, ISSN: 0375-9474. DOI: [https://doi.org/10.1016/S0375-9474\(02\)00962-4](https://doi.org/10.1016/S0375-9474(02)00962-4). [Online]. Available: <https://www.sciencedirect.com/science/article/pii/S0375947402009624>.
- [299] R. Gupta and A. Kumar, “Charge changing cross-sections for 300 a mev fe26+ ion beam in al target,” *AIP Conf. Proc.*, vol. 1536, no. 1, pp. 1095–1096, 2013. DOI: 10.1063/1.4810617. eprint: <https://aip.scitation.org/doi/pdf/10.1063/1.4810617>. [Online]. Available: <https://aip.scitation.org/doi/abs/10.1063/1.4810617>.
- [300] A Korejwo, T Dzikowski, M Giller, J Wdowczyk, V. V. Perelygin, and A. V. Zarubin, “The measurement of isotopic cross sections of  $^{12}\text{C}$  beam fragmentation on liquid hydrogen at 3.66 GeV/nucleon,” *J. Phys. G Nucl. Part. Phys.*, vol. 26, no. 8, pp. 1171–1186, 2000. DOI: 10.1088/0954-3899/26/8/306. [Online]. Available: <https://doi.org/10.1088/0954-3899/26/8/306>.
- [301] A Korejwo, M Giller, T Dzikowski, V. V. Perelygin, and A. V. Zarubin, “Isotopic cross sections of  $^{12}\text{C}$  fragmentation on hydrogen measured at 1.87 and 2.69 GeV/nucleon,” *J. Phys. G Nucl. Part. Phys.*, vol. 28, no. 6, pp. 1199–1208, 2002. DOI: 10.1088/0954-3899/28/6/304. [Online]. Available: <https://doi.org/10.1088/0954-3899/28/6/304>.
- [302] S. Nagamiya *et al.*, “Production of pions and light fragments at large angles in high-energy nuclear collisions,” *Phys. Rev. C*, vol. 24, pp. 971–1009, 3 1981. DOI: 10.1103/PhysRevC.24.971. [Online]. Available: <https://link.aps.org/doi/10.1103/PhysRevC.24.971>.

- 
- [303] R. L. Auble *et al.*, “Light ion emission from reactions induced by 0.8-2.4 gev  $^{16}\text{O}$  projectiles,” *Phys. Rev. C*, vol. 28, pp. 1552–1564, 4 1983. doi: 10.1103/PhysRevC.28.1552. [Online]. Available: <https://link.aps.org/doi/10.1103/PhysRevC.28.1552>.
- [304] D. L. Olson, B. L. Berman, D. E. Greiner, H. H. Heckman, P. J. Lindstrom, and H. J. Crawford, “Factorization of fragment-production cross sections in relativistic heavy-ion collisions,” *Phys. Rev. C*, vol. 28, pp. 1602–1613, 4 1983. doi: 10.1103/PhysRevC.28.1602. [Online]. Available: <https://link.aps.org/doi/10.1103/PhysRevC.28.1602>.
- [305] W. R. Webber, J. C. Kish, and D. A. Schrier, “Individual charge changing fragmentation cross sections of relativistic nuclei in hydrogen, helium, and carbon targets,” *Phys. Rev. C*, vol. 41, pp. 533–546, 2 1990. doi: 10.1103/PhysRevC.41.533. [Online]. Available: <https://link.aps.org/doi/10.1103/PhysRevC.41.533>.
- [306] W. R. Webber, J. C. Kish, and D. A. Schrier, “Individual isotopic fragmentation cross sections of relativistic nuclei in hydrogen, helium, and carbon targets,” *Phys. Rev. C*, vol. 41, pp. 547–565, 2 1990. doi: 10.1103/PhysRevC.41.547. [Online]. Available: <https://link.aps.org/doi/10.1103/PhysRevC.41.547>.
- [307] J. R. Cummings *et al.*, “Determination of the cross sections for the production of fragments from relativistic nucleus-nucleus interactions. i. measurements,” *Phys. Rev. C*, vol. 42, pp. 2508–2529, 6 1990. doi: 10.1103/PhysRevC.42.2508. [Online]. Available: <https://link.aps.org/doi/10.1103/PhysRevC.42.2508>.
- [308] C. N. Knott *et al.*, “Interactions of relativistic neon to nickel projectiles in hydrogen, elemental production cross sections,” *Phys. Rev. C*, vol. 53, pp. 347–357, 1 1996. doi: 10.1103/PhysRevC.53.347. [Online]. Available: <https://link.aps.org/doi/10.1103/PhysRevC.53.347>.
- [309] C. Zeitlin *et al.*, “Heavy fragment production cross sections from 1.05 gev/nucleon  $^{56}\text{Fe}$  in c, al, cu, pb, and  $\text{CH}_2$  targets,” *Phys. Rev. C*, vol. 56, pp. 388–397, 1 1997. doi: 10.1103/PhysRevC.56.388. [Online]. Available: <https://link.aps.org/doi/10.1103/PhysRevC.56.388>.
- [310] C. N. Knott *et al.*, “Interactions of relativistic  $^{36}\text{Ar}$  and  $^{40}\text{Ar}$  nuclei in hydrogen: Isotopic production cross sections,” *Phys. Rev. C*, vol. 56, pp. 398–406, 1 1997. doi: 10.1103/PhysRevC.56.398. [Online]. Available: <https://link.aps.org/doi/10.1103/PhysRevC.56.398>.
- [311] A. Leistenschneider *et al.*, “Fragmentation of unstable neutron-rich oxygen beams,” *Phys. Rev. C*, vol. 65, p. 064607, 6 2002. doi: 10.1103/PhysRevC.65.064607. [Online]. Available: <https://link.aps.org/doi/10.1103/PhysRevC.65.064607>.
- [312] P. Napolitani, K.-H. Schmidt, A. S. Botvina, F. Rejmund, L. Tassan-Got, and C. Villagrasa, “High-resolution velocity measurements on fully identified light nuclides produced in  $^{56}\text{Fe}$  + hydrogen and  $^{56}\text{Fe}$  + titanium systems,” *Phys. Rev. C*, vol. 70, p. 054607, 5 2004. doi: 10.1103/PhysRevC.70.054607. [Online]. Available: <https://link.aps.org/doi/10.1103/PhysRevC.70.054607>.
- [313] C. Zeitlin *et al.*, “Fragmentation cross sections of 290 and 400 mev/nucleon  $^{12}\text{C}$  beams on elemental targets,” *Phys. Rev. C*, vol. 76, p. 014911, 1 2007. doi: <https://doi.org/10.1103/PhysRevC.76.014911>.
- [314] P. Bém *et al.*, “Low and medium energy deuteron-induced reactions on  $^{27}\text{Al}$ ,” *Phys. Rev. C*, vol. 79, p. 044610, 4 2009. doi: 10.1103/PhysRevC.79.044610. [Online]. Available: <https://link.aps.org/doi/10.1103/PhysRevC.79.044610>.

- 
- [315] T. Ye, S. Hashimoto, Y. Watanabe, K. Ogata, and M. Yahiro, “Analysis of inclusive ( $d, xp$ ) reactions on nuclei from  $^9\text{Be}$  to  $^{238}\text{U}$  at 100 mev,” *Phys. Rev. C*, vol. 84, p. 054606, 5 2011. doi: 10.1103/PhysRevC.84.054606. [Online]. Available: <https://link.aps.org/doi/10.1103/PhysRevC.84.054606>.
- [316] O Sokol *et al.*, “Oxygen beams for therapy: Advanced biological treatment planning and experimental verification,” *Phys. Med. Biol.*, vol. 62, no. 19, pp. 7798–7813, 2017. doi: 10.1088/1361-6560/aa88a0. [Online]. Available: <https://doi.org/10.1088/1361-6560/aa88a0>.

## List of Figures

2.1	Classic paradigm of radiation damage. . . . .	5
2.2	Schematic representation of the biological damage caused to the DNA by low and high-LET radiation [24]. . . . .	6
2.3	Comparison of the tracks of $0.45 \text{ MeV u}^{-1} {}^4\text{He}$ , $10 \text{ MeV u}^{-1} {}^{12}\text{C}$ , and $1000 \text{ MeV u}^{-1} {}^{56}\text{Fe}$ ions. They all have an LET of $150 \text{ keV } \mu\text{m}^{-1}$ . The simulations were performed with the TRAX code [25–27] software by Dr. Daria Boscolo. . . . .	7
2.4	Dose response curves of deterministic and stochastic effects [33]. . . . .	7
2.5	The global exploration roadmap [1]. . . . .	8
2.6	Proton fluence spectra of the most intense recorded SPEs [42]. . . . .	10
2.7	Relative contributions of the different elements to the baryonic component of the GCR spectrum [3]. . . . .	11
2.8	Differential energy spectra for hydrogen, helium, oxygen, and iron for the 1977 solar minimum and 1959 solar maximum, which are the two cycles with the strongest modulation of the past 50 years [4]. . . . .	12
2.9	Schematic representation of the ionisation processes that occur when heavy charged particles interact with matter (“Projectile” is the incoming particle and “Target” is the material). . .	14
2.10	Schematic representation of the abrasion-ablation model [4]. . . . .	17
2.11	Panel (a): simulated Bragg curves of $200 \text{ MeV } {}^1\text{H}$ , $200 \text{ MeV u}^{-1} {}^4\text{He}$ , $400 \text{ MeV u}^{-1} {}^{12}\text{C}$ , and $1000 \text{ MeV u}^{-1} {}^{56}\text{Fe}$ in polyethylene. The primary energy of the ions have been chosen for them to have the same range, starting from the choice of $1 \text{ GeV u}^{-1}$ for iron, as it is its peak energy in the GCR spectrum for the case of solar minimum (see Figure 2.8). Panel (b): Bragg curves of 100, 500, 800, and $1000 \text{ MeV u}^{-1} {}^{56}\text{Fe}$ ions. This Figure was produced with FLUKA. . . . .	19
2.12	Calculated total normalised dose and relative contributions of primary ions and fragments for $403 \text{ MeV u}^{-1} {}^{28}\text{Si}$ and $980 \text{ MeV u}^{-1} {}^{48}\text{Ti}$ in PE [4, 81]. The total normalised dose is compared with experimental data. . . . .	20
2.13	Panel (a): zoom-in of Figure 2.11 over the first 0.6 cm of PE for carbon and iron ions. Panel (b): schematic representation of the equilibrium reached in the build up effect. The depth of the effect corresponds to the range of the secondary particles causing it. . . . .	21
2.14	Panel (a): simulated Bragg curves of $400 \text{ MeV u}^{-1} {}^1\text{H}$ and ${}^4\text{He}$ ions in PE. Panel (b): zoom-in over the first 30 cm. This Figure was produced with FLUKA. . . . .	22
2.15	Comparison of the effective dose values leading to 3% REID for male and female individuals (data from [92]). . . . .	24
2.16	Relative contribution in fluence (green circles), dose (blue triangles), and dose equivalent (red squares) of different GCR ion species. The calculation was performed as an average over 1 year of solar minimum (worst case scenario) behind a $5 \text{ g cm}^{-2}$ aluminium shield [4].	27
2.17	Increasing relevance of light ions behind thick shields: calculated contribution (%) of different ions to GCR blood forming organs (BFO) dose equivalent in free space (from the left) and increasing thickness of simple spherical geometries (adapted from [109]). . . . .	28

2.18	Total dose equivalent as a function of aluminium (left) and polyethylene (right) shield thickness for the full GCR spectrum (adapted from [115]). . . . .	29
2.19	Representation of the inter-dependence of MC codes, cross-section models, theory, and experimental data. . . . .	32
3.1	Details about the ionisation chambers used for the experimental campaigns. . . . .	42
3.2	Panel (a): experimental setup used for 1 GeV $u^{-1}$ $^{56}\text{Fe}$ , 480 MeV $^1\text{H}$ and 430 MeV $u^{-1}$ $^4\text{He}$ beam irradiations: $d_3 = d_4 = 4$ cm, $d_1$ and $d_2$ are beam time dependent, $d_1$ being about 15 cm for iron ions and 26.5 cm for protons and helium ions, and $d_2$ about 1 m for iron ions and 135 cm for protons and helium ions. The distance between the target and the IC2 is also beam time dependent and varies between 0 and 2 cm. Panel (b): experimental setup used for 2 GeV $^1\text{H}$ beam irradiations: $d_3 = d_4 = d_5 = 4$ cm, $d_1 = 13.5$ cm, and $d_2 = 95.5$ cm. The distance between the target and the IC2 was 0 in this case. . . . .	43
3.3	1 GeV $u^{-1}$ $^{56}\text{Fe}$ -ion beam dose attenuation results for all tested materials up to $16 \text{ g cm}^{-2}$ . The dashed lines simply connect the experimental points. . . . .	45
3.4	Dose attenuation results obtained with 1 GeV $u^{-1}$ $^{56}\text{Fe}$ ions for three different aluminium alloys generally used in space. The dashed lines simply connect the experimental points. . . . .	46
3.5	Full paraffin Bragg curve measured with 1 GeV $u^{-1}$ $^{56}\text{Fe}$ ions. The dashed lines simply connect the experimental points. . . . .	46
3.6	Dose attenuation results obtained merely by exchanging the relative order of aluminium (spacecraft structural material) and lithium-based hydrides (shielding material). The dashed lines simply connect the experimental points. All experimental results were obtained with a 1 GeV $u^{-1}$ $^{56}\text{Fe}$ -ion beam. . . . .	47
3.7	Bragg-curves experimental results obtained with 480 MeV protons (Panel (a)) and 430 MeV $u^{-1}$ $^4\text{He}$ ions (Panel (b)) in HDPE and Moon regolith simulant. The dashed lines simply connect the experimental points. . . . .	48
3.8	Experimental results obtained with 480 MeV protons (Panel (a)) and 430 MeV $u^{-1}$ $^4\text{He}$ ions (Panel (b)) in HDPE, Moon regolith simulant, and LiH, up to the maximum irradiated LiH thickness ( $11.2 \text{ g cm}^{-2}$ ). HDPE and Moon regolith simulant data are the same as in Figure 3.7. The dashed lines simply connect the experimental points. . . . .	48
3.9	Same results of Figures 3.7 and 3.8 plotted by grouping them by target: HDPE data in Panel (a), Moon regolith simulant in Panel (b), and LiH in Panel (c). The dashed lines simply connect the experimental points. . . . .	49
3.10	Panel (a): 2 GeV proton beam $D_2/D_1$ experimental results. Panel (b): zoom-in the first $4 \text{ g cm}^{-2}$ , which correspond to the maximum LiH thickness available. The dashed lines simply connect the experimental points. . . . .	50
3.11	Panel (a): 2 GeV proton beam $D_3/D_1$ experimental results. Panel (b): zoom-in the first $4 \text{ g cm}^{-2}$ , which correspond to the maximum LiH thickness available. The dashed lines simply connect the experimental points. . . . .	51
3.12	Panel (a): Comparison between $D_2/D_1$ and $D_3/D_1$ experimental results for LiH and the 2 GeV proton beam. Panel (b): Same as Panel (a), but for PMMA. The dashed lines simply connect the experimental points. . . . .	52
3.13	Results obtained with all the different ion beams for LiH. The dashed lines simply connect the experimental points. . . . .	52



4.1	Comparison between experimental data and MC simulation results for the three tested aluminium alloys and for HDPE irradiated with the $1 \text{ GeV u}^{-1} {}^{56}\text{Fe}$ beam. The PHITS simulations were performed by Dr. Martina Giraudo and Claudio Cipriani. The Geant4 simulations were performed by Luca Bocchini. . . . .	58
4.2	Comparison between experimental data and MC simulation results for the pure and composite lithium-based hydrides irradiated with the $1 \text{ GeV u}^{-1} {}^{56}\text{Fe}$ beam. The PHITS simulations were performed by Dr. Martina Giraudo. The Geant4 simulations were performed by Luca Bocchini. . . . .	59
4.3	Comparison between experimental data and MC simulation results for Si, $\text{SiO}_2$ and highland Moon regolith irradiated with the $1 \text{ GeV u}^{-1} {}^{56}\text{Fe}$ beam. The PHITS simulations were performed by Claudio Cipriani. The Geant4 simulations were performed by Luca Bocchini. . . . .	60
4.4	Comparison between experimental data and simulation results for paraffin irradiated with the $1 \text{ GeV u}^{-1} {}^{56}\text{Fe}$ beam. In Panel (a) simulation results obtained with FLUKA, PHITS and Geant4 physics list QGSP_INCLXX are reported. In Panel (b) results obtained with several Geant4 physics lists are shown. The PHITS simulations were performed by Dr. Martina Giraudo. The Geant4 simulations were performed by Luca Bocchini. . . . .	61
4.5	Comparison between the result of MC simulations performed with FLUKA for pure-LiH target (Panel (a)) and Al2219 (Panel (b)), including (light green) and excluding (magenta) the dose contribution of delta electrons. The experimental data were obtained through irradiation with the $1 \text{ GeV u}^{-1} {}^{56}\text{Fe}$ beam and are the same as reported in Figure 3.3. The simulation results including the delta-electron contribution are the same as reported in Figure 4.2. . . . .	61
4.6	Comparison between $D_2/D_1$ experimental data and MC simulation results for PMMA and LiH irradiated with the $2 \text{ GeV } {}^1\text{H}$ beam. The PHITS simulations were performed by Dr. Martina Giraudo. The Geant4 simulations were performed by Luca Bocchini. . . . .	62
4.7	Comparison between $D_3/D_1$ experimental data and MC simulation results for PMMA and LiH irradiated with the $2 \text{ GeV } {}^1\text{H}$ beam. The PHITS simulations were performed by Dr. Martina Giraudo. The Geant4 simulations were performed by Luca Bocchini. . . . .	62
4.8	Comparison between the result of MC simulations performed with FLUKA for LiH (Panel (a)) and PMMA (Panel (b)), including (light green) and excluding (magenta) the dose contribution of delta electrons. The experimental data were obtained through irradiation with the $2 \text{ GeV } {}^1\text{H}$ beam. The experimental data and simulation results including the delta-electron contribution the same as reported in Figures 4.7 and 4.6. . . . .	64
5.1	Number of cross-section data reported in the reaction cross-section database as a function of the atomic number of the projectile nucleus $Z_p$ . Charge-changing cross-section entry numbers are shown in red and reaction in green. In Panel (a) all entries are shown, in Panel (b) only entries up to nickel projectiles. . . . .	68
5.2	Data collection for ${}^4\text{He}$ projectiles on different targets alongside the predictions of the Kox-Shen semi-empirical model (see section 5.1.2) to guide the reader's eyes. IK stands for Inverse Kinematic data (see Section 5.1.2). Different colours represent different targets. Both reaction and charge-changing cross-sections are plotted. The data are from references [156, 166, 167, 179, 180, 187, 188, 220, 229–232, 238, 251, 253]. . . . .	69
5.3	Same as Figure 5.2, but for ${}^{12}\text{C}$ projectiles. The data are from references [161, 166, 168, 170, 181, 184, 186, 189, 203, 208, 209, 211, 218, 220, 223, 225, 226, 234–236, 238, 239, 242, 248, 249, 251]. . . . .	69

- 
- 5.4 Same as Figure 5.2, but for  $^{56}\text{Fe}$  projectiles. For  $^{56}\text{Fe} + ^{64}\text{Cu}$ ,  $^{107}\text{Ar}$ ,  $^{238}\text{U}$ , both charge and mass-changing cross-section data were measured by Westfall *et al.* [174]. Therefore, two data points are reported for each system for the same energy. The data are from references [157, 161, 166, 170, 174, 178, 193, 196, 198, 220, 230, 235, 242]. . . . . 70
- 5.5 Data collections for  $^3\text{He}$ ,  $^4\text{He}$ ,  $^{12}\text{C}$ ,  $^{16}\text{O}$  and  $^{20}\text{Ne}$  projectiles on water alongside the predictions of the Kox-Shen semi-empirical model (see section 5.1.2) to guide the reader's eyes. Different colours represent different projectiles. Both reaction and charge-changing cross-sections are plotted. For  $^4\text{He} + \text{H}_2\text{O}$  both charge and mass-changing cross-section data were measured by Horst *et al.* [155, 156]. Mass-changing cross-sections were only measured by Horst *et al.* [156] for  $^3\text{He}$  and  $^4\text{He}$ . For all other projectiles, the data are charge-changing only. Therefore, the data points lie below the model predictions (see section 5.1.3). Data are from references [155, 156, 170, 211, 218]. . . . . 71
- 5.6 Dependence of Tripathi96 and Tripathi99 semi-empirical cross-section formulae on the nuclear radius for  $^4\text{He} + ^{56}\text{Fe}$  and  $^4\text{He} + ^{237}\text{Np}$ . Solid lines have been chosen for the version of the models that has been implemented within the present work. Data in Panel (a) are from references [178, 220, 230], in Panel (b) from reference [250]. . . . . 76
- 5.7 Comparison between the results of Tripathi99 for the systems  $^4\text{He} + ^9\text{Be}$  and  $^4\text{He} + ^{27}\text{Al}$ , obtained by using  $X_m = 1$  or  $X_m$  from Equation 5.21, which is recommended in Ref. [263] ("rec.  $X_m$ "), and the curves presented in Ref. [263]. The experimental data from the database have been plotted as well. For the case of  $X_m$  from Equation 5.21, the low-energy check implemented in Geant4 has been used: below  $6 \text{ MeV u}^{-1}$ , if the first derivative of the cross-section as a function of the energy is negative (i.e. values becoming smaller with increasing energy) the cross-section values are set to zero. IK stands for Inverse Kinematic data. Data in Panel (a) are from references [179, 187, 230], in Panel (b) from references [187, 220, 230, 238]. . . . . 77
- 5.8 Ratio of charge-changing to total reaction cross-section  $\sigma_{\text{cc}}/\sigma_{\text{R}}$  as a function of the projectile mass number, computed for projectile kinetic energy  $1 \text{ GeV.u}^{-1}$  and for different target materials. The total reaction cross-sections were calculated using the Kox-Shen model [261] and the neutron-removal cross-sections using the parametrisation by Mei *et al.* [79]. . . . . 79
- 5.9 Comparison between parametrisation results and cross-section data for the following systems:  $^4\text{He} + ^7\text{Li}$ ,  $^{12}\text{C}$ . IK stands for Inverse Kinematic data. To be noted that Tripathi96 is not the original model [262], but optimisations from Horst *et al.* [156] for  $^4\text{He}$  projectile are included. Data in Panel (a) are from reference [238], in Panel (b) from references [156, 167, 179, 180, 187, 188, 220, 229–231, 238, 251]. Error bar types of the Webber1990 and Igo1963 datasets are not specified to be only statistical or systematic as well. For Labie1973 and DeVries1982 they are only statistical. The rest are both statistical and systematic. . . . 81
- 5.10 Comparison between parametrisation results and cross-section data for the following systems:  $^4\text{He} + ^{16}\text{O}$ ,  $^{27}\text{Al}$ ,  $^{28}\text{Si}$ . IK stands for Inverse Kinematic data. To be noted that Tripathi96 is not the original model [262], but optimisations from Horst *et al.* [156] for  $^4\text{He}$  projectile are included. Data in Panel (a) from references [156, 179, 220], in Panel (b) from references [187, 220, 230, 238], in Panel (c) from references [156, 179, 253]. Error bar types of the Webber1990 and Igo1963 datasets are not specified to be only statistical or systematic as well. The rest are both statistical and systematic. . . . . 82
-



5.11	Comparison between parametrisation results and cross-section data for the following systems: $^{12}\text{C} + ^7\text{Li}$ , $^{12}\text{C}$ . IK stands for Inverse Kinematic data. Data in Panel (a) are from references [189], in Panel (b) from references [186, 220, 234, 236, 238, 239, 242, 248, 249, 251]. Error bar types of the Webber1990 and Takechi2009 datasets are not specified to be only statistical or systematic too. Hostachy1987 error bars are only statistical. The rest are both statistical and systematic. . . . .	83
5.12	Comparison between parametrisation results and cross-section data for the following systems: $^{12}\text{C} + ^{16}\text{O}$ , $^{27}\text{Al}$ , $^{28}\text{Si}$ . IK stands for Inverse Kinematic data. Data in Panel (a) from references [220, 248, 249], in Panel (b) from references [177, 220, 236, 242], in Panel (c) from references [177, 220, 238]. Error bar types of the Webber1990 and Takechi2009 datasets are not specified to be only statistical or systematic too. The rest are both statistical and systematic. . . . .	84
5.13	Comparison between parametrisation results and cross-section data for the following system: $^{16}\text{O} + ^{27}\text{Al}$ . The data point is from reference [242]. Uncertainties are both statistical and systematic. . . . .	85
5.14	Comparison between parametrisation results and cross-section data for the following systems: $^{20}\text{Ne} + ^{12}\text{C}$ , $^{27}\text{Al}$ . IK stands for Inverse Kinematic data. Data in Panel (a) are from references [175–177, 192, 220, 238, 242], in Panel (b) from reference [242]. Bochkarev1998 error bars are only statistical, while Webber1990 error bar type is not specified. The rest are both statistical and systematic. . . . .	85
5.15	Comparison between parametrisation results and cross-section data for the following system: $^{24}\text{Mg} + ^{12}\text{C}$ . Data are from references [177, 220]. The Webber1990 error bar type is not specified and Fang2001 are both statistical and systematic. . . . .	86
5.16	Comparison between parametrisation results and cross-section data for the following system: $^{28}\text{Si} + ^7\text{Li}$ . Data are from reference [253]. Error bars are both statistical and systematic. . . . .	86
5.17	Comparison between parametrisation results and cross-section data for the following systems: $^{56}\text{Fe} + ^7\text{Li}$ , $^{12}\text{C}$ . IK stands for Inverse Kinematic data. Data in Panel (a) are from reference [174] and data in Panel (b) from references [174, 220, 242]. Webber1990 error bar type is not specified, the rest are both statistical and systematic. . . . .	87
5.18	Comparison between Kox1987 mass and charge-changing cross-section data collected during different experimental campaigns for the following systems: $^{20}\text{Ne} + ^{27}\text{Al}$ and $^{56}\text{Fe} + ^{12}\text{C}$ . IK stands for Inverse Kinematic data, “cc” for charge-changing and “mc” for mass-changing cross-sections. Data in Panel (a) are from references [157, 182, 224, 228, 235, 242], in Panel (b) from references [157, 166, 170, 174, 196, 198, 220, 235, 242]. . . . .	88
5.19	Comparison between parametrisation results and cross-section data for the following systems: $^4\text{He} + ^{207}\text{Pb}$ and $^{56}\text{Fe} + ^{207}\text{Pb}$ . Data in Panel (a) are from references [179, 230, 238], in Panel (b) from reference [174]. . . . .	89
5.20	Relative differences between the maximum and minimum cross-section values predicted by the different parametrisations at $10\text{ GeV u}^{-1}$ (divided by the average value for all models) for different projectile nuclei as a function of the target atomic number. The dashed lines connect the points to guide the reader’s eyes. . . . .	89
5.21	Tripathi96 computed both using $D$ from Equation 5.15 (choice followed in the present work) and $D/3$ (as recommended in Ref. [262]) for the following systems: $^7\text{Li} + ^{12}\text{C}$ , $^{56}\text{Fe}$ . IK stands for Inverse Kinematic data. Data in Panel (a) are from reference [189], in Panel (b) from reference [174]. . . . .	90

5.22	Comparison between the results obtained for $^2\text{H}$ using Tripathi99 with the parameters reported in Ref. [263] and in this work (see Table 5.4). The experimental data from the database are plotted as well. For the case of $^2\text{H} + ^{56}\text{Fe}$ the agreement is shifted from the Wilkins1962 set of data with the parameters from Ref. [263], to Mayo1965 with the parameters from this work. The reason is that Mayo1965 data are an upgraded version of Wilkins1962 data, which were found out to be an underestimation of the real values. . . .	93
5.23	Comparison between the results obtained for $^3\text{He}$ using Tripathi99 with the parameters reported in Ref. [263] and in this work (see Table 5.5). The experimental data from the database are plotted as well. . . . .	95
5.24	Comparison between the results obtained for $^4\text{He}$ using Tripathi99 with the parameters reported in Ref. [263] and in this work (see Table 5.6). The experimental data from the database are plotted as well. . . . .	96
5.25	Number of cross-section data reported in the production cross-section database as a function of the atomic number of the projectile nucleus $Z_p$ . Elemental cross-section entry numbers are shown in blue and isotopic in cyan. In Panel (a) all entries are shown, in Panel (b) only entries up to nickel projectiles. . . . .	97
5.26	Total inclusive elemental fragment production cross-section data as a function of the fragment atomic number $Z_f$ for the following systems: $^{12}\text{C} + ^1\text{H}$ , $^{12}\text{C}$ , $^{27}\text{Al}$ , $\text{H}_2\text{O}$ . Data in Panel (a) are from references [166, 225, 300, 305], data in Panel (b) from references [170, 211, 225, 305], data in Panel (c) from references [170, 225], and data in Panel (d) from references [170, 211]. . . . .	99
5.27	Total inclusive elemental fragment production cross-section data as a function of the fragment atomic number $Z_f$ for the following system: $^{16}\text{O} + ^1\text{H}$ , $^{12}\text{C}$ , $^{27}\text{Al}$ . Data in Panel (a) are from references [166, 213, 228, 305], in Panel (b) from references [213, 228, 305], and in Panel (c) from references [213, 228]. . . . .	100
5.28	Total inclusive elemental fragment production cross-section data as a function of the fragment atomic number $Z_f$ for the following systems: $^{20}\text{Ne} + ^1\text{H}$ , $^{12}\text{C}$ , $^{27}\text{Al}$ . Data in Panel (a) are from references [157, 224, 228, 305], data in Panel (b) from references [157, 224, 228, 289, 305], and in Panel (c) from [157, 224, 228]. . . . .	101
5.29	Total inclusive elemental fragment production cross-section data as a function of the fragment atomic number $Z_f$ for the following systems: $^{24}\text{Mg} + ^1\text{H}$ , $^{12}\text{C}$ , $^{27}\text{Al}$ . Data in Panel (a) are from references [228, 305, 308], data in Panel (b) from references [217, 228, 305], and in Panel (c) from [217, 228]. . . . .	102
5.30	Total inclusive elemental fragment production cross-section data as a function of the fragment atomic number $Z_f$ for the following systems: $^{28}\text{Si} + ^1\text{H}$ , $^{12}\text{C}$ , $^{27}\text{Al}$ . Data in Panel (a) are from references [203, 209, 226, 305], in Panel (b) from references [168, 203, 209, 226, 305], and in Panel (c) from references [203, 209, 226]. . . . .	103
5.31	Total inclusive elemental fragment production cross-section data as a function of the fragment atomic number $Z_f$ for the following systems: $^{56}\text{Fe} + ^1\text{H}$ , $^7\text{Li}$ , $^{12}\text{C}$ , $^{27}\text{Al}$ . Data in Panel (a) are from references [166, 174, 198, 285, 305, 309], data in Panel (b) from [174], in Panel (c) from [174, 198, 285, 305, 307, 309], and data in Panel (d) from [285, 299, 307, 309]. . .	104
5.32	Total inclusive isotopic fragment production cross-section data as a function of the fragment mass number $A_f$ for the following systems: $^4\text{He} + ^{12}\text{C}$ . Data are from reference [167] at energies of 83.5, 125 and 176 MeV $\text{u}^{-1}$ . . . . .	105

---

5.33	Total inclusive isotopic fragment production cross-section data as a function of the fragment mass number $A_f$ for the following systems: $^{12}\text{C} + ^1\text{H}$ , $^{12}\text{C}$ , $^{16}\text{O}$ , $^{27}\text{Al}$ . Data in Panel (a) are from references [277, 286, 300, 301, 304], in Panel (b) from [220, 277, 278, 286, 288, 296, 302, 304], in Panel (c) from [277], and in Panel (d) from [277, 286, 304]. . . . .	106
5.34	Total inclusive isotopic fragment production cross-section data as a function of the fragment mass number $A_f$ for the following systems: $^{16}\text{O} + ^1\text{H}$ , $^{12}\text{C}$ , $^{27}\text{Al}$ . Data in Panel (a) are from references [286, 296], in Panel (b) from [286, 296, 297], and in Panel (c) from references [303, 304]. . . . .	107
5.35	Total inclusive isotopic fragment production cross-section data as a function of the fragment mass number $A_f$ for the following systems: $^{56}\text{Fe} + ^1\text{H}$ , $^{12}\text{C}$ . Data in Panel (a) are from reference [312] and in Panel (b) from [306]. . . . .	108
5.36	Total inclusive isotopic production cross-section data as a function of the projectile kinetic energy for the following reaction: $^4\text{He} + ^{12}\text{C} \rightarrow ^3\text{He}$ . Data are from reference [167]. . . . .	108
5.37	Total inclusive isotopic fragment production cross-section data as a function of the projectile kinetic energy for the following reactions: $^{12}\text{C} + ^1\text{H} \rightarrow ^1\text{H}$ , $^2\text{H}$ , $^3\text{H}$ , $^3\text{He}$ , $^4\text{He}$ , $^6\text{He}$ . Data are from references [277, 286, 300, 301]. . . . .	109
5.38	Total inclusive isotopic fragment production cross-section data as a function of the projectile kinetic energy for the following reactions: $^{12}\text{C} + ^{12}\text{C} \rightarrow ^1\text{H}$ , $^2\text{H}$ , $^3\text{H}$ , $^3\text{He}$ , $^4\text{He}$ , $^6\text{He}$ . Data are from references [277, 286, 302]. . . . .	110
5.39	Total inclusive isotopic fragment production cross-section data as a function of the projectile kinetic energy for the following reactions: $^{12}\text{C} + ^{27}\text{Al} \rightarrow ^1\text{H}$ , $^2\text{H}$ , $^3\text{H}$ , $^3\text{He}$ , $^4\text{He}$ , $^6\text{He}$ . Data are from references [277, 286]. . . . .	111
5.40	Screenshots of the web application. Panel (a) is from the data section of the total reaction cross-section database, without any filters applied. Panel (b) is from the plot section of the total reaction cross-section database, for the system $^{12}\text{C} + ^{12}\text{C}$ , including only mass-changing cross-section data and all parametrisation. . . . .	113



---

## List of Tables

---

2.1	Radiation weighting factors from ICRP 103 [22]. . . . .	4
2.2	Tissue weighting factors from ICRP 103 [22]. . . . .	5
2.3	Comparison of dose equivalent exposures in different scenarios. The variability on the Moon and Mars is due to the solar cycle and the altitude of the exposure. . . . .	22
2.4	Career effective dose limits (Sv) as recommended by different space agencies before 2021. . . . .	24
3.1	Beams used for the experimental campaigns of this work, listed in chronological order. Alongside the ion type, are reported details about the beam kinetic energy in $\text{MeV u}^{-1}$ , the beam full-width-half-maximum (FWHM) in mm, the beam intensity in ions per spill, the facility where the experiments were performed, and the project of which the experiments were part. . . . .	36
3.2	Aluminium 2024 average mass percentage composition. . . . .	37
3.3	Aluminium 2219 average mass percentage composition. . . . .	38
3.4	Aluminium 2195 average mass percentage composition. . . . .	38
3.5	Highland Moon regolith simulants mass percentage composition. LOI stands for Low-Order Impurities. . . . .	38
3.6	List of the materials used for the $1 \text{ GeV u}^{-1} {}^{56}\text{Fe}$ beam irradiations, alongside their mass densities ( $\rho$ ), areas perpendicular to the beam line ( $A$ ) and irradiated thicknesses ( $t$ ) with associated uncertainties. The thicknesses are given in areal densities. The numbers in parentheses refer to the uncertainties of the values and apply to the least significant digits. . . . .	40
3.7	List of the materials used for the $2 \text{ GeV } {}^1\text{H}$ beam irradiations, alongside their mass densities ( $\rho$ ), areas perpendicular to the beam line ( $A$ ) and irradiated thicknesses ( $t$ ) with associated uncertainties. The thicknesses are given in areal densities. The numbers in parentheses refer to the uncertainties of the values and apply to the least significant digits. . . . .	41
3.8	List of the materials used for the $480 \text{ MeV } {}^1\text{H}$ and $430 \text{ MeV u}^{-1} {}^4\text{He}$ beam irradiations, alongside their mass densities ( $\rho$ ), areas perpendicular to the beam line ( $A$ ) and irradiated thicknesses ( $t$ ) with associated uncertainties. The thicknesses are given in areal densities. The numbers in parentheses refer to the uncertainties of the values and apply to the least significant digits. . . . .	41
5.1	System-dependent values for $T_1$ and $D$ used in the Tripathi subroutine of PHITS and in the present work. . . . .	78
5.2	Recommendations for parameters to be used for Li isotopes projectiles within Tripathi96. In Reference [262], $T_1 = 40$ , $d = 1.75$ , and $f = 1$ for all of the systems. . . . .	91
5.3	Recommendations for parameters to be used for different projectiles within Tripathi96. In Reference [262], $T_1 = 40$ , $d = 1.75$ , $A = 0.292$ , and $f = 1$ for all of the systems. . . . .	91

---

5.4	Recommendations of parameters to be used for $^2\text{H}$ projectiles within Tripathi99, from Ref. [263] and this work. In the PHITS implementation, the parameters presented within Ref. [263] plus specific ones for $^2\text{H} + ^4\text{He}$ are used. Systems that did not require any change with respect to the PHITS implementation (e.g. $^2\text{H} + ^2\text{H}$ , $^4\text{He}$ ) are not reported. Exceptions to the rules are reported right under it (see $^2\text{H} + ^{56}\text{Fe}$ ). When no specifications about the isotope are there, the recommendations are to be considered valid for every isotope of the element. . . . .	92
5.5	Recommendations for parameters $R_C$ , $T_1$ , and $\alpha$ to be used for $^3\text{He}$ projectiles in Tripathi99 [263]. The parameters from the original model are compared to the parameters recommended in this work. Systems that did not require any change in these parameters (e.g. $^3\text{He} + ^{12}\text{C}$ , $^{27}\text{Al}$ ) are not reported. . . . .	93
5.6	Recommendations of parameters to be used for $^4\text{He}$ projectiles within Tripathi99, from Ref. [263] and this work. Eq. 5.16 comes from Ref. [262, 263], Eq. 5.19 from Ref. [156]. Systems that did not require any change to the parametrisation presented in Ref. [263] are not reported. When no specifications about the isotope are there, the recommendations are to be considered valid for every isotope of the element. . . . .	94
5.7	Recommendations of parametrisations to be used for systems of interest for radiation protection in space for light and heavy systems and at different energy ranges. . . . .	95

---

# Acknowledgments

---

I would like to acknowledge all the people whose work, guidance, and support made this thesis work possible.

I would like to thank Professor Marco Durante for giving me the opportunity of starting a PhD in the biophysics department of GSI, for trusting me with a project such as the generation of the cross-section databases, for assigning me the review of papers, for giving me the opportunity to teach at the TUDa, teaching me, and most importantly mentoring and taking care of me during my PhD. He assigned me to the Space Physics group led by Dr Uli Weber, who I would like to thank for the help, support, teachings, caring and understanding during my PhD. I was lucky to have them guiding me through the path. I would also to thank my second supervisor Professor Markus Roth for taking the time to participate in the periodic PhD meetings and giving me feedback about my work.

I would also like to thank Maria Didonna-Schnellbacher, Dr Corinna Kausch, Martine Kräckmann, and Dr Markus Domschke for the help with all the bureaucracy and technical aspects of the PhD.

I would also like to thank my colleagues, in particular, Dr Felix Horst, who included me in many of his projects, taught me about making good science and helped me through all of my projects, Dr Daria Boscolo, P.I. of the DEIMOS campaign, who helped me through all the experimental campaigns and MC simulations, Dr Claire-Anne Reidel, who helped me in the cross-section parametrisation work and experiments, and Dr Christoph Schuy for the help with the experiments. I also thank them for giving me feedback about the thesis, together with Dr Tabea Pfuhl, Dr Alexander Helm, and Timo Steinsberger.

I would like to thank Uli, my group, and the rest of the GSI Biophysics Department for the support, ideas, help, and the fun beam times we did together. I have learned a lot during my PhD.

I would also like to thank the students that helped me through their time at GSI, in particular Laura Bagnale for her contribution to the reaction cross-section database creation, Anastasiia Quarz for the generation of the web application, and Moritz Westermayer for the discussions about the DEIMOS data.

I would like to thank all the ROSSINI3 team, in particular Dr Giovanni Santin, project officer, Dr Martina Giraudo, in charge of the management and PHITS simulations, Luca Bocchini and Claudio Cipriani for the Geant4 and PHITS simulations, and Professor Marcello Baricco, Gianluca Fiore, and Andrea Binello from the lithium-based hydrides and the paraffin targets production.

I would also like to thank our US collaborators to the cross-section databases: Dr Wouter De Wet, Dr Ryan Norman and, in particular, Dr John Norbury, who became a mentor and a guide to me, gave me precious advice, trusted me with the project, presenting at the WANDA conference, and reviewing papers. I would also like to thank Dr Tatsuhiko Sato and Dr Hiroshi Iwase for helping and supporting the implementation of Tripathi99 and Hybrid-Kurotama models, Dr Albana Topi and Dr Michael Krämer for the help and suggestions regarding the data collections, and Dr Maurizio Spurio, Dr Z Y Sun, Dr Jean-Éric Ducret, Dr David Perez Loureiro, Dr Jun-Sheng LI, Dr Dong-Hai Zhang, Dr Andrea Jungclaus, Dr Ingrid Schall and Dr Maya Takechi for providing further details about the data reported in their publications that have been included in the databases.

For the realisation of the ROSSINI3 experiments, I would like to additionally thank the GSI operational team and, for the DEIMOS experiments, the HIT operational team.

The HGS-HiRe graduate school allowed me to participate in learning schools and events, and in the soft

---

skills courses, which were extremely useful to my personal development as a colleague and as a person. A special thanks go to Gerard, Emma, Michael, and Steve.

I would also like to thank all my other colleagues who helped me during my PhD, from a personal and professional point of view, my family, in particular my mum, who corrected the English of several of my works, and my friends, in particular Salmo who helped me in many technical aspects. I would need too many additional pages to thank all of you properly.

Last but not least, I thank my partner, Masood, who has been a key personal and professional support and helped me through each step.



---

## Erklärungen laut Promotionsordnung

---

### § 8 Abs. 1 lit. c PromO

---

Ich versichere hiermit, dass die elektronische Version meiner Dissertation mit der schriftlichen Version übereinstimmt.

### § 8 Abs. 1 lit. d PromO

---

Ich versichere hiermit, dass zu einem vorherigen Zeitpunkt noch keine Promotion versucht wurde. In diesem Fall sind nähere Angaben über Zeitpunkt, Hochschule, Dissertationsthema und Ergebnis dieses Versuchs mitzuteilen.

### § 9 Abs. 1 PromO

---

Ich versichere hiermit, dass die vorliegende Dissertation selbstständig und nur unter Verwendung der angegebenen Quellen verfasst wurde.

### § 9 Abs. 2 PromO

---

Die Arbeit hat bisher noch nicht zu Prüfungszwecken gedient.

Darmstadt, 11. Mai 2022

---

F. Luoni